

**A Novel SCP-RICM Assay Application:
Indirect Detection of Analytes by Modulation
of Protein-Protein Interactions**

DISSERTATION

zur Erlangung des akademischen Grades

Doctor rerum naturalium

(Dr. rer. nat.)

vorgelegt

**der Fakultät Biologie
der Technischen Universität Dresden**

von

Lisa Hannusch

Geboren am 21.03.1989 in Cottbus

Eingereicht am 14.04.2021

Die Dissertation wurde in der Zeit von 11/2015 bis 04/2021
im Institut für Genetik angefertigt.

LIST OF PUBLICATIONS

Patent

Hannusch L, Rödel G, Dahmann C, Ostermann K, Pompe T, Rettke D. Verfahren und Kit zum Nachweis von Toxinen und Pathogenen. September 2020, DE102020124279.4 (submitted).

Conference contributions

Hannusch L, Pompe T, Rödel G, Ostermann K. Quantification of specific protein-protein interactions using Soft Colloidal Probes. *Dresdener Sensor Symposium*, December 2017, Dresden (Germany), *poster presentation*.

Hannusch L, Pompe T, Rödel G, Ostermann K. Quantification of specific protein-protein interactions using Soft Colloidal Probes. *Biomolecular Interactions: Methods & Applications*, September 2018, Prague (Czech Republic), *poster presentation and short talk session*.

TABLE OF CONTENT

Table of Content	I
List of Figures	VII
List of Tables	IX
List of Abbreviations	XI
1 Introduction	1
1.1 Biosensors	1
1.2 Analytical Detection Methods: Copper	2
1.3 SCP-RICM Assay	3
1.3.1 Sensor Chip Surface	4
1.3.2 Soft Colloidal Probes	5
1.3.3 Reflection Interference Contrast Microscopy	6
1.4 Hydrophobins	9
1.4.1 Structure and Functions of Hydrophobins	9
1.4.2 <i>Ex vivo</i> Applications of Hydrophobins	11
1.4.3 Class I Hydrophobin: Ccg-2	12
1.5 Mitochondrial Respiratory Chain	14
1.5.1 Copper Transport in Yeast	14
1.5.2 <i>S. cerevisiae</i> Sco1 protein	18
1.5.3 <i>S. cerevisiae</i> Cox17 protein	21
1.6 SCP-RICM Assay for Copper Detection	23
1.7 Aim of the Study	24
2 Materials and Methods	25
2.1 Laboratory Equipment	25
2.1.1 Devices	25
2.1.2 Chemicals	26

2.1.3	Consumables	28
2.1.4	Antibodies.....	29
2.1.5	Enzymes.....	30
2.1.6	Molecular Weight Standards.....	30
2.1.7	DNA Oligonucleotides.....	31
2.1.8	Plasmids and Vectors.....	32
2.2	Microorganisms	33
2.2.1	Strains	33
2.2.2	Cultivation of Microorganisms.....	34
2.2.3	Preparation of Electrocompetent <i>E. coli</i> Cells.....	36
2.2.4	Preparation of <i>E. coli</i> Glycerol Stocks.....	36
2.3	Protein Design.....	37
2.4	Molecular Cloning Methods	38
2.4.1	Vector Template Preparation.....	38
2.4.2	Agarose Gel Electrophoresis	40
2.4.3	DNA Extraction from Agarose Gels	41
2.4.4	Polymerase Chain Reaction	41
2.4.5	DNA Restriction Digest.....	42
2.4.6	DNA Dialysis	43
2.4.7	Ligation of DNA Fragments	43
2.4.8	Isolation of DNA from <i>E. coli</i>	44
2.4.9	DNA Sequencing	45
2.4.10	Transformation of <i>E. coli</i> via Electroporation	45
2.5	Protein Detection and Quantification	46
2.5.1	SDS PAGE	46
2.5.2	Coomassie Staining	50
2.5.3	Western Blot Analysis	51

2.5.4	Immunological Detection	51
2.5.5	Protein Quantification: Lowry Assay	52
2.5.6	Protein Quantification: Bradford Assay.....	53
2.5.7	Protein Quantification: NanoDrop Measurement	53
2.6	Protein Purification and Storage	54
2.6.1	Expression Analysis of Recombinant Proteins	54
2.6.2	Solubility Analysis	54
2.6.3	Protein Purification by Ni ²⁺ Affinity Chromatography	55
2.6.4	Quantification of Purified Proteins	64
2.6.5	Dialysis of Purified Proteins	65
2.7	Glass Surface Functionalization	65
2.7.1	Glass Surface Preparation	66
2.7.2	Hydrophobin and Fusion Protein-Based Coating	66
2.7.3	Contact Angle Measurement	67
2.7.4	DroPS Test	67
2.7.5	Atomic Force Microscopy	67
2.8	SCP Functionalization.....	68
2.8.1	Functionalization of SCPs with Proteins	68
2.8.2	Validation of SCP Functionalization with FITC Staining	69
2.9	SCP-RICM Assay and Its Analysis	69
3	Results	73
3.1	Generation of Recombinant Fusion Proteins	73
3.1.1	Sco1 and Sco1Δ95.....	73
3.1.2	Cox17	84
3.1.3	Ccg-2.....	88
3.1.4	Overview: Optimization of Expression and Purification of Recombinant Proteins.....	90
3.2	His-Tag Cleavage.....	92

3.3	Chip Surface Functionalization	94
3.3.1	Optimization of the Glass Chip Preparation	94
3.3.2	Macroscopic Properties of the Functionalized Chip Surface	95
3.3.3	AFM Measurements	102
3.3.4	Theoretical Package of Hydrophobin Ccg-2 on the Chip Surface	103
3.4	SCP Functionalization.....	104
3.4.1	SCP Functionalization and FITC Staining	104
3.4.2	Theoretical Package of Proteins on SCPs	106
3.5	SCP-RICM Assay	107
4	Discussion and Further Prospectives	113
4.1	Discussion: SCP-RICM Assay and Protein-Protein Interaction.....	113
4.2	Outlook and Further Prospects	119
4.2.1	Heterologous Protein Expression and Purification: Methods, Cleavage and Refolding 119	
4.2.2	Further Analysis of Chip Surface Functionalization	124
4.2.3	Alternative Chip Surface Functionalization Methods	126
4.2.4	SCP-RICM Assay: Data Acquisition and Evaluation	128
4.2.5	SCP-RICM Assay: Copper Detection	130
4.2.6	Exploiting the SCP-RICM Assay using Protein-Protein Interactions.....	131
4.2.7	Exploiting the SCP-RICM Assay with Alternative Interactions.....	133
5	Summary.....	137
6	Bibliography.....	141
7	Appendix	165
7.1	Sequences of Protein Constructs	165
7.1.1	Sequences of the Protein Construct Cox17_a	165
7.1.2	Sequences of the Hydrophobin-Cox17 Fusion Protein Cox17_b	165
7.1.3	Sequences of the Hydrophobin-Cox17 Fusion Protein Construct Cox17_c	166
7.1.4	Sequences of the Protein Construct Sco1_a and Sco1Δ95_a.....	167

7.1.5	Sequences of the Hydrophobin-Sco1 Fusion Protein Constructs Sco1_b and Sco1 Δ 95_b	169
7.1.6	Sequences of the Hydrophobin-Sco1 Fusion Protein Constructs Sco1_c and Sco1 Δ 95_c	171
7.1.7	Sequences of the Hydrophobin Ccg-2	173
7.2	pET-28b(+): Plasmid Map	173
7.3	Nickel Removal During Dialysis	175
7.4	DGR Assay.....	176
7.5	SCP diameter	179
Acknowledgements.....		181
Declaration of Authorship.....		183

LIST OF FIGURES

FIGURE 1. MICROFLUIDIC PRODUCTION OF HYDROGEL SPHERES.	5
FIGURE 2. SCHEMATIC REPRESENTATION OF THE SCP-FUNCTIONALIZATION WITH PROTEINS VIA EDC/NHS CHEMISTRY.	6
FIGURE 3. MICROSCOPY SETUP FOR A TYPICAL SCP-RICM ASSAY.	7
FIGURE 4. STRUCTURAL COMPARISON OF CLASS I AND CLASS II HYDROPHOBINS.	10
FIGURE 5. RIBBON DIAGRAM FROM THE CLASS I HYDROPHOBIN CCG-2.	13
FIGURE 6. MECHANISTIC SCHEME OF THE CHAPERONE-TARGET-INTERACTION FOR COPPER EXCHANGE.	15
FIGURE 7. COPPER HOMEOSTASIS IN <i>S. CEREVISIAE</i> AND PROPOSED MODEL OF CHAPERONE-TARGET INTERACTION.	16
FIGURE 8. SIMPLIFIED SCHEME OF COPPER TRANSFER AT THE MITOCHONDRIAL IM.	16
FIGURE 9. CRYSTAL STRUCTURE OF THE YSCO1 PROTEIN WITH TRUNCATED TRANSMEMBRANE DOMAIN AND HYDROPHOBICITY COLOR-CODING.	19
FIGURE 10. REPRESENTATION OF ELECTROSTATIC SURFACES OF Cu(I)-YCOX17 (LEFT), APO-YSCO1 (CENTER), AND MODELLED YCOX2 (RIGHT).	20
FIGURE 11. SCHEME OF PROPOSED COPPER UPTAKE FOR YSCO1.	21
FIGURE 12. SOLUTION STRUCTURE OF YCOX17 WITH ONE Cu(I) ION BOUND.	22
FIGURE 13. SCHEMATIC REPRESENTATION OF THE SCP-RICM ASSAY FOR INDIRECT ANALYTE DETECTION.	23
FIGURE 14. THE CHARACTERISTIC APPEARANCE OF MARKERS ON AGAROSE GELS, SDS PAGE GELS, AND WESTERN BLOTS, RESPECTIVELY.	31
FIGURE 15. SCHEMATIC REPRESENTATION OF THE PROTEIN DESIGN OF THREE CONSTRUCTS USED IN DIFFERENT WAYS WITHIN THE EXPERIMENTAL SETUP.	38
FIGURE 16. EXEMPLARY IMAGES OF AN SCP AND ITS INTERFERENCE PATTERN.	71
FIGURE 17. IMAGES FROM AGAROSE GEL ELECTROPHORESIS AFTER A PCR (A) AND DIGESTION (B) OF CLONES OF LIGATED SAMPLES. ..	74
FIGURE 18. EXPRESSION ANALYSIS IN T7 SHUFFLE EXPRESS LYSY <i>E. COLI</i> AND PURIFICATION OF SCO1_A.	75
FIGURE 19. EXPRESSION ANALYSIS IN T7 SHUFFLE EXPRESS LYSY <i>E. COLI</i> AND PURIFICATION OF SCO1_B.	77
FIGURE 20. EXPRESSION ANALYSIS IN T7 SHUFFLE EXPRESS LYSY <i>E. COLI</i> AND PURIFICATION OF SCO1_C.	78
FIGURE 21. EXPRESSION ANALYSIS IN LEMO21 (DE3) <i>E. COLI</i> AND PURIFICATION OF SCO1Δ95_A.	79
FIGURE 22. EXPRESSION ANALYSIS IN T7 SHUFFLE EXPRESS LYSY <i>E. COLI</i> AND PURIFICATION OF SCO1Δ95_B.	81
FIGURE 23. EXPRESSION ANALYSIS IN T7 SHUFFLE EXPRESS LYSY <i>E. COLI</i> AND PURIFICATION OF SCO1Δ95_C.	82
FIGURE 24. EXEMPLARY EXPRESSION AND SOLUBILITY ANALYSIS OF SCO1Δ95_C IN LEMO21 (DE3) <i>E. COLI</i> TESTED DIFFERENT L-RHAMNOSE CONCENTRATIONS IN μM.	83
FIGURE 25. EXPRESSION ANALYSIS IN LEMO21 (DE3) <i>E. COLI</i> AND NATIVE PURIFICATION OF COX17_A.	85
FIGURE 26. EXPRESSION ANALYSIS IN T7 SHUFFLE EXPRESS LYSY <i>E. COLI</i> AND PURIFICATION OF COX17_B.	86
FIGURE 27. EXPRESSION ANALYSIS IN T7 SHUFFLE EXPRESS LYSY AND NATIVE PURIFICATION OF COX17_C.	87
FIGURE 28. EXPRESSION ANALYSIS IN T7 SHUFFLE EXPRESS LYSY <i>E. COLI</i> AND DENATURED PURIFICATION OF CCG-2.	89
FIGURE 29. CLEAVAGE AT THE TEV RECOGNITION SITE WITH THE ACTEV PROTEASE TO REMOVE THE HIS-TAG.	92
FIGURE 30. DROPS TEST OF PURIFIED PROTEIN CONSTRUCT CCG-2.	96

FIGURE 31. CAMS WITH DDH ₂ O DROPS ON GLASS CHIP SURFACES, FUNCTIONALIZED WITH DIFFERENT HYDROPHOBIN CCG-2 CONCENTRATIONS.....	97
FIGURE 32. COMPARING CAM ON CCG-2-FUNCTIONALIZED GLASS CHIPS AFTER WASHING WITH SDS.	100
FIGURE 33. CAM OF FUNCTIONALIZED SURFACES WITH DIFFERENT FUSION PROTEINS, THE HYDROPHOBIN CCG-2, AND THEIR MIXTURES.	101
FIGURE 34. AFM IMAGES OF SURFACES FUNCTIONALIZED WITH CCG-2 AND OF THE COX17_C PROTEIN CONSTRUCT.	102
FIGURE 35. FITC STAINING OF SCO1Δ95_A-FUNCTIONALIZED SCPS.	105
FIGURE 36. SPECTROSCOPIC ABSORBANCE MEASUREMENTS OF DIFFERENT CU(I)CL SOLUTIONS.	108
FIGURE 37. CU(I)-DEPENDENT RICM MEASUREMENTS ON COX17_C COATED CHIPS WITH CLSCO1Δ95_A-SCPS (A) AND WITH BSA-SCPS (B).....	109
FIGURE 38. CU(I)-DEPENDENT RICM MEASUREMENTS WITH DIFFERENT COX17 AND SCO1 PROTEIN DERIVATIVES.....	110
FIGURE 39. SCHEMATIC DESCRIPTION OF THE WORK.....	138
FIGURE 40. NOVAGEN PET-28A-C(+) VECTOR MAP AND DISPLAY OF THE CLONING REGION. (ADAPTED FROM MERCK KGAA (GERMANY))	174
FIGURE 41. QUANTIFICATION OF Ni ²⁺ RESIDUES IN DIALYZED PROTEIN SAMPLES VIA THE NH ₃ AND DMG COMPLEXATION.	175
FIGURE 42. RUBIC BUFFER SCREEN SETUP.	176
FIGURE 43. DGR MEASUREMENTS OF HYDROPHOBIN CCG-2 FOR ALL 96 BUFFERS.	177
FIGURE 44. SELECTION OF GRAPHS AND 96 WELL-PLATE REPRESENTATION OF THE MELTING TEMPERATURES T _M	178
FIGURE 45. MEASUREMENTS OF SCP DIAMETERS.....	179

LIST OF TABLES

TABLE 1. LIST OF DEVICES USED IN THIS WORK.	25
TABLE 2. LIST OF LABORATORY CHEMICALS USED IN THIS WORK.	27
TABLE 3. LIST OF CONSUMABLES USED FOR THIS WORK.	28
TABLE 4. LIST OF ANTIBODIES AND THEIR CONCENTRATIONS USED WITHIN THIS STUDY.	30
TABLE 5. LIST OF OLIGONUCLEOTIDES USED IN THIS STUDY. THE RED COLOR MARKS THE RESTRICTION SITES (RS), THE PURPLE THE CODING FOR TEV CLEAVAGE SITE, THE ORANGE COLOR THE GLYCINE-SERINE LINKER, AND THE BLACK CAPITAL LETTERS MARK THE OVERLAPPING REGIONS.	31
TABLE 6. LIST OF VECTORS USED IN THIS STUDY.	32
TABLE 7. PROTOCOL FOR LB MEDIA AND LB AGAR PLATES.	35
TABLE 8. PROTOCOL FOR YEAST EXTRACT-PEPTONE-DEXTROSE (YPD) MEDIA	36
TABLE 9. PROTOCOL FOR LYSIS BUFFER.	39
TABLE 10. PROTOCOL FOR 1X TRIS-ACETATE-EDTA (TAE) BUFFER SOLUTION. IT CAN BE STORED IN A UP TO 50X TAE STOCK SOLUTION.	40
TABLE 11. PROTOCOL FOR 6X DNA LOADING DYE.	40
TABLE 12. OVERVIEW OF SAMPLE CONDITIONS FOR PREPARATION AND RUNNING OF AGAROSE GEL ELECTROPHORESIS.	40
TABLE 13. PROTOCOL FOR A PCR WITH THE PHUSION POLYMERASE. FOR THE NEGATIVE CONTROL, SUBSTITUTE THE TEMPLATE DNA WITH DDH ₂ O. IT CAN BE PREPARED AS A MASTER MIX.	41
TABLE 14. OLIGONUCLEOTIDE COMBINATIONS TO AMPLIFY THE <i>ySc01</i> TARGET SEQUENCES VIA PCR.	42
TABLE 15. THERMO-CYCLING PROTOCOL FOR PCR AMPLIFICATION WITH PHUSION POLYMERASE.	42
TABLE 16. A PROTOCOL FOR A 25 µL RESTRICTION DIGEST WITH TWO DIFFERENT ENZYMES. ALL ENZYMES USED FOR THE RESTRICTION DIGESTS WERE PURCHASED (NEW ENGLAND BIOLABS GMBH (GERMANY)). DIFFERENT REACTION VOLUMES CAN BE DOWN- OR UPSCALED.	43
TABLE 17. PROTOCOL FOR DNA LIGATION WITH ONE INSERT AND TWO INSERT DNA (ITALIC).	44
TABLE 18. PROTOCOL FOR SOC-MEDIUM. PREPARE A SEPARATE MAGNESIUM SOLUTION FROM MgCl ₂ *6H ₂ O AND MgSO ₄ *7H ₂ O, WHICH IS STERILE FILTERED, AND A SEPARATE A-D-GLUCOSE (ANHYDROUS) SOLUTION WHICH IS AUTOCLAVED BEFORE MIXING WITH THE OTHER CHEMICALS.	45
TABLE 19. PROTOCOL FOR 1X PBS BUFFER. IT CAN ALSO BE PREPARED IN A 10X PBS STOCK SOLUTION.	47
TABLE 20. PROTOCOL FOR PREPARING THE 6X LOADING BUFFER FOR THE GLYCINE SDS PAGE. THIS BUFFER IS ALSO CALLED LAEMMLI BUFFER.	47
TABLE 21. PROTOCOL FOR PREPARING A SEPARATION WITH 15% W/V POLYACRYLAMIDE 1.5 AND A STACKING GEL WITH 4% W/V POLYACRYLAMIDE FOR A GLYCINE SDS PAGE.	48
TABLE 22. PROTOCOL FOR PREPARING THE RUNNING BUFFER FOR THE GLYCINE SDS PAGE.	48
TABLE 23. PROTOCOL FOR PREPARING 15 ML SEPARATION GEL WITH 18% W/V POLYACRYLAMIDE AND 10 ML STACKING GEL WITH 2.5% W/V POLYACRYLAMIDE FOR A TRICINE SDS PAGE.	49
TABLE 24. PROTOCOL FOR PREPARING THE RUNNING BUFFER FOR THE TRICINE SDS PAGE.	49
TABLE 25. PROTOCOL FOR PREPARING THE 2X LOADING BUFFER FOR THE TRICINE SDS PAGE.	50

TABLE 26. PROTOCOL FOR COLLOIDAL COOMASSIE FIXER. THE SOLUTION CAN BE PREPARED IN ADVANCE AND STORED AT ROOM TEMPERATURE.	50
TABLE 27. PROTOCOL FOR COLLOIDAL STAINING SOLUTION. THE SOLUTION HAS TO BE FILTERED THROUGH A FLUTED FILTER AFTER MIXING. IT CAN BE PREPARED IN ADVANCE AND STORED AT ROOM TEMPERATURE.....	50
TABLE 28. TRANSFER BUFFER FOR SEMI-DRY WESTERN BLOT.....	51
TABLE 29. PROTOCOL FOR TBS WITH THE ADDITION OF THE DETERGENT TWEEN 20.....	52
TABLE 30. PROTOCOL FOR BUFFER B PREPARATION. PREPARE THE BUFFER WITHOUT TRITON X-100, ADJUST THE PH, AUTOCLAVE AND THEN ADD THE TRITON X-100 AT ROOM TEMPERATURE AND MIX UNDER MODERATE STIRRING.	55
TABLE 31. PROTOCOL FOR WASH BUFFER W1 PREPARATION USED FOR NATIVE PURIFICATION. THE BUFFER WAS PREPARED WITHOUT TRITON X-100, THE PH ADJUSTER, AUTOCLAVED, AND THEN THE TRITON X-100 WAS ADDED AT ROOM TEMPERATURE AND MIXED UNDER MODERATE STIRRING. THE BUFFER WAS STORED AT 4 °C.	57
TABLE 32. PROTOCOL FOR WASH BUFFER W2 PREPARATION USED FOR NATIVE PURIFICATION. THE BUFFER WITHOUT TRITON X-100 WAS PREPARED, THE PH ADJUSTED, AUTOCLAVED, AND THEN THE TRITON X-100 WAS ADDED AT ROOM TEMPERATURE AND MIXED UNDER MODERATE STIRRING. THE BUFFER WAS STORED AT 4 °C.....	57
TABLE 33. PROTOCOL FOR ELUTION BUFFER E PREPARATION USED FOR NATIVE PURIFICATION. THE BUFFER WAS PREPARED WITHOUT TRITON X-100, THE PH ADJUSTED, AUTOCLAVED, AND THEN TRITON X-100 WAS ADDED AT ROOM TEMPERATURE AND MIXED UNDER MODERATE STIRRING. THE BUFFER WAS STORED AT 4 °C.	58
TABLE 34. PROTOCOL FOR LYSIS BUFFER PREPARATION USED FOR DENATURED PURIFICATION.	61
TABLE 35. PROTOCOL FOR WASH BUFFER A PREPARATION.....	62
TABLE 36. PROTOCOL FOR WASH BUFFER B PREPARATION.....	63
TABLE 37. PROTOCOL FOR ELUTION BUFFER PREPARATION.	63
TABLE 38. PROTOCOL FOR REDOX-REFOLDING BUFFER (RRB) PREPARATION. THE BUFFER WAS FRESHLY PREPARED WITH COLD WATER FOR PROPER PH ADJUSTMENT.	65
TABLE 39. PROTOCOL FOR Cu(I)Cl SOLUTION PREPARATION.	70
TABLE 40. EXEMPLARY PROTOCOL FOR 1 mL OF 1 mM Cu(I) STOCK BUFFER PREPARATION FROM FRESHLY PREPARED 100 mM STOCK SOLUTIONS OF EACH OF THE COMPONENTS. THE DILUTION WAS MADE IN THE CORRESPONDING PROTEIN BUFFER OR DDH ₂ O...	70
TABLE 41. OVERVIEW OF ALL THE PRODUCED PROTEIN CONSTRUCTS AND THEIR OPTIMAL EXPRESSION AND PURIFICATION CONDITIONS. IN ALL CASES, T7 SHUFFLE EXPRESS <i>LYSY E. COLI</i> (T7 SHUFFLE) OR LEMO21 (DE3) <i>E. COLI</i> (LEMO21) CULTIVATED IN LB-MEDIA WERE USED AS HOST CELLS. THE DIALYSIS OF PURIFIED PROTEIN WAS CONDUCTED IN TWO STEPS, WHILE EACH INCUBATION STEP WAS FOR AT LEAST 20 H. 5 mM EDTA WAS ADDED IN THE FIRST DIALYSIS STEP FOR ALL THE COPPER-BINDING PROTEINS. ALL PROTEINS FROM DENATURED PURIFICATION WERE DIALYZED AND STORED IN THE REDOX-REFOLDING BUFFER (RRB, TABLE 38). THE PBS WAS MADE ACCORDING TO TABLE 19.	91

LIST OF ABBREVIATIONS

AFM	Atomic force microscope
APS	Ammonium persulfate
ATP	Adenosine triphosphate
<i>B. subtilis</i>	<i>Bacillus subtilis</i>
BF	Bright field image
BSA	Bovine serum albumin
Cam	Chloramphenicol
CAM	Contact angle measurement
Ccg-2	Neurospora circadian clock-controlled gene; allelic to Eas
Ccs	Copper chaperone for superoxide dismutase
Cox17	Cytochrome c-oxidase copper chaperone
COX	Cytochrome c-oxidase
cl	Protein with cleaved off His-tag by the TEV protease (e.g. clCox17)
Cu	Copper
Cys	Cysteine residue
ddH ₂ O	Double-distilled water
dAAm	Diacrylamide
DGR	Differential scanning fluorimetry guided refolding
DRoPS	Direct reversion of the properties of surfaces
DSF	Differential scanning fluorimetry
Eas	Easily wettable; allelic to Ccg-2
EDC/NHS	Ethyl(dimethylaminopropyl) carbodiimide / N-hydroxysuccinimide
ELISA	Enzyme-linked immunosorbent assay
ETC	Electron transport chain
FADH ₂	Flavin adenine dinucleotide in hydroquinone form
FITC	Fluorescein isothiocyanate
GFP	Green fluorescent protein
HCl	Hydrochloric acid
His	Histidine residue
His-tag	Polyhistidine tag, His ₆ -tag
HRP	Horseradish peroxidase
IM	Inner mitochondria membrane

IMS	Inner mitochondria space
JKR model	Johnson-Kendall-Roberts model
Kan	Kanamycin
LB	Lysogeny broth
LOD	Limit of detection, detection limit
MIP	Molecular imprinted polymers
MRC	Mitochondrial respiratory chain
MWCO	Molecular weight cut-off
<i>N. crassa</i>	<i>Neurospora crassa</i>
NA	Numerical aperture
NADH	Nicotinamide adenine dinucleotide hydrogen
Ni	Nickel
NMR	Nuclear magnetic resonance
OD	Optical density
<i>P. pastoris</i>	<i>Pichia pastoris</i>
PAGE	Polyacrylamide gel electrophoresis
PBS	Phosphate buffered saline
PCR	Polymerase chain reaction
PDMS	polydimethylsiloxane
PEG	Poly(ethylene) glycol
PI	Protease inhibitor
pLDH	Plasmodium lactate dehydrogenase
PS	Polystyrene
qPCR	Quantitative PCR
RICM	Reflection interference contrast microscopy
RDT	Rapid diagnostic test
RM	Reflection mode image
<i>S. cerevisiae</i>	<i>Saccharomyces cerevisiae</i>
<i>S. commune</i>	<i>Schizophyllum commune</i>
Sco1	Cytochrome c oxidase assembly protein 1
Sco1Δ95	Cytochrome c oxidase assembly protein 1 with the first 95 nt truncated
SCP	Soft colloidal probes
SDS	Sodium dodecyl sulfate
Sod1	Superoxide dismutase 1

<i>T. reesei</i>	<i>Trichoderma reesei</i>
TAE	Tris-Acetate EDTA
TBS	Tris-buffered saline
TEM	Transmission electron microscopy
TEV	Tobacco etch virus
TFA	Trifluoroacetic acid
TSA	Thermal shift assay
W_{adh}	Adhesive surface energy
y	Protein from <i>S. cerevisiae</i> (e.g. yCox17, later only Cox17)
YPD	Yeast extract peptone dextrose
Zn	Zinc

1 INTRODUCTION

1.1 BIOSENSORS

Biosensors are a class of sensor systems, with an inner biological core as an analyte-specific detector and a signal-transducing detector unit (Justino et al. 2015; Yoo et al. 2020). It can be translated, for instance, in optical, mechanical, electronic, thermal, piezoelectric, acoustic, or electrochemical signals, which then can be measured. Optical methods are most widely used (Mehrotra 2016). The biological inner core detector unit can rely, for example, on analyte-interacting specific DNA or RNA sequences (Drummond et al. 2003), such as oligonucleotides or aptamers (Fischer et al. 2007), on proteins such as antibodies (Lévêque et al. 2015), receptors (Pussak et al. 2013), enzymes (Döring et al. 2019; Sorrentino et al. 2019), or also on whole cells (Johnston and Kim 2005; Radhika et al. 2007; Hennig et al. 2016; Hahne et al. 2021). The spectrum of target analytes is broad: it can range from genetic abnormalities, pathogens, biological markers of disease, viruses, bacteria (Adducci et al. 2016), toxins, drug residues up to pesticides (Döring et al. 2019; Kim Hong and Jang 2020; Rettke et al. 2020), heavy metals or in general trace elements (Abdulazeez et al. 2018; Casanueva-Marengo et al. 2020), to name but a few. Consequently, the importance of biosensors has increased tremendously with applications in the fields of healthcare (Casanueva-Marengo et al. 2020), environmental monitoring (Ejeian et al. 2018), research, food processing (Casanueva-Marengo et al. 2020), agriculture (Döring et al. 2019), and biosecurity (Fischer et al. 2007; Adducci et al. 2016). New materials like smart polymers and carbon-based nano-materials give rise to the emerging field of lab-on-a-chip techniques and application as Point-of-Care diagnostics (González-Guerrero et al. 2016; Chan et al. 2017; Jaiswal and Tiwari 2017).

Up to now, the techniques are often based on the immobilization of the biological detector unit with its inherent characteristic of highly sensitive and selective binding to a substrate and the target analyte, respectively. When the target analyte and the biological detector unit interact, a signal is produced that can be transduced and translated into a measurable physical signal. When microorganisms are used, they might have to be encapsulated, entrapped, or crosslinked (Su et al. 2011). Commonly, adsorption, ionic bonding, and covalent binding are used as immobilizing strategies (Wang 2008; Akyilmaz et al. 2010). Self-assembling proteins displayed on the biological detector unit have also been employed to increase the homogeneous organization on the surface (Ch. 1.4) (Pussak et al. 2013; Döring et al. 2019; Rettke et al. 2020).

Conventional chemical and physical techniques typically yield very accurate results. Those techniques include spectroscopy, mass spectroscopy, chromatography methods, resonance (NMR) analysis, electron, X-ray, and fluorescent microscopy. On the downside, these techniques are typically time-consuming, need trained and experienced personnel, a laboratory environment, high investment in specialized machines, and often costly equipment for sample preparation or assay performance. Novel biosensors aim to overcome most of those aspects. Biosensors should be self-contained devices – when using microorganisms –, with low production costs, fast-response times, easy to handle for untrained users, and at best small and transportable for on-site detection (Su et al. 2011; Mehrotra 2016). Studies showed comparable results with conventional techniques in some cases. In other cases, this might come at the expense of sensitivity, selectivity, or detection limit, but the biosensors can still be highly adequate for their applied fields (Su et al. 2011).

1.2 ANALYTICAL DETECTION METHODS: COPPER

The here presented novel biosensor is based on an indirect detection using the SCP-RICM assay (Ch. 1.3) of analytes that cannot or should not be immobilized, which is to date the strategy of choice for the competitive detection method of the SCP-RICM assay (Pussak et al. 2013). This assay uses the deformation of a soft colloidal probe (SCP) and the formation of a contact area upon analyte-dependent interaction with a chip surface, which is visualized employing reflection interference contrast microscopy (RICM). The analytes are chosen due to their inherent characteristics, like their toxicity, pathogenicity, abundance, binding capacity, or size. The latter is the reason why copper(I) (Cu(I)) as a low molecular, heavy metal ion is eligible as an analyte in a proof-of-concept setup for the indirect detection using the SCP-RICM assay. Immobilizing copper ions would disable the binding or coordination capability by a protein or aptamer. Therefore, the analyte-dependent interaction of two copper chaperones is exploited as an indirect detection mechanism transduced to the SCP-RICM system for a physical signal readout and quantification.

The trace element copper is essential for the human body with a delicate balance of deficiency and excess. A copper imbalance is linked, for instance, to Menkes and Wilson's disease (Pufahl et al. 1997; Niemiec et al. 2015). Furthermore, copper regulates copper-dependent catalytic activities of many enzymes involved in different physiological processes (Hasan and Lutsenko 2012). Nevertheless, copper and other heavy metal ions are also pollutants entering the environment through domestic and industrial usage. The concentration limits of copper in drinking water are, for instance, 1.3 mg/L ($\sim 20 \mu\text{M}$) in the USA (USEPA 2009) and 2 mg/L ($\sim 31 \mu\text{M}$) in the EU (Rat der Europäischen Union 2017). Therefore, it is essential to monitor copper ions in the environment, food, and industrial, waste, and drinking water (Robinson and Winge 2010).

The choice of an indirect detection method for the detection of small analytes is widespread, and the most common is the antibody-based enzyme-linked immunosorbent assay (ELISA) (Wang et al. 2018). The major limitation is the availability of appropriate antibodies. Another indirect approach is the deployment of recombinant *S. cerevisiae* cells combined with a Clark electrode as whole-cell amperometric microbial sensors. It can measure Cu(II) ions using flow injection analysis down to a limit of detection (LOD) of 6.7 µg/L (= 105 nM) (Tag et al. 2007).

Conventional copper methods that have been well studied but are also still highly researched are mass spectrometry (Lavanant et al. 1998), fluorescent probes (Wang and Zong 2015; Qu et al. 2019), electrochemical assays (Yang et al. 2017), and atomic absorption spectrometry (Bagherian et al. 2019). One example is a re-usable calorimetric sensor from Abdulazeez and colleagues (2018), who combined spectroscopy and density functional theory (DFT) analysis and claimed to yield a LOD of 0.34 µg/L (= 5.4 nM) for Cu(II) ions in solution. Another copper detector was created as a disposable, portable, and easy-to-use detector from He and colleagues (2019). They created a microcapsule array chip with encapsulated functional nucleic acids that yield a fluorescent signal when Cu(II) is present with a proposed LOD of 6.35 µg/L (\approx 100 nM) (He et al. 2019). Designs like that significantly contribute to the field of quick, on-site detection of trace elements. A fluorometric detection method commercially available as a kit, for example, the Copper Assay Kit from Merck KGaA (Germany), utilizes a chromogen that forms a colored complex specifically with copper ions. Under complex formation, the absorption at 359 nm changes. It is directly proportional to the copper concentration with an LOD of 70 µg/L (\approx 1.1 µM). It does not distinguish between Cu(I) and Cu(II) ions. While it is an easy to handle and fast method, a significant drawback is the toxicity of used chemicals in the kit.

1.3 SCP-RICM ASSAY

In this study, the SCP-RICM assay is adjusted to be applied as an indirect detection method of analytes in solution. The assay is based on measuring the elastic deformation of beads using RICM, which Moy and colleagues had already performed in 1999. However, these authors used agarose beads dependent on the avidin and biotin interaction (Moy et al. 1999). The combination of elastic beads and RICM was further investigated by Pussak et al. (2012) using polymeric spheres, called soft colloidal probes (SCPs). Their interaction with a hard surface is dependent on their functionalization, typically in conjunction with SCPs as colloidal atomic force microscopy (AFM) probes. The authors demonstrated the successful usage of SCPs to measure the adhesion energy on surfaces and, therefore, to detect weak interactions (Pussak et al. 2012). Subsequently, this method has been improved and applied to more areas (Pussak et al. 2014; Schmidt et al. 2015; Martin et al. 2016; H. Wang et al. 2017) and used in a biosensor application (Rettke et al. 2020).

The presented SCP-RICM assay is applied to detect the analyte copper (Figure 13). Two interaction protein partners serve as the core, analyte-specific detection unit. Here, the copper-binding proteins from the yeast *Saccharomyces cerevisiae* (*S. cerevisiae*) ySco1 and yCox17 were chosen that transfer copper(I) (Cu(I)) ions in the mitochondrial intermembrane space. A suitable and adequately prepared sensor chip surface (Ch. 1.3.1) and the SCPs (Ch. 1.3.2) were functionalized with one protein; each is necessary to translate the interaction into a physical, detectable signal, i.e., the contact area between SCP and chip surface. RICM is used to visualize and measure that signal. It visualizes the interference fringes of the SCP and its contact area with the chip surface, which can be measured *via* image post-processing and facilitates the calculation of the adhesion energy W_{adh} (Ch. 1.3.3). The higher the copper concentration, the higher the W_{adh} at the surface.

1.3.1 Sensor Chip Surface

The sensor chip is one of the core detection components necessary for the SCP-RICM assay. On the one hand, the sensor chip has to be compliant for protein functionalization. On the other hand, it has to be compatible with the application in RICM, a microscopy technique with visible light (Limozin and Sengupta 2009).

The visible light has to penetrate the glass chip twice since the RICM method bases on the interference of reflected beams at the SCP interface and the chip surface using an inverse microscope (for details, see Ch. 1.3.3). The chip surface should therefore be transparent, the material highly homogeneous and thin. Those chip parameters ensure that the alteration of the light's pathway is minimal. The light travels through the chip by diffraction at the two interfaces of the chip surface (bottom and topside) is minimal. Glass cover slides are known to increase the contrast in RICM (Rädler and Sackmann 1993) and were, therefore, found to meet all those requirements.

Surface functionalization with proteins, like hydrophobins (Ch. 1.4), has been performed for many different materials (Piscitelli et al. 2017; Winandy et al. 2018). Hydrophobins self-assemble on hydrophilic glass surfaces. Therefore, the glass surfaces, that have a high chemical stability, were treated with harsh chemicals such as the Piranha solution for thorough cleaning.

To sum up, glass cover slides appear as an appropriate choice for the chip used for hydrophobin functionalization and in the SCP-RICM assay application.

1.3.2 Soft Colloidal Probes

In the SCP-RICM assay, the sensor chip (Ch. 1.3.1) and the SCPs are the two core detector components measuring the probe's deformation with RICM. The SCPs are spheres of crosslinked polymers like poly(ethylene) glycol (PEG), creating small, spheric hydrogels with an adjustable Young's modulus. Their diameter typically ranges between 40 and 70 μm , and they show no unspecific interaction with charged or hydrophobic species.

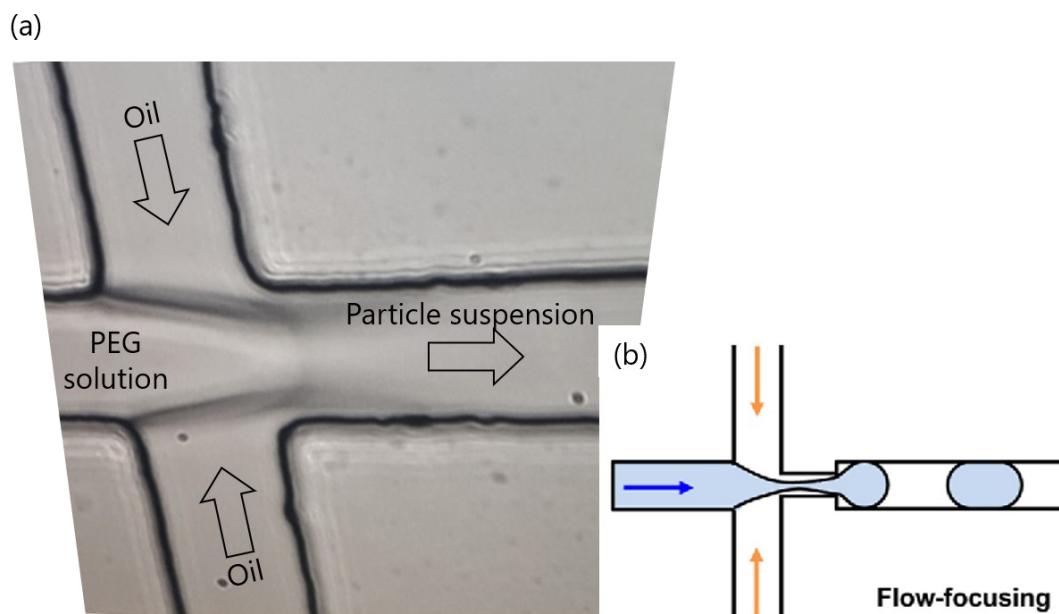


Figure 1. Microfluidic production of hydrogel spheres.

The microscopy image of the polydimethylsiloxane (PDMS) chip (a) and a schematic representation (b, adapted from Zhu and Yang 2017) of microfluidic channels producing a hydrogel particle suspension is shown. When the streams of oil meet the stream of the PEG solution with a well-defined velocity at the intersection of the microfluidic channels, the oil will segregate the PEG solution into PEG droplets with a very uniform size of about the microfluidic channel's width.

One possible synthesis of PEG-SCPs using a dispersion of PEG-diacrylamide (dAAm) macromolecular droplets has been well reported (Flake et al. 2011; Pussak et al. 2012; Pussak et al. 2013). The PEG-SCPs polymerize when adding a photoinitiator and exposing the dispersion to UV-light under vigorously shaking. While this dispersion-based synthesis produces SCPs in high quantity, there is low control of the droplet formation. The SCPs' size distribution is broad, and the occurrence of SCPs with encapsulated air is high. Another synthesis method is using microfluidic chips (Zhu and Yang 2017) (Figure 1). The SCPs' size can be well controlled through the channel width, and their purity was found to be high while the production of a comparable quantity takes several hours of mainly automated synthesis

(Elbert 2011; Kung et al. 2020). It can be optimized by creating multichannel systems that run in parallel. The resulting PEG-droplet-oil emulsion also has to be photopolymerized to form stable SCPs.

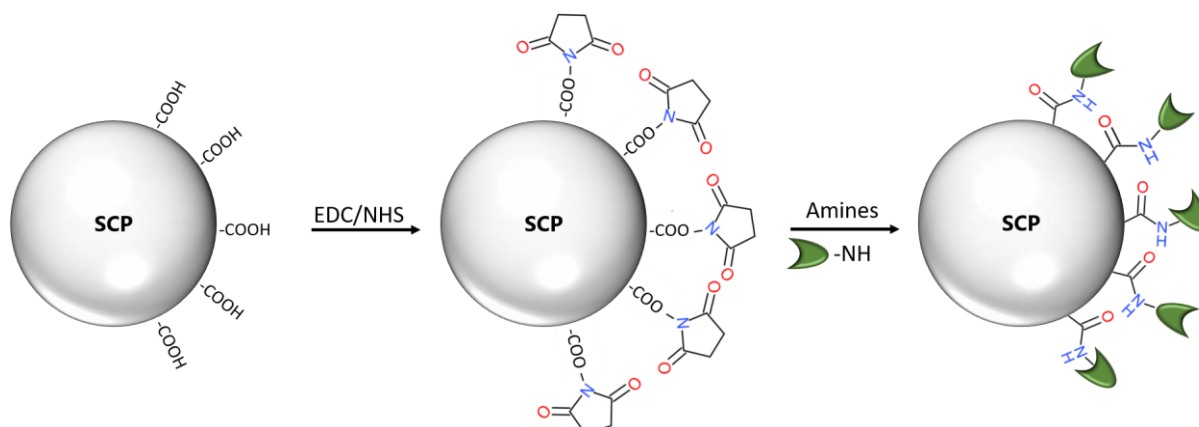


Figure 2. Schematic representation of the SCP-functionalization with proteins *via* EDC/NHS chemistry.

In the interest of clarity, the residues are only shown on one side of the SCP. The residues and the finally bound proteins will be homogeneously distributed throughout the surface of the three-dimensional spheres. The SCPs are crosslinked PEG chains with pre-functionalized carboxyl residues (COOH) (left), activated by ethyl(dimethylaminopropyl) carbodiimide/N-hydroxysuccinimide (EDC/NHS) chemistry (center), and the target protein (green) can be functionalized to the SCP at any amine residues (right). The components are not true to scale.

For further functionalization of the SCPs, the PEG has to be grafted with reactive residues, and a linker of selectable size or a coupling molecule can be introduced if required. Radical benzophenone-based photochemistry has to be conducted on the SCPs followed by crotonic acid monomers' addition to decorate the SCPs with carboxylic (COOH) residues (Schmidt et al. 2015). The successful grafting has been shown for different ligands, for example, for multivalent sugars (Pussak et al. 2012; Strzelczyk et al. 2017; H. Wang et al. 2017), antigens (Strzelczyk et al. 2017), the vitamin biotin (H. Wang et al. 2017), receptors (Pussak et al. 2013) and recently with the organophosphate and herbicide Glyphosate (Rettke et al. 2020). For the presented study, proteins were bound to the SCP by functionalizing the COOH-activated SCPs with the protein using EDC/NHS chemistry. Each amide residue of the protein presents a possible binding site (Figure 2). The functionalized SCPs are now ready to use in the SCP-RICM assay.

1.3.3 Reflection Interference Contrast Microscopy

The SCP-RICM assay is based on measuring the contact area resulting from an SCP interaction with a transparent glass chip surface with RIC microscopy. The interference of two waves of coherent light

yields constructively and destructively interfered regions. When prompting the interference on a plane screen, it results in a characteristic interference pattern depending on the path length difference, nature of the initial wave, and the diffraction object's geometry. The diffraction pattern of a spherical SCP near the chip surface is interference rings. When the SCP interacts with the chip surface, it will form a contact area under the SCP deformation, which appears as a dark center area of the interference rings (Rädler and Sackmann 1993; Moy et al. 1999). In the SCP-RICM assay, this mechanism of RICM is employed to visualize the contact area and make it visible (Figure 3).

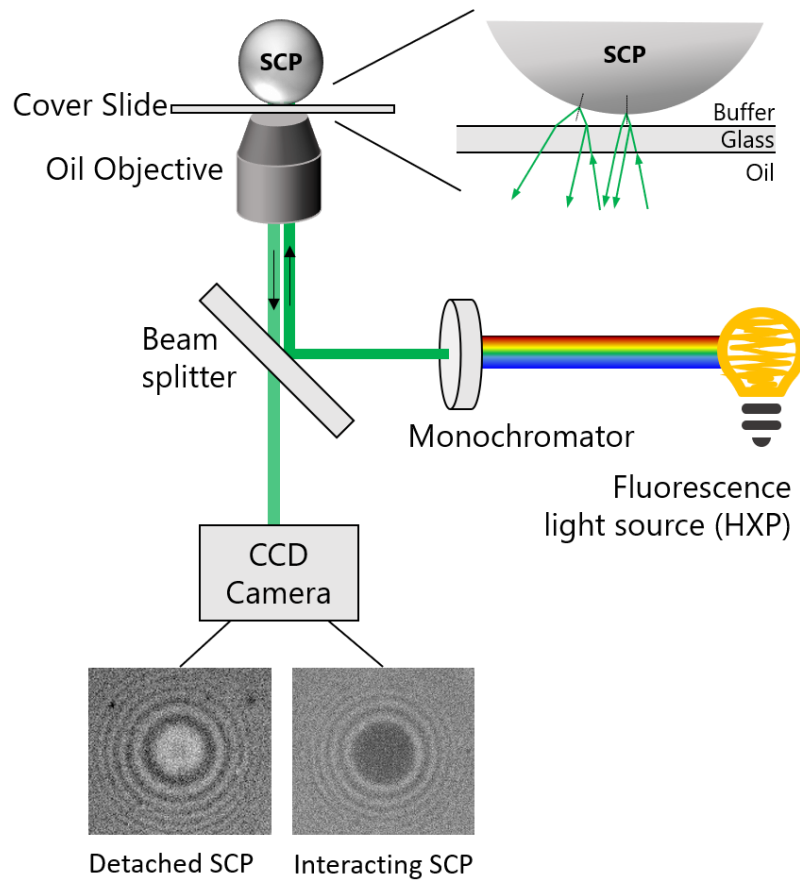


Figure 3. Microscopy Setup for a typical SCP-RICM assay.

The green fraction of the incident light travels through the monochromator and is directed to the specimen, here the SCP. The reflected proportion is analyzed by a CCD camera and visualized. The resulting RICM images (example images at the bottom) are analyzed towards the interference pattern and the contact area's size. The upper right zoom depicts the optical path of two exemplary rays traveling from the immersion oil through the glass coverslip (both have about the same refractive index), surrounding buffer, and meet the SCP at two different spots of the SCP's spherical surface. Each interface of different refractive indices presents an interface where partial refraction and penetration occur. A fraction of the light will penetrate the glass slide and the SCP (not

shown here), and a fraction is refracted. The refracted ray of different path lengths can then interfere with each other, resulting in RICM images. The components are not to scale.

A typical RICM setup used in the SCP-RICM assay is depicted in Figure 3 in an inverse microscope setting. A high-power density fluorescent light source in conjunction with a monochromator or a laser light source provides incoherent light, directed onto the cover slide and the SCP with a beam splitter and an oil immersion objective. Scattered light should be minimized to increase the contrast. It can be achieved using a high-quality oil objective (high numerical aperture (NA)) with an anti flex technique and an additional $\lambda/4$ -plate, immersion oil refractive index that resembles the one from the glass cover slide, and an aperture diaphragm. The reflected light beam will be analyzed with a CCD camera towards the diffraction rings of the SCPs. It is often used for biological applications like the adhesion of vesicles, colloidal beads' dynamics close to a surface, single-molecule receptor-ligand kinetics, and cell adhesion (Limozin and Sengupta 2009). Typically, a layer of 100 nm thickness can be examined – according to calculating the penetration depth $d = \frac{\lambda}{2 \cdot n}$ with the refraction index n – with a vertical resolution of about a few nanometers and a lateral resolution of around 260 nm when using green light.

The value of interest is the adhesive energy W_{adh} . It was found that the theoretical description of the interaction between a rigid and an elastic surface, one being a half-space and the other a sphere, or of two elastic spheres, is best met by the Johnson-Kendall-Roberts (JKR) contact mechanics model (Johnson et al. 1971). It is an extension of the Hertz-model, which first successfully described two elastic spheres' contact, giving a relationship between the applied force, indentation depth, contact radius, and Young's modulus (Butt et al. 2017). The JKR model additionally considers adhesion-triggered surface forces (Johnson et al. 1971). The model can also be applied for low Young's moduli; however, it might fail for materials with Young's moduli below 10 kPa. The contact radius a of the presented case of deformable spheres in contact with a rigid plane is given by

$$a^3 = \frac{R}{E_{eff}} * \left(F + 3\pi R W_{adh} + \sqrt{6\pi R W_{adh} F + [3\pi R W_{adh}]^2} \right) \quad (1)$$

With the SCP radius R , the external load F , and the adhesive energy W_{adh} (Butt and Kappl 2010; Butt et al. 2017). The effective elastic modulus E_{eff} is calculated with

$$E_{eff} = \frac{4E}{3(1 + \nu^2)}$$

Which takes Young's modulus E and the Poisson's ratio $\nu = 0.5$ for all PEG SCPs into account. The Young's modulus of the deformable sphere – here the polymeric SCP – is determined by AFM measurements. The SCP radius is determined by image analysis of the SCP's brightfield image for each SCP. In the case of the SCP-RICM assay, there is no external load, so that equation (1) can be simplified to:

$$a^3 = \frac{6\pi * W_{adh}}{E_{eff}} R^2 \quad (2)$$

Solving the equation (2) to W_{adh} gives the wanted dependency of $W_{adh}(a)$. The contact radius a is measured by image analysis of the contact area in the reflected light image for each SCP.

1.4 HYDROPHOBINS

The SCP-RICM assay fundamental mechanism is based on the SCP interaction with the surface, so the SCPs and the chip surfaces have to be functionalized with the interaction proteins, here derivatives of the copper chaperones yCox17 and ySco1. The glass chip surface functionalization should yield a monodispersed monolayer of one of the proteins of interest with its functional region upright and ready for interaction. To ensure the displaying of the protein of interest, we exploit the self-assembly properties on hydrophobic-hydrophilic interfaces of class I hydrophobins (Ch. 1.4.1 and Ch. 1.4.3). The resulting fusion proteins consist of the protein of interest and the hydrophobin. To date, research and the industry use hydrophobins broadly for surface functionalization, for example for stabilizing foams in the pharma and food industry (Ch. 1.4.2).

1.4.1 Structure and Functions of Hydrophobins

Since the first hydrophobin protein SC3 was analyzed in *Schizophyllum commune* (*S. commune*) in 1991 by Wessels and colleagues (1991), the knowledge about different hydrophobins was deepened, and their broad range of applications was explored (Piscitelli et al. 2017; Berger and Sallada 2019). Hydrophobins form a large family of low molecular weight proteins (≤ 15 kDa). They are unique to filamentous fungi, where they are part of hyphae, spores, and fruit bodies (Wessels 1997; Kershaw and Talbot 1998). Hydrophobins have been employed due to their specific biophysical properties, e.g., their assembly into robust monomeric layers at hydrophilic-hydrophobic interfaces (Wösten et al. 1994), their amphipathicity (Wösten et al. 1994), and the change of surface wettability (Gruner et al. 2012).

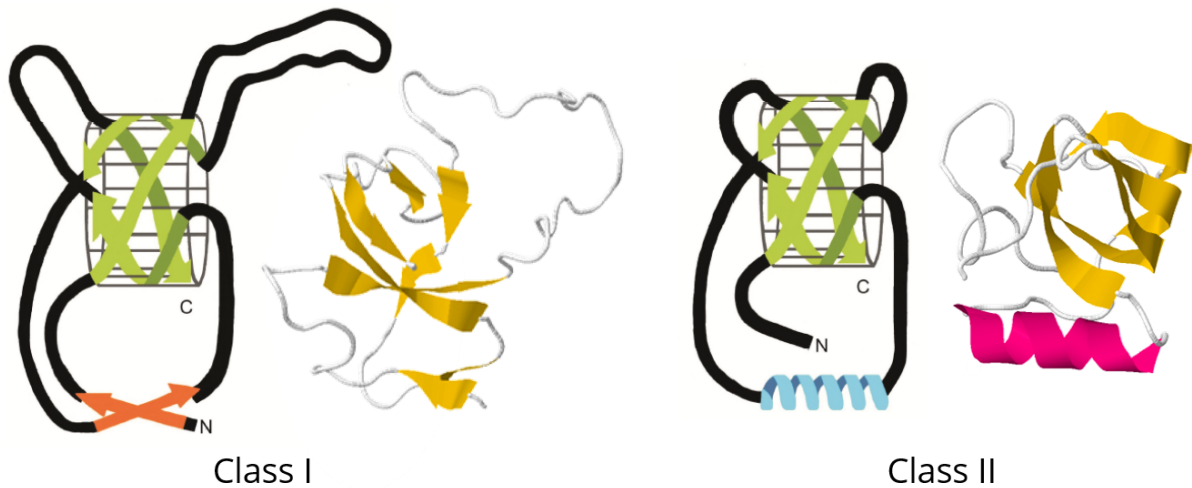


Figure 4. Structural comparison of class I and class II hydrophobins.

The schematic representation clearly shows structural similarities like the β -sheet barrel structure (green) in both hydrophobin classes but also differences like the length and presence of unstructured loops, an additional double β -sheet (orange), and α -helix (blue), respectively (adapted from Zampieri et al. 2010). As an example for each class, the solution structures of class I hydrophobin Ccg-2 from *Neurospora (N.) crassa* (PDB: 2FMC; Kwan et al. 2006) and of class II hydrophobin HFBI from *Trichoderma (T.) reesei* (PDB: 2FZ6; Zhao et al. 2015; Hakanpää et al. 2006) are shown on the right of the schematics with β -sheets marked in yellow and the α -helix marked in pink (adapted from Rose et al. 2018).

Genomic analysis revealed that the family of hydrophobins shows low primary sequence similarities. However, it also indicated that small gene families with a high degree of sequence similarity exist, typically containing two to ten members (Sunde et al. 2008; Littlejohn et al. 2012). Nevertheless, for historical reasons, the scientific community categorizes hydrophobins in class I and class II hydrophobins according to their hydropathy plot, solubility, and type of layer (Wessels 1994; Wessels 1997) (Figure 4). Class I hydrophobins stand out due to their rodlet structured layers at interfaces and strong adhesion to surfaces. The formed layers can only be removed by harsh acids like Trifluoroacetic acid (TFA) (ch. 1.4.3). Class II hydrophobins are typically by about a quarter smaller and form less stable layers, which are more reliably monolayers. Despite their differences, a few properties cluster them into one group of morphogenetic proteins (Kershaw et al. 1998). All hydrophobins possess eight cysteine residues that form four disulfide bonds and thereby create unstructured regions (loops) that are partially known to facilitate the assembly (Wessels et al. 1991; Kwan et al. 2006) and a four-stranded β -barrel secondary structure. Class I hydrophobins show another short, two-stranded antiparallel β -strand, while class II hydrophobins have one α -helix at this position. AFM measurements show that class I hydrophobins form a mosaic pattern of rodlets, while class II hydrophobins form a less robust layer of hexagonal,

honeycomb-like packing (Ren et al. 2013; Kordts et al. 2018). The hydrophobin proteins became of interest to applications through their characteristics to self-assemble to monolayers (Wösten et al. 1994) and their strong adhesion to hydrophilic-hydrophobic interfaces like air/water interfaces.

1.4.2 *Ex vivo* Applications of Hydrophobins

Applications that rely on hydrophobins are possible in various fields. The hydrophobins' main characteristics that render them advantageous are their high surface activity and self-assembling manner at interfaces (Wösten et al. 1999). It shows potential for creating a predictable, extremely stable, and well-defined surface layer to one's specific needs (Scholtmeijer et al. 2002; Zampieri et al. 2010; Piscitelli et al. 2017; Liu et al. 2019). Especially in the nanotechnology and pharmaceutical industry, applications and their implementation are in the foreseeable future (Bayry et al. 2012). Some examples are the usage in cosmetics, for foams (Murray 2007), for protein glue (Wang et al. 2010), and much research is dedicated to the drug delivery process (Sarparanta et al. 2012; Fang et al. 2014). Hydrophobins – both class I and class II – have been precious in stabilizing drugs by including them in the formulation of hydrophobic drugs (Valo et al. 2010), coating of drug nanoparticles (Fang et al. 2014), or creation of a cellulose-based coating fused with hydrophobins for enhancing drug stability (Valo et al. 2011). Hence, several studies show that hydrophobin can act as an adjuvant and improve drug solubility, drug stability, and bioavailability. The potential of hydrophobin-based drug formulations is just one example of the need to enhance and deepen our detailed understanding of the structure, folding, and function of hydrophobins.

However, for biotechnology applications, the low yield of the difficult production of recombinant proteins and the large-scale requirements are still the bottleneck of implementation. That is why there is a high effort on a better understanding and improvement of the hydrophobin folding process (Yamaguchi and Miyazaki 2014; Chang et al. 2019), optimizing buffer conditions (Wang et al. 2017; Lee et al. 2019) and methods for recombinant protein purification (Wingfield 2016; Berger and Sallada 2019). An example of the latter is the work of Lahtinen et al. (2008). They present a one-step purification method of class II hydrophobin HFBI from *Trichoderma reesei* (*T. reesei*) using aqueous micellar two-phase purification and the non-ionic surfactant Agrimul. Baculovirus-infected insect cells could not actively secrete HFBI and its tagged fusion proteins into the medium but expressed them well in the cytosol. The authors propose this method as an option for high purity and easy up-scalable purification (Lahtinen et al. 2008; Reuter et al. 2016). Other hosts like the yeast *Pichia pastoris* (*P. pastoris*) have been reported, which advantageously secrete low amounts but very pure recombinant protein (Kottmeier et al. 2012; Niu et al. 2012).

Nevertheless, most hydrophobin expression is still performed in *E. coli*. Many applications were proposed, including creating biomineralization templates (Melcher et al. 2016), application in electronics (Laaksonen et al. 2010), in microfluidics (Wang et al. 2007), as fusion tags (Reuter et al. 2016), tools for peptide, protein, and cell immobilization (Hou et al. 2009; Hennig et al. 2016). For application in biosensors, class I and class II hydrophobins were successfully tested on glassy carbon electrodes (Corvis et al. 2005), silicon nanoparticles (Sarparanta et al. 2012) and wafers (Gruner et al. 2012), polystyrene (Hennig et al. 2016), PDMS (Qin et al. 2007; Wang et al. 2007; Hou et al. 2009), mica (Qin et al. 2007), gold (Zhao et al. 2009), and many more surfaces. They have also been tested for parameters like pH values from 1 to 13 and different temperatures regarding their self-assembling properties (Zhao et al. 2009). The class II hydrophobin HFBI was shown to self-assemble well and to reverse the gold surface wettability, allowing immobilization of the enzyme choline oxidase and enabling amperometric choline biosensing (Zhao et al. 2009). On the other hand, class I hydrophobin Ccg-2 was used to create a very stable and re-usable biosensor using a mixture of unlabelled and alpha-factor labeled Ccg-2 fusion proteins in an extremely high-sensitive yeast pheromone detector (Hennig et al. 2016). Class I hydrophobins are known to have higher stability on a functionalized surface than class II hydrophobins and still reverse surface wettability after two washes with hot 2% sodium dodecyl sulfate (SDS) (Hou et al. 2009). In terms of our application, surface stability would enable us to re-use the chip surface, reducing valuable fusion protein consumption. It seems worth improving hydrophobin production by simplifying it and increasing its yield. Despite the still existing limitations, it is already possible to develop functional applications and even biosensors employing the hydrophobin's unique characteristics.

1.4.3 Class I Hydrophobin: Ccg-2

Due to its properties described above, a class I hydrophobin was used to functionalize chip surfaces in this work. The class I hydrophobin circadian clock-controlled gene (Ccg-2), also called EAS, from *Neurospora crassa* (*N. crassa*), was found to cover the fungal spore surface and was thoroughly investigated (Bell-Pedersen et al. 1992) and also successfully imaged by Kwan and colleagues (2006) (Figure 5).

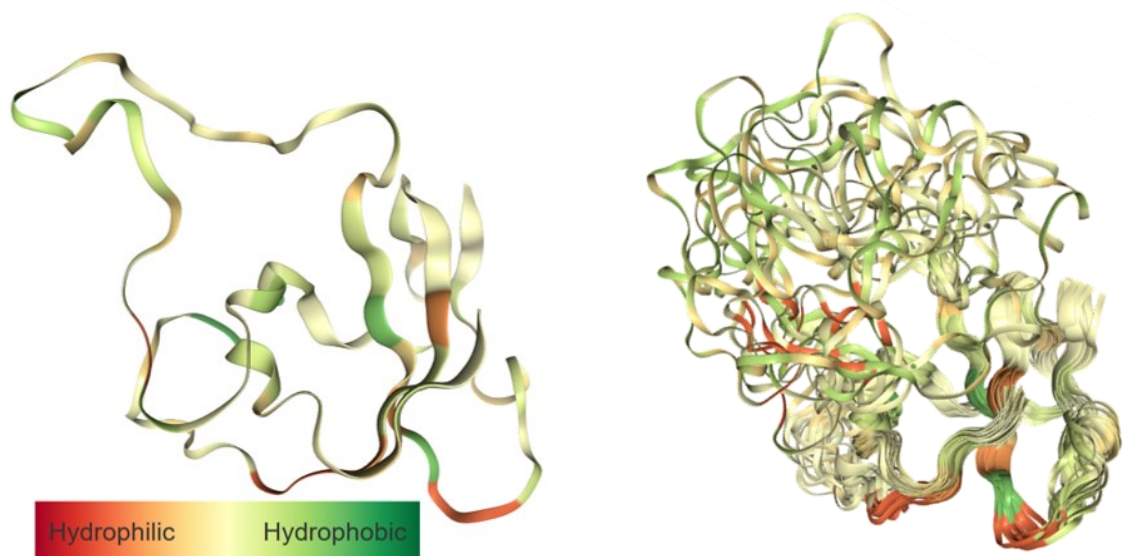


Figure 5. Ribbon diagram from the class I hydrophobin Ccg-2.

The structures are in hydropathy plot representation showing one model (left) and as a comparison the overlay of all 20 models in cartoon representation (right) (PDB ID: 2FMC; Kwan et al. 2006; Rose et al. 2018).

In contrast to the monolayer, honeycomb-like formation of class II hydrophobins, the rodlet formation seems to be strongly associated with significant structural rearrangements finalized with the unstructured loops' high flexibility (Chang et al. 2019), high β -sheet content, and amyloid characteristics (Vocht et al. 1998). Negatively stained transmission electron microscopy (TEM) images of purified Ccg-2 and SC3 from *S. commune* rodlet layers suggest that the rodlets are either hollow or possess a groove running down the middle (Dempsey and Beever, 1979; Wessels, 1999; Gebbink et al., 2005). The rodlets have a diameter of ~10 nm and visible lengths ranging between 35 and 240 nm (Dempsey and Beever, 1979). Comparing work on SC3 with Ccg-2 implied that the mechanism of rodlet formation depends on the interaction of the unstructured loops and might vary with the sequence. SC3 experiments indicate that the Cys3-Cys4 loop is crucial for rodlet formation (Wang et al. 2005), while the Cys7-Cys8 loop is the important one in Ccg-2 rodlet formation (Kwan et al. 2008; Macindoe et al. 2012; Chang et al. 2019). Consequently, it was shown that Ccg-2 Δ 15 (EAS Δ 15) is a highly surface-active hydrophobin at hydrophilic/hydrophobic interfaces (Pham et al. 2018). In Ccg-2 Δ 15, 15 of the 25 residues long Cys3-Cys4 loops are deleted, leaving six highly charged residues. It exhibits a very similar assembling mechanism compared to full-length Ccg-2 (Kwan et al. 2008).

1.5 MITOCHONDRIAL RESPIRATORY CHAIN

During the synthesis of adenosine triphosphate (ATP), energy is chemically stored. This mechanism is based on the mitochondrial respiratory chain (MRC), also known as the electron transport chain (ETC). The ETC describes the transfer of electrons from donor to acceptor molecules through a series of redox reactions. The respective enzyme complexes use the energy to propel protons across the inner mitochondrial membrane, thereby creating an electrochemical gradient, which drives ATP synthesis.

The electrons are transferred from nicotinamide adenine dinucleotide hydrogen (NADH) or flavin adenine dinucleotide in hydroquinone form (FADH₂) through several spatially separated, big molecular complexes in the mitochondrial inner membrane (IM). They finally react with molecular oxygen, which is reduced to water (Sousa et al. 2018). The mitochondrion possesses four membrane-bound respiratory protein complexes named complex I – IV, of which each is a very complex transmembrane protein assembly. This study focuses on two proteins involved in the terminal oxidase of the MRC called MRC complex IV or cytochrome c-oxidase (COX).

The biogenesis of COX has been subject to many studies. COX carries two essential copper centers, which are involved in the electron transfer through the enzyme complex. The safe transport of this highly reactive metal to mitochondria and the controlled incorporation in the complex is vital for its correct assembly and function.

1.5.1 Copper Transport in Yeast

Metal ions are essential in many cellular processes. One of them is copper, which the cell uses as a structural element and exploits it for single-electron-transfer reactions. Copper is indispensable in the mitochondrial ETC. The importance of this highly reactive yet toxic trace element bases on its ability to exist *in vivo* in the two oxidation states, Cu(I) and Cu(II), under physiological conditions. At the same time, this redox cycling between the two oxidation states can catalyze the formation of highly reactive, toxic hydroxyl radicals with a lifetime of only 10⁻⁹ s that can damage virtually any macromolecule (Halliwell and Gutteridge 1985; Sies 1993). Although it is still not fully solved where the copper ions in the different compartments come from and how their transfer works, discovering the protein class of metallochaperones in the 1990s already answered many questions (Lee et al. 1993; Culotta et al. 1997; Pufahl et al. 1997). Their biological role is to transport copper in the cytoplasm and the mitochondria sheltered from interaction partners to the next copper chaperone or a copper-dependent protein complex. One proposed and often implied copper exchange mechanism is a 'key-and-lock' interaction between the copper chaperone and the target protein, as shown in Figure 6.

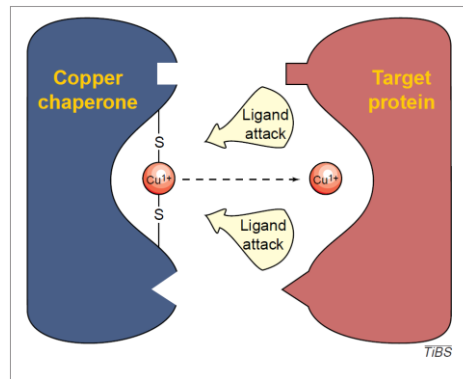


Figure 6. Mechanistic scheme of the chaperone-target-interaction for copper exchange.

A copper chaperone ligates Cu(I) through sulfur bonds from cysteine amino acid residues in a diagonal or seldom in a trigonal fashion. The metal binding region of a target protein can make attacking ligands available, typically sulfur, nitrogen, or oxygen atoms. This is often paired with a conformational change of the chaperon, destabilizes the binding of Cu(I), and transfers it to the target protein. This process happens with high specificity. (From Harrison et al. 2000)

In prokaryotes, copper action is limited to being a cofactor for COX. However, in eukaryotes, copper has significant functions in the cytoplasm, the endoplasmic reticulum, and the mitochondria (Robinson and Winge 2010). Concentrating on the ETC in yeast *Saccharomyces cerevisiae*, the influx of Cu(I) ions into the cytoplasm is ensured by high (γ Ctr1/3) and low-affinity (γ Fet4/ γ Smf1) transporters, as shown in Figure 7. The transmembrane Cu-ATPases control the copper concentration in the different cell compartments, and even their localization is dependent on it. Cu-ATPases are found in the *trans*-Golgi membranes at limiting or normal copper concentrations to pump copper ions from the cytosol into the *trans*-Golgi where they are incorporated into copper enzymes. At elevated copper concentrations or other stimuli, a re-localization into cellular and vesicular membranes takes place to control the copper efflux into the extracellular matrix and the cytoplasmic vesicles, respectively (Petrís et al. 1996; La Fontaine and Mercer 2007). The copper chaperone Atx1 transfers Cu(I) within the cytoplasm between the plasma membrane and the *trans*-Golgi membrane. The copper exchange mechanism is suggested to be a charge-competitive, ligand-driven exchange reaction (Figure 6). The specific copper chaperone for superoxide dismutase (γ Ccs) supplies another copper-dependent protein complex, the superoxide dismutase Cu,Zn-SOD. It is located in the cytoplasm and the mitochondrial intermembrane space (IMS) (Culotta et al. 1997; Robinson and Winge 2010).

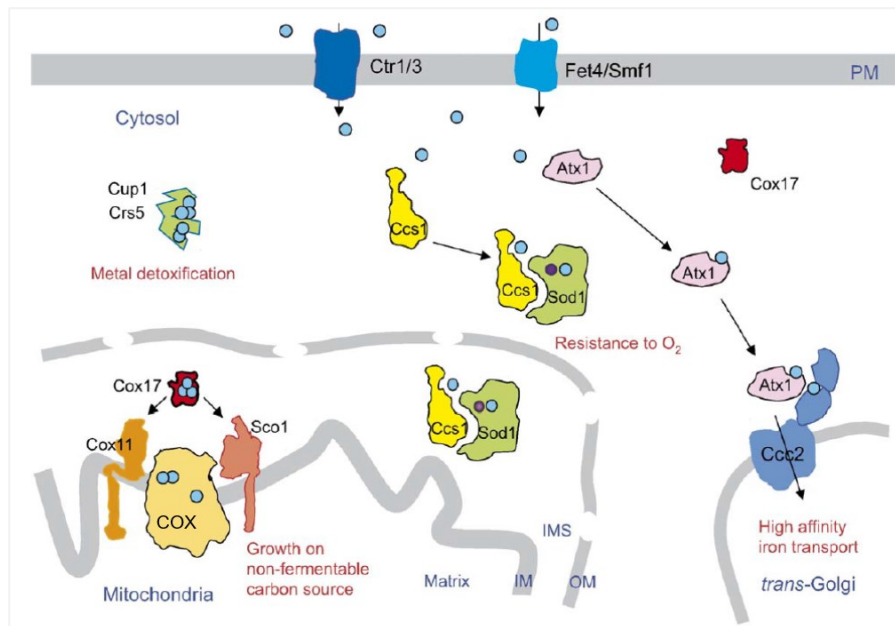


Figure 7. Copper homeostasis in *S. cerevisiae* and proposed model of chaperone-target interaction.

Affinity transporters transfer/bring Cu(I) ions (blue circles) through the plasma membrane (PM) into the cell. They release the ions to the cytosol or – most likely – transfer them directly to copper chaperones, which transport the copper to ySod1 (purple circles mark Zn^{2+}) via yCcs1, the *trans*-Golgi via yAtx1 and yCcc2, and to COX in the IM of the mitochondria via yCox17, yCox11, and ySco1. (From Cobine et al. 2006)

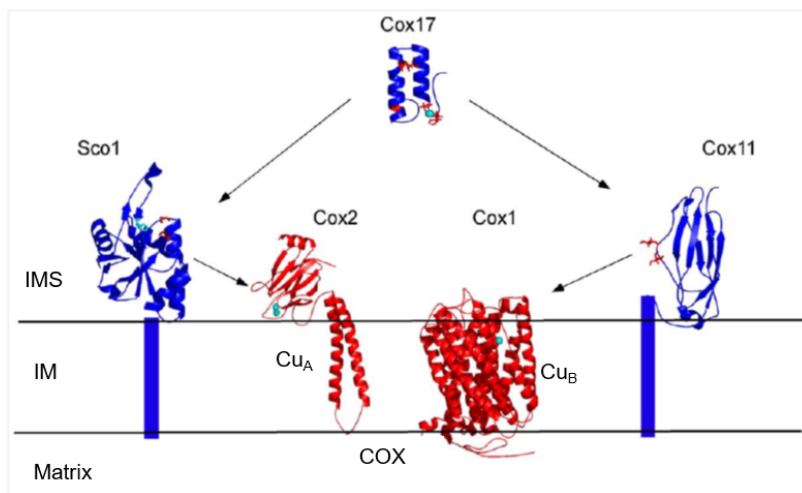


Figure 8. Simplified scheme of copper transfer at the mitochondrial IM.

In the mitochondrial IMS, yCox17 binds Cu(I) ions (turquoise spheres) and transfers them to yCox11 and ySco1. yCox11 interacts with the Cu_B center of COX, while ySco1 interacts with the Cu_A center for the copper insertion into COX. All solved crystal structures are shown in cartoon representation. The transmembrane domains of ySco1 and yCox11 have not been solved yet. (From Cobine et al. 2006)

Finally, copper supplementation is crucial for the essential transmembrane, aerobic respiratory enzyme complex COX, located in the IM (Tsukihara et al. 1996) (Figure 8). Copper must be transported from the cytosol to the IM and inserted into two different subunits, yCox1 and yCox2, with their copper-binding sites Cu_B and Cu_A, respectively. The three soluble proteins yCox17, yCox19, and yCox23 have been found to be responsible for copper transport through the cytosol and are denoted as copper chaperones for COX. yCox17 is a soluble protein located in the cytosol and mainly in the IMS. It participates in the Cu(I) ion transfer to yCox11 and ySco1, both tethered to the IM. Those specific functions of yCox17 are closely linked to its particular characteristic of possessing three different oxidative states (for further detail, see Ch. 1.5.3) (Abajian et al. 2004). Copper-loaded yCox11 is required for metalation of the yCox1 domain and the formation of COX's Cu_B site. Their copper transfer mechanism is still not fully understood since the C-terminal metal-binding domain of the IM transmembrane protein yCox11 is located in the IMS. The Cu_B site is buried in the IM (Carr et al. 2002; Banci et al. 2004; Khalimonchuk et al. 2005). This location makes the explanation unlikely that it is a putative ligand concentration-driven metal exchange, as suggested for other copper exchange events. It might instead be a co-translational formation of Cu_B by the interaction of yCox11 and nascent yCox1 in the IMS (Khalimonchuk et al. 2005). yCox11 shows a β -immunoglobulin-like fold and a CFCF copper-binding motif (C for cysteine, F for phenylalanine). This copper-binding motif has 2 cysteine (Cys) residues, which bind two Cu(I) ions as functional yCox11 dimers in a dinuclear Cu₂S₄ cluster positioned at the dimeric interface but transfers only one copper ion to the mononuclear Cu_B site (Carr et al. 2002; Banci et al. 2004). For the assembly of the Cu_A site of the yCox2 subunit of COX the need of more proteins for the copper transfer was shown. The Sco proteins (synthesis of cytochrome c oxidase), denoted as ySco1 and ySco2, are anchored in the mitochondrial IM with a single transmembrane helix. As copper-loaded ySco1 interacts with yCox2, it seems plausible that it is responsible for metallization of the Cu_B site with two Cu(I) ions (Lode et al. 2000; Arnesano et al. 2005) (for further detail, see Ch. 1.5.2). The involvement of yeast ySco2 in the mitochondrial copper transfer to COX is not completely clear, as it is not essential for forming a functional COX (Ekim Kocabey et al. 2019). Two additional copper chaperones that are involved in the COX assembly are yCox19 and yCox23. They exhibit four conserved Cys residues in two metal-binding motifs and might be relevant in the copper transfer (Lucia Banci et al. 2008). They are essential in the COX activation (Nobrega et al. 2002; Barros et al. 2004). yCox19 has been suggested to interact with yCox11 to facilitate COX biogenesis (Bode et al. 2015). Further functions and interaction partners are still widely unknown (Palumaa 2013).

It is interesting to notice that various copper chaperones and their interaction partners are greatly heterogeneous and present multifunctionality. To date, the quest continues to find novel metallochaperones and reveal their functionality (Bode et al. 2015; Furukawa et al. 2018).

1.5.2 *S. cerevisiae* Sco1 protein

Sco (synthesis of cytochrome c oxidase) proteins can be found in prokaryotic and eukaryotic organisms. They occur in different quantities and varying copper affinities depending on the organism, making them an interesting object for homology studies (Leary et al. 2009; Ekim Kocabey et al. 2019). Most eukaryotic organisms harbor two Sco proteins, namely Sco1 and Sco2.

Sco1 and Sco2 possess homologous sequences - for example, they show 71% sequence similarity - and structures in yeast. Both exhibit a characteristic thioredoxin-like fold (Balatri et al. 2003; Abajian and Rosenzweig 2006). Sco1 was extensively studied from bacteria *Bacillus subtilis* (BsSco1) (Balatri et al. 2003), human (hSco1) (Williams et al. 2005), and yeast *S. cerevisiae* (ySco1 or Sco1p) (Nittis et al. 2001; Abajian and Rosenzweig 2006). They all exhibit the metal-binding motif CXXXC with two conserved cysteine residues and a conserved histidine residue. In ySco1, these conserved residues are Cys-148 and Cys-152, which have a redox potential in the crystal, and the His-239 at the C-terminal end of the flexible loop, respectively ligating one Cu(I) ion (Nittis et al. 2001). Abajian and Rosenzweig (2006) surprisingly found that only for ySco1 are there two non-conserved cysteine residues Cys-181 and Cys-216, that could also potentially coordinate copper together with His-239. Asp-238, which is located on the disordered loop, was shown to facilitate Cu(II) binding - but not Cu(I) binding - of ySco1 when positioned close to one of the two cysteine pairs through conformational rearrangement. It seems to be somehow crucial for target recognition (Horng et al. 2005). ySco1 anchors with its 95 aa N-terminal α -helix into the IM. The remaining soluble part rises into the IMS and contains all the essential residues necessary for copper-binding and target recognition (Buchwald et al. 1991). Its thioredoxin-like fold contains a four-stranded β -sheet alternately interspersed with four α -helices. The unstructured loop between residues 219 and 241 connects α_4 to β_6 and is also referred to as the SCO-loop (Williams et al. 2005). Additionally, ySco1 includes a two-stranded β -sheet followed by a 3_{10} loop at the soluble truncate's N-terminus and an α -helix followed by a β -strand at the C-terminus (Figure 9). It has also been implied that ySco1 functions as a thiol:disulfide oxidoreductase (Chinenov 2000) but at the same time doubted to have this function *in vivo* and instead act as a secondary Cu(II) storage (Abajian and Rosenzweig 2006).

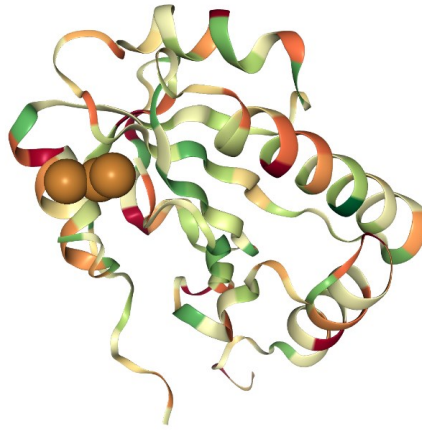


Figure 9. Crystal structure of the ySco1 protein with truncated transmembrane domain and hydrophobicity color-coding.

Three Cu(II) ions (brown spheres) are bound, which is the only copper-binding representation that has been resolved by crystallography so far. The colors vary from red (hydrophobic) through yellow up to green (hydrophilic). (From PDB ID: 2FMC, Abajian and Rosenzweig 2006; Rose et al. 2018)

Within the MRC, yCox17 loads ySco1 in its apo form (apo-ySco1) with copper forming a complex (Cu-ySco1), which then transfers copper to the subunit yCox2 of COX. Those three proteins are very different concerning their sequence and structure. Their interaction most likely occurs between their complementary electrostatic surfaces. An interaction between ySco1 and yCox2 has been shown by immunoprecipitation. The copper-transfer has so far only been implied (Lode et al. 2000). Interactions due to charged residues are known, for example, for the interaction between copper metallochaperones and ATPases or between thioredoxins and target proteins. This interaction mechanism is also proposed for the ySco1-yCox17 interaction. ySco1 exhibits a negative patch close to the metal-binding motif CXXXC (C for cysteine, X for an arbitrary amino acid). yCox17 and yCox2 exhibit positive patches due to their positively charged residues surrounding their metal-binding sites (Xu et al. 2015). Further, negatively charged residues close to the metal-binding motif of ySco1 could facilitate the protein-protein interaction. Therefore, Asp-238 might participate in Cu(II) binding and target recognition since mutagenesis experiments exchanging Asp-238 with an alanine residue yielded non-functional ySco1 (Horng et al. 2005). It was further studied that the truncated ySco1 Δ 95 lacking the transmembrane domain is still able to bind copper and act as a monomer upon interaction with yCox17 and copper (Nittis et al. 2001)

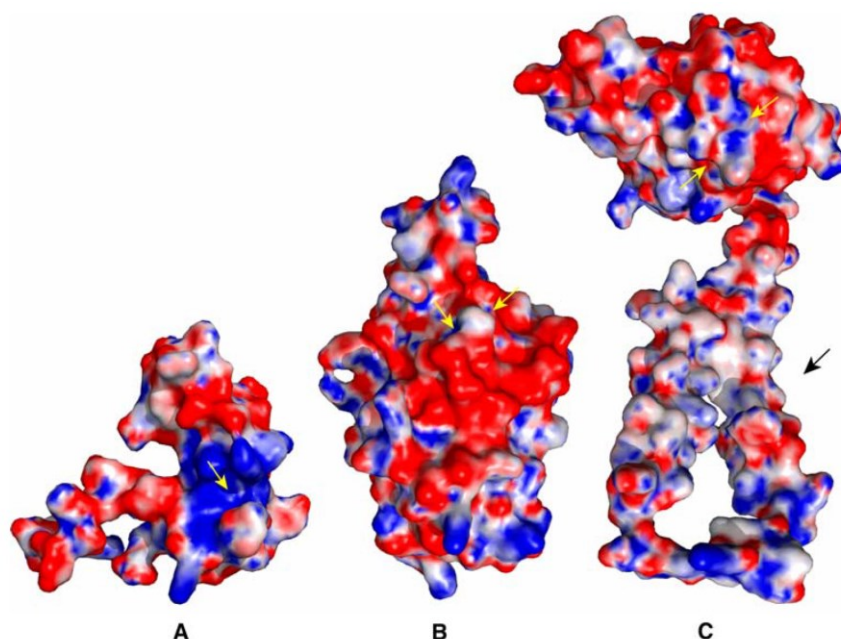


Figure 10. Representation of electrostatic surfaces of Cu(I)-yCox17 (left), apo-ySco1 (center), and modelled yCox2 (right).

The color-coded electrostatic potential shows positive patches (red) for Cu(I)-yCox17(left) and modeled yCox2 (center) and negative patches (blue) for apo-ySco1(right) around the cysteines involved in the copper-binding site (yellow arrow). Red stands for -10 kT, white for 0 kT, and blue for 10 kT. The black arrow points towards the transmembrane domain. (From Abajian and Rosenzweig 2006)

The three conserved ligands, His-239 at the end of the disordered ySco loop and Cys-148 and Cys-152 from the metal-binding motif CXXXC, ligate one Cu(I) ion per monomer and appear to be very stably reduced in apo-ySco1. They were found to be oxidized to a disulfide bond in Cu-ySco1 (Abajian and Rosenzweig 2006). Furthermore, a re-location of His-239 further away from the metal-binding motif is possible due to a certain flexibility of the disordered ySco loop. In that case, there is a certain probability that the three ligands, the His-239 and the non-conserved cysteines Cys-181 and Cys-216, coordinate one copper ion per protein monomer but at three possible locations close to each other. Those locations are all in coordination distance to the non-conserved two cysteine residues. This Cu-ySco1 complex was so far the only resolved copper-bound version in the X-ray crystallization experiment (Abajian and Rosenzweig 2006).

Xu and colleagues state that ySco1 has a higher affinity to Cu(II) with an approximated affinity constant of $K_{D, Cu(II)} \approx 1$ pM over the affinity of binding to Cu(I) of $K_{D, Cu(I)} \approx 10$ μ M (Xu et al. 2015). This suggestion is contrary to expectations and previous implications of ySco1 being a Cu(I) specific protein (comparable to human hSco1 $K_{D, Cu(I)} \approx 0.1$ fM) (Nittis et al. 2001). Their proposed mechanism is that ySco1 harvests

Cu(II) from the low-affinity cellular pool, and the Cu(II)-ySco1 complex is stable. It would only release copper directly to its target upon reduction of Cu(II) to Cu(I) (Figure 11).

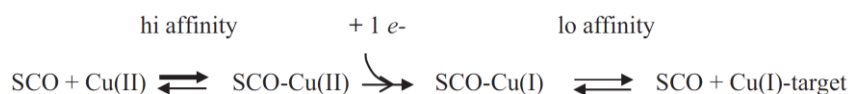


Figure 11. Scheme of proposed copper uptake for ySco1.

ySco1 takes up Cu(II) from the large pool of weakly bound Cu(II) ions in the IMS and forms a high-affinity Cu(II)-ySco1 complex. It then gets reduced to a Cu(I)-ySco1 complex with lower affinity, which subsequently transfers the Cu(I) ion to a target molecule. (From Xu et al. 2015)

Although contradictory, two supplemental processes could also be possible. *In vivo*, uptake of a free Cu(I) ion in solution is not probable. However, a transfer of one Cu(I) ion from yCox17 *via* protein-protein interaction is often reported (Nittis et al. 2001; Horng et al. 2005; Abajian and Rosenzweig 2006) and still possible. The Cu(I) ion could then be oxidized under conformational change and stored as Cu(II) until the target protein is reduced and released.

1.5.3 *S. cerevisiae* Cox17 protein

The Cox17 protein is a copper chaperone unique to eukaryotes (Arnesano et al. 2005), which also contributes to mitochondrial COX's biogenesis through its copper-binding and transferring capacity (Glerum et al. 1996). Cox17 in *S. cerevisiae* (yCox17 or Cox17p) is a small, only 69-residue long protein that has been localized in the cytosol and the mitochondrial IMS (Beers et al. 1997) without shuttling between those loci (Maxfield et al. 2004). While it is not yet fully understood how yCox17 is loaded with copper (Timón-Gómez et al. 2018), it has been shown that it transfers copper to the two copper chaperones ySco1 and yCox11, both tethered with a single α -helix to the IM (Figure 7 and Figure 8). Furthermore, those interactions also seem to transfer to *in vitro* situations (Horng et al. 2004).

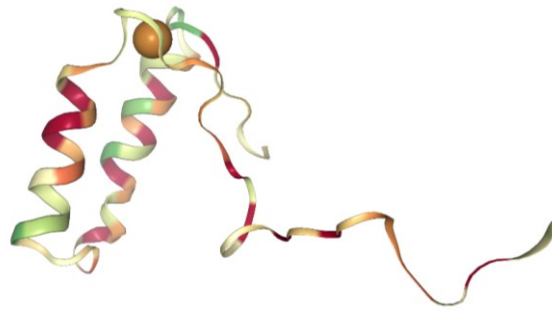


Figure 12. Solution structure of yCox17 with one Cu(I) ion bound.

The solution structure of the yCox17 protein is shown here in cartoon representation and hydrophobicity color-coding. One Cu(I) ion (brown sphere) is bound to yCox17. The C-terminus is five unstructured amino acid residues long, followed by two, about 12 residues long, α -helices separated by ten residues, and finalized by 20 residues long, unstructured N-terminus. The colors vary from red (hydrophobic) through yellow up to green (hydrophilic). (From PDB ID: 1U96, Abajian et al. 2004)

yCox17's solution structure (Abajian et al. 2004) reveals some structural and functional features (Figure 12). Besides the two α -helices, yCox17 consists of about 40% unstructured portion with a dominant 20 residues long N-terminus. It has been proposed that the unstructured regions enable easy adoption to different conformations to allow the interaction with different target proteins and efficient copper transfer. Especially the long N-terminus is suspected of playing a critical role in ySco1 recognition. Furthermore, yCox17 exhibits seven cysteine residues. Mutagenesis experiments in the metal-binding motif CCXC show that all three residues Cys-23, Cys-24, and Cys-26, are essential for COX assembly. Therefore, those three residues are also essential for ySco1 and yCox11 target recognition and copper transport, but only two of the three are necessary for copper-binding (Heaton et al. 2000). Supported by NMR data, the Cu(I) ion seems to be coordinated by only two cysteine residues (Abajian et al. 2004). The other four residues are not involved in the yCox17 binding of one Cu(I) ion. The function of Cys-16 is not yet known, and Cys-36, Cys-47, and Cys-57 seem to be relevant for target recognition, especially Cys-57 for ySco1 recognition (Hornig et al. 2004).

yCox17 is oligomeric at high protein concentrations (Heaton et al. 2001). When handling low protein concentrations of around $\leq 5 \mu\text{M}$, it is expected to be monomeric in solution. In contrast to ySco1, it only binds Cu(I) and no Cu(II). Poly copper clusters have been identified for yCox17 (Glerum et al. 1996; Heaton et al. 2001) in addition to the previously described binding of one Cu(I) ion, which is realized by a twin CX9C metal-binding site (Glerum et al. 1996). Three possible oxidative states have been identified (Palumaa et al. 2004): yCox17(0S-S) can cooperatively bind four Cu(I) ions, yCox17(2S-S) can bind one

Cu(I) ion, and yCox17(3S-S) without any Cu(I) ion bound. The partially oxidized state of yCox17(2S-S) with two disulfide bridges and one bound copper ion was found to be the most stable and therefore present oxidized state in the yeast IMS (Voronova et al. 2007) and makes the transfer of one Cu(I) ion from yCox17 to ySco1 the presumed scenario (Horng et al. 2005; Banci et al. 2007).

1.6 SCP-RICM ASSAY FOR COPPER DETECTION

In this study, a novel application of the SCP-RICM assay was investigated, combining an indirect detection system with SCPs and the RICM technique. So far, the SCP-RICM assay has been mainly used as a detector in the context of ligand-receptor model systems. A new scope of analytes that cannot be immobilized, like the ligands in the ligand-receptor system, was approached here. A suitable set of proteins that interact analyte-dependent was chosen for immobilization.

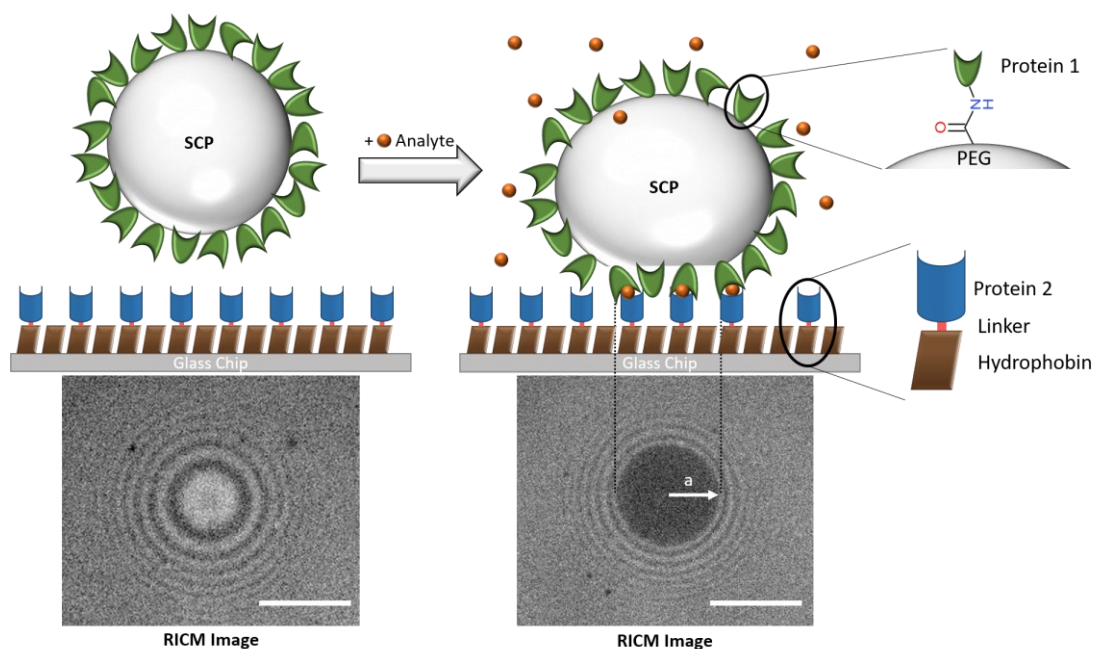


Figure 13. Schematic representation of the SCP-RICM assay for indirect analyte detection.

The SCP is functionalized with one interaction partner (protein 1) and the glass chip with the other interaction partner's (protein 2) hydrophobin fusion protein. The SCP and the glass surface do not interact specifically with each other and do not show any or only a minimal contact area in the RICM image (left). When the analyte is added, protein 1 and protein 2 interact, dependent on the analyte and its concentration. The interaction leads to a deformation of the SCP and an increase in contact area (radius a) in the RICM image (right). Scale in RICM images: 5 μm . The individual components are not true to scale.

As a proof-of-principle system, the interaction partners and copper chaperones ySco1 and yCox17 from the mitochondria in *S. cerevisiae* were chosen for the detection of Cu(I). *In vivo*, it is proposed that yCox17

binds one Cu(I) ion and transfers it to ySco1 *via* electrostatic protein-protein interaction. Copper is an example of an analyte that cannot be immobilized to one of the detector components and still can interact with, for example, a receptor due to limited binding sites. Analytes could be targets with a not sufficient number of binding sites, rare availability, or analyte toxicity. The fundamental operating principle of the proposed detector system is shown in Figure 13. When applying it to the here chosen proof-of-principle system, the analyte is Cu(I) (Figure 13, bronze spheres), protein 1 is, for example, the ySco1 derivative (Figure 13, green), and protein 2 is the fusion protein of the hydrophobin Ccg-2 (Figure 13, brown) and for example the yCox17 derivative (Figure 13, blue). Employing hydrophobin surface assembly yields a highly controlled, homogeneous functionalization of the chip surface. Exemplary, pure hydrophobin and a fusion protein of hydrophobin and yCox17 are used to functionalize the surface. It is aimed to achieve a monodispersed layer of yCox17 on display and ready for copper detection. The SCPs are functionalized *via* EDC/NHS chemistry, meaning that the carboxylic residues of the SCPs are linked with the amine residues of the proteins, which are distributed sequence-specific throughout the protein and at the N-terminus. Consequently, the protein is randomly oriented on the surface of the SCPs. The interaction of the two proteins and the subsequent deformation of the SCP can be directly observed as a life output in the RICM image. The more analytes are present, the more interaction partners interact, the higher the deformation and the bigger the contact area's radius.

1.7 AIM OF THE STUDY

This study aims to develop an indirect detection system of analyte solutions where the analyte cannot be immobilized within the detector based on the analyte-dependent interaction of interaction partners to expand the application range of the SCP-RICM assay. Each detector component should be prepared and characterized. Therefore, the recombinant hydrophobin Ccg-2, each interaction partner, and the fusion proteins of Ccg-2 with each interaction derivatives were created. They were cloned, heterologously expressed, and purified in a native or denatured manner, dependent on their solubility. The resulting protein constructs were used for chip surface and SCP functionalization. This novel detector relies on the analyte-dependent interaction of the two interaction partners, which can be visualized and measured *via* the inverse microscopy technique RICM and, therefore, enable an indirect detection of the analyte. The proof-of-concept detector bases on the Cu(I) detection employing the copper-dependent protein-protein interaction of the copper-chaperones ySco1 and yCox17. To our knowledge, it is the first time that the SCP-RICM assay is used as an indirect detection system for analytes.

2 MATERIALS AND METHODS

The following chapters introduce the necessary equipment (Ch. 2.1), microorganisms (Ch. 2.2), and protein designs (Ch. 2.3). Used methods ranging from molecular cloning (Ch. 2.4), protein handling (Ch. 2.4.10 and Ch. 2.6) to the functionalization of the chip's components (Ch. 2.7 and Ch. 2.8) are presented. It also introduces the SCP-RICM assay and explains its data analysis (Ch. 2.9).

2.1 LABORATORY EQUIPMENT

2.1.1 Devices

In the following, Table 1 presents a list of the used devices.

Table 1. List of devices used in this work.

DEVICE	DETAILS	MANUFACTURER
Atomic Force Microscopy Module	NanoWizard®4 AFM	JPK BioAFM Business by Bruker Nano GmbH (Germany)
Centrifugal evaporator	Concentrator 5301	Eppendorf AG (Germany)
Contact angle measurement instrument	OCA15 LJ	Data Physics Instruments GmbH (Germany)
Desiccator	VWR™ Borosilicat 3.3 with stopcock	VWR International GmbH (Germany)
Electroporation system	Gene Pulser II	Bio-Rad Laboratories GmbH (Germany)
Fluorescence microscope	Biozero BZ-8000	Keyence Corporation (Japan)
Gel documentation and analysis system	G:BOX	Syngene, A Division of SynGene Ltd (United Kingdom)
Microplate reader	infinite M200Pro	Tecan Group Ltd. (Switzerland)

Microscope for RCM	Axio Observer.Z1	Carl Zeiss Microscopy GmbH (Germany)
Microscope for AFM	NanoWizard4 AFM	JPK Instruments AG
Semi-dry electrotransfer system	PerfectBlue™ Semi-dry Electro Blotter Sedec M	Peqlab Biotechnologie GmbH (Germany)
Spectrophotometer	Visible spectrophotometer V-1200	VWR International GmbH (Germany)
Thermoblock	Eppendorf Thermomixer R	Eppendorf AG (Germany)
Thermocycler	Mastercycler ep gradient S	Eppendorf AG (Germany)
Ultrasonic bath	Emmi-20MC	EMAG AG (Germany)
Ultrasonic homogenizer	Sonoplus GM 2070 and UW 2070	BANDELIN electronic GmbH & Co. KG (Germany)
UV/Vis Spectrophotometer	Nanodrop ND-1000	Peqlab Biotechnologie GmbH (Germany)
UV/Vis Spectrophotometer	NanoPhotometer® NP80	Implen GmbH (Germany)
Vacuum Concentrator	Concentrator 5301	Thermo Fisher Scientific Inc. (USA)
Vertical gel electrophoresis device	PerfectBlue™ Twin ExW S Vertical Gel System	Peqlab Biotechnologie GmbH (Germany)

2.1.2 Chemicals

Chemicals not listed below were purchased in analytical grade or higher purity from one of the following suppliers: Merck KGaA (Germany) or its affiliates, Carl Roth GmbH + CO. KG (Germany), AppliChem GmbH (Germany), VWR International GmbH (Germany). The used double-distilled water (ddH₂O) was either heat-sterilized at 121 °C with the AnalaR NORMAPUR® ISO 3696 Grade 3 water from VWR international GmbH (Germany) or filter-sterilized water by a Milli-Q® Integral water purification system for ultrapure water from Merck KGaA (Germany).

Table 2. List of laboratory chemicals used in this work.

CHEMICAL	SUPPLIER
Acetic acid	Fisher Scientific GmbH (Germany)
Agar	Formedium™ (UK)
Agarose	Biozym Scientific GmbH (Germany)
Bromophenol blue	SERVA Electrophoresis GmbH (Germany)
Bio-RAD DC™ Protein Assay	Bio-Rad Laboratories GmbH (Germany)
Chemiluminescence substrate – WesternBright™ ECL	Advansta Inc. (USA)
Chemiluminescence substrate, Amersham™ ECL™ Prime	GE Healthcare UK Ltd. (United Kingdom)
cOmplete EDTA-free Protease Inhibitor Cocktail Tablets	Roche Diagnostics GmbH (Germany)
Copper(I) chloride, Reagent Plus®, purified ≥ 99%	Merck KGaA (Germany)
Coomassie® (Bradford) Protein Assay Kit	Thermo Fisher Scientific Inc. (USA)
Coomassie® Brilliant Blue G 250	SERVA Electrophoresis GmbH (Germany)
Fluorescein-5-Isothiocyanate (FITC-'Isomer I')	Thermo Fisher Scientific Inc. (USA) Invitrogen™
His·Bind® Resin	Novagen (Germany)
Hydrogen peroxide 50 % (w/v), stabilized	Acros Organics (USA)
Isopropyl-β-D-thiogalactoside	Calbiochem (USA)
KODAK GBX developer and replenisher	Eastman Kodak Company (USA)

KODAK GBX fixer and replenisher	Eastman Kodak Company (USA)
Molybdc trioxide ICN	Biomedicals Inc. (USA)
Ni-NTA Agarose Resin	Serva Electrophoresis GmbH (Germany)
PageRuler™ Plus Prestained Protein Ladder	Thermo Fisher Scientific Inc. (USA)
Peptone	Formedium™ (UK)
RedSafe™ Nucleic Acid Staining Solution	iNtRON Biotechnology Inc. (Korea)
Roti®-Mark 10-150	Carl Roth GmbH – Co. KG (Germany)
TWEEN® 20	SERVA Electrophoresis GmbH (Germany)
Yeast extract powder	Formedium™ (UK)

2.1.3 Consumables

A list of used consumables is given in Table 3.

Table 3. List of consumables used for this work.

CONSUMABLE	DETAILS	SUPPLIER
96-well Polystyrene Micro-plates	Flat bottom (No. 473-800)	Dr. Ilona Schubert Labor-fachhandel (Germany)
Autoradiography films	Amersham Hyperfilm™ ECL	GE Healthcare GmbH (Germany)
Blotting filter paper	Rotilabo®-blotting paper, 36 mm	Carl Roth GmbH + Co. KG (Germany)
Blotting transfer membrane	Immobilon®-P, Type: PVDF, Pore size: 0.45 µm	Merck KGaA (Germany)

Columns for protein purification	Protino® Columns, 35 mL	MACHEREY-NAGEL GmbH & Co. KG (Germany)
Dialysis Cassettes	Slide-A-Lyzer® (Extra Strength)	Thermo Fisher Scientific Inc. (USA)
Dialysis membrane	MF-Millipore V-series membrane, 0.025 µm pore size	Merck KGaA (Germany)
Dialysis tubes	Spectra/Por® 1 Dialysis Membrane, 6 – 8 kDa MWCO	Spectrum Laboratories Inc. (USA)
Electroporation cuvettes	Signature™ Disposable Electroporation Cuvettes, 2 mm gap distance	VWR International (Germany)
Glass beads	0.25 – 0.5 mm diameter	Carl Roth GmbH + Co. KG (Germany)
Spectrophotometer cuvettes	Rotilabo® single-use cells (Polystyrene)	Carl Roth GmbH + Co. KG (Germany)
Sterile filters for syringes	Rotilabo®-syringe filters, PES, 0.22 µm pore size	Carl Roth GmbH + Co. KG (Germany)
Syringes	BD 1 mL/10 mL/50 mL syringe with Luer-Lok™ tip	BD Diagnostics (USA)
Tubes, protein low-bind	Protein LoBind Tubes	Eppendorf AG (Germany)
Ultrafiltration column	Vivaspin 20, 5,000 Da MWCO, PES	Sartorius AG (Germany)

2.1.4 Antibodies

Antibodies presented in Table 4 were used for immunological staining and diluted in a 5% non-fat dried milk powder dissolved in TBS-T (Table 29).

Table 4. List of antibodies and their concentrations used within this study.

ANTIBODY	DILUTION	SUPPLIER
Anti-6xHis (mouse)	1 : 20,000 (primary antibody)	Roche Diagnostics GmbH (Germany)
Anti-Sco1, middle region epitope (from rabbit)	1 : 1,000 (primary antibody)	Antibodies-online GmbH (Germany)
ECL™ Anti-Mouse IgG, HRP conjugated, whole antibody (from sheep)	1 : 10,000 (secondary antibody)	GE Healthcare GmbH (Ger- many)
Anti-Rabbit IgG (H&L), HRP conjugated, whole antibody (from goat)	1 : 10,000 (secondary antibody)	Agrisera AB (Sweden)

2.1.5 Enzymes

Polymerases, restriction endonucleases, and ligases used for molecular cloning were purchased from New England Biolabs GmbH (Germany). Commonly used enzymes for protein purification procedures were purchased from AppliChem GmbH (Germany), Merck KGaA (Germany), or Carl Roth GmbH + Co. KG (Germany). The AcTEV™ protease from the *Tobacco etch virus* (TEV) for His-tag cleavage was purchased from invitrogen AG (USA).

2.1.6 Molecular Weight Standards

Molecular standards (Figure 14) were used in DNA agarose gels and protein SDS PAGE gels.

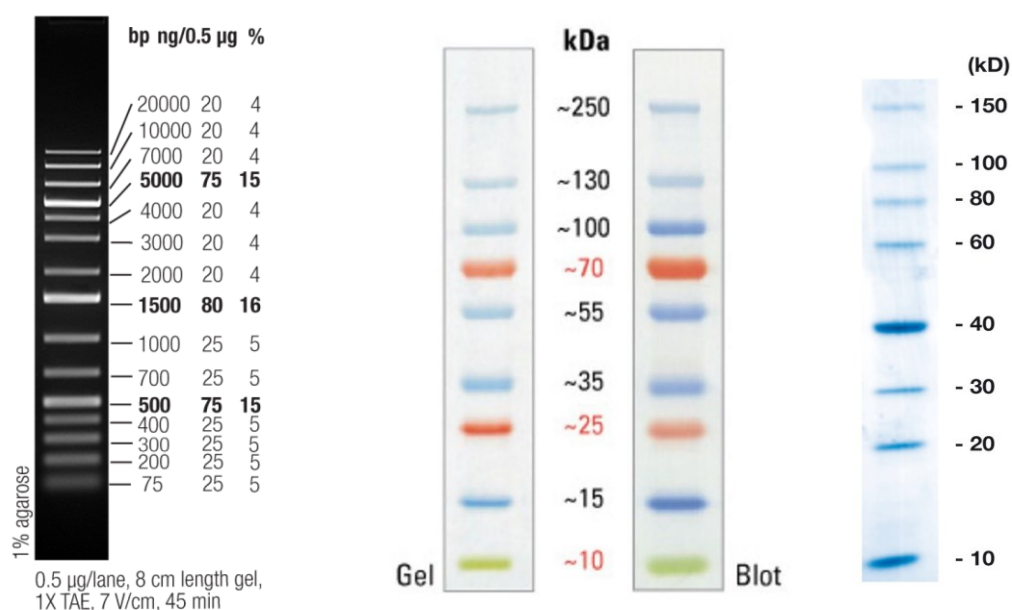


Figure 14. The characteristic appearance of markers on agarose gels, SDS PAGE gels, and western blots, respectively.

Left: GeneRuler 1 kb Plus DNA Ladder on 1% agarose gels (Thermo Fisher Scientific Inc. 2000). Center: PAGE Ruler™ Prestained Protein Ladder 10 to 250 kDa (Thermo Fisher Scientific Inc. 2019). Right: ROTI® Mark 10-150 protein marker (Carl Roth GmbH + Co. KG 2020). It is His-tagged and, therefore, directly visible on developed photo films.

2.1.7 DNA Oligonucleotides

The company biomers.net GmbH (Germany) synthesized the DNA oligonucleotides. The lyophilized oligonucleotides were dissolved in ddH₂O and stored at -20 °C. All oligonucleotides listed in Table 5 were used as primers in polymerase chain reactions in this study.

Table 5. List of oligonucleotides used in this study. The red color marks the restriction sites (RS), the purple the coding for TEV cleavage site, the orange color the glycine-serine linker, and the black capital letters mark the overlapping regions.

NAME	SEQUENCE (5' → 3')	SPECIFICATION AND RS
P1_Sco1_NheI_TEV_For	tatata GCTAGCG AGAACCTTTACTTTCAGG- GAATGCTGAAGTTGTCAAGAAGTGCC	<i>NheI</i> , TEV
P2_Sco1_XhoI_Rev	tatata CTCGAG TTATTTGAATAAGAAGGAGTAC- CATGCC	<i>XhoI</i>
P3_Sco1_wo_St_EcoRI_Rev	tatata GAATTC TTTGAATAAGAAGGAGTACCAT- GCCTC	<i>EcoRI</i> , without stop co- don

P4_Sco1_EcoRI_G4S3_For	tatataGAATT-CGGCGGCGGCGGCAGCGGCGGCGGCGGCAGC GGCGGCGGCAGCATGCTGAAGTTGTCA-AGAAGTGCC	EcoRI, insertion of glycine-serine linker
P5_Sco1Δ95_NheI_TEV_For	tatataGCTAGCGAGAACCTTTACTTTCAGG-GACGCAGATTGGAAACACAGAAGG	NheI, TEV
P6_Sco1Δ95_EcoRI_G4S3_For	tatataGAATT-CGGCGGCGGCGGCAGCGGCGGCGGCGGCAGC GGCGGCGGCAGCCGCAGATTG-GAAACACAGAAGG	EcoRI, insertion of glycine-serine linker
P7_Ccg-2_NheI_TEV_For	tatataGCTAGCGAGAACCTTTACTTTCAGG-GAATCGGCCCAACACCTGC	NheI, TEV
P8_Ccg-2_wo_St_EcoRI_Rev	tatataGAATTCGGCAACGCAGTTGGCAGC	EcoRI, without stop codon
P9_pET28b_Seq_For	tatataATGGGCAGCAGCCATCATCATC	Used for sequencing
P10_pET28b_Seq_Rev	tatataGGGCTTTGTAGCAGCCGGATC	Used for sequencing
P17_Sco1D95a_NheI_TEV_For	tatataGCTAGCGAGAACCTTTACTTTCAGGGA	NheI, TEV

2.1.8 Plasmids and Vectors

A list of vectors created and used in this study is shown in Table 6.

Table 6. List of vectors used in this study.

VECTOR	FEATURES	SUPPLIER
pET-28b(+)	pBR322 origin, kanR, lacI, T7 promoter, T7 terminator	Merck KGaA (Germany)
pET28b_ccg2	T7 promoter, Ccg-2	Julia Döring, Institute of Genetics, Technische Universität Dresden
pET28b_Cox17_a	T7 promoter, yCox17	From this study
pET28b_Cox17_b	T7 promoter, yCox17, Ccg-2	From this study
pET28b_Cox17_c	T7 promoter, Ccg-2, yCox17	From this study
pET28b_Sco1_a	T7 promoter, ySco1	From this study

pET28b_Sco1_b	T7 promoter, ySco1, Ccg-2	From this study
pET28b_Sco1_c	T7 promoter, Ccg-2, ySco1	From this study
pET28b_Sco1Δ95_a	T7 promoter, ySco1Δ95	From this study
pET28b_Sco1Δ95_b	T7 promoter, ySco1Δ95, Ccg-2	From this study
pET28b_Sco1Δ95_c	T7 promoter, Ccg-2, ySco1Δ95	From this study

2.2 MICROORGANISMS

Used microorganisms and strains are listed in Ch. 2.2.1. Ch. 2.2.2 presents the microorganisms' cultivation parameters. While Ch. 2.2.3 explains the preparation of electrocompetent cells for the transformation by electroporation, Ch. 2.2.4 describes the method of preparing *E. coli* glycerol stock cultures for long-time storage.

2.2.1 Strains

STRAIN	GENOTYPE	SUPPLIER
<i>Escherichia coli</i>		
Top10F'	<i>F</i> { <i>lacIq</i> <i>Tn10</i> (<i>TetR</i>)} <i>mcrA</i> Δ(<i>mrr</i> - <i>hsdRMS</i> - <i>mcrBC</i>) Φ80 <i>lacZ</i> Δ <i>M15</i> Δ <i>lacX74</i> <i>recA1</i> <i>araD139</i> Δ(<i>ara-leu</i>)7697 <i>galU</i> <i>galK</i> <i>rpsL</i> <i>endA1</i> <i>nupG</i>	Invitrogen GmbH (Germany)
SHuffle® T7 Express <i>lysY</i>	<i>MiniF</i> <i>lysY</i> (<i>CamR</i>)/ <i>fhuA2</i> <i>lacZ</i> :: <i>T7 gene1</i> [<i>lon</i>] <i>ompT</i> <i>ahpC</i> <i>gal</i> λatt::pNEB3- <i>r1-cDsbC</i> (<i>SpecR</i> , <i>lacIq</i>)Δ <i>trx</i> <i>B</i> <i>sulA11</i> <i>R</i> (<i>mcr</i> -73::mini <i>Tn10</i> -- <i>TetS</i>)2 [<i>dcm</i>] <i>R</i> (<i>zgb</i> -210::Tn10 -- <i>TetS</i>) <i>endA1</i> Δ <i>gor</i> Δ(<i>mcrC</i> - <i>mrr</i>)114::IS10	New England Biolabs GmbH (Germany)
Lemo21 (DE3)	<i>fhuA2</i> [<i>lon</i>] <i>ompT</i> <i>gal</i> (λ DE3) [<i>dcm</i>] Δ <i>hsdS</i> / pLemo(<i>CamR</i>) λ DE3 = λ <i>sBamHI</i> Δ <i>EcoRI</i> - <i>B int</i> ::(<i>lacI</i> :: <i>PlacUV5</i> :: <i>T7 gene1</i>) <i>i21</i> Δ <i>nin5</i>	New England Biolabs GmbH (Germany)

pLemo = pACYC184-*PrhaBAD-lysY*

Saccharomyces cerevisiae

BY4741

MATa his3Δ1 leu2Δ0 met15Δ0 ura3Δ0

EUROSCARF (Germany)

2.2.2 Cultivation of Microorganisms

In this study, the *E. coli* strains were cultivated in lysogeny broth (LB) media (Table 7). The necessary antibiotics were kanamycin (Kan) 30 µg/mL and chloramphenicol (Cam) 30 µg/mL. All *E. coli* liquid pre-cultures or overnight cultures were incubated at 30 °C while the protein expression was performed at 16 °C or 30 °C (Ch. 3.1). *E. coli* strains plated on LB agar plates were incubated for at least 24 h at 37 °C.

For the cultivation of the *E. coli* strains, the following steps were taken: Inoculate a liquid culture with a colony or colonies from a plate, cells from a glycerol stock culture (Ch. 2.2.4), or with freshly transformed cells (Ch. 2.4.10) and add the appropriate antibiotics. The growth rate can be determined by monitoring the optical density at 600 nm (OD₆₀₀) *via* photospectrometric measurements. The yeast cells are cultivated in yeast extract-peptone-dextrose (YPD) media (

Table 8).

Table 7. Protocol for LB media and LB agar plates.

LB MEDIA

5 g/L	Yeast Extract
10 g/L	Peptone
5 g/L	NaCl
(1.5%	Agar, only for solid media)
Adjust to pH 7.4 with NaOH. Autoclave.	

Table 8. Protocol for yeast extract-peptone-dextrose (YPD) media

YPD MEDIA	
10 g/L	Yeast extract
20 g/L	Peptone
20 g/L	Glucose
(15 g/L	Agar, only for solid media)
Adjust to pH 7.4 with NaOH. Autoclave.	

2.2.3 Preparation of Electrocompetent *E. coli* Cells

E. coli cells from a glycerol stock solution (Ch. 2.2.4) were plated onto an LB-agar plate with appropriate antibiotics and incubated at least overnight at 37 °C. A single colony was picked from the plate, an LB liquid pre-culture (10 mL) with appropriate antibiotics inoculated and incubated overnight at 30 °C. 400 mL LB liquid culture with appropriate antibiotics were inoculated with the pre-culture with a 1:50 ratio to reach an OD₆₀₀ of approximately 0.1. The culture was incubated at 30 °C until the OD₆₀₀ reached the mid-log phase of 0.4 to 0.7. The culture was cooled on ice for 30 min and the *E. coli* cells were harvested at 4000 rpm and 4 °C for 10 min. The cell pellet was washed three times, first, with 400 mL, then with 200 mL ice-cold ddH₂O, and at last, with ice-cold 10% sterile glycerol under centrifugation conditions mentioned above. The cell pellet was suspended in 2 mL ice-cold 10% sterile glycerol. The cell suspension was pipetted into ice-cold reaction tubes in 40 µL aliquots.

2.2.4 Preparation of *E. coli* Glycerol Stocks

A liquid culture (10 mL) was inoculated with a single colony from an LB-plate with *E. coli* cells of interest, the appropriate antibiotics were added and incubated at 30 °C until the liquid culture reaches an optical density in its mid-log phase of roughly OD₆₀₀ = 0.4 – 0.7. 1 mL of culture was taken off, centrifuged at 3,500 x g for 5 min, and the supernatant was discarded. The cell pellet was suspended in 900 µL LB media with the appropriate antibiotics. 100 µL of 87% sterile glycerol was added, mixed well and incubated for 30 min at 4 °C to enable the glycerol to diffuse into the cells before storing this 1 mL *E. coli* glycerol stock at -70 °C.

2.3 PROTEIN DESIGN

The basis of the final fusion proteins is the corresponding DNA sequences. The pET28b(+) plasmid was used as a vector template. It possesses an inducible *77* promoter followed by a start codon. Subsequently, it is coding for six repeats of histidine (His₆-tag; His-tag) and a thrombin cleavage site. The genes encoding the target proteins and hydrophobin Ccg-2 derivatives, respectively, are inserted at the vector's DNA restriction sites *NheI* and *XhoI*. All constructs code for the target protein and a TEV cleavage site for a second option – besides the thrombin cleavage site – to remove the His-tag from the target protein. The term protein construct stands for a protein with the specific insert (target protein), combined with additional components needed for the preparation or the insertion into the experimental setup (Ch. 2.7, Ch. 2.8). Figure 15 shows a sketch of the three protein constructs. Construct 'a' describes a His-tagged target protein. It is used for the functionalization of the soft colloidal probes (SCP). Construct 'b' describes the His-tagged fusion protein with the target protein N'-terminally and the hydrophobin C'-terminally. In contrast, construct 'c' exhibits the hydrophobin at the N'-terminus and the C'-terminus target protein. Those constructs are used in the hydrophobin assembly driven chip surface functionalization. The glycine-serine linker ((G₄S)₃ linker) (Zhao et al. 2015) is a flexible polypeptide chain that connects the target protein and the hydrophobin Ccg-2. A flexible linker was chosen (Van Rosmalen et al. 2017) to enable correct protein folding and, therefore, maximize the correct surface activity of the hydrophobin and the target protein's functionality. An *EcoRI* DNA restriction site is located between the DNA coding for the target protein and the hydrophobin to enable an easy exchange of the different protein-coding components. The stop codon is incorporated at the target protein's end (for construct a and c) or the hydrophobin's end (for construct b). Their DNA sequence includes a stop codon. There are some nucleic acids and amino acids, respectively, which are not mentioned in the sketch but result from the template plasmid constitution or are necessary for cloning and the protein design.

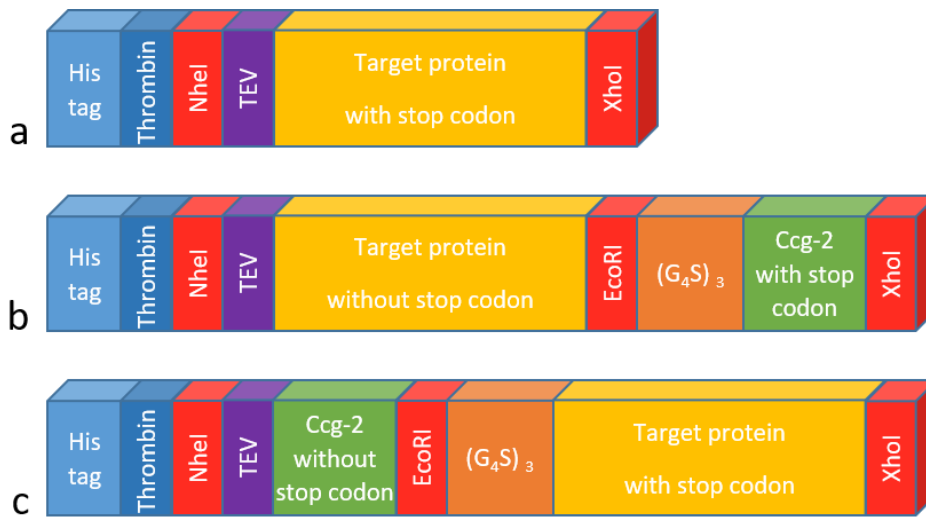


Figure 15. Schematic representation of the protein design of three constructs used in different ways within the experimental setup.

The His-tag (light blue) is needed in protein-specific immunological detection and for immobilization during protein purification. The DNA restriction sites are marked in red. The restriction sites thrombin (dark blue) and TEV (purple) can be addressed by the thrombin protease and TEV protease, respectively. The target protein (yellow) is interchangeable, depending on its application. The flexible glycine-serine linker $(G_4S)_3$ (orange) connects the hydrophobin Ccg-2 (green) and the target protein sequence.

The different order of protein components of the fusion protein is marked by a, b or c. For example, in the case of ySco1, the different constructs of the fusion proteins are named Sco1_a, Sco1_b, or Sco1_c. The truncation of the N'-terminal transmembrane domain, which means the deletion of 95 amino acids, is denoted as Sco1 Δ 95_a, Sco1 Δ 95_b, or Sco1 Δ 95_c. In some cases, the His-tag cleavage at the TEV cleavage site is necessary. The cleaved protein construct will be denoted as cISco1 Δ 95_a and so on.

2.4 MOLECULAR CLONING METHODS

The following Ch. 2.4.1 to Ch. 2.4.9 describe the necessary steps to generate the final DNA vectors that include the DNA fragment of interest, which codes for the respective target proteins (Ch. 2.3).

2.4.1 Vector Template Preparation

Respective DNA vectors have been designed and generated for achieving the recombinant proteins explained in Ch. 2.2.4.

The described target genes for Cox17_a, Cox17_b, and Cox17_c were codon-optimized and synthesized by BioCat GmbH (Germany) and cloned into the expression vector pET-28b(+) creating the plasmids

pET28b_Cox17_a, pET28b_Cox17_b and pET28b_Cox17_c (Ch. 2.1.8). The DNA target sequence of yCox17 from *S. cerevisiae* contains three restriction sites needed for the following cloning procedure. The relevant nucleotides were substituted in the sequence according to the genetic code chart before synthesis.

The described target genes for Sco1_a, Sco1_b, and Sco1_c and for Sco1Δ95_a, Sco1Δ95_b, and Sco1Δ95_c were isolated from chromosomal DNA of *S. cerevisiae*. For the isolation of genomic DNA from *S. cerevisiae*, centrifuge 2 mL sample from a liquid culture were centrifuged at 3,500 x g for 5 min, and the supernatant was discarded. The resulting pellet was washed once with 1 mL dH₂O under the conditions mentioned above. The pellet was dissolved in 500 µL lysis buffer (Table 9) and about the same volume (roughly 400 µL) of glass beads was added. The sample was treated with the vibrating mill for 2 min at 30 Hz to lyse the cells. It was worked on ice from here on because the cell walls were disrupted. After the glass beads have sedimented, the supernatant was pipetted off, transferred into a new centrifugation tube and 275 µL 7 M ammonium acetate (pH 7.0) was added. The solution was vortexed and incubated first for 5 min at 65 °C, then for 5 min on ice. 500 µL chloroform was added and the mixture was vortexed until the phase separation has vanished. The solution was centrifuged for 2 min at 13,000 x g, the upper phase was carefully transferred into 1 mL isopropanol, vortexed, and incubated for at least 5 min at room temperature for DNA precipitation. The solution was centrifuged for 5 min at 13,000 x g, the supernatant was discarded, the pellet was re-suspended in 70% EtOH, and washed by centrifugation for 10 s at 13,000 x g. For storage, the pellet was dried using a vacuum concentrator for about 10 min at 45 °C and full speed. The pellet was re-suspended in 50 µL ddH₂O and 1 µL RNase A (10 mg/mL) was added. The DNA concentration was then determined by measuring the absorption at 260 nm with a UV/Vis spectrophotometer.

Table 9. Protocol for lysis buffer.

LYSIS BUFFER

100 mM	Tris/HCl
50 mM	EDTA
1% w/v	SDS

The pH was adjusted to 8.0 with HCl.

2.4.2 Agarose Gel Electrophoresis

The DNA samples were separated according to their molecular weight in 0.8 – 1% agarose gels. The appropriate amount of agarose was melted in TAE buffer (Table 10). 0.25 µL RedSafe™ nucleic acid Staining solution (iNtRON Biotechnology Inc. (Korea)) was added per 1 mL agarose gel solution (0.025%). Polymerisation takes at least 30 min.

Table 10. Protocol for 1x Tris-acetate-EDTA (TAE) buffer solution. It can be stored in a up to 50x TAE stock solution.

TAE	
40 mM	Tris/HCl
20 mM	Acetic acid
1 mM	EDTA (sodium salt dehydrate)

The DNA samples were prepared by adding the appropriate amount of 6x DNA loading dye (Table 11). The separation ran with TAE buffer under conditions described in Table 12.

Table 11. Protocol for 6x DNA loading dye.

6X DNA LOADING DYE	
0.2% w/v	Bromophenol blue
100 mM	EDTA
30% v/v	Glycerol
Adjust to pH 8.0	

Table 12. Overview of sample conditions for preparation and running of agarose gel electrophoresis.

SAMPLE CONDITIONS FOR AGAROSE GEL ELECTROPHORESIS		
Gel Volume	40 mL	120 mL

RedSafe™ (0.25 µL/1 mL)	10 µL	30 µL
Voltage	90 V	100 – 110 V
Duration	50 min	70 min

2.4.3 DNA Extraction from Agarose Gels

The DNA was extracted from the agarose gel using the NucleoSpin® Gel and PCR Clean-up mini kit for gel extraction and PCR clean up (Macherey-Nagel GmbH & Co. KG (Deutschland)).

2.4.4 Polymerase Chain Reaction

The polymerase chain reaction (PCR) enables the efficient amplification of a specific DNA target sequence. The *Taq* and the Phusion DNA polymerases were used. A standard PCR reaction protocol with the Phusion polymerase is shown in Table 13 and, the corresponding thermocycling protocol is given in Table 15.

Table 13. Protocol for a PCR with the Phusion polymerase. For the negative control, substitute the template DNA with ddH₂O. It can be prepared as a master mix.

PCR PROTOCOL

Add to the reaction volume	ddH ₂ O
1x	Phusion HF buffer (5x)
0.2 mM	dNTP (10 mM)
50 - 250 ng or: 1 pg – 10 ng	Genomic Template DNA or: Plasmid Template DNA
0.5 µM	Forward Primer (10 µM)
0.5 µM	Reverse Primer (10 µM)
1 unit/50 µL volume	Phusion HF DNA Polymerase

For a PCR reaction, all components from Table 13 were added into a PCR-reaction tube. The polymerase was added last. All components were kept on ice at all times and were mixed carefully by pipetting.

The used oligonucleotide sequences are listed in Appendix Ch. 7.1. The following oligonucleotide combinations shown in Table 14 were needed to amplify the target sequences for the final constructs of *ySco1* described in Ch. 2.3. The final constructs of *Cox17* were synthesized and, therefore, did not need any oligonucleotides.

Table 14. Oligonucleotide combinations to amplify the *ySco1* target sequences *via* PCR.

	Sco1_a	Sco1_b	Sco1_c	Sco1Δ95_a	Sco1Δ95_b	Sco1Δ95_c
Forward	P1	P1	P4	P5	P5	P6
Reverse	P2	P3	P2	P2	P3	P2

The thermocycling conditions were chosen as described in Table 15. The annealing temperature depends on the primers' DNA, and the elongation time depends on the length of the DNA fragment that is amplified.

Table 15. Thermo-cycling protocol for PCR amplification with Phusion polymerase.

PCR CYCLING PROTOCOL

STEP	TEMP	TIME
Initial Denaturation	98°C	30 sec
30 Cycles	98°C	5 - 10 sec
	50 - 72°C	10 - 30 sec (Annealing)
	72°C	15 - 30 sec/kb (Elongation)
Final Extension	72°C	5 min
Hold	4-10°C	

The amplified DNA fragments are ready for further use or kept at 4 °C or even frozen.

2.4.5 DNA Restriction Digest

The amplified DNA fragments from Ch. 2.4.4 were prepared for DNA ligation into the final cloning vector by a DNA restriction digest.

Table 16. A protocol for a 25 μL restriction digest with two different enzymes. All enzymes used for the restriction digests were purchased (New England Biolabs GmbH (Germany)). Different reaction volumes can be down- or upscaled.

RESTRICTION DIGEST PROTOCOL

25 μL REACTION VOLUME

Add to 25 μL	ddH ₂ O
0.5 μL	Restriction Enzyme 1
0.5 μL	Restriction Enzyme 2
0.5 μg	DNA
2.5 μL	CutSmart (CS) Buffer (10x)

The protocol for digesting the DNA fragments is shown in Table 16. All fragments were added to a reaction tube, working on the ice at all times. After adding the enzymes, the reaction solution was only mixed by careful pipetting and then incubated at 37 °C for 1 hr. The Cut Smart buffer enables the digestion with two enzymes at the same time under the same conditions. The enzymes were inactivated by heat if possible. The inactivation temperature and time are enzyme-specific. The choice of restriction enzymes depends on the protein construct design, as displayed in Figure 15.

2.4.6 DNA Dialysis

The DNA samples were dialyzed to remove interfering salts before ligating DNA fragments together and before transforming *E. coli* cells with the DNA vector of interest or ligation-mixture by electroporation.

5 – 100 μL DNA sample was pipetted onto the dialysis membrane (MF-Millipore Membrane Filter V-series 0.025 μm pore size, Merck KGaA (Germany)), which was carefully placed onto a ddH₂O reservoir of at least 50 times the volume. It was incubated for 20 min at room temperature. Pipette the sample carefully off and use it directly.

2.4.7 Ligation of DNA Fragments

A recombinant DNA vector was designed by creating the specific DNA insert or inserts and choosing the suitable cloning vector. It was followed by ligating them together using a DNA ligase enzyme.

Table 17. Protocol for DNA ligation with one insert and two insert DNA (italic).

DNA Ligation

T4 DNA Ligase	2 μ L
Buffer (10x)	
Vector DNA	0.020 pmol
Insert DNA	0.060 pmol
Nuclease-free water	To 20 μ L
T4 DNA Ligase	1 μ L
Incubate at room temperature for 30 min.	
<i>In case of ligating two inserts, add:</i>	
<i>2nd Insert DNA</i>	<i>0.060 pmol</i>
<i>T4 DNA Ligase</i>	<i>0.5 μL</i>
<i>Incubate at room temperature for 30 min</i>	
Heat inactivation at 65 °C for 10 min	

The DNA samples were dialysed as described in Ch. 2.4.6 before usage. All the components from Table 17 were pipetted together on ice as described in the table. The mixture was incubated at room temperature and heat-inactivated at 65 °C. The sample was frozen at -20 °C or directly used to transform *E. coli* cells as described in Ch. 2.4.10.

2.4.8 Isolation of DNA from *E. coli*

The plasmid DNA was isolated from *E. coli* cells and purified using a plasmid preparation procedure. Here, the preparation was performed using the ZR Plasmid Miniprep – Classic kit (Zymo Research Europe GmbH (Deutschland)). The elution was done with ddH₂O, and the concentration was measured with the UV/Vis spectrophotometer NanoDrop.

2.4.9 DNA Sequencing

The identity of each nucleic acid of the target area was verified by sequencing analysis to confirm the recombinant DNA samples' sequence. Eurofins Genomics GmbH (Germany) carried out the sequencing. Biomers.net GmbH (Germany) synthesized suitable oligonucleotides for sequencing or the vector-specific oligonucleotides were used (see Table 5).

2.4.10 Transformation of *E. coli* via Electroporation

For uptake of DNA into *E. coli*, electroporation was applied (Neumann et al. 1982). The DNA samples were dialysed as described in Ch. 2.4.6 before the transformation.

Table 18. Protocol for SOC-Medium. Prepare a separate magnesium solution from $\text{MgCl}_2 \cdot 6\text{H}_2\text{O}$ and $\text{MgSO}_4 \cdot 7\text{H}_2\text{O}$, which is sterile filtered, and a separate α -D-Glucose (anhydrous) solution which is autoclaved before mixing with the other chemicals.

SOC MEDIUM

20 g/L	Tryptone or peptone
5 g/L	Yeast extract
10 mM	NaCl
2.5 mM	KCl
20 mM	$\text{MgCl}_2 \cdot 6\text{H}_2\text{O}$
20 mM	$\text{MgSO}_4 \cdot 7\text{H}_2\text{O}$
20 mM	α -D-Glucose (anhydrous)

50 ng purified DNA vector or 3 – 5 μL ligated DNA sample was added to 30 μL electrocompetent *E. coli* Top10F' cells. The electroporation of this mixture was conducted in an electroporation cuvette at 2,500 V for 6 ms. The electroporated mixture was added to 1 mL SOC medium (Table 18) and incubated at 37 °C for 1 h for a first cell recovery. The solution was concentrated by centrifugation to a final volume of around 300 μL . 50 μL concentrated cell mixture was plated onto an LB agar plate with the appropriate antibiotics depending on the antibiotic resistance marker of the DNA vector. The plate was incubated at 37 °C for at least 24 h.

2.5 PROTEIN DETECTION AND QUANTIFICATION

A sample's protein content was separated according to their molecular weight using the protein gel electrophoresis method (Ch. 2.5.1). In case the overall content of protein is of interest, the amino acid-specific Coomassie staining (Ch. 2.5.2) makes it visible. All of the recombinant target proteins are fused with a His-tag. These proteins can be specifically addressed when blotted on a membrane, e.g., with the western blot method (Ch. 2.5.3) by anti-6xHis antibodies in an immunodetection analysis (Ch. 2.5.4).

There are different ways of quantifying the protein concentration of a sample. The methods are based on the amino acid content of the protein sample, and, consequently, they rely on the choice of a suitable reference sample. Ch. 2.5.5, 2.5.6, and 2.5.7 describe three ways of protein quantification methods and name their application areas.

2.5.1 SDS PAGE

The sodium dodecyl sulfate polyacrylamide gel electrophoresis (SDS PAGE) is a one-dimensional gel electrophoresis method under denatured conditions (Ch. 2.5.1.1) to separate the proteins according to their molecular weight fractions. The samples were applied in the gel's well, and voltage was applied. Due to the negative charge of the proteins, the protein samples enter the stacking gel. The border between stacking and separation gel shows a jump in pH. The proteins stack at this border and enter the porous separation gel collectively, where the proteins show a velocity of movement, which is proportional to their molecular weight. The gels were prepared based on glycine (Ch. 2.5.1.2) (Ornstein 1964; Laemmli 1970) or based on tricine for small proteins of interest (Ch. 2.5.1.3) (Haider et al. 2012).

2.5.1.1 Sample Preparation

An *E. coli* cell lysate was prepared by washing and re-suspending the cells in phosphate-buffered saline (PBS) buffer (Table 19) two times and heating the sample for 10 min at 95 °C to disrupt the cells. This step can be omitted if the disruption has already been performed previously in the experiment or if purified proteins were used.

The protein content of the samples were quantified and the appropriate dilution to apply 19 ng protein content per well were prepared. The appropriate protein loading buffer was added and the sample was heated to 95 °C for 10 min to facilitate the protein denaturation and the binding of DTT to the denatured amino acid residues. The samples were cooled on ice for 1 min and spun down. The samples were then used in a glycine (Ch.2.5.1.2) or tricine SDS PAGE (Ch. 2.5.1.3).

Table 19. Protocol for 1x PBS buffer. It can also be prepared in a 10x PBS stock solution.

PBS	
8 g/L	NaCl
0.2 g/L	KCl
1.11 g/L	Na ₂ HPO ₄ (anhydrous)
0.2 g/L	KH ₂ PO ₄
Adjust to pH 7.4 with NaOH	

2.5.1.2 Glycine SDS PAGE

The separation gel (Table 21) was prepared and the appropriate amount was filled into the vertical gel electrophoresis device. The separation gel was covered with isopropanol to form a clean and even edge. Polymerization can be seen after 30 min. The isopropanol was removed, the stacking gel was prepared and added on top of the separation gel. The initial polymerization takes 15 min. Afterwards, the device was packed in a humid environment to keep it from drying out and incubate overnight to enable a full and homogeneous polymerization.

Table 20. Protocol for preparing the 6x loading buffer for the glycine SDS PAGE. This buffer is also called Laemmli buffer.

GLYCINE SDS PAGE PROTEIN LOADING BUFFER	
300 mM	Tris/HCl
12.0% w/v	SDS
0.6% w/v	Bromophenol blue
26.3% w/v	99.9% Glycerol
Adjust to pH 6.8 with HCl	

Table 21. Protocol for preparing a separation with 15% w/v polyacrylamide1.5 and a stacking gel with 4% w/v polyacrylamide for a glycine SDS PAGE.

COMPONENTS	SEPARATION GEL (15%)	STACKING GEL (4%)
30% w/v Acrylamide:bis-acrylamide, 37.5:1	5.0 mL	1.3 mL
1.5 M Tris/HCl, pH 8.8	2.5 mL	/
1.0 M Tris/HCl, pH 6.8	/	2.5 mL
10% w/v SDS	100 µL	100 µL
10% w/v Ammonium persulfate (APS)	50 µL	50 µL
TEMED	5 µL	10 µL
ddH ₂ O	2.4 mL	6.1 mL

The comb was carefully pull out of the fully polymerized gel and the prepared protein samples mixed with the glycine protein loading buffer (Table 20) was loaded onto the gel. The protein marker PageRuler™ Plus Prestained was used. Additionally, in some cases the protein marker Roti®-Mark 10-150 which is His-tagged and therefore detectable by immunological staining in the same way as the target proteins.

Table 22. Protocol for preparing the running buffer for the glycine SDS PAGE.

GLYCINE SDS PAGE RUNNING BUFFER	
24.9 mM	Tris/HCl
191.8 mM	Glycine
0.1%	SDS

The SDS PAGE chamber was flooded with the glycine running buffer (Table 22). The glycine SDS PAGE runs at 120 V for 2:30 h.

2.5.1.3 Tricine SDS PAGE

A slight modification of the glycine SDS PAGE is the tricine SDS PAGE applied in low molecular weight protein samples. The gel chamber preparation and the preparation of the gels were done following the protocol shown in Table 23. Also, the preparation and the loading were done analogous to the glycine SDS PAGE protocol, but the tricine SDS PAGE loading buffer is used (Table 25).

Table 23. Protocol for preparing 15 mL separation gel with 18% w/v polyacrylamide and 10 mL stacking gel with 2.5% w/v polyacrylamide for a tricine SDS PAGE.

COMPONENTS	SEPARATION GEL (18%)	STACKING GEL (2.5%)
30% w/v Acrylamide:bis-acrylamide, 37.5:1	5.0 mL	1.32 mL
2.5 M Tris/HCl, pH 8.8	8.4 mL	1.52 mL
3% w/v APS	225 µL	300 µL
TEMED	9 µL	10 µL
ddH ₂ O	1.35 mL	6.84 mL

Table 24. Protocol for preparing the running buffer for the tricine SDS PAGE.

TRICINE SDS PAGE RUNNING BUFFER	
25 mM	Tris/HCl
25 mM	Tricine
0.05% w/v	SDS

The SDS PAGE chamber needs to be flooded with the tricine running buffer (Table 24). The glycine SDS PAGE runs at 130 V and 100 mA for 1:30 – 2 h.

Table 25. Protocol for preparing the 2x loading buffer for the tricine SDS PAGE.

TRICINE SDS PAGE LOADING BUFFER (2X)	
100 mM	Tris/HCl solution, pH 6.8
1% w/v	SDS
0.02%	Coomassie Brilliant Blue
24% w/v	99.9% Glycerol
100 mM	DTT

2.5.2 Coomassie Staining

When the overall protein content is relevant, the proteins embedded and separated on the SDS PAGE gel were stained with colloidal Coomassie® Blue G250. The gel was incubated for 30 min in a colloidal Coomassie fixer (Table 26) and subsequently incubated for at least 24 h in the colloidal Coomassie staining solution (Table 27). The gel was washed by incubation in dH₂O for at least three times.

Table 26. Protocol for colloidal Coomassie fixer. The solution can be prepared in advance and stored at room temperature.

COLLOIDAL COOMASSIE FIXER	
40% v/v	EtOH
10% v/v	Acetic acid

Table 27. Protocol for colloidal staining solution. The solution has to be filtered through a fluted filter after mixing. It can be prepared in advance and stored at room temperature.

COLLOIDAL COOMASSIE STAINING SOLUTION	
0.8 g/L	Coomassie brilliant blue G-250
80 g/L	Ammonium sulfate
0.82% v/v	Phosphoric acid
20% v/v	MeOH

2.5.3 Western Blot Analysis

The method used is a semi-dry blotting technique, transferring proteins out of the gel onto a membrane for further analysis by applying a voltage in a semi-dry environment (PerfectBlue 'Semi-Dry'-Blotter, Sedec) (Burnette 1981). After the separation process in the SDS PAGE, the gels were incubated for 15 min in transfer buffer (Table 28). The PVDF membrane, two times thin blotting filter paper, and two times thick blotting filter paper were cut in the size of the gel and incubated in transfer buffer for 15 min. The PVDF membrane was activated by 1 min incubation in 100% MeOH before the transfer buffer incubation. The components were placed on one of the electrodes in a sandwich-like manner: thick filter paper, thin filter paper, membrane, gel, thin filter paper, thick filter paper. Western blot was run for 1 h at 1.5 mA/cm² while the voltage should not exceed 10 V. Afterwards, the membrane was dried at room temperature to fix the proteins on the membrane. The membrane was then ready to use in immunodetection. The gel was stained after transfer as described in Ch. 2.5.2 to compare it with the not blotted, directly stained gel to evaluate the transfer efficiency.

Table 28. Transfer buffer for semi-dry western blot.

TRANSFER BUFFER	
3.02 g/L	Tris/HCl
14.4 g/L	Glycine
0.1% v/v	10% SDS
20% v/v	MeOH

2.5.4 Immunological Detection

The blocking solution's concentration was 5% non-fat dried milk powder dissolved in tris-buffered saline with Tween-20 (TBS-T) (Table 1). The used antibody concentration depended on the antibody and was used as described in Table 4 in Ch. 2.1.4. All incubation and washing steps were conducted on a platform rocker at room temperature.

The dried membrane has to be re-activated by incubation for 1 min in 100% MeOH. The following incubation steps start with blocking the membrane with the milk powder solution for 60 min. Afterward, the membrane was incubated with the primary antibody specific against the target protein or its tag diluted in the milk powder solution for 60 min and washed at least three times for 10 min with TBS-T. Subsequently, perform an incubation with horseradish peroxidase (HRP) tagged secondary antibody

diluted in the milk powder solution for 45 min. Finally, the membrane was washed at least three times 10 min with TBS-T. The HRP enzyme complex produces a chemiluminescent signal detectable with autoradiography films or with the gel documentation and analysis system G:BOX.

Table 29. Protocol for TBS with the addition of the detergent Tween 20.

TBS-T	
8.01 g/L	Tris/HCl
2.43 g/L	NaCl
Adjust to pH 7.6 with HCl	
0.1%	Tween 20

The ECL component and the peroxide component were mixed in a 1:1 ratio in an appropriate volume and protected from light. The ECL mixture was evenly applied to the membrane and incubated as instructed. If using the G:BOX system, the membrane was placed inside the machine, and the manufacturer's instructions were followed. The exposure time of the chemiluminescent signal onto the camera chip can be optimized. If using autoradiography films, the manufacturer's instructions were followed. The signal intensity can be optimized by the chemiluminescent exposure time onto the film and the incubation time in the developer solution.

2.5.5 Protein Quantification: Lowry Assay

The Bio-RAD *DC™* Protein Assay (Bio-Rad Laboratories GmbH (Germany)) was used for quantifying the protein content of a cell lysate in preparation, for example, for the usage in SDS PAGE and following western blot analysis. This protein assay bases on the Lowry assay (Lowry et al. 1951), which describes a two-step procedure: First, protein and copper interact in an alkaline medium, and secondly, this copper-treated protein reduces Folin producing reduced species, which show the characteristic blue color. Especially the absorption of the amino acids tyrosine (Y), tryptophan (W), and to a lesser extent, cysteine (C) and histidine (H) are responsible for the measurable color change.

The standard assay protocol was carried out according to the manufacturer's instruction, and the spectrophotometer was used for detection. When using an untreated cell lysate from protein expression, the sample was lysed at 95 °C for 10 min before the protein assay was carried out.

2.5.6 Protein Quantification: Bradford Assay

The quantification of a sample's protein content using an adapted version of the Bradford Coomassie-binding colorimetric method (Bradford 1976) was carried out using the Coomassie® (Bradford) Protein Assay Kit (Thermo Fisher Scientific Inc. (USA)). The method bases on a shift in absorption from 465 nm to 595 nm upon Coomassie dye binding to proteins and primarily to the basic amino acids arginine (R), lysine (K), and a lesser extent, also histidine (H). The number of Coomassie bound ligands is closely proportional to the number of positive charges in a protein molecule. The unknown sample's protein concentration is estimated by comparison with the absorbance of a reference protein sample. The standard reference protein is the albumin standard containing bovine serum albumin (BSA).

The Bradford assay was carried out as described by the manufacturer as a microplate procedure. While the standard protocol requires only 5 µL reference and unknown protein sample, respectively, with a sensitivity range of 125 – 1,500 µg/mL, the micro protocol requires as much as 150 µL protein sample.

2.5.7 Protein Quantification: NanoDrop Measurement

An alternative protein quantification method is using the NanoDrop UV/Vis spectrophotometer. It measures the absorption spectra of a 2 µL protein sample and calculates the protein concentration based on the absorption value at 280 nm. The standard is comparing the sample with the absorption spectra of BSA or the basic settings of a 0.1% protein solution producing an absorbance of 1 A for calculating the concentration. Protein specific parameters such as the molecular weight MW [Da] and the molar extinction coefficient at 280 nm wavelength ϵ_{280} [M⁻¹cm⁻¹] can also be inserted manually, derived from an analysis of the amino acid sequence:

$$\epsilon_{280} = (nW * 5,500 + nY * 1,490 + nC * 125) \frac{1}{Mcm}$$

Where nW, nY, and nC denote the number of tryptophan, tyrosine, and cysteine present in the protein, respectively. The ratio of A260/A280 gives an impression of the sample's purity and should be below 1. Otherwise, it might be an indication of nucleic acid contamination.

The method bases mainly on the absorption of cyclic amino acids tyrosine (Y), tryptophan (W), and cysteine (C). A limitation of the assay is the possible absorption of the buffer in the case of imidazole or other complex buffer systems present. Buffers like PBS and the redox-refolding buffer (see Ch. 2.6.3.2) are no problem. The instruments' range of detection is 0.03 – 478 mg/mL for the NanoPhotometer® NP80 (Implen GmbH (Germany)). The assay's biggest advantages are the quick procedure without any different substrates, no need for a reference standard curve, usage of only a low amount of protein sample, and the possibility of inserting protein-specific parameters from the theoretical evaluation.

2.6 PROTEIN PURIFICATION AND STORAGE

2.6.1 Expression Analysis of Recombinant Proteins

The described protocol in Ch. 2.2.2 was followed to cultivate microorganisms to receive a pre-culture with a high cell density. The main culture of appropriate LB media and antibiotics mixture was inoculated with the pre-culture in a 1:50 ratio to achieve an optical density of OD₆₀₀ of roughly 0.1. The main culture was incubated at 30 °C and 180 rpm until the exponential growth regime at around OD₆₀₀ = 0.45-0.75. Then the culture was incubated on ice for 15 min, and a null sample is taken. The cells were washed by centrifuging the culture at 4 °C and 15,000 x g for 10 min; the supernatant was discarded, the pellet was suspended in 4 °C 50 mM Tris/HCl pH 7.5, and the centrifugation step was repeated under the conditions mentioned above. The pellet was then used directly for experiments or stored at -20 °C until for use.

2.6.2 Solubility Analysis

Whether the expressed protein of interest is soluble or insoluble is essential for further purifying the protein under native or denatured conditions.

The protein of interest was expressed as described in Ch. 2.6.1, but the first washing step was done with ice-cold LB media. The washing was repeated, and the cell pellet was suspended in a 30 mL solution of 1x protease inhibitor mixture (PI mix) in buffer B (Table 30). Add 30% v/v benzonase A and 13% w/v lysozyme to the suspension. The solution was incubated for 30 min at 30 °C and 180 rpm to facilitate the cells' enzymatic disruption. Afterward, the cells rested for 15 min on ice. Subsequently, the cells were disrupted mechanically by ultrasonication with a Sonopuls GM 2070 ultrasonic homogenizer (BANDELIN electronic GmbH & Co. KG (Germany)) under the following conditions: 5 x 1 min impulses, 9 x 10% per cycle, 74% power, and 1 min pause after each cycle. During the treatment, the protein samples were kept on ice at all times to hinder overheating. The cells are now disrupted, and the lysate is homogenized (take sample L). The cell lysate was topped up with PI mix and buffer B mixture to 50 mL. The solid and the liquid phases were separated by centrifugation at 1,5000 x g for 30 min at 4 °C. The supernatant carries the soluble expressed proteins (take sample S), while the insoluble proteins are in the pellet (suspend the pellet with 2 mL 1 x PBS and take sample P).

Table 30. Protocol for buffer B preparation. Prepare the buffer without Triton X-100, adjust the pH, autoclave and then add the Triton X-100 at room temperature and mix under moderate stirring.

BUFFER B

20 mM	Tris/HCl
500 mM	NaCl
5 mM	Imidazole
It was adjusted to pH 7.9 with HCl and autoclave.	
0.2%	Triton X-100

The samples were frozen right after sample collection. The samples were analyzed *via* SDS PAGE and western blot analysis and immunological detection, respectively.

2.6.3 Protein Purification by Ni²⁺ Affinity Chromatography

The choice of Ni²⁺ affinity chromatography purification protocol (Hochuli et al. 1987) depends on the solubility of the expressed recombinant protein. The solubility was tested by performing a solubility analysis described in Ch. 2.6.2 and evaluated by western blot analysis (Ch. 2.5.3) and immunological staining (Ch. 2.5.4). The protein was purified natively, as described in Ch. 2.6.3.1, if a high amount of the recombinant protein is soluble in the cell lysate (adapted from Serva Electrophoresis GmbH n.d.). On the contrary, the protein's aggregates and inclusion bodies were extracted before purification of the denatured proteins, as described in Ch. 2.6.3.2, if the expressed protein is only in the insoluble pellet fraction (Kwan et al. 2006; Hennig et al. 2016).

2.6.3.1 Native Purification of Soluble Proteins

Heterologous Expression

The described protocol in Ch. 2.2.2 was followed to receive a pre-culture with a high cell density of cells with the inserts of interest. For the native purification, the soluble protein constructs were cultivated either in T7 SHuffle Express *lysY E. coli* or in Lemo21 (DE3) *E. coli* by inoculating a 400 mL LB-media culture with 1:50 ratio incubating the culture and inducing it with 1 mM IPTG in the mid-log growth phase. For details on the construct-specific conditions, see Ch. 3.1.4.

After protein expression, the culture was set on ice for 15 min. The cells were harvested by centrifugation at $3,500 \times g$ for 10 min at 4 °C. The cells were re-suspended once with 4 °C cold 1 x PBS at pH 7.4 and harvested again under the conditions mentioned above. Finally, the cell pellet was stored at -20 °C until further use in protein purification.

Preparation of soluble fraction cell lysate

The cells were thawed on ice and re-suspend the cell pellet in 30 mL buffer B (Table 30) containing protease inhibitors.

10 µL benzonase and a tip of a spatula of lysozyme, DNase I, and RNase A were added. The cell disruption was performed by six sonication steps (1 min, 90 % cycles, 70 % power, and a settling time of 2 min before starting the next sonication step) in a Sonopuls GM2070 ultrasonic homogenizer. The cell solution was kept on the ice to prevent overheating. The sonication tip was always placed right in the middle of the solution. Subsequently, the suspension was incubated at 37 °C for 30 min in an incubating shaker, followed by chilling the cell suspension on ice for 15 min (take sample L).

The suspension was centrifuged at $15,000 \times g$ for 30 min at 4 °C to separate the soluble from the insoluble fraction. The supernatant – the soluble fraction – was kept for the purification (take sample S). The pellet was re-suspended with 5 mL 1x PBS by vortexing (take sample P).

Preparation of the Ni^{2+} affinity chromatography column

While preparing the recombinant proteins of the soluble fraction, the chromatography column was packed, loaded with Ni^{2+} , and washed. It was worked under cold room conditions to ensure that the prepared column is cold before applying the protein solution.

A Protino® Column (MACHEREY-NAGEL GmbH & Co. KG (Germany)) was closed with a plug before filling it with 10 mL His Bind® Resin sepharose matrix (Novagen (Germany)). After 5 min of incubation, the solid fraction of the sepharose suspension has separated and settled. The plug was opened and the EtOH was drained. The built-in filter frit stops the solid fractions – the sepharose beads – from draining. Another filter frit was added level on top of the sepharose matrix to avoid matrix disturbance during the purification steps. The column is now packed. The column was washed with ddH₂O by filling up the remaining column volume three times with ice-cold ddH₂O. The column was loaded with 15 mL 1 M NiSO₄. The column was washed three times with ddH₂O to remove the excess of unbound Ni^{2+} ions and washed at least seven times with buffer B (Table 30) to equilibrate the matrix to the binding buffer.

Purification of recombinant, His-tagged proteins

The supernatant was applied from the last centrifugation step onto the prepared column and flowed through twice (take samples P1 and P2). The column was washed twice with buffer B (take sample P3), twice with buffer W1 (Table 31) (take sample P4), and, finally, twice with buffer W2 (Table 32) (take sample P5). All the used buffers have to be 4 °C cold. These buffers introduce an increasing imidazole concentration, which helps to decrease unspecific bindings. The elution buffer E (Table 33) was added to elute the final protein of interest, and seven fractions of 2 mL each (samples P6 – P12) were taken.

Table 31. Protocol for wash buffer W1 preparation used for native purification. The buffer was prepared without Triton X-100, the pH adjuster, autoclaved, and then the Triton X-100 was added at room temperature and mixed under moderate stirring. The buffer was stored at 4 °C.

BUFFER W1

20 mM	Tris/HCl
500 mM	NaCl
10 mM	Imidazole
The pH was added to 7.9 with HCl and autoclaved.	
0.2% v/v	Triton X-100

Table 32. Protocol for wash buffer W2 preparation used for native purification. The buffer without Triton X-100 was prepared, the pH adjusted, autoclaved, and then the Triton X-100 was added at room temperature and mixed under moderate stirring. The buffer was stored at 4 °C.

BUFFER W2

20 mM	Tris/HCl
500 mM	NaCl
40 mM	Imidazole
The pH was adjusted to 7.9 with HCl and autoclaved.	
0.2% v/v	Triton X-100

Table 33. Protocol for elution buffer E preparation used for native purification. The buffer was prepared without Triton X-100, the pH adjusted, autoclaved, and then Triton X-100 was added at room temperature and mixed under moderate stirring. The buffer was stored at 4 °C.

BUFFER E

20 mM	Tris/HCl
500 mM	NaCl
1 M	Imidazole
The pH was adjusted to 7.9 with HCl and autoclaved.	
0.2% v/v	Triton X-100

Analysis of the samples from protein purification

The samples L, S, P, and P1 to P12 were collected, and their protein content was measured. The samples were frozen until further use. They were analyzed using SDS PAGE and immunological detection described in Ch. 2.5.1 to Ch. 2.5.4. Based on the results, elution fractions were pooled, and, if necessary, the sample was further concentrated by ultrafiltration. If the latter is necessary, the Vivaspın 20 ultrafiltration columns with a molecular weight cut-off (MWCO) of at least half the target protein's molecular weight were used to reduce the volume of the pooled eluate fractions to about ½ to ⅓ of the original volume, depending on the results of the SDS PAGE.

Dialysis of denatured, purified proteins

The subsequent dialysis is described in detail in Ch. 2.6.5. The recovered target protein concentration was measured with the Bradford assay and the NanoDrop, respectively, and the protein was stored at 4 °C.

Regeneration of resin and column

The first step of regenerating the column is removing the Ni²⁺ to ensure separate and save waste disposal by washing three times with 1% SDS. Subsequently, the resin was washed three times with EDTA (100 mM) and three times with dH₂O. The resin was stored in 10 mL 30% EtOH at 4 °C. Washing with SDS and EDTA removes most of the protein on the matrix, but small amounts can remain in the resin. Therefore, one batch of resin should only be used to purify one specific protein construct to prevent contamination.

Overview of samples taken during purification

L – cell lysate

S – soluble fraction

P – pelleted fraction

P1 – first round of flow-through of the soluble fraction through the column

P2 – second round of flow-through of the soluble fraction through the column

P3 – washing step with buffer B

P4 – washing step with buffer W1

P5 – washing step with buffer W2

P6 – 1st elution step of the target protein

P7 – 2nd elution step of the target protein

P8 – 3rd elution step of the target protein

P9 – 4th elution step of the target protein

P10 – 5th elution step of the target protein

P11 – 6th elution step of the target protein

P12 – 7th elution step of the target protein

2.6.3.2 Denatured Purification of Insoluble Proteins

The purification of insoluble recombinant proteins with Ni²⁺ affinity chromatography was mainly carried out as described before (Kwan et al. 2006; Gruner et al. 2012; Hennig et al. 2016). The recombinant target protein expression encompasses extracting the protein from the cell lysate's insoluble fraction, denaturing the contained proteins and the inclusion bodies. For instance, hydrophobins are known to favor assembling in insoluble inclusion bodies, which present a high resource of the target protein, which is, on the other hand, correctly but also partially or fully misfolded (Wang et al. 2017). The extracted and denatured proteins are then ready for purification with Ni²⁺ affinity chromatography. The subsequent dialysis has the particular function to enable proper refolding of the protein to its native form.

General Remarks

All buffers containing urea should be stored less than a week because urea is easily subjected to degradation. Preferentially the buffer is freshly prepared the day before the extraction and purification experiment. First, the urea was solved and carefully heated to up to 50 °C to facilitate solving. Then the remaining chemicals were added. All urea-containing buffers were kept at room temperature. Also, the redox-refolding dialysis buffer is prone to degradation. Therefore, the buffers were prepared with 4 °C cold water right before usage. An accurate adjustment of the pH of all of the buffers is essential.

Heterologous Expression

The described protocol in Ch. 2.2.2 was followed to receive a pre-culture with a high cell density of cells of interest. In this study, the cells of interest – exhibiting the insoluble protein constructs – were cultivated in T7 SHuffle Express *lysY E. coli* containing the heterologous protein-encoding plasmid. A 400 mL LB-media culture was inoculated with a 1:50 ratio, incubated at 30 °C for 4 h after induction with 1 mM IPTG in the mid-log growth phase.

After 4 h of protein expression, the culture was incubated on ice for 15 min. The cells were harvested by centrifugation (15,000 × g, 10 min, 4 °C). The cells were re-suspended once with 4 °C cold 50 mM Tris/HCl at pH 7.5 and harvested again under the same conditions. Finally, the cell pellet was stored at -20 °C until used for protein purification. The pellet can be prepared a few days in advance but long-time storage can impede the inclusion body extraction.

Extraction and solubilization of insoluble protein fraction

The previously harvested *E. coli* culture was thawed on ice and re-suspended in 4 °C cold 30 mL 50 mM Tris/HCl pH 7.5 containing protease inhibitors. 2 mg/mL lysozyme, 0.1 mg/mL DNase I, 0.1 mg/mL RNase A, and 15 µL Benzonase (or 8 U/mL) were added.

Cell disruption was performed with ten sonication steps in a Sonopuls GM2070 ultrasonic homogenizer (one step: 1 min, 90 % cycles, 70 % power, settle time of 2 min before starting the next sonication step). The cell solution was kept on ice at all times to prevent overheating, and the sonication tip was placed right in the middle of the solution. Subsequently, the suspension was incubated at 37 °C for 30 min in an incubating shaker, followed by chilling the cell suspension on ice for 15 min (sample P1).

The following washing steps were all performed on ice: The insoluble fractions of the well-suspended cell lysate were harvested by centrifugation at 20,000 × g for 10 min at 4 °C (sample P2 from the supernatant). The sample was washed by resuspension in 4 °C 50 mM Tris/HCl pH 7.5 containing protease

inhibitor mixture (sample P3) and centrifuged under conditions mentioned above. The washing step (sample P4) and the centrifugation step were repeated. The supernatants were discarded each time.

The following steps for hydrophobin extraction are repeated three times and are performed at room temperature if not indicated differently.

- The pelleted insoluble lysate fraction was resuspended in 15 mL lysis buffer (Table 34) (sample P5 from the suspension from the first round).
- The suspension was incubated for 30 min. The first round was performed at room temperature on a rotation wheel. The second and third round was performed at 37 °C in an incubating shaker.
- The suspension was centrifuged at 20,000 x g for 10 min at room temperature. The supernatant (samples P6, P7, and P8 from each round) was kept because it contains the extracted hydrophobins. It was pooled from the three rounds.

The remaining pellet was re-suspended in 3 mL 1 x PBS by vortexing (sample P9).

The pooled supernatants from the extraction were sonicated again under the conditions mentioned above to decrease the sample viscosity caused by residual genomic DNA. The solution was now ready to be applied to the Ni²⁺ affinity chromatography column for purification.

Table 34. Protocol for lysis buffer preparation used for denatured purification.

LYSIS BUFFER

50 mM	KH ₂ PO ₄ (136 g/mol)
50 mM	Na ₂ HPO ₄ (141 g/mol)
10 mM	Tris/HCl (121 g/mol)
8 M	Urea (60 g/mol)
The pH was adjusted to 8.0 with HCl	

Preparation of the Ni²⁺ affinity chromatography column

A Protino® Column was closed with a plug before filling it with 12 mL His Bind® Resin sepharose matrix. After 5 min of incubation, the sepharose suspension's solid fraction has separated and settled; The plug was oped, and the EtOH was drained. The built-in filter frit stops the solid fractions – the sepharose

beads – from draining. Another filter frit level was added on top of the sepharose matrix to avoid matrix disturbance during the following purification steps. The column was washed with ddH₂O by filling up the remaining column volume three times with ddH₂O. The column was loaded with 15 mL 1 M NiSO₄. The column was washed three times with ddH₂O to remove an excess of unbound Ni²⁺ ions and at least seven times with lysis buffer (Table 34) to equilibrate the matrix to the binding buffer.

Purification of proteins extracted from inclusion bodies

The packed and Ni²⁺ loaded column was then loaded with the extracted and solubilized inclusion bodies (sample P10 of flowthrough). The flowthrough was loaded onto the column a second time (sample P11). The protein-loaded column was washed with 100 mL lysis buffer, 100 mL wash buffer A (Table 35) (sample P12), and 100 mL wash buffer B () (sample P13) to remove non-specifically bound proteins. 25 mL elution buffer was added to the column to elute the recombinant proteins by competitive binding with imidazole. The flowthrough was collected in 5 fractions of 5 mL (samples P14 – P18).

Table 35. Protocol for wash buffer A preparation.

WASH BUFFER A

50 mM	KH ₂ PO ₄ (136 g/mol)
50 mM	Na ₂ HPO ₄ (141 g/mol)
10 mM	Tris/HCl (121 g/mol)
8 M	Urea (60 g/mol)
20 mM	Imidazole (68 g/mol)
Adjust pH to 6.4 with HCl	

The collected samples P1 to P18 were then applied to SDS PAGE and immunological detection as described in Ch. 2.5.1 to Ch. 2.5.4. The results are necessary to evaluate the success of the purification steps and the content and amount of target protein in the elution fractions. The latter is needed to decide about pooling elution fractions and whether another step of concentrating the sample by ultrafiltration is necessary. If the latter is necessary, the Vivaspin 20 ultrafiltration columns with a molecular weight cut-off (MWCO) of at least half the target protein's molecular weight were used to reduce the volume of the pooled eluate fractions to about ½ to ⅓ of the original volume, depending on the results of the SDS PAGE.

Table 36. Protocol for wash buffer B preparation.

WASH BUFFER B	
50 mM	KH ₂ PO ₄ (136 g/mol)
50 mM	Na ₂ HPO ₄ (141 g/mol)
10 mM	Tris/HCl (121 g/mol)
8 M	Urea (60 g/mol)
40 mM	Imidazole (68 g/mol)
Adjust pH to 5.9 with HCl	

Table 37. Protocol for elution buffer preparation.

ELUTION BUFFER	
50 mM	KH ₂ PO ₄ (136 g/mol)
50 mM	Na ₂ HPO ₄ (141 g/mol)
10 mM	Tris/HCl (121 g/mol)
8 M	Urea (60 g/mol)
250 mM	Imidazole (68 g/mol)
The pH was adjusted to 4.5 with HCl.	

Dialysis of denatured, purified proteins

The subsequent dialysis is described in detail in Ch. 2.6.5.

Cleaning of the His Bind® Resin sepharose matrix and the Protino® Column

For the column cleaning, the Ni²⁺ was removed to ensure separate and save waste disposal by washing three times with 1% SDS, three times with EDTA (100 mM), and three times with dH₂O. The column and the resin were then discarded. The resin and the column with its build-in filter frit was not re-used.

Overview of samples taken during purification

L – complete lysate

S – pelleted fraction

P – pelleted fraction after the first washing step

P1 – pelleted fraction after the second washing step

P2 – a re-suspended pelleted fraction with lysis buffer for hydrophobin extraction; only from the first round

P3 – supernatant from first extraction round

P4 – supernatant from second extraction round

P5 – supernatant from third extraction round

P6 – pellet with PBS re-suspended

P7 – solubilized hydrophobins from the column; first flow-through

P8 – solubilized hydrophobins from the column; second flow-through

P9 – column washing step with buffer A

P10 – column washing step with buffer B

P11 – 1st elution step of recombinant target proteins

P12 – 2nd elution step of recombinant target proteins

P13 – 3rd elution step of recombinant target proteins

P14 – 4th elution step of recombinant target proteins

P15 – 5th elution step of recombinant target proteins

2.6.4 Quantification of Purified Proteins

The quantification of the purified proteins is essential for evaluating the success of purification and further work with the proteins. The different quantification procedures of proteins and their advantages and disadvantages are described in Ch. 2.5.5, Ch. 2.5.6, and Ch. 2.5.7. The Bradford Assay was typically used as described in Ch. 2.5.6, and in some cases, the NanoDrop Method was applied as described in Ch. 2.5.7.

2.6.5 Dialysis of Purified Proteins

Spectra/Por® 1 Dialysis tubes (6,000 – 8,000 Da MWCO) were used to dialyze purified proteins. Dialysis tubes were cut into pieces of about 30 cm length and boiled in a buffer of 2% (w/v) sodium carbonate and 1 mM EDTA (pH 8.0) for 10 min each. Each boiling step was followed by excessive rinsing of the dialysis tubes with water. Finally, dialysis tubes were stored in 1 mM EDTA (pH 8.0) at 4 °C until use. The tubes were prepared in advance and stored. Alternatively, “ready-to-use” dialysis cassettes Slide-A-Lyzer (Thermo Fischer Scientific Inc. (USA)) were used in some cases.

The purified protein fractions were filled into dialysis tubes, sealed tightly with clips, filled into the dialysis cassettes, and sealed as described in the manual. The dialysis conditions are protein-dependent, but dialysis was conducted at 4 °C, and each incubation with dialysis buffer was conducted for at least 20 h. The proteins that were purified under denatured conditions were refolded during dialysis. Therefore, the dialysis was done using the redox-refolding buffer (Table 38) (Kwan et al. 2006). Most of the unwanted salts, excessive nickel, and urea - if applicable - were removed after dialysis. Finally, the protein samples were recovered, and insoluble protein aggregates were removed by centrifugation at $3,500 \times g$ for 5 min at 4 °C.

Table 38. Protocol for redox-refolding buffer (RRB) preparation. The buffer was freshly prepared with cold water for proper pH adjustment.

REDOX-REFOLDING BUFFER

10 mM	Glutathione reduced (307 g/mol)
1 mM	Glutathione oxidized (612 g/mol)

The pH was adjusted to 5.4 with HCl.

2.7 GLASS SURFACE FUNCTIONALIZATION

The surface of the chip is a well-cleaned glass cover slide. The piranha cleaning additionally activates the surface hydroxyl groups as described in Ch. 2.7.1. The careful functionalization of the surface with a protein mixture is further explained in Ch. 2.7.2. In Ch. 2.7.3 and Ch. 2.7.3, two macroscopic methods are presented that were used for quality control of the surface and the protein functionalization, namely the droplet test and contact angle measurements.

2.7.1 Glass Surface Preparation

The glass cover slides were cleaned by a protocol using so-called piranha etch or piranha solution for all experiments. It has to be handled with great care at any time.

The glass cover slides were rinsed with dH₂O and placed in a Teflon carousel in a glass beaker. The beaker was filled with absolute EtOH until the glass slides are fully covered, placed in an ultrasonic bath for 15 min, and repeated one more time. The cover slides were rinsed with ddH₂O. Each cover slide was placed in one small glass beaker, and piranha solution was added to cover the glass. The piranha solution was prepared freshly right before the experiment. For this, sulfuric acid (H₂SO₄) was placed in a glass container, and 30 % hydrogen peroxide (H₂O₂) was slowly added under stirring in a ratio of 7:3. The glass slides were incubated in boiling piranha solution for 15 to 30 min. The cover slides were rinsed with ddH₂O and placed twice with ddH₂O in an ultrasonic bath for 15 min. The glass was dried with compressed air.

The cleaned and dry glass slides were stored in a Teflon carousel in a desiccator at 30 – 150 mbar at room temperature. Short-time storage for a few weeks is possible. It has been reported and experienced that long-time storage can decrease the hydrophilicity of the piranha-cleaned glass surface.

The piranha solution was directly re-used as long as a reaction is visible as bubbles forming at the edge of the glass slide or the piranha solution was pooled. It was kept under the hood overnight. It was neutralized with sodium hydroxide pellets and discarded *via* the drain.

2.7.2 Hydrophobin and Fusion Protein-Based Coating

Before starting the coating procedure, decide on the desired final concentration and ratio of the hydrophobin and fusion protein mixture. Here, typical concentrations are 3 – 10 µM protein content and ratios of 1:3 to 1:6 of hydrophobin vs. fusion protein. Especially the latter is protein construct dependent. The solution was mixed very carefully to prevent inclusion body formation and degradation of the hydrophobins. The mixture was incubated for 10 min at 4 °C and centrifuged at 15,000 x g for 10 min at 4 °C to sediment aggregates. The protein mixture was applied with a pipet as slowly as possible onto the glass surface, starting right at the center until it has slowly covered the whole glass chip. If necessary, the glass surface was carefully tilted to help achieve an even distribution of the solution. Hydrophobins and, therefore, the protein coating will assemble at the interfaces. The chip was incubated for 30 min at room temperature. The solution was taken off by pipetting. The glass cover slide was waved in ddH₂O a few times, followed by three rounds of incubation in ddH₂O at room temperature on a

shaking plate for 5 min each. It was dried at room temperature for at least 30 min and was then ready to use in the SCP-RICM assay. The functionalized glass slide was not stored.

2.7.3 Contact Angle Measurement

For conducting contact angle measurements (CAM), a glass chip – or surface of choice – is functionalized according to the descriptions of Ch. 2.7.2. The syringe of the contact angle instrument OCA15 LJ (Data Physics Instruments GmbH (Germany)) can be loaded with a liquid of choice. Typically, ddH₂O was used. A 1 µL drop is pushed out of the syringe using the motorized stage and triggered by the provided software. The glass surface is moved on the sample table manually toward the syringe's tip to take it off. An image is taken with the incorporated camera roughly 2 s after the drop touched the functionalized surface. The software's image analysis program determines the contact angle between the glass surface and the drop's surface on the right and the left side of the drop. If the difference between those two angles is 1 ° or lower, these measurements were used for further evaluation. At least 15 measurements were taken for every surface condition.

2.7.4 DRoPS Test

The rapid test of the direct reversion of the property of surfaces (DRoPS test) gives the first impression of whether surface coating works with the chosen protein or protein mixture. Every freshly purified hydrophobin batch or hydrophobin fusion protein was tested with the DRoPS test.

A polymeric petri dish was functionalized with a 10 µL drop of protein solution and incubated for 10 - 15 min at room temperature while covered to prevent evaporation. The protein solution was carefully pipetted off, and the petri dish was thoroughly washed with dH₂O by flushing and rocking the petri dish. If the functionalization with hydrophobin or one of its fusion proteins was successful, the initially hydrophobic and water-repelling polystyrene (PS) surface of the petri dish was then hydrophilic and water-attracting. About 5 mL of 0.25 mg/mL DAPI were added onto the functionalized surface and poured off again to check the functionalization. The DAPI solution was re-used multiple times. The remaining drops of solution, for example, on the successfully functionalized areas, were visualized with a UV-illuminator, and an image was taken.

2.7.5 Atomic Force Microscopy

Measurements with an atomic force microscope (AFM) can uncover further information about the microscopic structure of the surface layer. The substrate mica or the chip surface was functionalized with the protein mixture as described in Ch. 2.7.5. Those samples were directly analysed with the AFM. The

AFM measurements were conducted with the NanoWizard®4 AFM module from JPK BioAFM Business combined with an inverted light microscope by Carl Zeiss Microscopy GmbH made available by MIM Facility at B CUBE, Dresden. The images were analyzed with the software Gwyddion (Nečas and Klapetek 2012).

2.8 SCP FUNCTIONALIZATION

One core feature of this biosensor approach is the functionalization of SCPs directly with proteins. The functionalization was done using EDC/NHS chemistry (Ch. 2.8.1). To verify the functionalization of the SCPs, they were stained with FITC (Ch. 2.8.2).

2.8.1 Functionalization of SCPs with Proteins

The SCPs are polymeric spheres of PEG synthesized in a microfluidic manner to achieve a well-defined and monodispersed particle solution. The SCPs display carboxylic acid residues on their surface. The solution was stored at 4 °C with the addition of 30 µg/mL Kanamycin and 30 µg/mL Chloramphenicol to hinder bacteria growth. They were centrifuged and handled with great care.

1 mL SCP solution was centrifuged at 1,840 x g for 5 – 10 min in a Protein LoBind Tube. The supernatant was discarded, and 1 mL of HEPES buffer, 100 mM, pH 7.0, was added. The washing step was repeated twice.

EDC/NHS solution was freshly prepared by dissolving 20 mM EDC and 50 mM NHS in 100 mM MES buffer, pH 6.0. After centrifugation, 1 mL EDC/NHS solution was added to SCP solution. The SCP solution was incubated for 30 min at room temperature to activate the carboxylic acid groups and rewashed three times under the conditions mentioned above. 1 mL of 1 mg/mL protein solution was added to the SCPs, incubated for 2 h at room temperature, and rewashed three times under the conditions mentioned above. In the final step, the desired volume of the optimal buffer for the protein. The protein functionalized SCPs were then ready to use. Long-time storage is not recommended. Short-time storage of, for instance, two weeks at 4 °C is possible, but the SCP solution was washed at least twice before used in further experiments.

2.8.2 Validation of SCP Functionalization with FITC Staining

The SCPs were functionalized with proteins as described in Ch. 2.8.1.

50 μ M Fluorescein-5-Isothiocyanate (FITC-'Isomer I') (FITC) solution was freshly prepared in 100 mM borate buffer, pH 9.0. FITC solution was added to the protein functionalized SCP solution and – as a negative control – to the uncoated SCPs. The mixture was incubated overnight at room temperature or 4 °C if necessary for protein stability. The mixture was then washed three times with HEPES buffer, 100 mM, pH 7.0 at 1,840 x g for 10 min. The SCPs were then ready to use under a fluorescent microscope.

Here, the fluorescent microscope Biozero BZ-8000 (Keyence Corporation (Japan)) was used. FITC has an excitation wavelength of 495 nm and an emission wavelength of 519 nm. Therefore, the green fluorescent protein (GFP) channel of the microscope with 470 nm excitation and 525 nm emission wavelength can be used. The fluorescent signal of the protein functionalized SCPs was compared to the negative control of non-functionalized SCPs.

2.9 SCP-RICM ASSAY AND ITS ANALYSIS

The reflection interference contrast microscopy (RICM) employs the appearance of a shape-specific interference pattern when the reflected light waves of an object are collected. Here, the object is the SCP, a sphere that has a circular interference pattern. This circular interference pattern changes in appearance when interacting with the glass surface chip. When the SCPs and the chip surface are functionalized with proteins, these interactions can be triggered by protein-protein interactions. Hence, a change in the interference pattern allows deducing the interaction of the proteins. In the following, it will be described how the previously prepared components were merged for the SCP-RICM assay. Furthermore, the analysis of the microscopy images will be explained.

The glass chips were cleaned and stored as described in Ch. 2.7.1 and functionalized with the protein combination and concentration of choice as described in Ch. 2.7.2. The glass surface was typically fully dry, but it does not have to be. The functionalized glass surface was attached to a 16-well plate by gently pushing the glass cover slide onto the lower rubber layer. The rubber was attached to the well plate and has 16 holes that match the plate's wells.

The functionalized SCPs have to be washed before usage in RICM measurements by centrifuging for 10 min at 1,840 x g and 4 °C, discarding the supernatant, and suspending the SCPs in the corresponding buffer. Usually, a buffer is chosen that suits the protein that the SCPs are functionalized with.

Cu(I)Cl was stored as a 200 mM solution (Table 39). A solution with the only Cu(I) ions present would be clear to light yellow. Right after dissolving Cu(I)Cl as described, the solution is bright yellow. Due to oxidation at 4 °C and normal pressure, most of the copper in the solution will be available as Cu(II), and the solution turns dark green. That makes the use of reducing agents for the Cu(I) buffer necessary. All the components for this Cu(I) buffer were prepared freshly as 100 mM stock solutions. A 1 mM Cu(I) stock buffer (Table 40) was prepared and briefly centrifuged to remove aggregates that disturb microscopy measurements. This stock buffer was diluted as necessary directly before the RICM measurements. The buffer is adopted from typical redox-refolding buffers that have been used before to image copper-binding proteins like *ySco1* in crystallography (Abajian and Rosenzweig 2006).

Table 39. Protocol for Cu(I)Cl solution preparation.

CU(I)CL SOLUTION	
200 mM	Cu(I)Cl (98.99 g/mol)
2.5 mM	HCl (37% = 12.2; 36.46 g/mol)
750 mM	NaCl (121 g/mol)
NaCl was dissolved in ddH ₂ O. Cu(I)Cl was added, and then HCl was added slowly using gentle stirring until the Cu(I)Cl was fully dissolved.	

Table 40. Exemplary protocol for 1 mL of 1 mM Cu(I) stock buffer preparation from freshly prepared 100 mM stock solutions of each of the components. The dilution was made in the corresponding protein buffer or ddH₂O.

CU(I) STOCK BUFFER	
10 µL	Cu(I)Cl (99 g/mol) solution
10 µL	Ascorbic acid (176 g/mol)
10 µL	TCEP (287 g/mol)
970 µL ddH ₂ O was added to the three components.	

The microscope for RICM measurements has to be an inverted microscope for conducting interference measurements. For this study, the Axio Observer.Z1 (Carl Zeiss Microscopy GmbH) was used. Because of the differential interference measurements, high-quality coherent light is needed at the functionalized chip surface interface and the SCP. Exact interference measurements need a precise adjustment

of the focal plane and the optical path, and a wise choice of filter and the objective is essential. Regarding the latter, a few available objectives were tested, while the best results were achieved with the Zeiss 63x Oil Antiflex Objective using the 518F immersion oil. The filter has to be a monochromatic filter of any color. Here, a green monochromatic filter (~ 550 nm) was chosen. The manufacturer's software AxioVision (Carl Zeiss Microscopy GmbH) was used to control the microscope and take the pictures.

200 μ L copper buffer of the desired concentration was added to one well. It was incubated for 20 min at room temperature and covered with a lid to prevent evaporation. The copper buffer was carefully pipetted off. 120 μ L SCP solution was added into the well immediately to equilibrate for 10 min at room temperature. The SCPs will start to settle and interact with the surface. It was searched for SCPs in bright field mode and focused through them to check for impurities or irregularities. A bright-field image (BF) was taken if the SCP's radius has to be measured for calculating the surface energy (Figure 16, left). The mode was changed to reflection mode (RM), focusing very precisely on the focal plane presenting the contact area and interference patterns (Figure 16, right). This plane is also the focal plane where the field diaphragm is in focus. An image was taken for further analysis. The procedure was repeated for at least 20 SCPs.

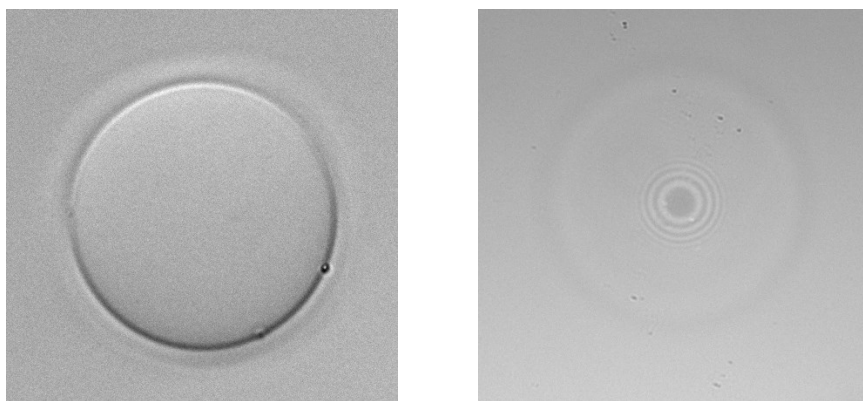


Figure 16. Exemplary images of an SCP and its interference pattern.

The bright-field image (left) shows an SCP's appearance focused on its focal plane of the largest circumference. The image in reflection mode (right) shows the interference pattern with the contact area (gray disc in the center) of the SCP from the left image. Measurements of the SCP's radius and the contact area's radius are based on those images.

The images (zvi format) were analyzed manually with the software Zen 3.2 (blue edition) from Carl Zeiss Microscopy GmbH. The integrated measurement feature enables the drawing of circles. It calculates and outputs the diameter in micrometers, necessary for further analysis of the adhesive energy W_{adh} .

3 RESULTS

Proteins were produced recombinantly for studying protein's specification or for using proteins for one of the many possible applications. The results for the recombinant expressions of all *Sco1* and *Cox17* constructs (Ch. 2.3) and of the hydrophobin *Ccg-2* will be discussed in Ch. 3.1.1, Ch. 3.1.2, and Ch. 3.1.3, respectively, and the optimized parameters summarized in Ch. 3.1.3.

One of the biosensor's core part is the glass chip (Ch. 1.3.1). Together with the SCPs (Ch. 1.3.2), it makes the detection unit enabling the use of the microscopy method RICM (Ch. 1.3.3). The method of functionalizing the chip surface was explained in Ch. 2.7. In Ch. 3.2 the results from the necessary optimization strategies and qualitative testing will be presented.

One way for covalently binding proteins to the PEG chains of the SCPs can be realized with EDC/NHS chemistry, as explained in Ch. 2.8. It connects the primary amines from the protein backbone to the COOH carboxylic acids (also called carboxyl groups) of the SCPs with the protein's random orientation. The immobilization of proteins on the SCP surface is presented in Ch. 3.4.

Combining all the successfully prepared components from Ch. 3.1, 3.2, and 3.4 and using a high-quality inverted light microscope finally allows to proceed with the SCP-RICM assay and analysis explained in Ch. 2.9. Measurements were conducted to test our assumptions of the general interaction mechanism of SCPs with the chip surface in various combinations and under several conditions, of which some are shown in Ch. 3.5. Furthermore, initial experiments are presented to test the proposed copper-dependent protein-protein interaction.

3.1 GENERATION OF RECOMBINANT FUSION PROTEINS

According to the exemplary agarose gel image (Figure 17) in Ch. 3.1.1, the same procedure of amplifying the target gene by PCR and analysis by agarose gel electrophoresis was conducted for all the other derivatives from *Sco1*. The *Cox17* DNA target vectors were synthesized. The *Ccg-2*-inserted vector was used from earlier work. The agarose images of each step are not explicitly shown here.

3.1.1 *Sco1* and *Sco1*Δ95

Genomic DNA from yeast wild type BY4741 was extracted and used as a template for the polymerase chain reactions (PCRs). The corresponding primers (Table 14) were used to generate the inserts for the protein constructs *Sco1_a*, *Sco1_b*, and *Sco1_c* and the truncated transmembrane domain *Sco1*Δ95_a, *Sco1*Δ95_b, and *Sco1*Δ95_c, respectively.

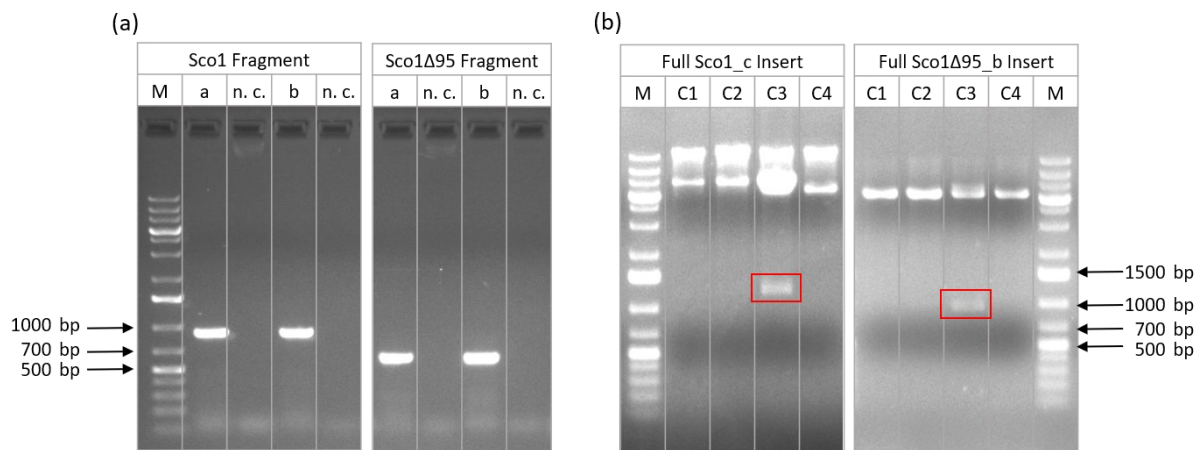


Figure 17. Images from agarose gel electrophoresis after a PCR (a) and digestion (b) of clones of ligated samples.

The agarose gel images of PCR products of Sco1_a, Sco1_b, Sco1Δ95_a, and Sco1Δ95_b DNA fragments and their corresponding negative controls (n. c.) are shown in (a). Here, the DNA samples only include the Sco1 and Sco1Δ95 fragments after PCR but before digestion or ligation steps. A clear band appears at the expected position, and no band appears for any negative control. In (b), the results from digestion of Sco1_c and Sco1Δ95_b samples are shown after ligation, transformation in TOP10F', and DNA isolation of some single colonies. For each sample, four clones were tested for inserts. The inserts include the Ccg-2 fragments and are therefore bigger than in (a). Here, the clone C3 for Sco1_c and the clone C3 for Sco1Δ95_b show inserts at the expected position and were subsequently sent in for sequencing. The DNA standard (marker M) is the GeneRuler™ 1 kb Plus DNA Ladder.

Figure 17 a shows an example of an agarose gel image with the final DNA inserts of Sco1_a, Sco1_b, Sco1Δ95_a, and Sco1Δ95_b. Those were obtained by PCR amplification from the genomic DNA of strain BY4741 using the respective primers. Subsequently, the PCR products and the target vector pET28a(+) from the pET-System were digested with the corresponding restriction enzymes. The digested insert was ligated into the target vector. Electrocompetent *E. coli* TOP10F' cells were transformed with the ligation product and cultivated on an appropriate agar plate. The following colony PCR on single colonies was conducted to find positive clones that carry the pET28a(+) vector with the target insert. To confirm the presence of an insert of the expected size, each clone was digested and analyzed with agarose gel electrophoresis. An example of an agarose electrophoresis of the digested vectors from colony PCR is shown in Figure 17 b. Positive clones were cultivated, and their DNA was isolated and sent off for sequencing. If the sequencing results match the target sequence, the respective DNA sample with the pET28a(+) vector with the final insert was used to transform the expression host by electroporation.

Each construct's protein expression was tested in *E. coli* T7 SHuffle Express *lysY* and *E. coli* Lemo21 (DE3) at 16 °C and 30 °C. After induction with IPTG, samples were taken at the indicated time points and tested regarding the solubility of the expressed protein. The decision on the condition to proceed with was made upon SDS PAGE and western blot analysis. If remarkable, the details are explained in the following. A summary of the chosen experimental conditions is presented in Table 41.

Sco1_a

An example of Sco1_a expression in *E. coli* T7 SHuffle Express *lysY*, solubility analysis, and protein purification under denatured conditions is shown in Figure 18.

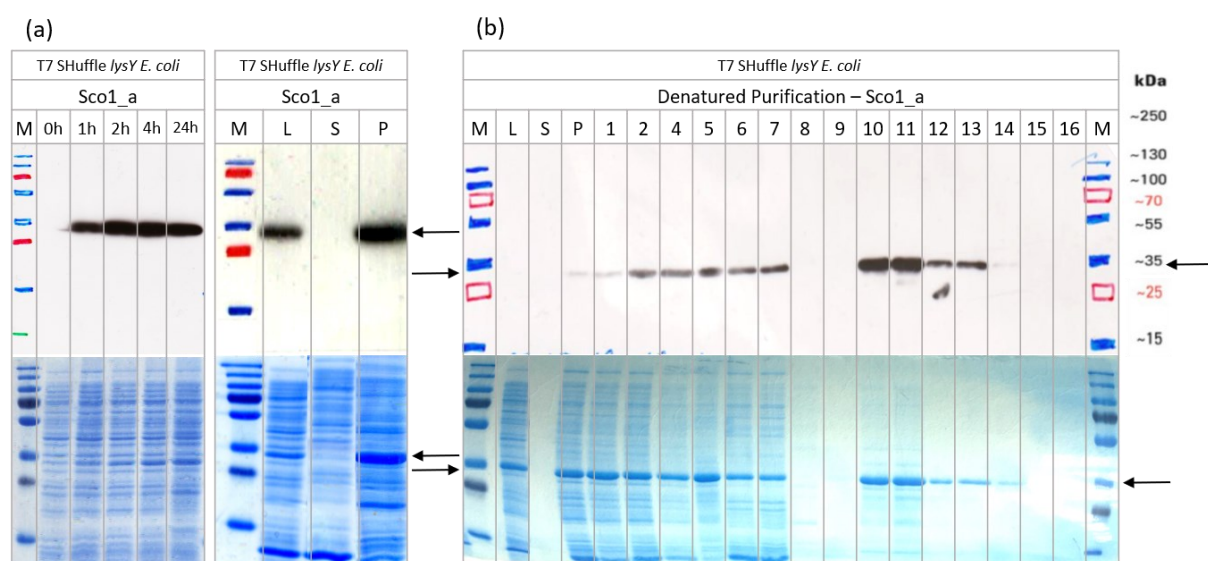


Figure 18. Expression analysis in T7 SHuffle Express *lysY* *E. coli* and purification of Sco1_a.

The upper panels show the immunological detection after western blot analysis, and the lower panels show the Coomassie-stained SDS PAGE gels. The expression at 30 °C demonstrates a gradual increase of the expressed target protein (black arrow) over time up to 4 h after induction with IPTG. A leaky expression cannot be observed (a, left). The solubility analysis of the lysate (L) after 4 h expression shows no target protein in the soluble fraction (S) but a prominent protein band in the insoluble, pelleted fraction (P) (a, right). The denatured purification yielded a clean target protein product (b) (10 – 16 – eluted protein; here seven elution fractions) compared to the lysate and its extraction and washing steps (b) (L, S, P, 1-9). The reason for the low or absent transfer of the samples L, S, P, and 1 in the western blot is not known. The SDS PAGE gel, however, shows the results as expected.

On the grounds of the results presented in Figure 18 a, the protein was expressed at 30 °C for 4 h after induction. Longer expression did not result in a higher quantity or quality of the target protein. The purification procedure successfully cleared the protein solution from the unwanted proteins, as seen

in the Coomassie-stained gel (Figure 18 b, lower panel). There are no apparent degradation products present, except for a very faint band in lane 11 below the highly expressed target protein band (Figure 18 b, upper panel). It is presumed that this weak degradation product will have no impact on further experiments. In this specific purification, seven elution fractions were taken and applied on the SDS PAGE gel – the protocol (Ch. 2.6.3.2) calls for five elution fractions. However, it can be seen that only the first four and slightly the fifth elution fraction contain any target protein (Figure 18 b, 10 – 14). Consequently, only the first five elution fractions were used in further experiments.

In summary, the Sco1_a protein was not expressed in a soluble form, neither in T7 SHuffle *lysY* *E. coli* nor Lemo21 (DE3) *E. coli*. However, in the *E. coli* strain, T7 SHuffle *lysY*, Sco1_a was well expressed as an insoluble protein (Figure 18 a) with a theoretical molecular weight of 36.1 kDa. The pelleted fraction was further used in the denatured protein purification step (Figure 18 b). The suitable elution fractions were chosen – here lane 10 to 14 from Figure 18 b –, pooled, concentrated, and refolded *via* dialysis in redox-refolding buffer supplemented in the first step with 5 mM EDTA and without EDTA in a second step.

Sco1_b

An example of Sco1_b expression in *E. coli* T7 SHuffle Express *lysY*, solubility analysis, and protein purification under denatured conditions is shown in Figure 19.

Based on the results presented in Figure 19 a, the protein was expressed at 30 °C for 4 h after induction. Longer expression did not result in a higher quantity or quality of target protein. The denatured protein purification procedure cleared the protein solution from most unwanted proteins, as shown in the Coomassie-stained gel (Figure 19 b, lower panel). The finally eluted protein (Figure 19 b, upper panel, lanes 11 – 15) shows only minimal degradation products (lanes 11 and 12). The elution fractions corresponding to lanes 11, 12, and 13 were refolded with extensive dialysis and used for further experiments.

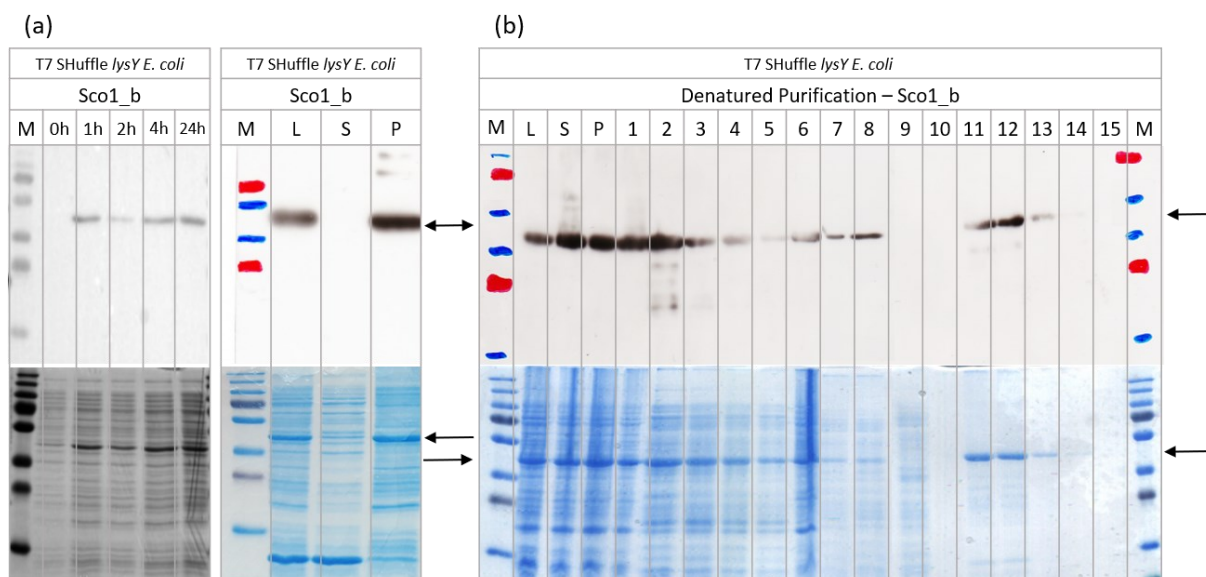


Figure 19. Expression analysis in T7 SHuffle Express *lysY E. coli* and purification of Sco1_b.

The upper panels show the immunological detection after western blot analysis, and the lower panels the corresponding Coomassie-stained SDS PAGE gels. At 30 °C, expression (a, left) of the target protein (black arrow) increases over time after induction with IPTG, while there is only a slight to no increase between 4 h and 24 h. No leaky expression can be observed. The solubility analysis of the lysate (L) after 4 h expression shows no target protein in the soluble fraction (S) but a prominent protein band in the insoluble, pelleted fraction (P) (a, right). The denatured protein purification yielded a clean target protein product (b) (11 – 15 – eluted protein) compared to the lysate and its extraction and washing steps (b) (L, S, P, 1-8, and 9 – 10).

To summarize, the Sco1_b protein could be expressed soluble in neither *E. coli* T7 SHuffle Express *lysY* nor *E. coli* Lemo21 (DE3). However, the *E. coli* strain T7 SHuffle Express *lysY* expressed Sco1_b well as an insoluble protein (Figure 19 a) with a theoretical molecular weight of 45.2 kDa. The respective pelleted fraction (Figure 19 a, right) was further used in a denatured protein purification step (Figure 19 b). The suitable elution fractions were chosen – here lanes 11 and 12 from Figure 19 b –, pooled, concentrated, and refolded *via* dialysis in redox-refolding buffer supplemented in the first step with 5 mM EDTA and without EDTA in a second step.

Sco1_c

An example of Sco1_c expression in *E. coli* T7 SHuffle Express *lysY*, solubility analysis, and protein purification under denatured conditions is shown in Figure 20.

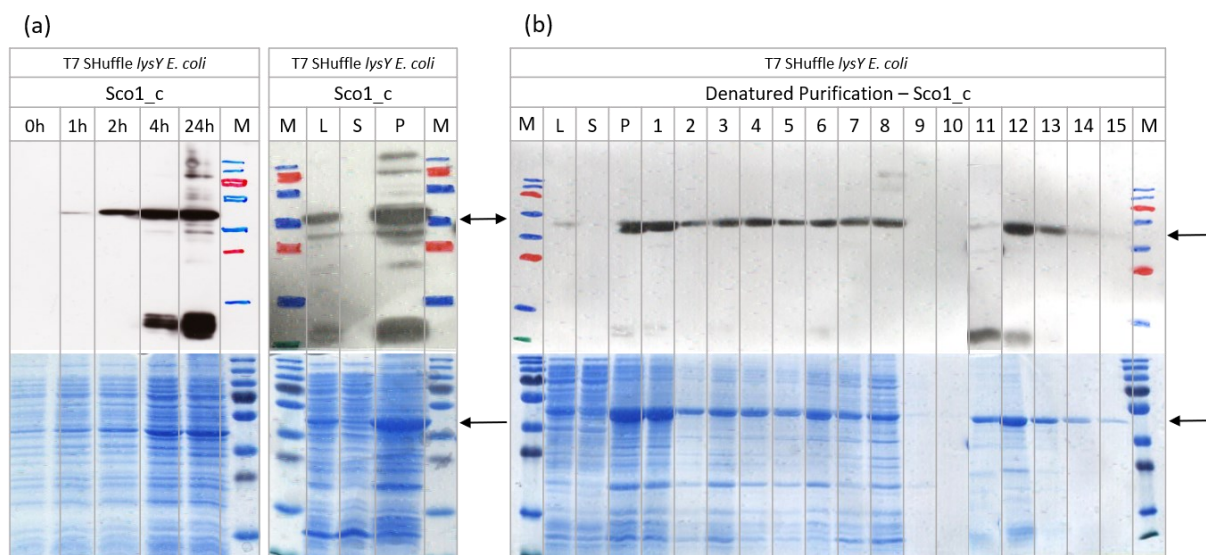


Figure 20. Expression analysis in T7 SHuffle Express *lysY E. coli* and purification of *Sco1_c*.

The upper panels show the immunological detection after western blot analysis, and the lower panels the Coomassie-stained SDS PAGE gels. At 30 °C, expression (a, left) of the target protein (black arrow) increases over time after induction with IPTG, while there is only a slight to no increase between 4 h and 24 h. No leaky expression can be observed. The solubility analysis of the lysate (L) after 4 h expression shows no target protein in the soluble fraction (S) but a prominent protein band in the insoluble, pelleted fraction (P) (a, right). The denatured protein purification yielded a clean target protein product (b) (11 – 15 – eluted protein) compared to the lysate, the pellet, and its extraction and washing steps (b) (L, P, 1-8, and 9 – 10). Lane 11 in (b) was cut into this picture because of improper initial loading. The extract comes from a gel and a western blot, which was run in parallel.

Based on the results presented in Figure 20 a, the protein was expressed at 30 °C for 4 h after induction. Longer expression did not result in a higher quantity or quality of target protein. The purification procedure cleared the protein solution from most unwanted proteins, as shown in the Coomassie-stained gel (Figure 20 b, lower panel). The finally eluted protein (b) (lanes 5 – 11) shows one prominent degradation product that could correspond to roughly the size of the Ccg-2 protein if the *Sco1_c* protein ruptured at the linker. Nevertheless, the Coomassie-stained gel confirms that the target protein is highly dominant in the elution fractions. These elution fractions corresponding to lanes 11, 12, and 13 were refolded in an extensive dialysis and used for further experiments.

To summarize, the *Sco1_c* protein could be expressed soluble in neither *E. coli* T7 SHuffle Express *lysY* nor *E. coli* Lemo21 (DE3). However, the T7 SHuffle Express *lysY E. coli* strain expressed *Sco1_c* well in its pelleted fraction (Figure 20 a) with a theoretical molecular weight of 45.2 kDa. The target protein's pelleted fraction (Figure 20 a, right) was further used in denatured purification of *Sco1_c* (Figure 20 b). The

suitable elution fractions were chosen – here lane 11 and 15 from Figure 20 –, pooled, concentrated, and refolded *via* dialysis in redox-refolding buffer supplemented in the first step with 5 mM EDTA and without EDTA in a second step.

Sco1Δ95_a

An example of Sco1Δ95_a expression in *E. coli* Lemo21 (DE3), solubility analysis, and protein purification under native conditions is shown in Figure 21.

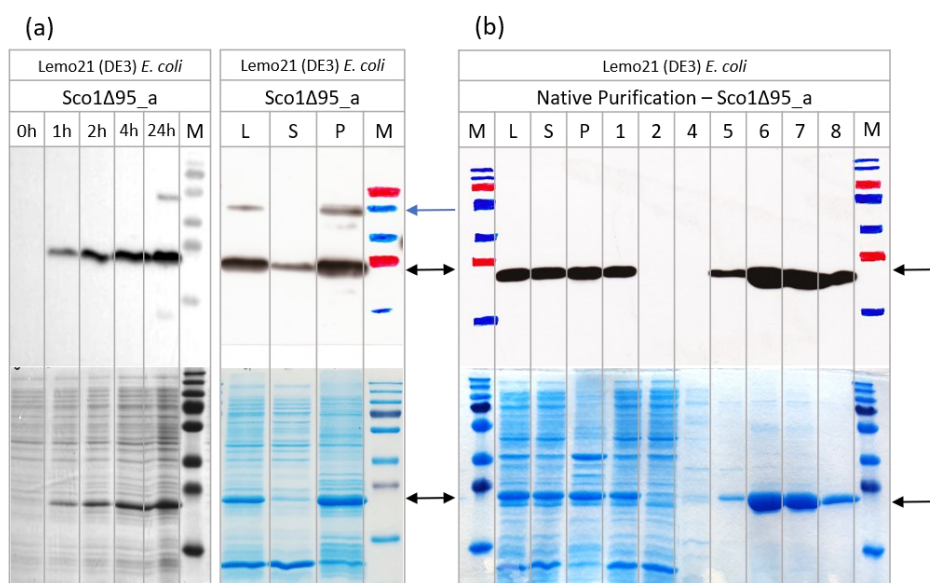


Figure 21. Expression analysis in Lemo21 (DE3) *E. coli* and purification of Sco1Δ95_a.

The upper panels show the immunological detection after western blot analysis, and the lower panels show the Coomassie-stained SDS PAGE gels. At 16 °C, expression (a, left) demonstrates a gradual increase of target protein (black arrow) over time up to 24 h after induction with IPTG. No leaky expression can be observed. The solubility analysis of the lysate (L) after 24 h expression shows some target protein in the soluble fraction (S). The most significant protein band is found in the insoluble, pelleted fraction (P) (a, right). However, a native purification was performed on the soluble fraction and yielded a high amount of protein and a clean target protein product (b) (6, 7, and 8 – here only three elution fractions) compared to the lysate and its components (b) (L, S, P, 1 and 2). The washing buffers 1 and 2 (b) (4 and 5) had a positive cleaning effect but washing buffer 2 already washed off a decent amount of target protein from the column. Some typical purification samples were not included on the gel and the western blot membrane due to space limitations.

Based on the results presented in Figure 21 a, the protein Sco1Δ95_a was expressed in Lemo21 (DE3) at 16 °C for 24 h after induction. Longer expression did not result in a higher quantity or quality of target protein. The purification procedure cleared the protein solution from most unwanted proteins, as

shown in the Coomassie-stained gel (Figure 21 b, lower panel). Only a slight background of unwanted bands and only on the Coomassie-stained gel can be seen for the eluted sample from lanes 6 and 7. However, the eluted target protein is presented highly dominantly and was expressed in a high amount, which is apparent on the gel and the membrane images. The elution fractions were, therefore, used for further experiments.

To summarize, the Sco1Δ95_a protein was expressed in T7 SHuffle Express *lysY* *E. coli* but not soluble. However, the Lemo21(DE3) *E. coli* strain expressed Sco1Δ95_a (Figure 21 a, left) well in its pelleted fraction and its soluble fraction in a lower amount theoretical molecular weight of 25.8 kDa. The target protein's soluble fraction (Figure 21 a, right) was further used in the native purification of Sco1Δ95_a (Figure 21 b). The suitable elution fractions were chosen – here lane 5 to 8 from Figure 21 b –, pooled, concentrated, and dialyzed in 2xPBS buffer supplemented in the first step with 5 mM EDTA and without EDTA in a second step.

Sco1Δ95_b

An example of Sco1Δ95_b expression in *E. coli* T7 SHuffle Express *lysY*, solubility analysis, and a protein purification under denatured conditions is shown in Figure 22.

On the grounds of the results presented in Figure 22 a, the protein Sco1Δ95_b was chosen to be expressed in Lemo21 (DE3) at 30 °C for 4 h after induction. Prolongated expression yielded a higher amount of target protein but is accompanied by a very high degree of additional bands and high degradation and was, therefore, not chosen (Figure 22, a, left). Expression at 16 °C did not achieve clear improvement, only a lower expression rate (not shown here). The purification procedure accumulated and partially cleared the protein solution from some unwanted protein fragments (Figure 22 b, lower panel). The preparation steps before column application (Figure 22, b) (1 – 5) of the expressed target protein successfully cleaned off the higher molecular weight proteins, which could be chaperoned target protein.

Nevertheless, Sco1Δ95_b seems to be prone to protein degradation (Figure 22, b, upper panel). However, the fraction of degraded protein compared to the overall protein content seems to be relatively low. Consequently, the target protein is dominantly present (b, lower panel).

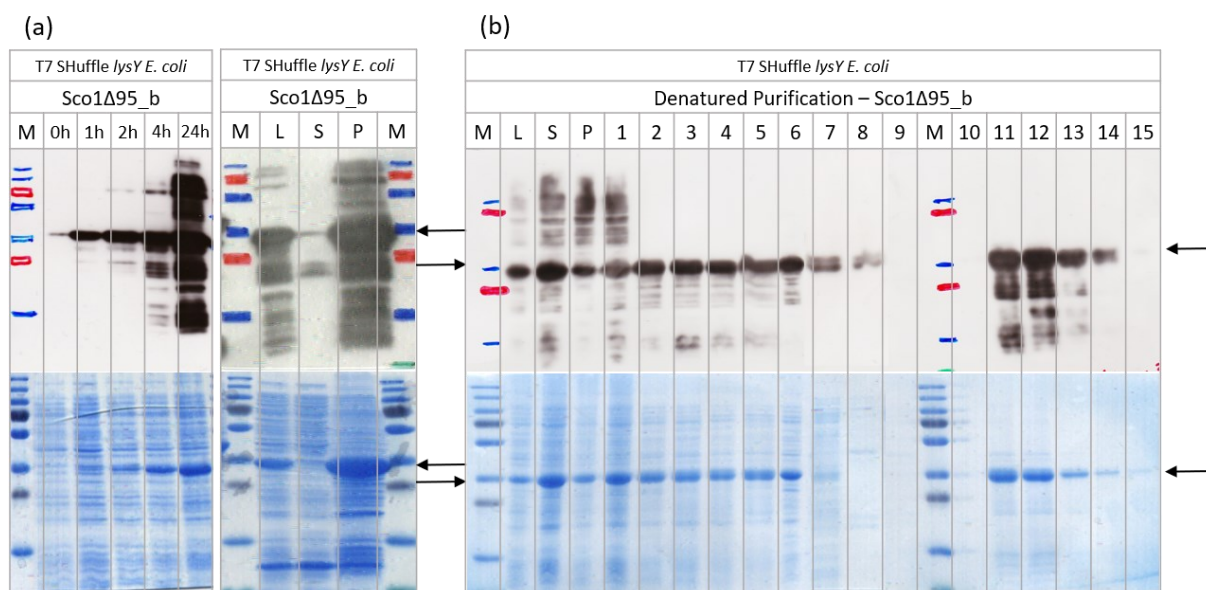


Figure 22. Expression analysis in T7 SHuffle Express *lysY E. coli* and purification of Sco1Δ95_b.

The upper panels show the immunological detection after western blot analysis, while the lower panels show the Coomassie-stained SDS PAGE gels. At 30 °C, expression (a, left) of the target protein (black arrow) increases over time up to 24 h after induction with IPTG. A small leaky expression can be observed. The lysate (L) solubility analysis after 4 h expression shows very little target protein in the soluble fraction (S). The most significant protein band is found in the insoluble, pelleted fraction (P) (a, right). Denatured purification was performed on the pelleted fraction and yielded a high amount of target protein product (b) (10 – 15) compared to the lysate and its components (b) (L, S, P).

To conclude, the Sco1Δ95_b protein could not be expressed soluble in a sufficient amount in neither *E. coli* T7 SHuffle Express *lysY* nor *E. coli* Lemo21 (DE3). However, the T7 SHuffle Express *lysY E. coli* strain expressed Sco1Δ95_b well (Figure 22 a, left) in its pelleted fraction with a theoretical molecular weight of 34.9 kDa. The target protein's pelleted fraction (Figure 26 a, right) was further used in denatured purification of Sco1Δ95_b (Figure 22 b). The suitable elution fractions were chosen – here lane 11 to 14 from Figure 22 b –, pooled, concentrated, and refolded *via* dialysis in redox-refolding buffer supplemented in the first step with 5 mM EDTA and without EDTA in a second step.

Sco1Δ95_c

An example of Sco1Δ95_c expression in *E. coli* T7 SHuffle Express *lysY*, solubility analysis, and protein purification under denatured conditions is shown in Figure 23.

The amount of protein expressed after 24 h was higher, but it showed degradation different than after 4 h. Therefore, the protein Sco1Δ95_c was chosen to be expressed for 4 h at 30 °C as presented in Figure 23 a. The purification shows a very high amount of target protein in almost all taken samples during denatured purification. The purification procedure purified the Sco1Δ95_c protein. While the immunological staining shows unwanted, prominent degradation bands of the eluted samples (Figure 23 b, upper panel), the Coomassie-stained gel (Figure 23 b, lower panel) shows that the target protein is highly dominant in the elution fractions. All elution fractions (Figure 23 b, lanes 11 – 15) were used for further tests.

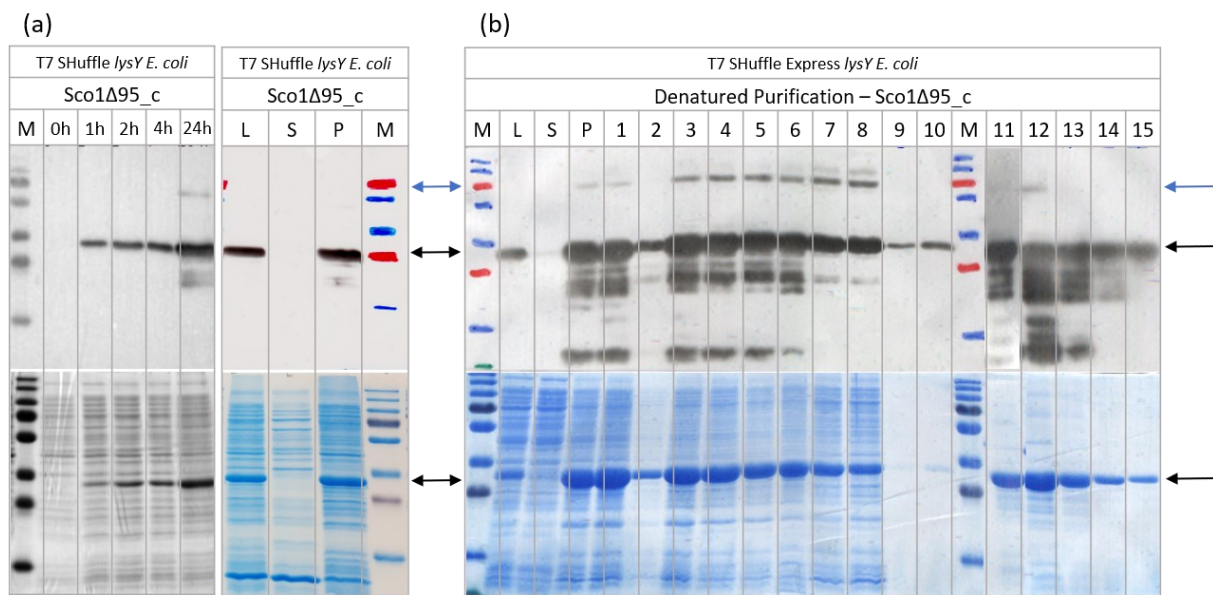


Figure 23. Expression analysis in T7 SHuffle Express *lysY E. coli* and purification of Sco1Δ95_c.

The upper panels show the immunological detection after western blot analysis, while the lower panels show the Coomassie-stained SDS PAGE gels. At 30 °C, expression (a, left) of the target protein (black arrow) increases over time after induction with IPTG, while there is only a slight to no increase between 4 h and 24 h. No leaky expression can be observed. Additionally, some samples with very high target protein content present a discrete band, assumed to containing dimeric target protein (blue arrow). The solubility analysis of the lysate (L) after 4 h expression shows a band at the position of the target protein for the insoluble, pelleted fraction (P) but no target protein band in the soluble fraction (S) (a, right). Denatured purification was performed on the pelleted fraction and yielded a high target protein product (b) (11 – 15). Lane 11 in (b) was cut into this picture because of improper initial loading. The extract was taken from a gel and a western blot, which was run in parallel.

To conclude, the Sco1Δ95_c protein could be expressed soluble in neither *E. coli* T7 SHuffle Express *lysY* nor *E. coli* Lemo21 (DE3). However, the T7 SHuffle Express *lysY E. coli* strain expressed Sco1Δ95_c well in

its pelleted fraction (Figure 23 a, left) with a theoretical molecular weight of 34.9 kDa. The target protein's pelleted fraction (Figure 23 a, right) was further used in denatured purification of Sco1Δ95_c (Figure 23 b). The suitable elution fractions were chosen – here lane 11 to 15 from Figure 23 b –, pooled, concentrated, and refolded *via* dialysis in redox-refolding buffer supplemented in the first step with 5 mM EDTA and without EDTA in a second step.

The addition of different L-rhamnose concentrations during protein expression after IPTG induction of the Lemo21 (DE3) cell culture was tested for most of the constructs and is here shown as an example for the Sco1Δ95_c protein construct (Figure 24). It is predicted that L-rhamnose's presence increases the expression of soluble target protein relative to the amount of expressed target protein in the lysate, which can be decreased. The amount of expressed soluble protein decreases again when exceeding an upper critical L-rhamnose concentration. This lower and upper critical L-rhamnose concentration depends on the target protein and can hardly be predicted.

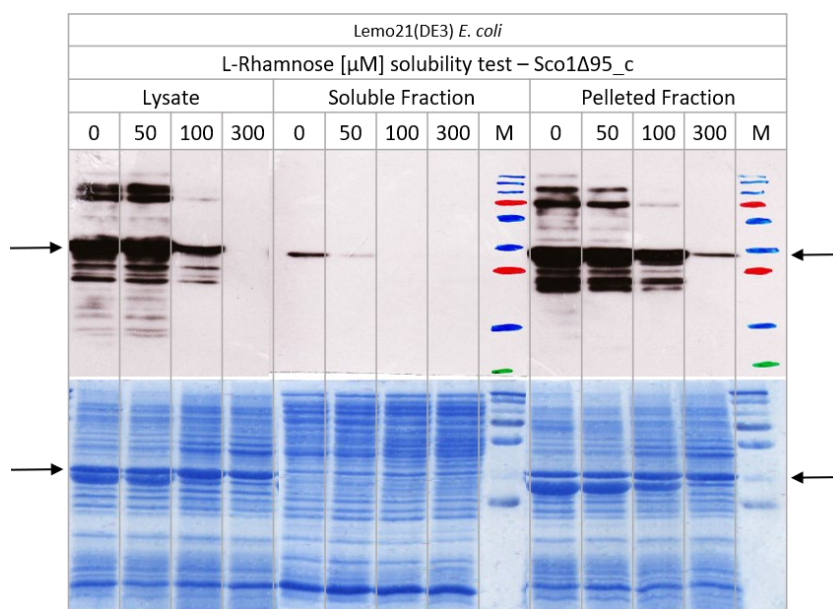


Figure 24. Exemplary expression and solubility analysis of Sco1Δ95_c in Lemo21 (DE3) *E. coli* tested different L-rhamnose concentrations in μM.

The upper panel shows the immunological detection after western blot analysis, and the lower panel shows the Coomassie staining of the solubility analysis of the Sco1Δ95_c protein construct (black arrows). The presented images were cropped to put them in a logical order, but all excerpts were taken from the same autoradiography film and gel, respectively.

The protein expression of Sco1Δ95_c was tested in *E. coli* T7 SHuffle Express *lysY* and *E. coli* Lemo21 (DE3), while the latter strain increased the solubility of Sco1Δ95_c at no addition of L-rhamnose. As expected, the highest expression is reached without the addition of L-rhamnose. However, the amount

of soluble protein is also maximum at no addition of L-rhamnose. The test of higher and lower concentrations did not change that effect (not shown here). On the grounds of the in Figure 24 presented results, the *E. coli* Lemo21 (DE3) strain was used, but no L-rhamnose was added. The expression of other protein constructs that were tested under L-rhamnose influence yielded similarly or the same results, and, therefore, no L-rhamnose was used in any protein expression.

3.1.2 Cox17

The synthesized DNA sequences for the constructs Cox17_a, b, and c were already delivered incorporated in the pET28a(+) vector. The electrocompetent TOP10F' *E. coli* cells were transformed with the corresponding plasmid, cultivated, and the DNA was isolated for plasmid propagation. The protein expression of each construct was tested in the expression hosts *E. coli* T7 SHuffle Express *lysY* and *E. coli* Lemo21 (DE3) at 16 °C and 30 °C. The cells were harvested after various time points, and the solubility of the protein was tested. The decision on which conditions to proceed with was made upon evaluating the SDS PAGE gels and western blot analysis. If remarkable, the details are explained in the following. A summary of the chosen experimental conditions is presented in Table 41.

Cox17_a

An example of Cox17_a expression in *E. coli* Lemo21 (DE3), solubility analysis, and a protein purification under native condition is shown in Figure 25.

The protein was expressed at 30 °C for 4 h after induction. Longer expression did not result in a higher quantity or quality of target protein. The purification procedure cleared the protein solution from most unwanted protein fragments, which can be seen in the Coomassie-stained gel (Figure 25 b, lower panel). The final, eluted protein shows lower amounts of large, unwanted proteins. The immunological staining (Figure 25 b, upper panel) indicates strong dimeric behavior and displays bands of high molecular weight. That implies possible chaperoning of Cox17_a by *E. coli* proteins since they are also visible in the His-specific immunological detection. Nevertheless, the Coomassie-stained gel shows that the target protein is highly dominant in the elution fractions. These fractions corresponding to lanes 5 to 11 were, therefore, used to work with for further experiments.

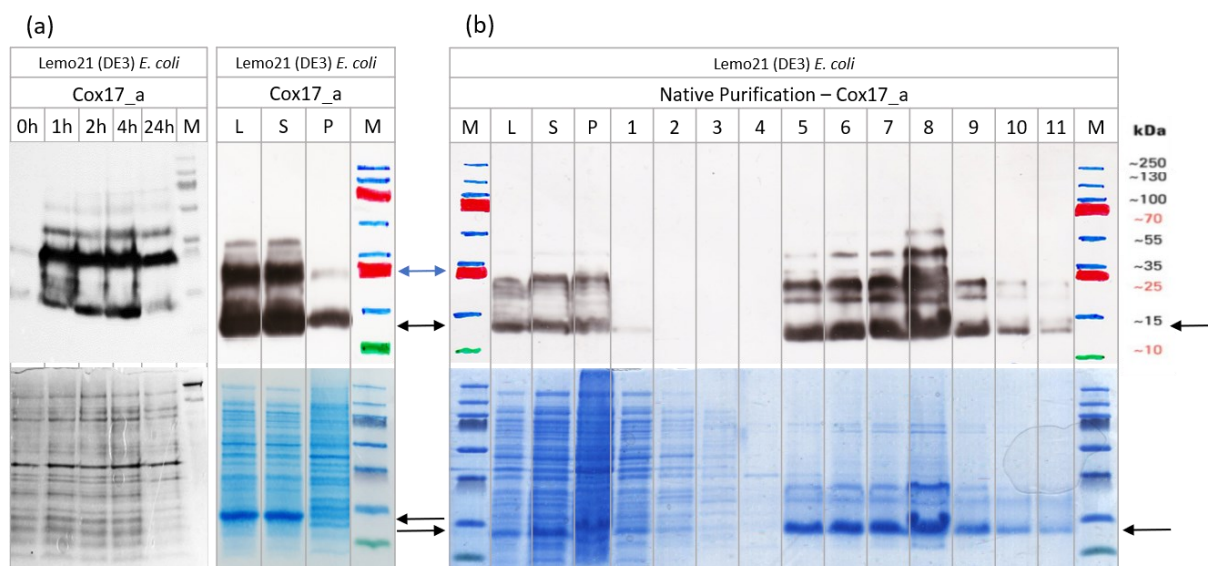


Figure 25. Expression analysis in Lemo21 (DE3) *E. coli* and native purification of Cox17_a.

The upper panels show the immunological detection after western blot analysis, and the lower panels show the corresponding Coomassie-stained SDS PAGE gels. At 30 °C, expression (a, left) of the target protein (black arrow) increases over time after induction with IPTG, while there is no increase between 4 h and 24 h. No leaky expression can be observed. The solubility analysis of the lysate (L) after 4 h expression displays a dominant protein band in the soluble fraction (S) and some in the insoluble, pelleted fraction (P) (a, right). The native purification yielded a high amount of target protein product (b, 5 – 11 – eluted protein) compared to the lysate and its extraction and washing steps (b, L, S, P, and 1-4). The protein shows a dominant band at the height of the theoretical molecular weight of dimeric Cox17_a protein (blue arrow).

In summary, the *E. coli* strain T7 SHuffle Express *lysY* could not express the Cox17_a protein (not shown here). However, expression of Cox17_a with a theoretical molecular weight of 11.0 kDa was successful in the Lemo21 (DE3) *E. coli* strain (Figure 25 a, left). The soluble target protein (Figure 25 a, right, S) was used for the following native purification of Cox17_a (Figure 25 b). The purified protein from lanes 5 to 11 (Figure 25 b) was pooled, concentrated, and dialyzed in 1xPBS buffer supplemented in the first step with 5 mM EDTA and without EDTA in a second step.

Cox17_b

An example of Cox17_b expression in *E. coli* T7 SHuffle Express *lysY*, a solubility analysis, and a protein purification under native condition is shown in Figure 26.

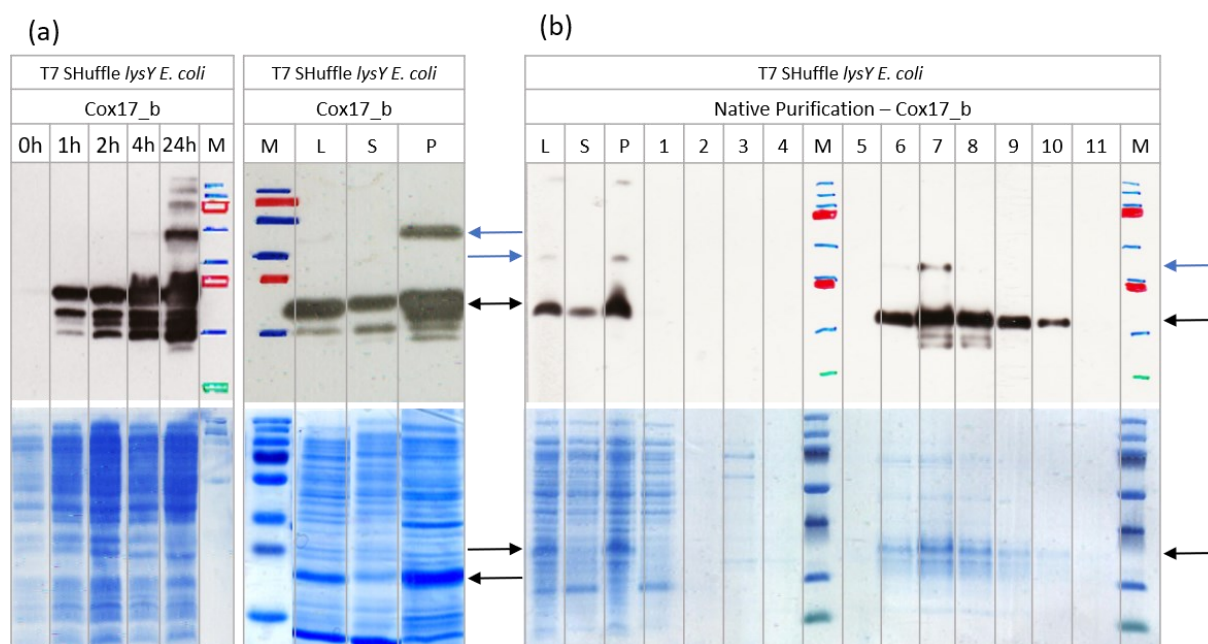


Figure 26. Expression analysis in T7 SHuffle Express *lysY E. coli* and purification of Cox17_b.

The upper panels show the immunological detection after western blot analysis, and the lower panels show the Coomassie-stained SDS PAGE gels. At 30 °C, expression (a, left) of the target protein (black arrow) increases over time after induction with IPTG. No leaky expression can be observed. The solubility analysis of the lysate (L) shows a protein band in the soluble fraction (S) and the insoluble, pelleted fraction (P) (a, right). The elution fractions of the native purification (b) (5 – 11 – eluted protein) yielded a clean target protein product in samples 6, 9, and 10. The elution fractions 7 and 8 have the highest target protein content, making faint degradation bands and a dimeric band for fraction 7 visible. The protein shows a clear but thin band at the position of dimeric Cox17_b protein (blue arrows) not exclusively but mainly in the pelleted fraction.

For using Cox17_b in follow-up experiments, the protein was expressed at 30 °C for 4 h after induction. Longer expression slightly increased the quantity but reduced the target protein's quality (Figure 26 a, upper panel). The native purification procedure cleared the protein solution from most unwanted protein compared to the lysate, which can be seen in the Coomassie-stained gel (Figure 26 b, lower panel). The final, eluted protein (Figure 26 b, upper panel, 5 – 11) shows slight degradation for the elution fraction with a very high protein product (7 and 8) and some dimer formation (7). The elution fractions of the target protein Cox17_b were used for the following experiments. The existence of the additional bands – especially in samples of the target protein from lanes 7 and 8 – should be kept in mind for further assessments.

Summarizing, the T7 SHuffle Express *lysY E. coli* strain expressed Cox17_b well with a theoretical molecular weight of 20.1 kDa (Figure 26 a, left). The target protein's soluble fraction (Figure 26 a, right, S) was

expressed dominantly enough to be further used in the native purification of Cox17_b (Figure 26 b). The elution fractions from purification from lane 6 to 10 (Figure 26b) were pooled, concentrated, and dialyzed in 1xPBS buffer supplemented in the first step with 5 mM EDTA and without EDTA in a second step.

Cox17_c

An example of Cox17_c expression in *E. coli* T7 SHuffle Express *lysY*, a solubility analysis, and a protein purification under native condition is shown in Figure 27.

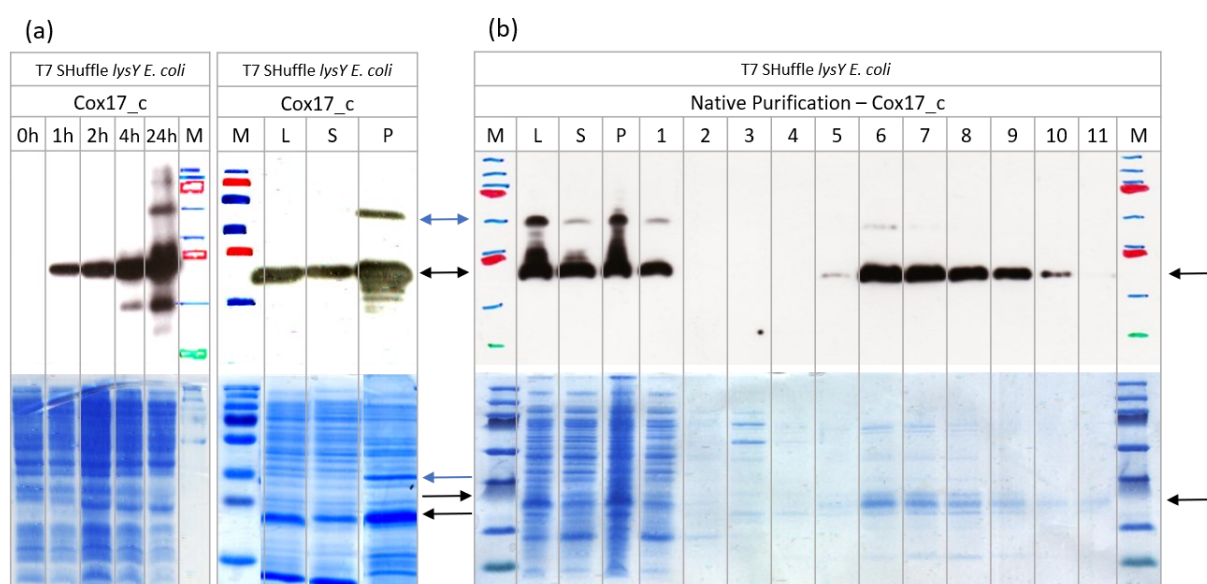


Figure 27. Expression analysis in T7 SHuffle Express *lysY E. coli* and native purification of Cox17_c.

The upper panels show the immunological detection after western blot analysis. The lower panels show the Coomassie-stained SDS PAGE gels. At 30 °C, expression (a, left) of the target protein (black arrow) increases over time after induction with IPTG. No leaky expression can be observed. The solubility analysis of the lysate (L) after 4 h expression shows the target protein in the soluble fraction (S) and the insoluble, pelleted fraction (P) (a, right). The protein shows a dominant band at the position of dimeric Cox17_c protein (blue arrow) after 24 h of expression and in the pelleted fraction. The native purification on the soluble fraction yielded a clean target protein product (b) (5 – 11 – eluted protein) and only a faint dimeric band in one elution fraction (Lane 6).

The protein Cox17_c was expressed in T7 SHuffle Express *lysY E. coli* at 30 °C for 4 h after induction. Longer expression slightly increased the quantity but reduced the target protein's quality (Figure 27 a, upper panel). The native purification was successful and yielded a clean Cox17_c protein sample (Figure 27 b, upper panel, black arrow) with only a little dimeric Cox17_c (blue arrow) in one elution fraction with high target protein content (Lane 6). The purification procedure removed most of the unwanted

proteins compared to the lysate, which can be seen in the Coomassie-stained gel (Figure 27 b, lower panel). While there are some faint, additional bands visible for the elution fractions, the target protein is dominantly present in protein samples.

The T7 SHuffle Express *lysY* *E. coli* strain expressed Cox17_c well with a theoretical molecular weight of 20.1 kDa (Figure 27 a, left). The amount of soluble target protein (Figure 27 a, right, S) was high enough to apply the native purification procedure (Figure 27 b). The elution fractions from lanes 5 to 10 from Figure 27 b were pooled, concentrated, and dialyzed in 1xPBS buffer supplemented in the first step with 5 mM EDTA and without EDTA in a second step.

3.1.3 Ccg-2

The pET28a(+) vector with the final Ccg-2 DNA target sequence incorporated in *E. coli* TOP10F' was provided (Döring et al. 2019). The *E. coli* TOP10F' pET28a(+)-Ccg-2 were cultivated, and the DNA isolated. The electrocompetent expression hosts were then transformed with the target DNA vector. *E. coli* T7 SHuffle Express *lysY* and *E. coli* Lemo21(DE3) were tested. After a solubility analysis, the Ccg-2 proteins were purified, concentrated, and refolded through dialysis. An example of hydrophobin Ccg-2 expression in *E. coli* T7 SHuffle Express *lysY* and a protein purification under denatured condition is shown in Figure 28. A summary of the chosen experimental conditions is presented in Table 41.

Based on the results presented in Figure 28 a, the protein Ccg-2 (black arrow) was expressed in *E. coli* T7 SHuffle Express *lysY* at 30 °C for 4 h after induction. Longer expression did not result in a higher quantity or quality of target protein. From former experiments, it is known that Ccg-2 is expressed well as an insoluble protein in *E. coli* T7 SHuffle Express *lysY*. Expression in Lemo21 (DE3) did not change the yield or solubility (data not shown). The denatured purification procedure cleared the protein solution from the unwanted protein s, which can be seen in the Coomassie-stained gel (Figure 28 b, lower panel) by comparing the elution fraction (11 – 15) to the samples of the lysate and its components (L, S, P). Dimeric Ccg-2 (blue arrow) can only be seen in the western blot analysis for high protein content. A strong tendency of dimeric and even multimeric behavior is, however, expected for the Ccg-2 protein. A dominant band appears in the Coomassie-stained gel from Figure 28 b (L, S, P, 1 – 10) running just above the Ccg-2-related band. That corresponds very likely to the size of lysozyme with a molecular weight of 14.3 kDa. It is added in excess to the cell lysate to facilitate the cell disruption procedure. The protein content of sample 15 was too low for detection. Therefore, the eluted proteins from 11 – 14 were used in further experiments.

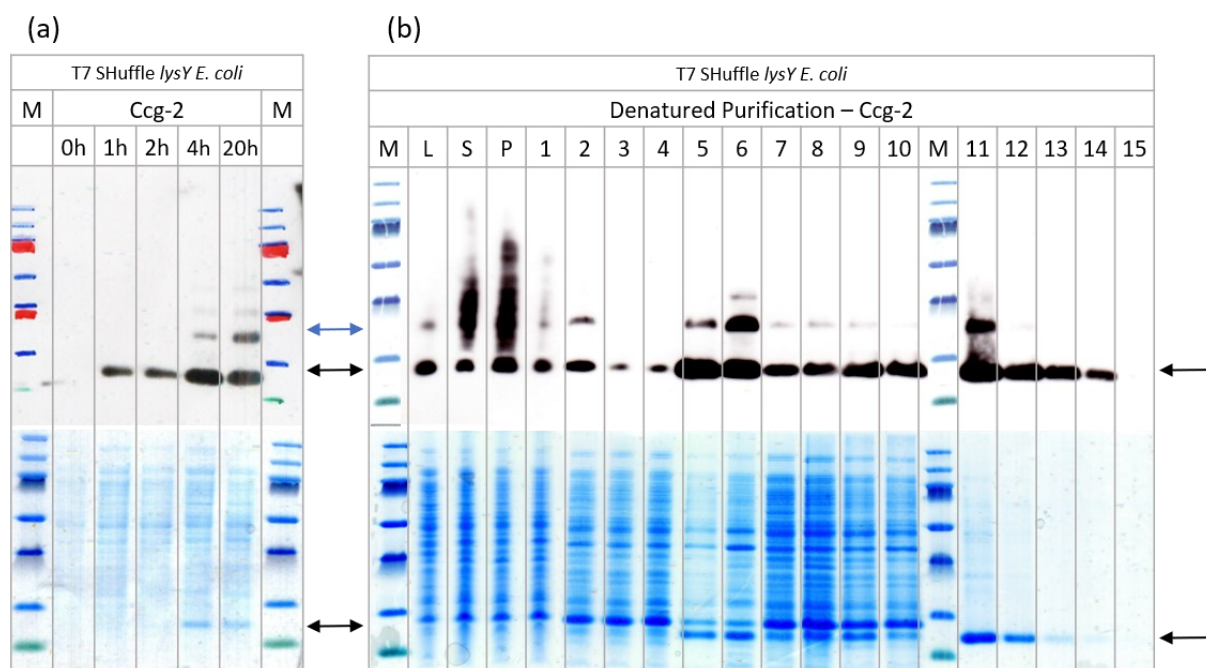


Figure 28. Expression analysis in T7 SHuffle Express *lysY E. coli* and denatured purification of Ccg-2.

The upper panels show the immunological detection after western blot analysis, and the lower panels show the corresponding Coomassie-stained SDS PAGE gels. At 30 °C, expression (a, left) of the target protein (black arrow) increases over time after induction with IPTG. There is no increase of target protein between 4 h and 24 h but a higher degree of dimer formation. No leaky expression can be observed. The denatured protein purification yielded a clean target protein product for 11 – 14 in the elution fractions (b) (11 – 15) compared to the lysate and its extraction and washing steps (b) (L, S, P, 1 – 10)

In summary, the protein expression at 30 °C in the *E. coli* strain T7 SHuffle Express *lysY* was successful with a theoretical molecular weight of approximately 10.9 kDa, harvesting the cell lysate after 4 h of expression after induction with 1 mM IPTG (Figure 28 a). Those conditions were hereby confirmed. They have been found in our lab in previous experiments. So has the insolubility of the Ccg-2 protein construct. Expressing Ccg-2 in Lemo21 (DE3) *E. coli* does not change its solubility (not shown here). The eluted protein from lanes 11 to 14 from Figure 28 b was pooled, concentrated, and refolded *via* dialysis in redox-refolding buffer supplemented in the first step with 5 mM EDTA and without EDTA in a second step.

3.1.4 Overview: Optimization of Expression and Purification of Recombinant Proteins

Table 41 provides an overview of the optimal conditions for the expression and purification of the various constructs. For details on the conditions, see previous subchapters Ch. 3.1.1, Ch. 3.1.2, and Ch. 3.1.3.

The choice of purification method, i.e., native or denatured purification, is crucial for the dialysis conditions, the expected yield, and the probability of receiving a functional protein, amongst others. Typically, denatured purification yields lower protein content than native purification, and the necessary refolding always increases the chance of protein misfold and subsequent malfunction. Therefore, Lemo21 (DE3) *E. coli* was tested for almost all protein constructs. It could preserve or even increase the solubility, such as Cox17_a and Sco1Δ95_a. Theoretically, the addition of L-rhamnose's right amount during protein expression in Lemo21 (DE3) *E. coli* controls the T7 promoter for more controlled protein production. Subsequently, it decreases the overall target protein amount it increases the amount of protein in the soluble fraction. While changing the host made a difference in protein solubility, the addition of different L-rhamnose concentrations only decreased the protein content in the lysate – as expected – and did not improve the soluble ratio insoluble fractions.

Based on the prior findings, it was decided not to continue with the Sco1_a, Sco1_b, and Sco1_c constructs because the yield after purification was very low and significantly lower than the corresponding constructs of Sco1Δ95. Furthermore, their purification had to be conducted under denatured conditions. Since it has been shown that the transmembrane domain truncated Sco1Δ95 protein also binds copper, the following tests and measurements were conducted with those truncated protein constructs. The protein constructs with a soluble expression, like Sco1Δ95_a and the Cox17 constructs, will be in the center of attention in the following experiments and their evaluation since their full functionality is most likely.

Table 41. Overview of all the produced protein constructs and their optimal expression and purification conditions. In all cases, T7 SHuffle Express *lysY E. coli* (T7 SHuffle) or Lemo21 (DE3) *E. coli* (Lemo21) cultivated in LB-media were used as host cells. The dialysis of purified protein was conducted in two steps, while each incubation step was for at least 20 h. 5 mM EDTA was added in the first dialysis step for all the copper-binding proteins. All proteins from denatured purification were dialyzed and stored in the redox-refolding buffer (RRB, Table 38). The PBS was made according to Table 19.

Construct	<i>E. coli</i> Expression host	Expression time	Expression temperature	Purification	Dialysis Conditions
Sco1_a	T7 SHuffle	4 h	30 °C	Denatured	1. RRB + EDTA 2. RRB
Sco1_b	T7 SHuffle	4 h	30 °C	Denatured	1. RRB + EDTA 2. RRB
Sco1_c	T7 SHuffle	4 h	30 °C	Denatured	1. RRB + EDTA 2. RRB
Sco1Δ95_a	Lemo21	24 h	16 °C	Native	1. 2xPBS + EDTA 2. 2xPBS
Sco1Δ95_b	T7 SHuffle	4 h	30 °C	Denatured	1. RRB + EDTA 2. RRB
Sco1Δ95_c	T7 SHuffle	4 h	30 °C	Denatured	1. RRB + EDTA 2. RRB
Cox17_a	Lemo21	4 h	16 °C	Native	1. 1xPBS + EDTA 2. 1xPBS
Cox17_b	T7 SHuffle	4 h	30 °C	Native	1. 1xPBS + EDTA 2. 1xPBS
Cox17_c	T7 SHuffle	4 h	30 °C	Native	1. 1xPBS + EDTA

2. 1xPBS					
Ccg-2	T7 SHuffle	4 h	30 °C	Denatured	1. RRB
2. RRB					

3.2 HIS-TAG CLEAVAGE

In some cases, it can be advisable to remove the His-tag to eliminate the risk of its interaction with copper during detection experiments. Therefore, it might distort the results of the copper-dependent interactions. The removal is done by the TEV protease cleaving the protein construct at its TEV recognition site. This recognition site was located between the His-tag and the target protein's beginning, only leaving one amino acid residue upfront. The results from His-tag cleavage are presented in Figure 29.

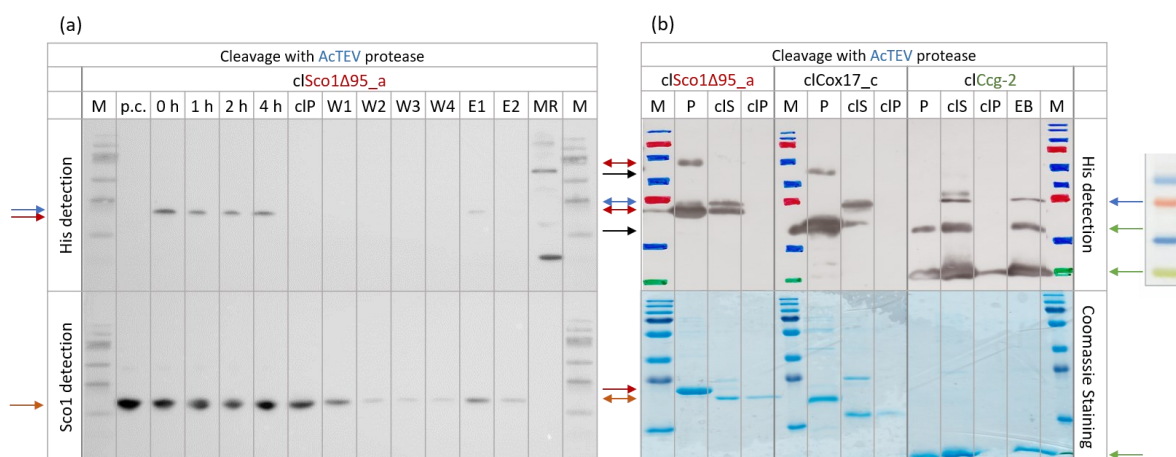


Figure 29. Cleavage at the TEV recognition site with the AcTEV protease to remove the His-tag.

The panels on the left (a) show the results of the western blot analysis after TEV cleavage of purified Sco1Δ95_a protein. Cleaved Sco1Δ95_a is used as the positive control (p.c.). Samples were taken during the cleavage reaction after 0, 1, 2, and 4 h, after application to the column (cIP), consecutive washing steps (W1 – W4), and elution steps (E1 – E4). As a secondary antibody for the immunological staining, first, an anti-His antibody was applied (upper panel), and then – after stripping the membrane – an anti-Sco1 antibody was applied (lower panel). The right panels (b) show the immunological staining (His-detection, upper panel) and the corresponding Coomassie-stained SDS PAGE gels (lower panel) of three proteins before (P) and after cleavage (cIS), after the consecutive purification procedure (cIP), and the elution of His-tagged protein (EB) with imidazole. The color of the protein labels matches the colored arrows that indicate the expected location of the particular protein; the orange arrow corresponds to the cleaved Sco1Δ95_a protein. The molecular weight standards are the ROTI® Mark 10-150 protein marker (MR) and the PAGE Ruler™ Prestained Protein Ladder (M and figure on far right).

The analysis of the cleavage procedure of cISco1Δ95_a in Figure 29 a documents the successful cleavage of the His-tag using the AcTEV protease. As expected, the positive control (p.c.) of the previously cleaved Sco1Δ95_a protein (21 kDa) only shows a signal for Sco1 detection. The samples were taken after 0, 1, 2, and 4 h of TEV protease cleavage at room temperature. They show a strong Sco1 signal (lower panel) and a faint His signal (upper panel). This signal could be due to the uncleaved Sco1Δ95_a protein (26 kDa) or the His-tagged AcTEV protease (28 kDa), whose molecular weights almost coincide. The observation that the Sco1 detection does not yield a second band closely above the cleaved protein suggests the absence of a significant amount of uncleaved protein. Hence the band probably originates from the AcTEV protease. The missing band of uncleaved protein in the Sco1 detection is unexpected since it is expected that the amount of uncleaved protein slowly decreases over time while the amount of cleaved protein slowly increases. However, it seems as if the total amount of protein is cleaved from the very beginning. It might be due to a combination of the very active AcTEV protease, which is still cleaving the protein after sampling, and of the experimental handling of not freezing or denaturing the protein samples quickly enough. Consequently, the AcTEV concentration can be lowered significantly, and cleavage may be possible at lower temperatures. The clean signal of cleaved Sco1Δ95_a protein (cIP) in Sco1 detection and the missing band in the His detection confirms a successful His-tag cleavage at the TEV recognition site.

The cleavage results confirm successful cleavage for Sco1Δ95_a (repeated), Cox17_a, and Ccg-2 shown in Figure 29 b. These experiments were conducted for a reduced incubation time of 2 h with 1 unit of AcTEV per 6 mg protein, i.e., half of the recommended concentration of AcTEV. All the cleaved protein samples (cIP) show no bands except for a thin band for Ccg-2. This band could correspond to a low amount of uncleaved protein or contamination from the neighboring wells, as can be seen for the marker of cISco1Δ95_a. However, comparing the immunological staining with anti-His antibody detection (upper panel) to the corresponding Coomassie-stained SDS PAGE gels (lower panel) are in line with the earlier results of high and efficient AcTEV protease activity and, therefore, a successful His-tag cleavage.

In summary, a 50 % reduced amount of AcTEV and an incubation time of only 2 h at room temperature is sufficient for the His-tag cleavage of the protein constructs used in this study. Given the high need for enzymes, further optimization could be an even higher reduction of AcTEV or cleavage at lower temperatures that are more convenient for the target protein.

3.3 CHIP SURFACE FUNCTIONALIZATION

A successfully functionalized chip surface is one crucial element for the detection of copper-dependent protein-protein interactions. Continuous testing of the purified proteins and the functionalized chip surfaces helps to choose adequate experimental conditions. Furthermore, it ensures a reproducible assay component. The functionalization and testing methods for the sensor chip are explained in Ch. 2.7. Now in Ch. 3.3.1 to Ch. 3.3.3, the results from the qualitative testing experiments and necessary optimization strategies will be presented. Ch. 3.3.4 considers a theoretical approach of the hydrophobin packaging of a protein layer on the surface. It estimates a minimum of protein necessary for a complete hydrophobin layer.

3.3.1 Optimization of the Glass Chip Preparation

The functionalization of the chip surface was adopted from former studies (Hennig et al. 2016) and adapted to the proteins' needs. Furthermore, new glass chip preparation protocols and storage conditions were tested. Parameters like optical cleanliness, the hydrophilicity of the surface after storage, and practical handling were used to decide upon the experimental conditions.

Removing residues from the glass surface and activating hydrophilic groups on the surface is essential. Cleaning the glass chips with a KOH-based protocol, the piranha cleaning protocol, and the RCA cleaning was tested. KOH-based cleaning tended to leave some stains on the surface compared to piranha cleaning, and its hydrophilicity was lower compared to a water droplet's behavior on the surface. The RCA-cleaning seemed to yield glass surfaces of comparable quality like from the piranha cleaning. Since the latter protocol was already established in the laboratory, it was decided to use the piranha cleaning before functionalizing the glass chips with protein solutions.

Since the glass chip cleaning takes about four hours, it is essential to be able to store the chips before their usage in RICM experiments. Therefore, the wet piranha-cleaned glass chips were dried with compressed air or – if available – nitrogen gas and put immediately in a Teflon carrousel placed in a covered glass beaker. The beaker was stored in a desiccator under vacuum conditions of roughly 50 – 100 mbar. A strong hydrophilic behavior on the glass chip could be observed even after four weeks of storage in the desiccator. When stored covered on the shelf at normal pressure, the hydrophilicity was diminished already after two weeks.

Finally, creating a self-assembling monolayer on the glass chip requires careful handling. The protein solution can be pipetted very slowly onto the surface. It is the highest priority to avoid any turbulence. A fast application would cause uneven, sometimes spotty surfaces that are prone to aggregates. The

pipetting onto the surface needs some practice. Alternatively, an automated application can be used. Here, the motorized syringe from the contact angle measurement instrument was employed. In this case, only turbulent-free uptake into the syringe and careful positioning of the syringe right above the glass chip has to be ensured.

The incubation of the protein solution on the glass chip was set to 30 min. Assembly of Ccg-2 could not be facilitated by incubation at 80 °C, because this temperature results in the denaturation of the proteins. Possibly further optimization of this step may be possible. However, rather than letting the solution dry, it was carefully pipetted off after incubation to avoid excessive and unspecific cluster formation. The glass chip was directly transferred to a water bath followed by multiple washing steps with ddH₂O under moderate shaking to remove clusters and unspecific adhesions. The glass chip was not washed with running water to prevent disruption of the freshly formed surface layer.

3.3.2 Macroscopic Properties of the Functionalized Chip Surface

Every freshly purified hydrophobin fusion protein construct was checked upon the hydrophobin's function of reversing the surface's hydrophilicity or hydrophobicity (DRoPS). Furthermore, the macroscopic quality of the functionalized chip surface (CAM) was tested.

Direct Reversion of Properties of Surfaces (DRoPS)

First, the surface functionalization's qualitative testing was conducted with the rapid test of checking the reversion of properties of the chip surface (DRoPS test). It gives the first clue whether the newly purified protein can invert the surface property from hydrophobic to hydrophilic or *vice versa*.

Every batch of freshly purified hydrophobin and its fusion protein constructs was tested with the rapid test of direct reversion of the properties of surfaces (DRoPS) described in Ch. 2.7.3. An exemplary result is shown in Figure 30 for freshly purified hydrophobin construct Ccg-2 in different concentrations ranging from 0.1 to 10 µM. Here, a positive result, i.e., hydrophobin assembly on the surface, can be seen when a water droplet remains at the area of functionalization. In the presented case, the fusion protein's hydrophobin assembles on the Petri dish's surface (polystyrene) and reverses its characteristic from hydrophobic to hydrophilic. The water repellent polystyrene is now hydrophilic in the areas of successful Ccg-2 functionalization and attracts – even captures – water molecules. Staining dH₂O with DAPI makes the residual water drop visible in UV-light.

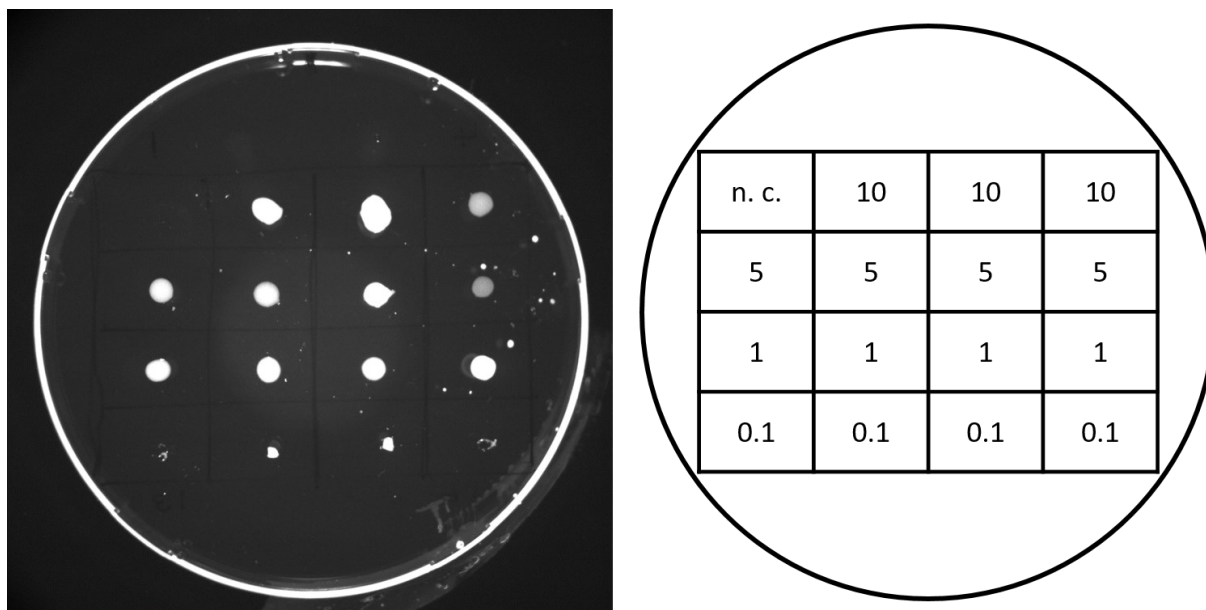


Figure 30. DROPS test of purified protein construct Ccg-2.

An exemplary image of a DROPS measurement of freshly purified Ccg-2 imaged with a UV-illuminator is shown on the left. DAPI-stained dH₂O appears white as a black and white camera is used. The scheme on the right represents where the samples were applied to the petri dish and the corresponding protein concentration used. The negative control (n. c.) refers to functionalization with dH₂O. The other boxes were functionalized with Ccg-2 of noted concentrations in μM .

The results shown in Figure 30 are an example of a successful DROPS test. The negative control (n. c.) does not show any signal under UV-light exposure. There are some deviations within experiments of the same concentrations. However, the protein-functionalized boxes show clear white spots with a decreasing signal intensity and drop diameter, respectively, as the protein concentration decreases. The white sprinkles are artifacts from the functionalization and washing steps. These results suggest that a concentration of 1 μM might be sufficient to functionalize the polystyrene surface. However, at this point, the most important result is that this batch of purified protein can successfully functionalize the surface and reverse the surface property of hydrophilicity/hydrophobicity.

Contact Angle Measurements (CAMs)

The static water CAMs are based on the same idea as the DROPS test: It aims at screening the surface's hydrophobicity/hydrophilicity. However, it gives a more quantitative although still macroscopic insight of the previously prepared chip surface layer composition. The chip surfaces were prepared as described in Ch. 2.7.1, and the measurements were conducted as described in Ch. 2.7.3.

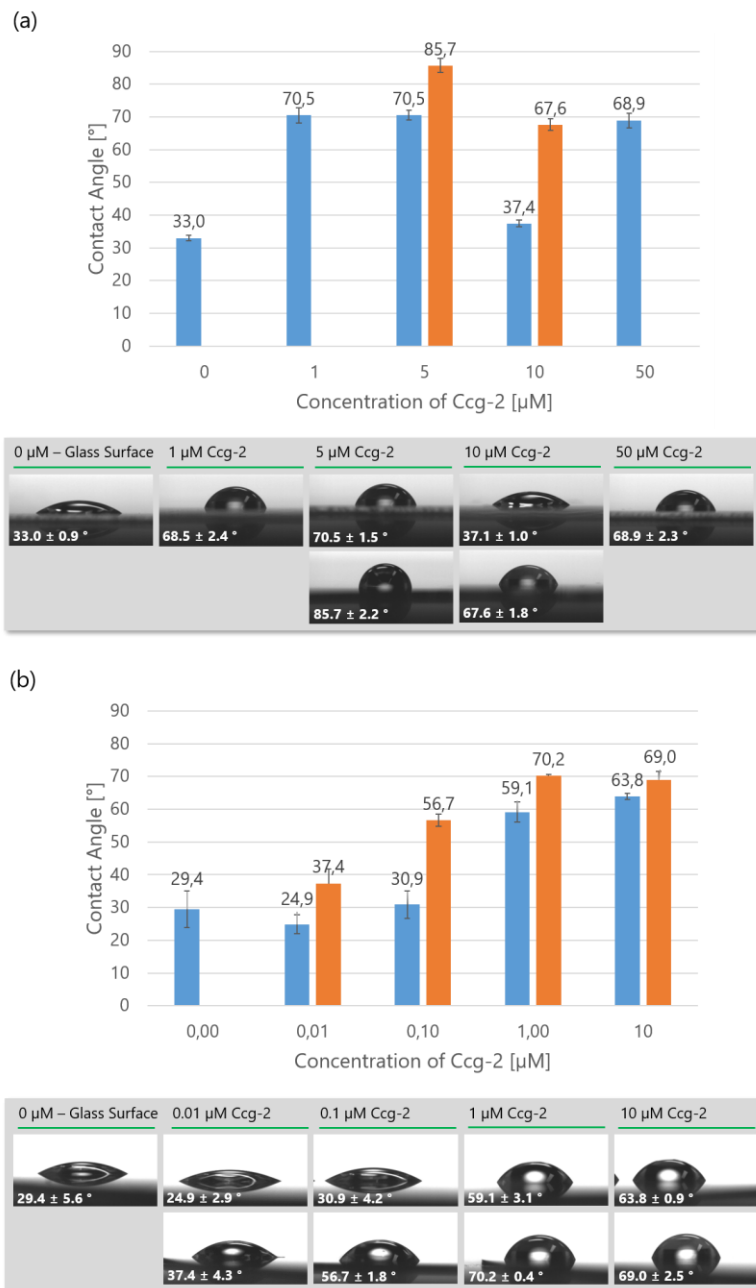


Figure 31. CAMs with ddH₂O drops on glass chip surfaces, functionalized with different hydrophobin Ccg-2 concentrations.

The lower panels show exemplary images of the droplet shapes for different Ccg-2 concentrations and different populations within one applied concentration, respectively, corresponding to the CAM data shown in the upper panels' graphs. Different populations of CAs are colored in blue and in orange. When using ddH₂O as a droplet substance, a small contact angle indicates hydrophilic surface properties, while a high contact angle indicates strong hydrophobic behavior. For each concentration, at least 15 drops were measured.

The data analysis of the contact angles from water droplets for a glass slide with one protein concentration shows, in some cases, a histogram with more than one clear maximum and a shifted Gaussian distribution, respectively. Two or more populations could be identified using binning analysis, then separated, and their mean values and standard deviations were calculated. The populations could refer to multiple, partially incomplete surface layers with alternating hydrophobicities.

The effect of functionalizing chip surfaces – here glass cover slides – with different Ccg-2 concentrations was investigated as presented in Figure 31. The concentration ranging between 0 and 50 μM (a) and between 0 and 10 μM (b), respectively, were tested. In this experiment, the negative controls of a surface functionalized with 0 μM Ccg-2 show a contact angle of around 30°. This value indicates a hydrophilic surface. Nevertheless, lower contact angles of around 15° can be achieved for this initial value on glass by Piranha-cleaning the surfaces and using them within four weeks after preparation. Furthermore, glass chips should be stored in an airtight desiccator in the meanwhile, which was not yet done in this case.

All tested concentrations equal to 1 μM protein or greater result in a high hydrophobicity with a contact angle of roughly 70° and above throughout the tested glass slide in one or more populations (a). The discrete populations within one applied concentration could indicate a mixture of one and two or even more assembled hydrophobin layers stacked onto each other either as homogeneous patches or in small clusters. The strong hydrophobic behavior of a contact angle of 85° for 5 μM is not clearly understood. It could indicate a long-range and very well-structured hydrophobin layer. Testing hydrophobin concentrations between 0 and 1 μM (b) show a gradual increase in hydrophobicity. It can also be suggested that for this concentration range, the protein content is not sufficient to form a homogeneous surface layer because there is a prominent contact angle population comparable to the initial value.

Variations between results from different chip surfaces treated with the same concentrations could result, for example, from applying the protein solution differently; sudden movements can increase the possibility of cluster formation, and washing might or might not clean off unstructured clusters. Variations can also be caused by different qualities of the protein sample depending on the batch and age. Moreover, the glass chip condition greatly influences the hydrophilicity, meaning the cleaning procedure, age, and storage conditions. In this particular case of Figure 31, the protein samples were the same. The chip surfaces' treatment and storage conditions were also comparable; only the chip surfaces in (b) have been stored for longer. The different storage times may explain the higher standard deviations of the initial value for 0 μM protein.

The reached maximum hydrophobicity values for functionalized Ccg-2 surfaces in (b) are lower for all the comparable samples. This difference could indicate a less homogeneous assembly due to the different surface conditions described above, or it may simply reflect differences between the functionalized surfaces.

The first stable layer appears to form, starting at a concentration of 1 μM . Consequently, a concentration between 3 or 5 μM was usually chosen.

To test the surface layer stability, CAM results from chip surfaces coated with different Ccg-2 protein concentrations and subsequently incubated with 2% sodium dodecyl sulfate (SDS) at 80 °C for 20 min up to two times were compared (Figure 32). An effect of SDS washing is very prominent for 0 μM protein content (Figure 32, blue) as the contact angle decreased. The surface became highly hydrophilic, with contact angles lower than what can be achieved for freshly Piranha-cleaned glass chips. Those results suggest that SDS molecules might be bound to the glass surface. There is no comparable effect visible for surfaces that were first coated with protein. Nevertheless, 1 x SDS treatment (Figure 32, orange) increases the tendency for a higher number of populations. On the other hand, 2 x SDS treatment (Figure 32, gray) decreases the number of populations again, some of which are very close together, for example, for 10 μM protein content. Besides the possibility of each population being a discrete layer, they could also be one population with a large standard deviation, indicating a hydrophobic but irregular surface layer.

CAMs reveal some changes in the surface composition when treated with SDS. No apparent washing-off for protein-coated glass surfaces can be observed, and the surface layer seems to be stable under the performed SDS treatments.

For the final setup, the glass chips were coated with a mixture of Ccg-2 and the fusion proteins of Ccg-2 with a derivative of the copper-binding proteins Cox17 and Sco1, respectively, and subsequently tested with CAM. Figure 33 shows the results for the Cox17 fusion protein constructs Cox17_b (a) and Cox17_c (b) and for Sco1 protein construct Sco1 Δ 95_c (c), for various ratios between the Ccg-2 construct and its fusion protein and different protein contents, respectively.

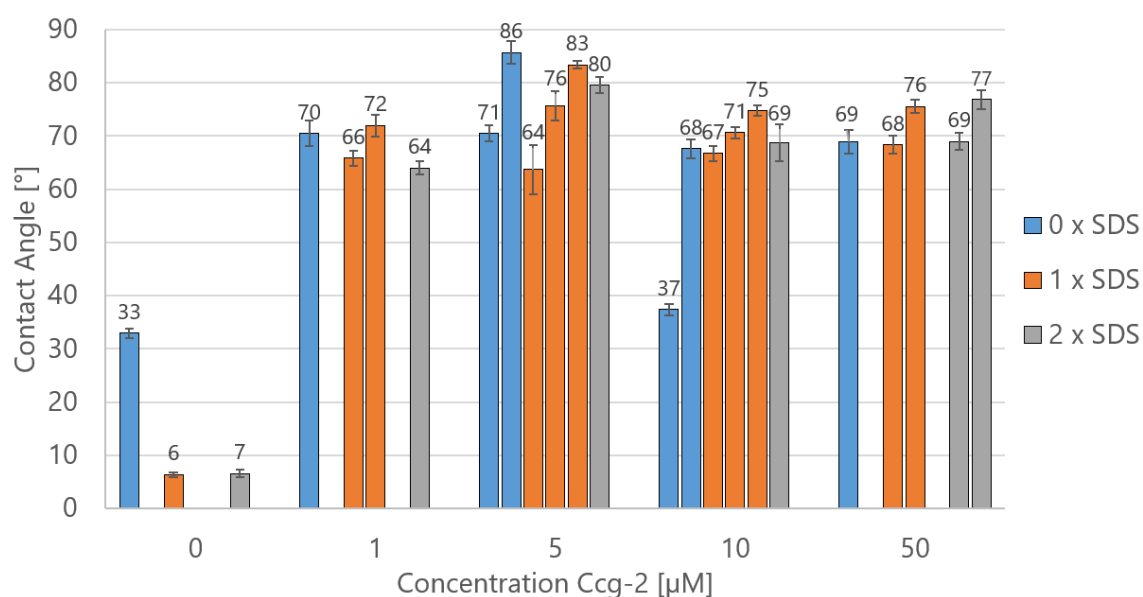


Figure 32. Comparing CAM on Ccg-2-functionalized glass chips after washing with SDS.

Glass chips were functionalized with different Ccg-2 concentrations. CAM was conducted after functionalization (blue, 0 x SDS), after a first washing step with 2% SDS (orange, 1 x SDS), and after a second washing step with 2% SDS (gray, 2 x SDS). The washing steps were performed at 80 °C for 20 min. Here, the different bars with one color show the occurrence of multiple populations of CAs within one set of conditions.

For the Cox17 fusion proteins, the surface's hydrophobicity change seems not affected by the orientation of Cox17 and Ccg-2. The hydrophobicity of measurements of different ratios of Ccg-2 mixed with Cox17_b (Figure 33 (a)) and Cox17_c (Figure 33 (b)) show about the same contact angles.

The high initial value for the Sco1Δ95_c functionalized glass chips in Figure 33 (c) could be due to a less hydrophilic glass surface owed to long-time storage. The hydroxylated surface is then mostly saturated, making it less hydrophilic. Particles like dust might have settled on the surface. The used glass slides had been Piranha-cleaned about two months ago.

Comparing Figure 33 (a) and (b) with (c) shows the different characteristics on the surface by different hydrophobin fusion proteins and their behaviors as mixtures with pure Ccg-2. Cox17_b (a) and Cox17_c (b) cause the surface to change from hydrophilic to hydrophobic. The Sco1Δ95_c functionalized surface stays hydrophilic like the negative control (functionalization with redox-refolding buffer). The latter could mean that either the surface properties are the same as for a pure glass surface, or the hydrophobicity is raised to a contact angle of around 46.6 ° compared to a freshly cleaned glass slide. In this particular case, those two possibilities cannot be well differentiated due to the very high initial value of

the negative control compared to previous measurements. However, when the Sco1Δ95_c fusion protein is mixed with the pure protein construct Ccg-2, hydrophobicity increases towards a contact angle of above 60 °. Only a decreased protein content of 1 μM uncover a second population with a lower contact angle of around 56 °. The second population might indicate that the protein content of 1 μM is too low to ensure a proper and homogeneous assembly on the surface.

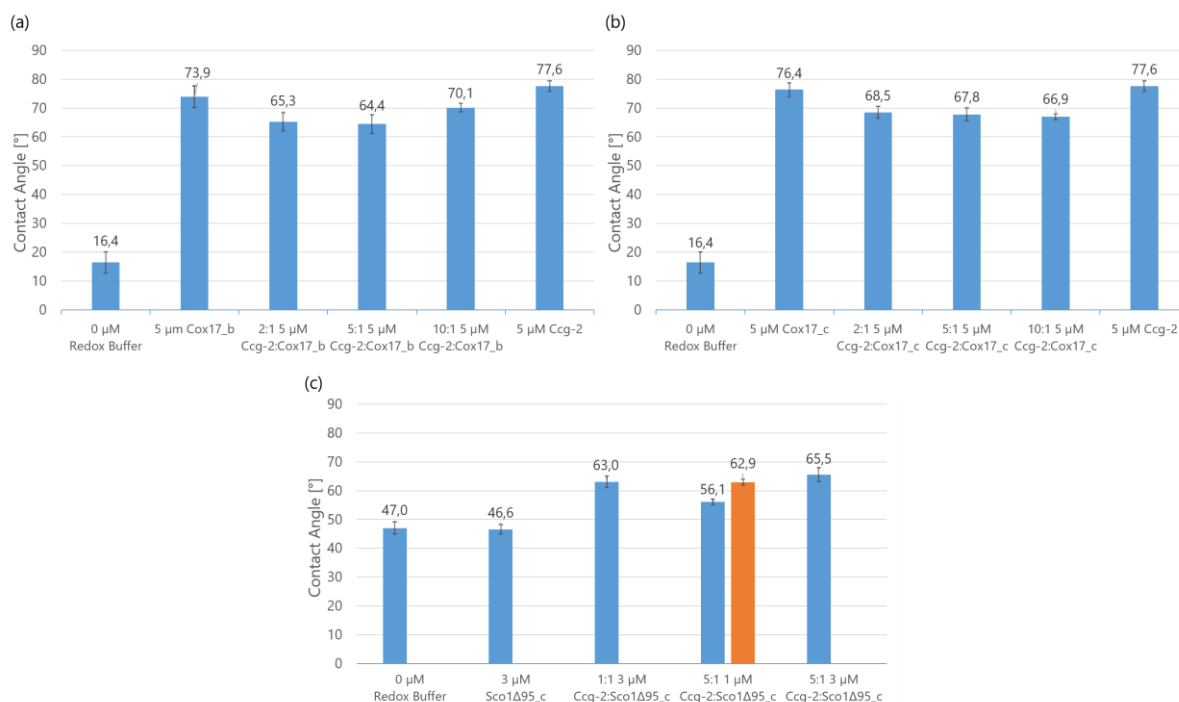


Figure 33. CAM of functionalized surfaces with different fusion proteins, the hydrophobin Ccg-2, and their mixtures.

The glass chip functionalized with redox buffer is the negative control, and, therefore, the notation of 0 μM refers to no protein content in the solution. The chip surfaces were coated either with the construct Cox17_b (a) or Cox17_c (b), with Ccg-2, and with mixtures of both in 2:1, 5:1, and 10:1 ratios. The overall protein content was adjusted to 5 μM. The data for 0 μM and 5 μM Ccg-2 in (a) and (b) were taken from the same measurements. For the protein construct Sco1Δ95_c (c), the chip surfaces were coated with Sco1Δ95_c and the mixture with Ccg-2 at ratios 1:1 and 5:1. The protein content was 3 μM for the 1:1 mixture and 1 μM for the 5:1 mixture. Except for one measurement (orange bar in (c)), all data revealed a single population of CAs.

In the final SCP-RICM assay experiments, typically, Cox17 was functionalized on the surface, and Sco1Δ95_a was functionalized onto the SCPs (see 3.4). More precisely, protein construct Cox17_c was used typically in a 5:1 ratio of Ccg-2 and Cox17_c and a protein content between 3 and 6 μM.

3.3.3 AFM Measurements

The chip surfaces were functionalized with samples of Ccg-2 and 5:1 mixtures of Ccg-2 to Cox17_c with 3 μM protein content followed by atomic force microscopy (AFM). AFM measurements can uncover further information about the microscopic structure of the surface layer.

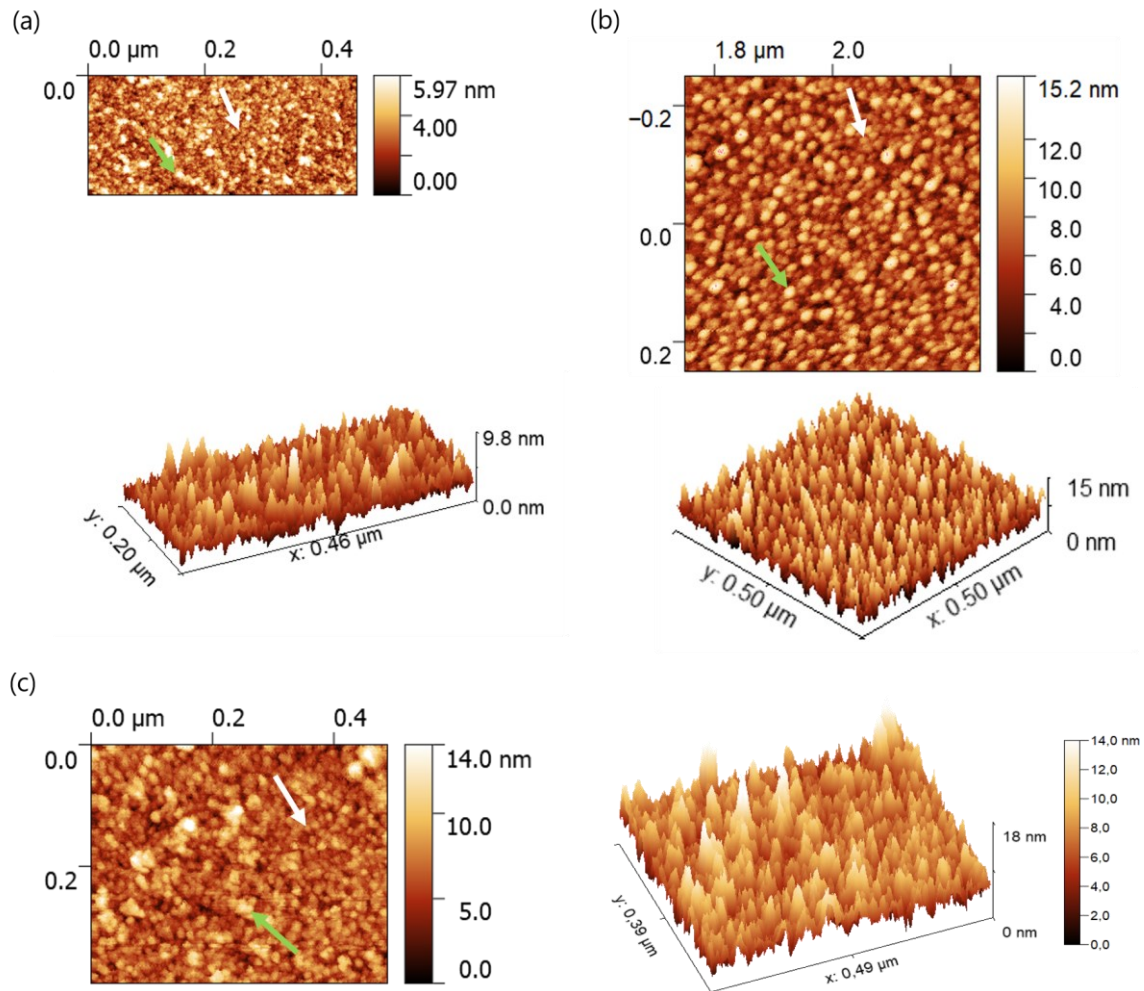


Figure 34. AFM images of surfaces functionalized with Ccg-2 and of the Cox17_c protein construct.

A glass chip (a) and a mica sheet (b) were functionalized with 3 μM Ccg-2, and subsequently, the surface layer was analyzed with an AFM. The same was done with the glass chip functionalized with a 5:1 ratio of Ccg-2 and Cox17_c with 3 μM protein content (c). For every condition, one panel shows the color-coded two-dimensional image of the scanned surface. In contrast, the other panel shows the three-dimensional representation marked with the same color-code. The arrows mark an exemplary small (white) and big (green) structure. The images in (a) and (c) were cropped to exclude defects on the surface and artifacts from imaging, respectively.

The functionalization of mica sheets with Ccg-2 (Figure 34 (b)) shows a repeating structure of closely-packed spikes, which have discrete shapes with a circular cross-section in x-y-direction. The smaller spikes have diameters of around 17 nm on average with a height of 3.1 nm, and the larger spikes show diameters of around 30.4 nm with a height of 12.5 nm. These structures resemble those of hydrophobin class II layers, as described for HFBI with a maximum height of 3.5 nm (Gruner et al. 2012). The Ccg-2-functionalized glass surface (Figure 34 (a)), however, presents as a layer of densely packed, very small structures with a width of roughly 5 nm and a corresponding height of 1.1 nm and with larger, regularly appearing spots on top. These spots with a width of around 14.5 nm and a height of around 2.7 nm seem to often accumulate in rows. They cannot, however, be considered as rodlet-like formations. The possibility of monomers adsorbed to the surface in different directions has previously been discussed (Hakanpää, Szilvay, et al. 2006; Hakanpää, Linder, et al. 2006; Kallio et al. 2007).

The first impression of the Cox17_c-functionalized glass chip (Figure 34 (c)) is very similar to the one functionalized with Ccg-2: The surface is densely packed with small structures, and some bigger structures are distributed throughout the surface. However, a closer examination reveals that even the small structures are more circular than in the case of pure Ccg-2 (Figure 34 (a)). They are bigger, with a diameter of roughly 13.6 nm and a height of 4.5 nm. The bigger structures have an average width of roughly 20.3 nm and a height of 5.8 nm. Remarkably, the structures are bigger, and the size difference between the small and the bigger structures is smaller than for the Ccg-2-functionalized surfaces. This difference may be caused by the upward orientation of Cox17 in the Cox17_c fusion protein construct. More AFM measurements are necessary to validate and better understand the details of the functionalized surface.

3.3.4 Theoretical Package of Hydrophobin Ccg-2 on the Chip Surface

Estimating the maximum surface density of hydrophobin class I Ccg-2 monomers packed as a monolayer on the chip surface gives an impression of the necessary minimal protein concentration and protein content needed for the functionalization of a chip surface.

In theory, the class I hydrophobin Ccg-2 forms a monolayer at interfaces. Kwan et al. (2006) reported that a Ccg-2 monomer at an air/water interface has a diameter of around 2.5 nm and is pictured as somewhat globular. In good agreement, it was proposed that the Ccg-2 monolayer on a hydrophilic surface shows a layer thickness of 2.74 ± 0.04 nm (Gruner et al. 2012). The Ccg-2 monomers most probably interact during monolayer formation by stacking of the β -barrels. This mechanism suggests that each monomer is packed right next to the other without leaving a decisive space in between.

Therefore, for the following calculations, the hydrophobin monomer's dimensions at a water-glass interface were assumed to be a cuboid with a width and length of $w = l = 2.5 \text{ nm}$ and a height of $h = 2.7 \text{ nm}$. This size results in coverage of an area of $A_{1H} = l \cdot w \approx 6.25 \text{ nm}^2$ for one hydrophobin monomer (1H). The protein layer at the water-glass interface produced by a drop of protein solution on the chip surface covers an area A_{chip} and depends on the geometry of the chip surface. As an example, the typical chips that were used for functionalization are round glass cover slides with a diameter $d = 30 \text{ mm}$ which were fully functionalized. Hence, it results in $A_{\text{chip}} = \pi \cdot \frac{d^2}{4}$. Therefore, the number of hydrophobins needed to cover the chip surface calculates to $N_{H,\text{chip}} = 1H \cdot \frac{A_{\text{chip}}}{A_{1H}}$ with H for hydrophobins. Estimating the minimal hydrophobin concentration calls for the minimal drop volume needed for functionalization. Testing showed that a volume of $V = 350 \text{ }\mu\text{L}$ of protein solution is sufficient to completely cover the chip surface. Applying the minimal required volume results in an approximately flat drop surface rather than a round-shaped surface. This air/water interface contributes to the number of hydrophobins in the same manner as $N_{H,\text{chip}}$ while neglecting the edges' contribution. Consequently, the number of minimal necessary hydrophobin monomers in solution is $N_H = N_{H,\text{air}} + N_{H,\text{chip}} = 2 \cdot N_{H,\text{chip}} = 2.262 \cdot 10^{14}$, the amount of substance is $n_H = \frac{N_H}{N_A} = 3.76 \cdot 10^{-10} \text{ mol}$ with the Avogadro constant N_A , and this results in the minimal necessary hydrophobin concentration in solution of $c_{H,\text{min}} = \frac{n_H}{V} = 1.073 \text{ }\mu\text{M}$. Suppose a ratio of pure hydrophobin to target fusion protein is used for functionalization. In that case, the number of monomers has to be distributed according to the ratio. At the same time, one fusion protein also contributes one hydrophobin monomer to the monomeric layer at the interfaces.

3.4 SCP FUNCTIONALIZATION

3.4.1 SCP Functionalization and FITC Staining

SCPs were functionalized with the Sco1_a protein construct, i.e., the Sco1 derivative without a Ccg-2 component, *via* EDC/NHS chemistry described in Ch. 2.8.1. As a negative control, SCPs were treated according to the functionalization protocol except for substituting buffer for protein solution. The Sco1_a-SCPs and the negative control were stained with the fluorescent dye FITC, which binds to primary amines (Ch. 2.8.2), to validate a successful functionalization. The fluorescent signal of the SCPs with and without Sco1_a functionalization was compared (Figure 35).

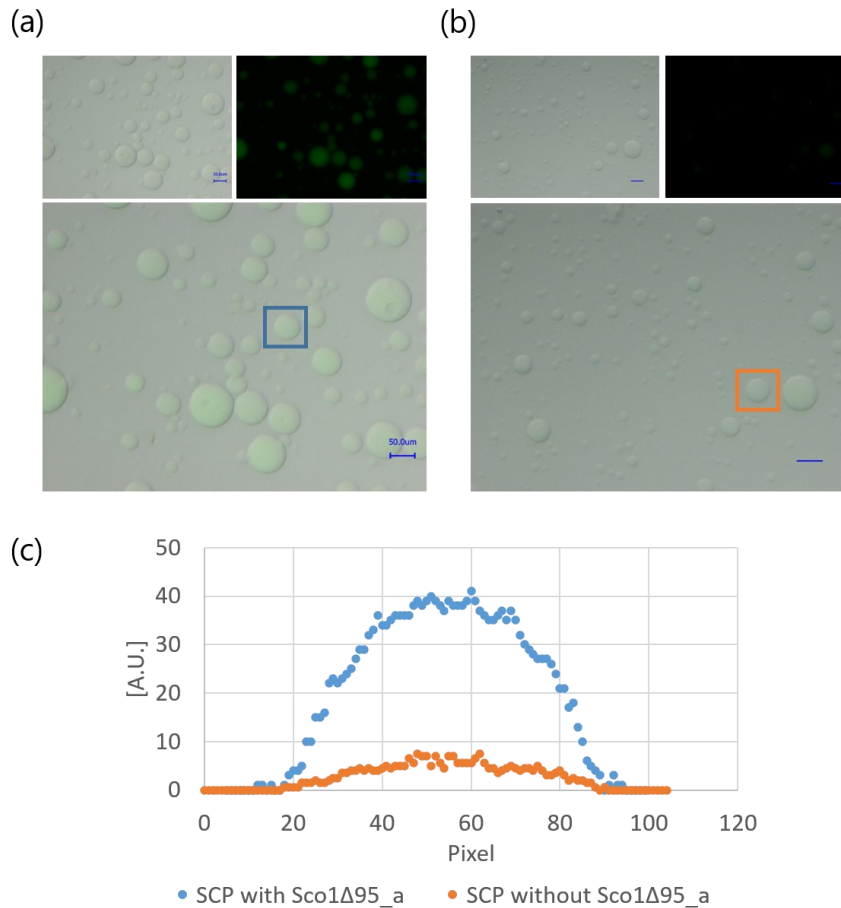


Figure 35. FITC staining of Sco1Δ95_a-functionalized SCPs.

SCPs were functionalized with (a) and without (b) Sco1Δ95_a and subsequently stained with FITC. The brightfield image (upper panel, left), the fluorescent signal (upper panel, right), and their overlay (lower panel) show successful staining. The exposure time for the fluorescent images was 5 sec. Comparing the results from a line profile of the SCPs marked with a blue and orange square, respectively, show a higher fluorescent signal for the Sco1Δ95_a-SCP than for the not functionalized SCP (c). Scale: 50 μm

The fluorescent signals of the SCPs marked with a square in Figure 35 (a) and (b) were analyzed and compared (Figure 35 (c)). SCPs of roughly the same size were chosen. The shape of the fluorescent signal throughout the SCP results from the sum signal of multiple layers in the z-direction, i.e., a projection. Consequently, the edges of the projection's line profile show a lower fluorescent signal than the center, where multiple layers of FITC stained proteins are summed up. The signal from the not functionalized SCP results from a low, unspecific binding capacity of FITC. The maximum fluorescent signal of the Sco1Δ95_a-SCPs is more than five times as high as the not functionalized SCP. Therefore, the functionalization of the SCPs with Sco1Δ95_a was successful. Nevertheless, the FITC-staining does not

give information on the functionality of Sco1Δ95_a regarding its copper-binding ability after functionalization to the SCP.

On the one hand, the functionalization procedure means stress on the protein resulting in possible protein denaturation. On the other hand – and probably more crucial – is the linking *via* EDC/NHS, which can address any available lysine residues and the N-terminus' primary amino group. Hence, it can be expected that the protein will face many different directions, some of which may allow the interaction with copper ions while others may not. The different directions should, however, not be a problem for the assay. Given the high protein density and an evenly distributed directionality of Sco1Δ95_a on the SCP surface, enough Sco1Δ95_a proteins should be available to contribute to copper binding.

3.4.2 Theoretical Package of Proteins on SCPs

Estimating the number of proteins packed on the surface of the SCPs is of interest to assess how many proteins are theoretically available for interaction with the functionalized chip surface and the copper ions in solution. Since the COOH residues and, therefore, the number of functionalization sites are theoretically densely packed on the SCP surface, the dominant factor of limitation is probably the size of the protein used for functionalization of the SCP in terms of the area occupied.

It is assumed that an abundant number of carboxylic residues (the sites of functionalization as described in Ch. 3.4.1) is present on the PEG chains of the SCP. The following estimation calculates a maximum number of functionalized and functional proteins.

According to their molecular weight, the protein size can be estimated based on the size-dependent prediction of folding domains (Erickson 2009). Both protein constructs Cox17_a, and Sco1Δ95_a are considered for SCP functionalization, and both proteins are relatively small with a molecular weight of about $M = 11$ kDa and 26 kDa, respectively. They can therefore be assumed to be globular in solution. In that case, a minimal radius ρ_{min} in nm can be calculated taking the molecular weight M in Da into account, using the following equation:

$$\rho_{min} = \left(\frac{3 * V}{4 * \pi} \right)^{\frac{1}{3}} = 0.066 * M^{\frac{1}{3}}$$

Consequently, the two proteins have a minimum radius of $\rho_{min, Cox17_a} = 1.47$ nm with a minimal area of $S_{min, Cox17_a} = \pi * \rho_{min}^2 = 6.79$ nm² and $\rho_{min, Sco1_a} = 1.95$ nm with an area of $S_{min, Sco1_a} = 11.95$ nm². If an average SCP radius of $R_{SCP} = 25$ μm is assumed, the SCP's surface area S_{SCP} calculates to:

$$S_{SCP} = 4 * \pi * R_{SCP}^2 = 7,854 \mu m^2$$

The number of proteins that maximally fit on an SCP surface is $A_{\text{Cox17}} = S_{\text{SCP}}/S_{\text{min, Cox17_a}} = 1.2 \cdot 10^9$ molecules, and $A_{\text{Sco1_a}} = 657 \cdot 10^6$ molecules. Using the well-known relation for the amount of substance $n = A/N_A$, with $N_A = 6.022 \cdot 10^{23}$ being the Avogadro number, it calculates to $n_{\text{Cox17_a}} = 1.99$ fmol and $n_{\text{Sco1_a}} = 1.09$ fmol, respectively, of protein per SCP with a radius of $R_{\text{SCP}} = 25$ μm . Since we assumed the minimal radius p_{min} for the extension of a single protein molecule, A and n represent the maximal number and amount of protein on the SCP's surface.

The protein functionalization on the SCP is random in direction. The EDC/NHS functionalization method aims to link primary amines of the lysine amino acids and the free nitrogen of the protein's N-terminus. Consequently, some of the arising orientations after functionalization will result in a functional protein, and some of them will be malfunctioning. Cox17_a sequence screening shows 12 possible binding sites. The sequence of Sco1 Δ 95_a shows 18 possible binding sites where lysine amino acids are relatively evenly distributed along. On the rough assumption that a third of the possible binding sites yield a functional protein orientation, there would be $400 \cdot 10^6$ Cox17_a molecules and about $219 \cdot 10^6$ Sco1 Δ 95_a molecules, respectively, functional per SCP. Proposing a binding efficiency of 1 Cu(I) ion per molecule for Cox17 (Abajian et al. 2004; Banci et al. 2008) and Sco1 (Abajian and Rosenzweig 2006), these numbers also correspond to the number of possibly bound Cu(I) ions per SCP. Approximating 5,000 SCPs/mL from absorption measurements concludes that at maximum, there would be $2,000 \cdot 10^9$ Cu(I) ions bound per milliliter Cox17_a-SCPs resulting in $n_{\text{Cu, Cox17_a}} = 3.32$ pmol, i.e. $C_{\text{Cu, Cox17_a}} = 3.32$ nM Cu(I). Equally, there would be at maximum $1,095 \cdot 10^9$ Cu(I) ions bound per millilitre Sco1 Δ 95_a-SCPs resulting in $n_{\text{Cu, Sco1}\Delta 95_a} = 1.82$ pmol, i.e. $C_{\text{Cu, Sco1}\Delta 95_a} = 1.82$ nM Cu(I).

3.5 SCP-RICM ASSAY

The SCP-RICM assay combines the previously presented and tested components and utilizes them to detect copper(I) ions in a sample solution. The copper-dependent interaction of the proteins displayed on the surfaces triggers a deformation of an SCP. The degree of deformation is examined by observing the SCP's interference pattern and measuring the contact area with the surface by inverse light microscopy.

The copper solutions used in the copper-dependent RICM experiments were prepared as described in Ch. 2.9. The effects of aerobic conditions on the Cu(I)Cl solution and the reduction by ascorbic acids were tested and are presented in Figure 36. The samples were measured by spectrophotometry with the microplate reader infinite M200Pro by Tecan Group Ltd. (Switzerland). A wavelength range between 300 and 900 nm was chosen, scanning every five nanometers.

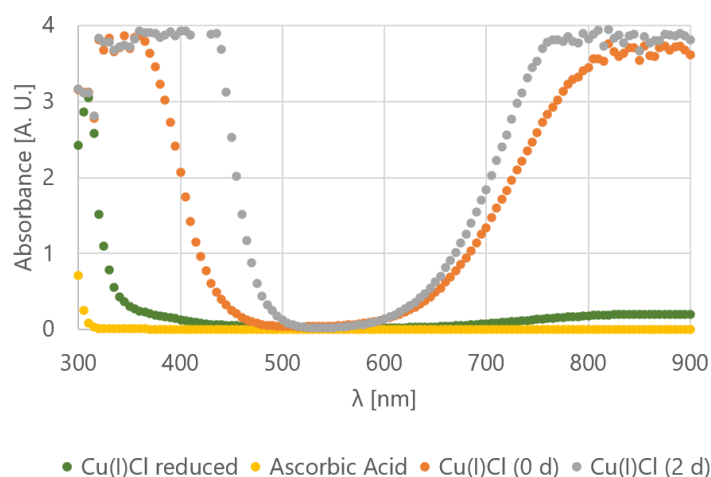


Figure 36. Spectroscopic absorbance measurements of different Cu(I)Cl solutions.

The Cu(I)Cl solution right after preparation under aerobic conditions (Cu(I)Cl (0 d)) appears dark green. Its spectrum shows dominant and broad peaks at the Cu(I)-related absorption around approximately 300 nm and at the Cu(II)-related absorption around approximately 770 nm (orange). Those peak areas broaden for the Cu(I)Cl solution that has been stored for two days (Cu(I)Cl (2 d)) while this solution appears bright green. The addition of ascorbic acid (yellow) is necessary to reduce the Cu(I)Cl (0 d) solution, which then appears light yellow to clear. The spectrum of reduced Cu(I)Cl (0 d) here shown is ascorbic acid corrected (Cu(I)Cl reduced, green). A clear shift in the Cu(II)/Cu(I) ratio is observable under reduced conditions. The Cu(I)Cl solutions had a copper concentration of 200 mM. The ascorbic acid solution had a concentration of 100 mM.

The tested solutions from Figure 36 had a copper concentration of 200 mM, which appears to be too high for photometric measurements. The absorption signal around the peaks is oversaturated. Consequently, no maximum value of the broad peaks can be determined (gray and orange). A decreased copper concentration would probably result in clear peaks with a precise maximum. However, a shift in the absorption spectrum can be seen when adding ascorbic acid and reducing the solution (Cu(I)Cl reduced, green). After reduction, the solution was handled quickly but under aerobic conditions and was then measured. Ascorbic acid reduces Cu(II) and copper complexes to Cu(I). The Cu(I)-related peak decreases and gets narrower, with a maximum now located at around 320 nm. There has always been a low amount of Cu(II) present in the solution, as indicated by a small peak for the reduced Cu(I)Cl solution at around 850 nm (Gomez et al. 2010). The absorption spectrum of chlorine (Cl) and chloride (Cl₂) lies in the ultraviolet range and overlays in the presented measurements with the absorption spectra of Cu(I) and ascorbic acid between 300 and 400 nm (Yin et al. 2018). In summary, the Cu(I)Cl solution was always reduced – here by ascorbic acid and TCEP – right before using it in a RICM experiment to ensure a dominant presence of Cu(I) over Cu(II).

In all the presented RICM experiments, the chip surfaces were functionalized with 6 μM protein with a ratio of 5:1 of Ccg-2 to Cox17_c. One exception is the experiment with cICcg-2 and cICox17_c (see below for details). The SCP-functionalization was done with a protein concentration of around 1 mg/mL.

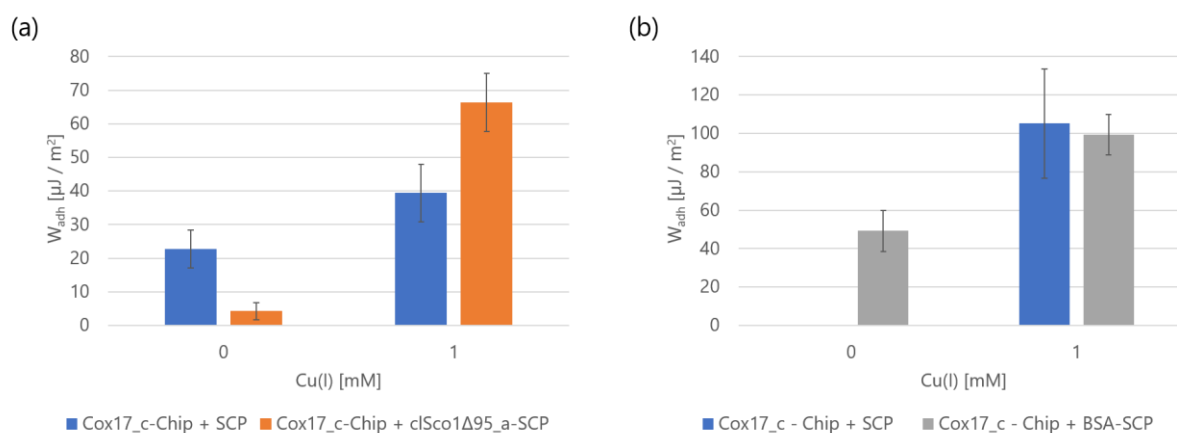


Figure 37. Cu(I)-dependent RICM measurements on Cox17_c coated chips with cISco1Δ95_a-SCPs (a) and with BSA-SCPs (b).

The adhesive work W_{adh} on the chip surface increases upon the addition of Cu(I). (a) In the presence of Cu(I), W_{adh} is higher for cISco1Δ95_a-SCPs (orange) compared to non-functionalized SCPs (blue). (b) The W_{adh} of BSA-SCPs (grey) increases clearly in the presence of 1 mM Cu(I) but in the range as its negative control of non-functionalized SCPs (blue). The SCPs' Young's modulus was roughly 10 kPa.

The RICM measurements in Figure 37 (a) show that the presence of 1 mM Cu(I) increases the adhesion energy W_{adh} for a Cox17_c-chip interacting with cISco1Δ95_a-SCPs by around twelvefold (orange). In the negative control for non-functionalized SCPs (blue), W_{adh} also increases under copper addition but to a smaller extent of less than twofold. Testing the interactions of Cox17_c-chips with SCPs (blue) and BSA-functionalised SCPs (grey) (Figure 37 (b)) yield a roughly two-fold increase in adhesion energy. Due to the limitation of resources, measurements with SCPs on the Cox17_c chip surface with 0 mM Cu(I) could not be conducted. However, comparing the two W_{adh} values for 1 mM Cu(I) shows similar behavior. The high standard deviation for the SCPs under 1 mM Cu(I) addition is prominent. Here, the BSA-SCPs function as a negative control of SCPs that were not functionalized with Sco1Δ95_a, i. e. not with a protein with a copper recognition site. The standard deviations are strikingly high, especially for Figure 37 (a) 1 mM Cu(I) for Cox17_c-chip with Sco1Δ95_a-SCPs. The measurements in (a) and (b) were conducted on different days and with SCP batches from different syntheses. Both batches have a low Young's modulus of around 10 kPa.

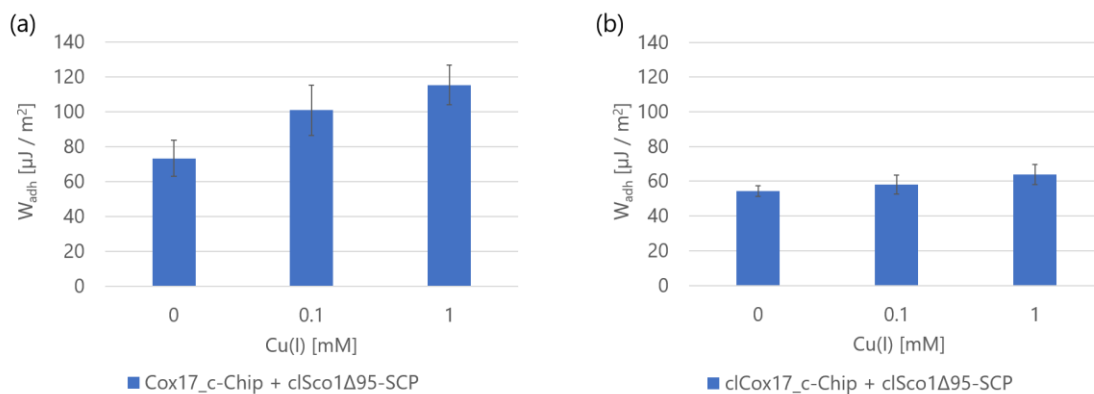


Figure 38. Cu(I)-dependent RICM measurements with different Cox17 and Sco1 protein derivatives.

The adhesion work W_{adh} increases gradually with an increasing Cu(I) concentration. The copper-dependent interactions between clSco1Δ95_a and Cox17_c yields W_{adh} between $73 \pm 10 \mu\text{J} / \text{m}^2$ and $115 \pm 11 \mu\text{J} / \text{m}^2$ for 0 to 1 mM Cu(I). The chip is functionalized with a 5:1 mixture of Ccg-2 and Cox17_c (a). The SCPs in this experiment had Young's modulus of around 10 kPa. The copper-dependent interactions between clSco1Δ95_a and clCox17_c yields W_{adh} between $54 \pm 3 \mu\text{J} / \text{m}^2$ and $64 \pm 6 \mu\text{J} / \text{m}^2$ for 0 to 1 mM Cu(I). The chip is functionalized with 2 μM protein in a 3:1 mixture of clCcg-2 and clCox17_c (b). The SCPs in this experiment had Young's modulus of only around 5 kPa.

Compared to previous measurements, the initial values of W_{adh} in Figure 38 are very high for both (a) and (b). The copper-dependent increase is lower than expected from previous measurements but still clearly visible. Possible reasons could be the functionality of proteins that would influence the chip surface layer formation, the proper exposition of Cox17_c on the chip, the proper exposition of Sco1Δ95_a on the SCPs, or the interaction of Cox17_c and Sco1Δ95_a. However, at least the proteins used in (a) were produced by the standardized methods. They are comparable to the proteins used in the experiments presented in Figure 37.

Moreover, the contact area measured from the microscopy images is the crucial parameter for calculating the adhesion energy W_{adh} and is strongly dependent on the SCP quality and its Young's modulus, which will also decrease with longer storage time depending on the synthesis method. Soft SCPs, i.e., with a low Young's modulus, will yield a high initial W_{adh} value due to its weight, which is, therefore, independent of protein functionalization. Pussak and colleagues (2012) have suggested to use SCPs with Young's modulus ~ 30 kPa for optimal exploitation of their characteristics. Negative control of unfunctionalized SCPs should always be taken along in RICM measurements. They minimize the influence of differently synthesized SCPs and physicochemical changes of the SCPs due to storage. The absolute mean values of W_{adh} cannot yet be compared, only the graph's copper-dependent trend.

The initial test of using all cleaved proteins yielded a low concentration-dependent difference in adhesion energy W_{adh} (Figure 38 (b)). cCox17_c and cCcg-2 were produced by TEV-cleavage after a denatured protein purification and followed by protein refolding with the redox-refolding buffer. The yield was meager, which is why the final protein content of the solution used for chip functionalization was rather 2 μ M with a ratio of 3:1 than the typically used 6 μ M protein content with a ratio of 5:1. The used concentration might be too low for proper surface layer formation, resulting in improper displaying of the copper-binding domain of Cox17 on the surface and too few possible interactions between Cox17_c and Sco1 Δ 95_a to have a visible and measurable impact on the SCP deformation. Additionally, the used SCPs only had Young's modulus of 5 kPa, which appears to result in SCPs too soft for proper RCM measurements.

4 DISCUSSION AND FURTHER PROSPECTIVES

In this study, the SCP-RICM assay was employed to develop a detector system based on an indirect analyte detection by the interaction of two analyte-binding partners as a novel field of application. The protein hydrophobin was used to form a robust self-assembled layer on the chip surface, spiked with fusion proteins of one analyte-binding partner. The second analyte-binding partner was bound to a polymeric soft colloidal probe (SCP) *via* EDC/NHS chemistry. The analyte is not directly linked to any of the detector's components but is free in solution. The chip surface coating method employs the self-assembling characteristic of the class I hydrophobin Ccg-2 forming a stable and monomer layer. The protein that functions as the binding partner is fused to Ccg-2 molecules by genetic engineering, enabling the displaying of the analyte-interacting binding site. In this study, the method was tested exemplarily for the analyte copper(I) and derivatives of the two proteins yCox17 and ySco1, which interact copper-dependent. Consequently, this method opens up the possibility to detect another large range of analytes.

4.1 DISCUSSION: SCP-RICM ASSAY AND PROTEIN-PROTEIN INTERACTION

The results from the SCP-RICM assay measurements presented in Ch. 3.5 show successful copper detection. The adhesion energy W_{adh} at the interface of SCP and glass chip surface increases with copper addition. The detector components, i.e., the glass chip and the SCPs, were functionalized with a derivative of the copper chaperone yCox17 – here called Cox17_c – and a derivative of the copper-binding trans-membrane protein ySco1 – here called Sco1 Δ 95_a with the truncated 95 aa transmembrane domain. Both copper-binding proteins were derived from the respective yeast proteins, which are located in the mitochondrial intermembrane space and inner membrane, respectively, of *Saccharomyces cerevisiae* (*S. cerevisiae*). They were expressed with a His-tag and a TEV cleavage site for Sco1 Δ 95_a and additionally with a fused hydrophobin Ccg-2 from *N. crassa* for Cox17_c (Ch. 2.3). The Ccg-2 is exploited to self-assemble at interfaces, like the hydrophilic/hydrophobic solid/air interface at the glass chip surface. *In vivo*, the soluble copper chaperone yCox17 can bind one Cu(I) ion (Voronova et al. 2007) and transfers it to ySco1, which is tethered to the inner membrane, using an oxidative release mechanism (Banci et al. 2006). This Cu(I) transfer has also been shown to function *in vitro* (Horng et al. 2004). There are discrepancies in the literature about the ySco1 copper-binding mechanism. While studies report ySco1 to be a specific Cu(I) transporter with affinities comparable to the human version hSco1 $K_{D, Cu(I)} \approx 0.1$ fM (Nittis et al. 2001), it has also been implied to favor Cu(II) with $K_{D, Cu(II)} \approx 1$ pM over Cu(I) with $K_{D, Cu(I)} \approx 10$ μ M. The latter is comparable with the affinity of the *B. subtilis* version BsSco (Xu et al. 2015).

However, yCox17 has a very high affinity to copper with $K_{D, Cu(I)} = 13 \text{ fM}$, and no metalation complexes with Cu(II) were reported (Palumaa et al. 2004). Because an interaction-dependent copper-binding is necessary, we would expect that the detection is dependent on Cu(I).

This study shows the transfer of the copper-mediated interaction into the *in vitro* SCP-RICM assay. Copper-dependent RICM measurements with those two proteins yielded an increase in W_{adh} higher than the negative controls' increases. The increase in W_{adh} was calculated, using the JKR model, from the increasing contact area caused by an increasing deformation of the SCP, which results from an increasing number of interactions between the functionalized SCP surface and the functionalized chip surface. The increase in W_{adh} seems to be triggered by the copper-dependent interaction of functional Sco1Δ95_a and Cox17_c. Functionalizing the glass chips only with 5 μM Cox17_c – i.e., without adding pure Ccg-2 – did not show a copper-dependent increase in W_{adh} (data not shown). One possible explanation is that the hydrophobin part of Cox17_c of the fusion protein has to stack very closely to form a monolayer. As a result, the Cox17 part will face upwards and be very close next to each other. The results imply that the Cox17 part's function of interacting with copper is disabled under those conditions. The densely-packed Cox17 proteins might sterically hinder each other, making it impossible for the copper-binding pockets to work correctly. Ccg-2 added in an appropriate amount facilitates the monolayer formation and functions as spacers between Cox17_c proteins. Here, a ratio of 5:1 between Ccg-2 and Cox17_c was found appropriate.

In the copper-dependent RICM measurements, the initial values for 0 mM Cu(I) yielded quite different W_{adh} values throughout the presented results in Figure 37 and Figure 38 for both protein-covered and uncovered SCPs. It is anticipated that these differences level out when the used SCPs always have at least nearly the same chemical and physical parameters. These could be influenced by many parameters, such as their synthesis method, settings throughout the synthesis, suitability for storage, and storage time and include parameters like the same Young's modulus, COOH-group density on the SCP surface, and the SCP diameters.

Standard deviations

Standard deviations of the measurements are very high (Ch. 3.5). An increase in the number of measurements n would improve the standard deviations since they are proportional to $\frac{1}{\sqrt{n}}$. The here presented mean values were typically derived from 15 data points. Using the mean value and the standard deviation implies an underlying normal distribution, i.e., asymmetric, bell-shaped distribution of data-points around the arithmetic mean. However, it is also conceivable that the SCP's deformation instead follows a positively skewed distribution rather than a normal distribution. Forces from the interacting

proteins cause deformation. The SCP's stiffness, though, physically restricts the deformation and the contact area's increase. The SCP movement is biased, with large statistical outliers only possible towards the direction of free movement of the SCP, meaning towards small or no contact areas, away from the surface. The median could rather be calculated to achieve high robustness against outliers. A typical representation of the median is the boxplot. The solid line marks the position of the median, the box (also called interquartile range, IQR) marks the range between the first quartile of 25% of data points that are below that value and the third quartile of 75% of data points that are below that value (McGill et al. 1978; Hubert and Vandervieren 2008; Wickham and Stryjewski 2011). A distribution with a non-zero skewness has not been observed for the datasets used for the presented results. Therefore, it was chosen to calculate the well-known mean value and standard deviation for statistic evaluation. One influencing factor could be the low stiffness of the used SCPs. It has, however, become evident in earlier measurements (data not shown) with stiffer SCPs (Young's modulus of ≥ 20 kPa rather than < 10 kPa) and a large number of data points that the distribution was skewed. Choosing the representation of the median and the quartiles yielded more robust and comparable results. When increasing the statistics supported by automation and increasing the SCPs' stiffness again, the usage of the median and the box plot representation should be considered again.

The calculation of W_{adh} – in this here used analysis method – bases on measuring the contact area's diameter and the SCP's diameter from the images. High image quality is one factor involved in the size of the standard deviation. That includes the image contrast and the right – as in the comparable – focal plane. Both were improved over time, selecting the suitable microscopy objective and filter sets, determining the field diaphragm parameters, and the aperture. That made the images more comparable between different experimenters and should not significantly influence the error anymore.

A second factor to consider is the choice of the evaluation method. The here chosen method of manually measuring the diameter of the SCP and its contact area with the chip surface is very susceptible to errors caused by the person that measures. The contact area, the boundary between the small contact area, and the first bright interference ring is slightly blurry. Therefore, small deviations in measuring the small contact areas of only a few micrometers and the influence on the adhesion energy of the radius of the contact area in the order of six (Eq. (2)) easily cause high standard deviations. Although all measurements were performed only by one person, leading to a decrease of the effect, this will be one major factor for the high standard deviations. An alternative to manually measuring the radius is using the software Radial Profile Finder (Waschke et al. 2019). It automatically finds the position of the SCPs. It compares the fringe pattern from the microscopy image with many theoretical templates (e.g., around 10,000) created by applying physical laws. Finding the best match within the templates makes

it possible to derive the contact area's size and the SCP's size from the best-matching template. As before, those parameters are then used to calculate the adhesion energy. Due to large range parameter screenings it is a computationally expensive method that requires adequate equipment. A significant additional advantage is the fast data acquisition and evaluation, while the manual measurements and the data organization are very time-consuming. At the time of use, the automated evaluation had problems finding the contact areas' correct locations. It was partially due to low image quality and later, due to struggling with the very soft SCPs (≈ 5 kPa) that show high deformation and large contact areas. For those reasons, the manual evaluation of the images was given priority over the standardized, automatic image analysis. Since both mentioned reasons can be forestalled in future measurements, it would be possible to use the Radial Profile Finder software to analyze RICM images.

Influences of the Young's modulus

Furthermore, a reliable determination of Young's modulus of the SCPs would increase the data's quality. So far, Young's modulus has been determined by AFM measurements (Butt et al. 2017; Wang et al. 2017), which are hard to perform on soft SCPs; for example, Young's modulus below 10 kPa (Wang et al. 2017). Correct measurement of Young's modulus and a profound prediction of its behavior with storage time is essential for data comparability of different SCP batches. However, assumed that the mechanical properties of the SCPs from the same batch and during conducting the SCP-RICM assay are the same, the error on Young's modulus is not a statical error but a systematic error and in a linear dependency to W_{adh} . Young's modulus's value does not affect the standard deviations and, therefore, does not affect the data within one set of measurements. Still, it is essential for the comparability of different sets of measurements from different SCP batches or after a particular storage time.

His-tag cleavage

It was shown that the His-tag of the purified proteins could be successfully cleaved at the integrated TEV cleavage site using the AcTEV protease (Ch. 3.2). Using the cleaved Sco1 Δ 95_a protein cSco1 Δ 95_a for the functionalization of the SCPs yields a positive result in the copper-dependent RICM experiments (Figure 38 (a)). All protein constructs possess a His-tag. With its high affinity to coordinate Ni^{2+} , His-tagged proteins can be used in protein purification using Ni^{2+} -affinity chromatography. A downside of this affinity to divalent metals is that the His-tag also has a high affinity to copper (Janson 2011). Considering the SCP-RICM assay, the His-tag could interfere with the copper ions in a solution if the His-tag is exposed on the surface. The exact direction of the His-tag – i.e., buried in the Ccg-2 layer or exposed on the surface – cannot be predicted. Thus, to eliminate possible interference for the copper-dependent SCP-RICM assay, all involved protein constructs should be cleaved. While Sco1 Δ 95_a has worked in the

SCP-RICM assay, the implementation of cICcg-2 and cICox17_c has not yet yielded the expected results (Figure 38, (b)). One significant parameter that needs adjustment was the available concentration of both cICcg-2 and cICox17_c at this point. After purification under denaturing conditions and subsequent TEV-cleavage and removal of the cleaved-off His-tag and the His-tagged protease, the protein yield is low. The concentration available for the chip functionalization (around 1 μ M instead of the usual 3 or 5 μ M protein content) could have possibly been too small so that no homogeneous chip layer could assemble. That would also complement the contact angle measurements testing the protein content needed for a layer formation (for details see Ch. 3.3.2, Figure 31), supporting the suggestion to use 3 or 5 μ M protein content rather than only 1 μ M. As a first step, the experiment should be repeated with a ratio of 5:1 of cICcg-2 to cICox17_c and a protein content of 5 μ M.

Testing Cox17_b and Cu(II)

Initial measurements also indicate that Cox17_b-chips functionalized with a typical ratio between Ccg-2 and Cox17_b and 5 μ M protein content combined with Sco1 Δ 95_a-SCPs yielded an apparent increase in W_{adh} when adding the Cu(I) solution. And so does adding Cu(II) (here: oxidized Cu(I) solution) to the system (data not shown). The negative controls were not conducted, testing the impact of Cu(I)Cl and Cu(II)Cl on the W_{adh} for measurements of the Cox17_c-chip and the Cox17_b-chip, respectively, with SCPs without protein functionalization. It would be interesting to repeat those experiments with the respective controls to test further the influence of Cox17_b instead of the Cox17_c and Cu(II)Cl solution instead of the Cu(I)Cl solution. The latter would be expected to have a Cu(II)-triggered increase in W_{adj} , which is, however, smaller than the Cu(I)-triggered increase. It has been shown in earlier studies that ySco1 can bind both Cu(I) and Cu(II) (Nittis et al. 2001; Balatri et al. 2003). It could bind Cu(II) *in vivo* if there was an excess of Cu(II) in the intermembrane space, but it shall only receive one Cu(I) ion from yCox17 (Horng et al. 2005). Furthermore, cleaved protein cCox17_b should be tested. Cleaving the His-tag ensures no interference of the 6xHis residues with copper ions. It would also display the unstructured N-terminal in solution, leaving it free for target recognition (Heaton et al. 2000).

Control experiments

A series of RICM experiments are necessary to understand and validate the suggested mechanism fully. Initial experiments of the complete SCP-RICM assay of Cox17_c-chips and Sco1 Δ 95_a-SCPs with copper-dependent measurements were shown in Figure 38. The analysis of the copper-dependency should be deepened. The results imply a monotonously increasing relation between copper addition and adhesion energy W_{adh} between 0 and 1 mM. A detection limit should be found by scanning different ranges of copper concentrations with the SCP-RICM assay. There are control experiments that still need to be

conducted. Some control experiments, however, have been presented in Ch. 3.5, and some could not yet be conducted.

One of those control experiments, for example, is the RICM assay with a non-functionalized chip and non-functionalized SCPs (data not shown). The SCP's heavy mass generates small contact areas. This behavior is real for freshly and well-cleaned chip surfaces following the presented protocol in Ch. 2.7.1. Older and less cleaned chip surfaces show more significant contact areas with large standard deviations, which could be traced back to increased unspecific interactions. Furthermore, the effect of increasing contact areas for SCPs with decreasing Young's modulus (Butt et al. 2017) can be seen. This experiment could be complemented by testing the copper-dependent behavior of the interaction between a non-functionalized chip and non-functionalized SCPs.

Another series of control experiments are conducting the SCP-RICM assay with only one of the key-components functionalized. The results in Figure 37 without and with copper on a Cox17_c-functionalized chip but non-functionalized SCPs (blue) show that a contact area at 0 mM Cu(I) is visible and seemed increased in measurements with functionalized SCPs. Adding copper increases the contact area and therefore also the interaction between chip and SCP, i.e., the adhesion energy W_{adh} , is increased. A probable explanation is the sandwich-like structure formation where Cox17_c weakly interacts with copper, which is also to some extent coordinated by the COOH-residues on the SCP surface. However, this interaction should have a small to no impact on the adhesion energy when Sco1Δ95_a is involved, and it seems to be in line with theory (Figure 37, (a), orange). For further testing, it would also be interesting to measure the copper-dependent behavior of a non-functionalized chip and Sco1Δ95_a-functionalized SCPs.

Another possible and similar setup of the SCP-RICM assay is swapping the protein. A copper-dependent experiment with a Sco1Δ95_b-chip and Cox17_a-SCPs was done once. They imply a very similar, positive result compared to the interaction of Cox17_c and Sco1Δ95_a but are not shown here because of low statistics. It would need repetition for verification.

A vital control experiment is the exchange of one of the copper-interacting proteins. Here, Sco1Δ95_a was exchanged with BSA, which is not known to bind copper (Figure 37 (b)) specifically. An effect of increased contact area and increased adhesion energy W_{adh} could also be seen in this case but in the same order as for the negative control of non-functionalized SCPs.

Further testing of the system could be done with another copper-dependent protein-protein interaction. Like Sco1, the copper-binding transmembrane domain yCox11 is also known to receive copper from yCox17 in the intermembrane space of *S. cerevisiae* (Figure 7) (Horng et al. 2004). yCox17 loads

yCox11 with one Cu(I) ion *via* protein-protein interaction. yCox11 then interacts with the Cu_B center of COX. The copper-mediated binding between yCox11 and yCox17 is weaker than between ySco1 and yCox17 (Carr et al. 2002; Banci et al. 2004; Radin et al. 2018). RICM experiments with Cox17_c-chips and Cox11_a-SCPs would be expected to yield an apparent copper-dependent increase in W_{adh} , which is, however, lower than the one measurable for Cox17_c and Sco1Δ95_a. The protein constructs of the soluble truncate of yCox11 that was also found to bind copper (Carr et al. 2002; Carr et al. 2005), of yCox11 were already generated in a different work (Thielemann 2019) but could not be tested in the SCP-RICM assay up to now.

Changing the analyte is another parameter of the SCP-RICM assay that would substantiate the SCP-RICM assay's functionality and specificity. So far, only Cu(I)Cl, which was stabilized by reducing agents, and Cu(II)Cl were tested. It has been shown that yCox17 binds Ag(I) in the same way as Cu(I), but a lower affinity is suspected. Furthermore, Zn(II) has an affinity to the fully reduced yCox17 (Palumaa et al. 2004). Additionally, typical alternative bivalent metal ions to test are cobalt and nickel. However, the increase in W_{adh} should be significantly less compared to copper as the analyte. According to theory, the interaction of ySco1 and yCox17 is triggered by a high-affinity complexation of copper ions (Horng et al. 2004; Banci et al. 2008).

Different possible setups of changing the functionalization or the analytes of detection will be explored in the following chapters.

4.2 OUTLOOK AND FURTHER PROSPECTS

4.2.1 Heterologous Protein Expression and Purification: Methods, Cleavage and Refolding

Successful heterologous protein expression in *E. coli* was shown for the hydrophobin Ccg-2, for derivatives of the yeast copper chaperones yCox17 (Cox17_a) and ySco1 (Sco1Δ95_a), and their fusion proteins with the hydrophobin Ccg-2 (Cox17_b, Cox17_c, Sco1Δ95_b, and Sco1Δ95_c) (Ch. 3.1). The subsequent protein purification *via* immobilized metal affinity chromatography (IMAC) is a well-established method (Charlton and Zachariou 2007), as is its specific adaption of Ni²⁺ affinity chromatography for His-tagged proteins (Hochuli et al. 1987; Spriestersbach et al. 2015). The here adapted method used to purify insoluble hydrophobin Ccg-2 samples and the Ccg-2 fusion proteins by denaturation and subsequent refolding after purification has been tested thoroughly (Kwan et al. 2006; Gruner et al. 2012; Hennig et al. 2016). The yield of hydrophobin (fusion) protein after expression in bacteria (*E. coli*) and purification was generally low (Wang et al. 2010; Kirkland and Keyhani 2011) (see below for more detailed remarks).

However, the target proteins Sco1Δ95_a, Cox17_a, Ccg-2, and their fusion proteins Cox17_b, Cox17_c, Sco1Δ95_b, and Sco1Δ95_c were successfully produced for use in further characterization experiments and application in the SCP-RICM assay. Nevertheless, there is still room for improvement in yield, high-quality product and quality control, time efficiency, costs, etc.

Choice of Resin in Ni²⁺ affinity chromatography

It can be time-saving to use pre-loaded Ni-NTA agarose resin, for example, from Serva Electrophoresis GmbH (Germany), due to the missing working step of loading the resin with nickel and subsequent column washing and the run-through time is shorter than for the here typically used His bind® resin from Novagen (Germany). The few times that it was used for native protein purification and His-tagged AcTEV protease removal it seemed to work well. It should, furthermore, be tested for denatured protein purification. It might also be especially recommended to use the pre-loaded Ni-NTA agarose resin to purify metal-binding proteins since the nickel seems to be bound tighter to the resin than when loaded manually. Less or even no nickel contamination can be seen in the later elution fractions in the pre-loaded resin case. Furthermore, it can also be used multiple times, and if necessary, the residual nickel can be removed and the resin re-loaded with fresh nickel solution. The binding capacity of re-loaded resin has not yet been tested.

HPLC - alternative protein purification method to IMAC

An alternative protein purification method to the presented IMAC method is the more automated chromatography method of preparative high-performance liquid chromatography (HPLC) or fast protein liquid chromatography (FPLC) (Niu et al. 2012). It can also be used for native and denatured protein purification (Beers et al. 1997; Banci et al. 2008; Hou et al. 2009; Wang et al. 2010). Its core functionality relies on Ni-loaded resin matrix columns for binding and elution depending on the proteins' affinity to the matrix. Still, it is set up in a closed system. Additionally, a pump applies external high pressure, which speeds up the runtime. Typically, a UV detector is interposed, which generates a close to a life output signal of the protein concentration for small fractions of the flow-through. It can be directly followed by size-exclusion chromatography (SEC) to examine the tertiary and quaternary structure and, therefore, the multimer formation of the target proteins in the purified sample (Wang et al. 2017).

Consequently, using preparative HPLC would be advantageous because of fast runtimes and a more comfortable and faster quick analysis of the elution fractions for subsequent pooling and dialysis. Furthermore, it would be possible to analyze the formation of dimers, multimers, or inclusion bodies if SEC

analysis is placed downstream, which would contribute to a quality increase of the product. Additionally, it would also facilitate the protein-specific adjustment of washing and elution buffers and their necessary volumes to achieve a cleaner protein of higher yield.

Lyophilization: Storage, protein characterization, and quantification

Lyophilization, also called freeze-drying, is a method often used to dehydrate biological samples, such as bacteria (Wessman et al. 2013), yeast (Adeniran et al. 2015), and also proteins (Vocht et al. 1998; Kwan et al. 2008; Zhao et al. 2009). In contrast to dehydration by heat, it maintains the shape and preserves the sample until rehydration. A typical lyophilization process includes freezing the sample with liquid nitrogen, lowering the pressure, which is followed by the sublimation of the ice (Ó'Fágáin 2004). The samples' lyophilization would allow omitting the up-concentration with Vivaspin 20 ultrafiltration columns from Sartorius AG (Germany) (Ch. 2.6.3) of the proteins after elution and before dialysis. The volume at which the protein is eluted is not that significant for the lyophilization process. It is suspected that some proteins will stick to the membrane of the columns, even the proteins from denatured protein purification. This amount is then lost for further usage. Additionally, time and resources would be saved.

If successful lyophilization and re-hydration with recovering all functions are possible, it would be a great tool to improve storage conditions, shelf-time, no or lower protein aggregation over time, protein quantification quality, and comparability between functionalizations and, therefore, also between RCM measurements. A dried sample of the pure, recombinant fusion proteins would create a protein-specific reference curve for the Lowry and Bradford assay, respectively, for more exact protein quantification. It would also improve the comparability between experimentation and used assay components. Finally, it would simplify using a specific protein amount by merely weighing and re-hydrating the dried protein in a buffer of choice. So far, the measured protein concentration has an unknown error, and this concentration of soluble protein in solution will change over time as the aggregation increases. Aggregates can be seen by eye in the centrifugation tube. Therefore, the used protein sample has an altered concentration, which adds a systematic error to the experiment. Alternatively, the concentration must be determined every time before an experiment, which is time- and resource-consuming. It would, therefore, improve the accuracy of the used amount of protein.

His-tag cleavage with AcTEV protease

The proteins Sco1Δ95_a, Cox17_c, and Ccg-2 were shown to be successfully cleaved, removing the His-tag (Ch. 3.2). Thrombin cleavage did not yield any useful protein product (data are not shown). However,

cleavage at the TEV cleavage site using the AcTEV protease, a derivative of the *Tobacco etch virus* protease, provided by Invitrogen AG (USA), was very efficient (Nittis et al. 2001; Banci et al. 2008). The amount of AcTEV protease used in the cleavage assay can probably be further optimized, i.e., decreased. Since the cleavage at room temperature was very efficient, it should also be tested at 4 °C because that is the recommended storage temperature for the proteins. The natively folded proteins during cleavage (here Sco1Δ95_a) are less prone to degradation. However, the output of cleaved, purified protein – especially the ones from denatured purification (Cox17_c and Ccg-2) – has to be increased to be used for surface functionalization for the SCP-RICM assay. Therefore, the protease amount, cleavage temperature, and the elution conditions during the separation process of the His-tag and the His-tagged AcTEV could be altered. If this is not improving the efficiency, the amount of input protein should be increased.

Refolding and Storage

It is known that different proteins require different refolding and storage – also called stabilization – buffers to achieve a high yield and a high quality of properly refolded target protein (Palmer and Wingfield 2004; Wingfield et al. 2014). The redox-refolding buffer (Table 38) was used in a two-step dialysis process as suggested by Kwan and co-workers and adjusted to the needs of refolding the hydrophobin Ccg-2 (Kwan et al. 2006). The same refolding buffer was used to refold the hydrophobin fusion proteins Cox17_b, Cox17_c, Sco1Δ95_b, and Sco1Δ95_c. The refolding buffer should ensure proper refolding of hydrophobin. Solely, 5 mM EDTA was added to facilitate the capturing of nickel ions that were washed out from the Ni-NTA resin-packed columns since they might interfere with the metal-binding sites of the copper chaperones.

Furthermore, the optimal refolding and storage buffer can differ (Baynes et al. 2005; Wang et al. 2017). Optimizing the refolding conditions is a complicated endeavor. Computational limits still require empirical determination of the proper folding parameters and are subject to many studies (Vagenende et al. 2009; Phillips and de la Peña 2011; Coutard et al. 2012; Yamaguchi and Miyazaki 2014; Y. Wang et al. 2017; Lee et al. 2019). One approach by Wang and colleagues (2017) describes a systematical screening of refolding conditions for proteins from inclusion bodies using differential scanning fluorimetry (DSF) guided refolding (DGR). They screened different proteins for pH conditions in the first step and for further additives to help the refolding in a second screening step in 96-well plates. The DSF is based on the fluorescent dye SYPRO Orange's behavior to have a higher binding affinity to folded protein than melted or aggregated proteins. The fluorescent signal is analyzed while altering the temperature between 20 and 90 °C (thermal shift assay, TSA) (Biter et al. 2016). Based on this idea, Lee and colleagues (2019) have published a protocol, including a description to analyze the MeltTraceur Web Software. This protocol has been modified with regards to the experimental needs of the here studied proteins. The

adjusted protocol and preliminary results testing Ccg-2 refolding are shown in Appendix Ch. 7.4. One major obstacle was the preparation of the protein solution. The denatured Ccg-2 from purification first had to be dialyzed to remove unwanted additives like urea and imidazole and highly concentrated to achieve a 1 mg/mL protein concentration. This pretreatment of the sample was very time-consuming and work-intensive, which might have also put a high load on the proteins. For instance, having lyophilized protein would simplify the protein solution preparation immensely. Thus, it has not yet come into effect but shows excellent potential for optimizing the refolding, dialysis, and storage conditions of recombinantly produced Ccg-2, copper chaperones, and their fusion proteins.

A selection of examples of further approaches for protein expression and purification methods

The recombinant expression and purification of hydrophobins have been the central topic of numerous studies. Their application has been tested in the field of electronics (Laaksonen et al. 2010), in microfluidics (Wang et al. 2007), in hydrophobic drug development (Valo et al. 2010), coating of drug nanoparticles (Fang et al. 2014), surface functionalization (Qin et al. 2007; Zhao et al. 2009; Hennig et al. 2016), and many more. The bottleneck for the transfer to an industrial scale is - besides the typically costly production (Häkkinen et al. 2018) - the low expression rate and low yield of high-quality, soluble hydrophobin discussed in this study. The expression host was changed, for example, from bacteria to human, plant, or fungi to target the problem of a low expression rate. The expression in bacterial hosts like here presented in *E. coli* is appealing due to its low demands in cultivation, high growth rate, and well-established. However, the hydrophobins are expressed in a low concentration of only about 10 to 100 mg/L soluble protein or lower (Kirkland and Keyhani 2011; Winandy et al. 2018). In the here presented study, the achieved concentrations of hydrophobin or one of its fusion proteins with Cox17 and Sco1 derivatives, respectively, were typically below 1 mg/mL. While this is very low, it was enough for the following experimental demands on a laboratory scale. The hydrophobins are instead captured in inclusion bodies when expressed in bacteria. They have to be extracted, solubilized through denaturation and refolded after purification (Ch. 2.6.3.2) (Kwan et al. 2006; Kirkland and Keyhani 2011; Hennig et al. 2016). This expression of insoluble proteins presents a significant disadvantage for further upscaling processes. Expression in fungi as functionally homologous host cells is expected to result in the highest quality of the recombinant protein. Still, the overproduction seems challenging, and most of the expressed protein was found cell-bound. The need for further extraction steps makes it rather unappealing to use, for example, *T. reesei* or *S. commune* (Schuurs et al. 1997; Askolin et al. 2001). The yeast expression shows high-quality hydrophobin products (Cregg et al. 2009; Niu et al. 2012) and secretion of the hydrophobins into the culture medium, which already corresponds to a first purification (Cereghino and Cregg 2000; Kottmeier et al. 2012). A high yield strongly depends on the purification

method of up to 300 mg/L pure hydrophobins (Song et al. 2016). The plant-based expression has shown the highest yield of hydrophobin production (Berger and Sallada 2019), and further investigation in that direction has emerged. Remarkable is the expression of the hydrophobin fusion protein GFP-HFBI in tobacco BY-2 suspension cells with a yield of 1.1 g/L soluble protein and successful cryo-preservation of the cultures (Joensuu et al. 2010; Reuter et al. 2014). Those two findings make that technology very attractive for upscaled production and cost-efficient industrial application (Häkkinen et al. 2018). However, an exception is the production of large amounts of the class I hydrophobin fusion proteins H*Protein A and H*Protein B expressed in *E. coli*, which might make it still feasible as a potential host (Wohlleben et al. 2010). Recently, Cheng et al. (2020) presented successful soluble – not yet quantified – production of soluble mutant forms of class I hydrophobin HGFI and class II hydrophobin HFBI in *E. coli*. In the context of the presented work, especially the mutant mHGFI is exciting and would open new possibilities of easier production and purification of class I hydrophobins in *E. coli* as an established expression host (Cheng et al. 2020).

The surfactant-based aqueous two-phase separation (ATPS) using a nonionic surfactant is one of many purification methods for recombinant hydrophobins. It presents an alternative to a chromatographic technique and has shown remarkable results. ATPS exploits hydrophobin's strong separation and assembly behavior at interfaces. More precisely, in the ATPS method, this is the recovery of the aqueous interface when mixing a water-based hydrophobin solution with a water-based nonionic surfactant. Therefore, it presents a hydrophobic selection tool in a one-step purification (Linder et al. 2001). Successful purification using ATPS has, however, not yet been shown for class I hydrophobins.

Furthermore, the class II hydrophobins HFBI, HFBII, and HFBIV have also been used as fusion tags. This approach enables hydrophobin fusion protein purification by phase separation (Linder et al. 2004; Reuter et al. 2016). With this method, it was possible to upscale the purification of recombinant, hydrophobin fusion proteins expressed in a plant cell suspension (Reuter et al. 2014).

4.2.2 Further Analysis of Chip Surface Functionalization

So far, successful functionalization of plane surfaces with class I hydrophobins has been shown, for example for silicon wafers (Gruner et al. 2012), Teflon (Askolin et al. 2006; Kwan et al. 2008), gold (Zhao et al. 2009), stainless steel (Ahlroos et al. 2011; Hakala et al. 2012), PCL (Zhang et al. 2011), multi-walled carbon nanotubes (Wang et al. 2010), and polystyrene (Wang et al. 2010; Hennig et al. 2016; Döring et al. 2019). Here, functionalization with Ccg-2 and its fusion proteins on glass (Askolin et al. 2006; Döring et al. 2019) was chosen as hydrophilic, chemically stable, and transparent chip surface for the SCP-RICM

assay (Pussak et al. 2012; Pussak et al. 2014; Schmidt et al. 2015). The functionalized glass chip was analyzed by the DROPS test, contact angle measurements, and AFM.

The Piranha-cleaned glass chip's protein-functionalization was successful, as the wettability of the surface changes from hydrophilic to hydrophobic when hydrophobic samples were applied, tested with the DROPS test, and with contact angle measurements (Ch. 3.3.1, Ch. 3.3.2). The degree of change in wettability differs between the samples. The chip surfaces that were functionalized with pure Ccg-2 showed the greatest change in wettability, i.e., they are very hydrophobic (Wösten et al. 1994; Winandy et al. 2018). Functionalization with the fusion proteins (Ccg-2 fused to Cox17 or Sco1Δ95) or combinations with Ccg-2 showed differing degrees of hydrophobicity. This variation might be caused by the fusion proteins that might display more or less hydrophilic or hydrophobic patches, respectively. It was visible that the increase in hydrophobicity of the surface was less dominant and the standard deviation increased when the glass surfaces were not Piranha-cleaned or have been stored for a long time of over two months (data not shown). These fluctuations point at the importance of thorough cleaning. Piranha etch removes all organic residues and generates silanol groups (Jonkheijm et al. 2008), producing a highly hydrophilic surface (Hewitt 2007). That should also be achieved by additionally applying oxygen plasma (Pussak et al. 2012; Pussak et al. 2014) or using Piranha etch. Although Piranha cleaning appears to lead to successful chip functionalization, it is recommended to use a different method due to its high risk and the need for cautious handling. Therefore, oxygen plasma cleaning and glass chip cleaning methods like RCA cleaning protocol are often used for gold surfaces (Kern 1970; Uddayasankar and Krull 2013; Raeesazadeh-Sarmazdeh et al. 2017) or dry ice blasting (Kohli 2018; Sherman 2018). Furthermore, the storage conditions could be optimized, testing, for instance, the influence on the shelf-life of drying the glass chip with Ni-gas rather than with compressed air or when freezing the chips in evacuated tubes rather than in an evacuated desiccator.

Further understanding of the protein layer on the glass chip on a microscopic level could be achieved through label-free techniques like quartz crystal-microbalance (QCM) (Hakala et al. 2012; Della Ventura et al. 2016) and ellipsometry (Gruner et al. 2012; Hakala et al. 2012; Della Ventura et al. 2016) to observe the protein-binding ability on the surface and predict a possible layer thickness. Fourier transform infrared (FTIR) spectroscopy and Raman-spectroscopy are more label-free, non-destructive methods, often used combined, to evaluate protein-functionalized surfaces (Wang et al. 2010). Multilayers can be observed, while monolayers also show only a very weak (Vocht et al. 1998), which always presents a particular challenge with only a few nanometer thick hydrophobin monolayers. Therefore, electron microscopic techniques like scanning electron microscopy (SEM) (Janssen et al. 2004; Liu et al. 2019) or transmission electron microscopy (TEM) (Dempsey and Beever 1979; Wessels 1999; Cicatiello et al.

2017) is used mainly for probing the sample's topography. Those techniques can yield nanometer resolution, but the specimen must be prepared on a specific graphene specimen holder (for TEM). Therefore the interface is pre-set, or the dried, functionalized surface has to be sputtered with a thin, heavy metal layer (for SEM). Another widely used technique is AFM (Gruner et al. 2012; Grünbacher et al. 2014; Cicatiello et al. 2017; Kordts et al. 2018; Liu et al. 2019). The here presented results (Ch. 3.3.3) show an AFM analysis of Ccg-2 and a 5:1 ratio of Ccg-2 to Cox17_c-functionalized glass surfaces, while unfortunately the expected rodlet formation for Ccg-2 could not clearly be resolved. Repetition of the AFM measurements might solve that. Measurements on surfaces functionalized with a chosen ratio of Ccg-2 and Sco1Δ95_b or c might be interesting too, since the Sco1 derivative is larger than the Cox17 derivative and might give a clearer insight on a monodispersed distribution of the fusion protein on the functionalized glass surface. In addition, further analysis of the surfaces functionalized with the cleaved proteins cCcg-2 and a chosen ratio of cCcg-2 and cCox17_c are necessary.

4.2.3 Alternative Chip Surface Functionalization Methods

It is widespread to functionalize a solid substrate by surface incubating with the hydrophobin solution. Hydrophobin layer assembly is temperature-dependent, and incubation at 80 °C is recommended for a more stable and more densely-packed hydrophobin layer. However, functional coating at 20 °C has also been shown before for different hydrophobins (Janssen et al. 2004; Santhiya et al. 2010; Rieder et al. 2011). Here, the chip surface exposure with the Ccg-2 protein solution was conducted at room temperature to ensure intact fusion proteins. It can be expected that elevated temperatures lead to denaturation of Cox17 and Sco1Δ95 as a part of the fusion proteins with Ccg-2. The assembly on glass at 20 °C seems sufficiently stable for the used hydrophobin fusion protein mixtures for application. Multiple drying and hydration steps combined with up to two times washing with 2% sodium dodecyl sulfate (SDS) at 80 °C still reversed the surface's wettability (Figure 32). The drop surface transfer method has also been introduced as a simple alternative to solid surface functionalization with hydrophobin solutions (Gruner et al. 2012). It uses the well-assembled hydrophobin layer at the air/water interface, i.e., hydrophobic/hydrophilic. The assembled layer is transferred to the target surface by contact and lifting the layer off. This method seems reasonable for the functionalization of hydrophobic surfaces.

Since the here used target surface is a hydrophilic glass chip, it was chosen to functionalize by incubation. Despite this consideration, Kordts and colleagues (2018) have presented an exciting study on transferring self-assembled hydrophobins from the air/water interface onto a (hydrophilic) mica surface. The impact on class I and class II hydrophobins were compared. The hydrophobin layer transfer was done with the Langmuir-Schaefer (LS) technique (Kordts et al. 2018). The transfer is similar to the

previously described drop surface transfer method but using a Langmuir trough. The assembled interface layer can be compressed and released before the transfer, and the surface tension during transfer can be controlled. The aggregates' shape and size, the layer density, and the uniformity strongly depended on the substrate preparation, the number of compression/release modes, deposition pressure, and the transfer mode. It stresses the necessity of comparable, particular conditions to achieve a reliable surface functionalization (Yu et al. 2008; Kordts et al. 2018).

The surface functionalization process, the purification method, the refolding buffer, the assembling, and the storage conditions ask for parameter tuning according to the hydrophobins' specific needs. However, the fused derivatives of the copper chaperones yCox17 and ySco1 have to be accounted for in the presented approaches. It was shown before (Ch. 3.1) that due to the insoluble expression of Ccg-2 in *E. coli*, the resulting fusion protein is also insoluble, which asks for a protein purification under denaturing conditions, resulting in low yields and the need for proper refolding of those problematic targets. It would be appealing, for instance, to ligate the recombinant proteins (Dawson et al. 1994). The two components of the fusion protein could be produced separately, ligated, and used for glass chip functionalization for the SCP-RICM assay. Necessary conditions for pure His-tagged Ccg-2 have been well-studied, and so have the conditions for expression, purification, and storing of yCox17 and ySco1. Furthermore, different protein construct design and expression might then be obsolete (Ch. 2.3). Examples for protein ligation systems are native chemical ligation (NCL) (Dawson et al. 1994; Conibear et al. 2018), expressed protein ligation (EPL) (Muir et al. 1998; Conibear et al. 2018), peptide hydrazide-based NCL (Fang et al. 2011), and Sortase A-mediated ligation (SML) (Policarpo et al. 2014; Schmidt et al. 2017). The most widely explored and used technique involves inteins (Muir et al. 1998; Xu and Evans 2001; Eryilmaz et al. 2014). Their strict requirement to undergo catalysis prevents the processing of many highly hydrophobic fusion proteins (Mueller et al. 2020), expressed insolubly, and presents challenging folding targets (Stevens et al. 2017). Maybe for that reason, it appears that protein ligation has never been used so far with hydrophobins. However, recently, many intein-free synthesis approaches are being investigated (Fang et al. 2011; Wang 2019; Luo et al. 2020; Qiao et al. 2020). Those studies might open the field also to hydrophobin-involved protein ligation with hydrophobins.

Analogous to the mechanism used in protein purification, the His-tag could be exploited regarding its nickel affinity. If the chip surface was coated with the Ni²⁺-bound NTA matrix, the His-tag proteins could directly be bound to the chip (Cherkouk et al. 2016). Thus, only the protein construct a (Ch. 2.3) – a target protein with His-tag – would be necessary. The difficult hydrophobin handling would be omitted, and the protein could probably be purified in its native form. On the downside, it would not be eligible

in this particular case since copper is the chosen analyte, which would be expected to show a competitive binding behavior with the nickel ions. Furthermore, the significant advantages of high layer stability on the surface and controlling the proteins' spacing through mixing ratios are not given in this case. Regarding the latter, this could lead to sterically hindering of two functional target proteins as it has been implied and discussed before (Ch. 4.1).

It could also be considered to exchange the hydrophobin. One option is to use the mutant mHGFI of class I hydrophobin HGFI from *Grifola frondosa* that Cheng and colleagues (2020) created to exploit further advantages of class I hydrophobins. They claim that their mHGFI, where all eight cysteines are changed to serines, can be expressed soluble in *E. coli* and will still correctly assemble at water/solid interfaces. The soluble expression of mHGFI would also hold hopes up to be soluble as a fusion protein, which would be a great benefit to purify the proteins in their native form without changing the expression host, making the refolding obsolete. Furthermore, the mutant mHFBI (also all eight cysteines changed to serines) of class II hydrophobin HFBI from *Trichoderma reesei* (*T. reesei*) showed expression in a soluble form in *E. coli* and would be a suitable choice. In general, the use of a class II hydrophobin would be a possible alternative to the here used class I hydrophobin Ccg-2. For example, the class II hydrophobins HFBI (Yamasaki et al. 2014) and HFBII from *T. reesei* (Hakanpää et al. 2004) could be used to functionalize hydrophilic glass chips (Grunér et al. 2012). They have been used in a sensor system to modify solid substrates, for example, in an amperometric glucose biosensor (Zhao et al. 2007). They, however, form layers that are less stable than the typical class I hydrophobins. They can be dissolved by detergents (2% SDS), organic solvent (60% EtOH) solutions, or high pressure (Hou et al. 2009). But when considering the possible application in a disposable detector chip, the presented stability might be sufficient. A positive consequence would be that they can be more easily monomerized and kept soluble in solution. Another advantage of HFBI or HFBII would be the more reliable formation of monolayers of class II hydrophobins interfaces in contrast to class I hydrophobins that tend to form multilayers (Linder et al. 2005).

4.2.4 SCP-RICM Assay: Data Acquisition and Evaluation

When copper is present in the sample solution, the two copper chaperone derivatives of Sco1 and Cox17 interact and form a contact area at the deformed SCP interface and the transparent RICM chip surface. The contact area and the emerging interference rings can be visualized *via* RIC microscopy. Some challenges during the experimental procedure and further potential have already been discussed before. For details on measured copper-dependency, standard deviations, comparison of manual and

software-aided evaluation, and necessary control experiments, see Ch. 4.1. Beyond the presented considerations, there are some more prospects for further experiments that can be proposed.

Ideally, this novel biosensor should be made available as an inexpensive, portable, on-site device (Ch. 1.1). Unfortunately, the biggest limitations, the high-quality objective (high NA) along with the necessary shielding from scattered light, could not yet be overcome. Those pre-requisites are necessary to achieve an interference pattern with high contrast and accurate contact area determination. As a result, the high-quality objective elevates the price, and the shielding from scattered light demands a bulky casing making it unattractive for field applications. However, it could be possible that a typical inverted microscope, available in analytic laboratories, can be used for conducting the SCP-RICM assay with an optional upgrade with, for example, the necessary filter set or similar. That way, the SCP-RICM assay would still be possible to use, expanding the range of applications of the inverted microscope and putting the sensor system's advantages forward. Those would be an easy-to-handle system with no need for highly trained personnel. Furthermore, it is a relatively fast assay of about 2 h for measuring the sample and a control sample and for its analysis. Those parameters are valid, presuming that the sample solution does not need further pre-treatment, the functionalized chip surface and functionalized SCPs are ready to use, and an automated data analysis is possible.

Automated image acquisition would present a significant improvement. The software AxioVision from the Zeiss microscope (Carl Zeiss Microscopy GmbH), used in this study, provides a tool named MosaicX. This tool enables the automated acquisition of $n \times m$ images. It can be corrected for any linear shift in z-direction between the field of views. It had already worked well for the bright field microscopy; imaging the SCPs to measure their radius R . Finding the exact focal plane is crucial for measuring the correct contact area and making automated image acquisition more challenging. The image quality must be good enough to be evaluated with the Radial Profile Finder (Waschke et al. 2019). When combining the recently achieved contrast with new SCPs with a higher Young's modulus (≥ 20 kDa), which is better suitable for software-aided analysis, it should be possible to use the automated image acquisition. The automated image acquisition would facilitate time-efficient measurements and a simple increase of data points to increase the statistics.

Another improvement towards faster data acquisition is the possibility of not having to measure the radius of each SCP. Once the microfluidic synthesis of the SCPs (Ch. 1.3.2) is robust and reliable, the radii's deviation should not affect the measurement. Already now, the SCP radii are quite comparable for the SCPs synthesized in a microfluidic chip. The SCPs from one batch and measured on one day had a mean radius with a relative error between 3.2 – 3.5% (Suppl. 7.5, Figure 45). In contrast, a part of this error was probably introduced by manually measuring the radius. Depending on the average quality of

the SCPs and the number of data points acquired, it should still be considered to check each SCP in bright field mode for irregularities and impurities.

4.2.5 SCP-RICM Assay: Copper Detection

The copper detection of Cu(I) ions *via* protein-protein interactions using the SCP-RICM assay has been shown in this study (Ch. 3.5). The initial results imply a copper-dependent protein interaction of Cox17 and Sco1 that causes the deformation of SCPs and an increase in adhesive surface energy (W_{adh}): the more copper in the Cu(I)-buffer, the higher the deformation. Some necessary control experiments were already discussed in Ch. 4.1.

There cannot yet be a limit of detection deduced from the data. The applied Cu(I) concentrations still have to be closely screened for the low concentration regime between 0 and 100 μ M. Copper detectors with the lowest value of the linear regime of 1.1 μ M (Copper Assay Kit from Merck KGa) or detection limits (also limit of detection, LOD) as low as 100 nM (Tag et al. 2007; He et al. 2019) and even 5.4 nM (Abdulazeez et al. 2018) have been presented. The linear interval of the calibration curve for concentration measurements, which often corresponds to a sigmoidal fit, allows reliable prediction of the sample's analyte concentration. The lowest measured concentration value in this linear interval is a good measure for a reliable detection limit. However, typically the lower detection limit is given a relation between the measurement of the blank y_{nc} and three times the standard deviation of the blank measurement, which roughly corresponds to a confidence interval of 95%: $LOD = y_{nc} + 3 \cdot \sigma_{nc}$ (Shrivastava and Gupta 2011). For the presented case, one reasonable goal would be a LOD below the accepted limits of drinking water, such as 20 μ M in the USA (USEPA 2009) and 31 μ M in the EU (Rat der Europäischen Union 2017).

Comparing the influence of Cu(I) and Cu(II) would be exciting to test. Cu(I) is relatively unstable in solution under aerobic conditions, as presented here. The added reducing agents, ascorbic acid and TCEP, help to stabilize the Cu(I), but it is still expected always also to have a Cu(II) fraction present in the Cu(I) stock buffer (Table 40) used in the assay. It would be expected that Cu(II) addition increases W_{adh} , as all negative controls seem to affect the interaction between SCP and chip surface. Still, the impact should be lower than for Cu(I) addition. The experiment was conducted, and the Cox17_c-functionalized chip surface was incubated with the Cu(I) buffer. It is known from theory that one Cox17 protein binds one Cu(I) ion but no implication for Cu(II)-binding neither *in vivo* nor *in vitro* experiments have been found (Glerum et al. 1996; Palumaa et al. 2004). The copper solution was carefully removed from the surface, leaving at best no excessive, unbound copper. Adding the Sco1 Δ 95_a-SCPs to the Cu(I)-Cox17_c-chip no – or only a low – amount of copper ions is available to block the copper-binding sites of Sco1 Δ 95_a and

Cox17, and Sco1 can interact highly specific to transfer a Cu(I) ion. It was found that Sco1 can also bind Cu(II) ions when present excessively in solution (Xu et al. 2015). However, the experimental design should prefer the Cu(I)-dependent interaction of the two copper chaperones. If the copper in a sample solution is present as Cu(II), it can easily be reduced to Cu(I) as presented and done here.

4.2.6 Exploiting the SCP-RICM Assay using Protein-Protein Interactions

The usage of two proteins in an analyte-dependent interaction and an indirect analyte detection is the novel feature of the presented SCP-RICM assay application. The detection of copper and the copper-dependent interaction of the two copper chaperones yCox17 and ySco1 was chosen as a proof-of-principle system. The results imply successful copper-detection (Ch. 3.5). There are different proteins and other analytes that could be tested towards a detector-application in the SCP-RICM assay.

For copper detection, the alternative interaction partner of yCox17 in the mitochondrial IM is yCox11. It is a transmembrane protein, anchoring with one alpha-helix into the IM (Banci et al. 2004). The helix can be truncated and its soluble fraction used in the SCP-RICM assay. yCox17 also transfers one Cu(I) ion to yCox11, but their interaction has been reported to be weaker than between yCox17 and ySco1 (Carr et al. 2002; Horng et al. 2004). Therefore, measuring with a Cox17-Cox11 detector, a copper-dependent increase is expected that is clear but lower than for the Cox17-Sco1 detector. Another possible interaction to investigate in this context is the loading of the COX subunit yCox2. ySco1 has been shown responsible for the copper delivery to yCox2 (Lode et al. 2000).

When experimental evidence shows that the assay is sensitive enough to distinguish between interaction partners, it could also be possible to extend the scope of the usage of the copper chaperone interaction in the SCP-RICM assay. Analyzing the static RICM images gives a good impression of the general interaction state of the two proteins. When analyzing the time-dependent change of the interference rings, i.e., the change in the SCP height in respect to the chip surface, it would enable the dynamic evaluation of the protein-protein interaction. Even parameters like the binding strength, analyte-dependent interaction strength, or the binding constant could be retrieved from the data. The SCP has a known shape and, therefore, a predictable circular fringe pattern. This is why the dynamic behavior can be studied by calculating the height of the SCP from the fringe pattern – or the degree of deformation from the contact area – and comparing the frame-to-frame difference. It is claimed to achieve a height resolution of 3 nm for the absolute height and 0.4 nm for the relative height, respectively, i.e., subpixel accuracy (Robert et al. 2008; Limozin and Sengupta 2009). The observable interactions are, however, limited by the frame rate of the used camera. The used camera's maximal frame rate (AxioCam MRm, Carl Zeiss Microscopy GmbH) is 50 frames/s, meaning a 20 ms time-resolution. For low binding affinities

– i.e., high dissociation rates – of only $K_D = 10 \mu\text{M}$ as proposed for the Cu(I)-ySco1 complex, the dwell time (the time between two dissociation events) is about $\tau_{\text{dwell}} = 1 \text{ ms}$ (Kastritis and Bonvin 2013; Jarmoskaite et al. 2020). As proposed for the Cu(I)-yCox17 complex of around $K_D \sim 10 \text{ fM}$, the dwell time of high-affinity interactions calculates to $\tau_{\text{dwell}} = 10^6 \text{ s}$, which bears other experimental challenges. The binding affinity of the yCox17-ySco1 complex or even the Cu(I)-yCox17-ySco1 complex during copper transfer is unknown yet.

Further protein interaction partners could be investigated in this bulk experiment. Examples are the human antioxidant protein hAtox1 that transfers copper ions from the high-affinity copper uptake protein Ctr1 to the copper pump ATPaseA (Hatori and Lutsenko 2016; Hatori et al. 2017), possible crosstalk between hAtox1 and the human copper chaperone for superoxide dismutase (hCcs) (Petzoldt et al. 2015), or hCcs that acquires Cu(I) ions from the membrane transporter Ctr1 and transfers them to Cu, Zn superoxide dismutase (hSod1) (Banci et al. 2012; Fetherolf et al. 2017; Fetherolf et al. 2017), just to mention a few possible candidates with partially unclear interactions in the context of copper-dependent behavior.

As another example of two proteins directly and explicitly interacting with the target, the possible detection of bacteriophages with the SCP-RICM assay could be mentioned. They were associated with many diseases like diphtheria, pulmonary infections, cholera, and many more but have also raised medical application attention as biotechnologically engineered for bacterial infection therapy. Many bacteriophages with multiple receptors displayed on their surface and their different receptor-binding proteins have been found (Silva et al. 2016; Takeuchi et al. 2016; Letarov and Kulikov 2017). This structure could be employed in the SCP-RICM assay by functionalizing the SCPs with a receptor and the chip surfaces with the corresponding receptor-binding proteins. It could assist the detection and characterization of, for example, bacteriophages which are typically detected and enumerated with the more time-consuming double agar overlay assay (DLA) (Ács et al. 2020).

Furthermore, other metal ions like mercury, lead, zinc, and cadmium would be interesting to detect in analogy to using copper chaperones (Andruzzi et al. 2005; Banci et al. 2006). When reaching the aquatic ecosystem in high quantities, they can present an immense health threat by elevating the number of antibiotic-resistant bacterial pathogens (Imran et al. 2019). Another environmental issue is the increased incidence of so-called microplastics from all areas spanning from agriculture to cosmetics. It appears to have a major impact, such as in environmental health, aquatic organisms, bacteria, and humans on a cellular level (Rocha-Santos 2018; Prata et al. 2020). It is proposed to be a great future challenge to balance economic and industrial innovation and regulations to ensure environmental safety (Mitrano and Wohlleben 2020). By definition, microplastics are plastic particles – typically spheres

– with sizes from 0.1 μm to 5 mm and below a diameter of 100 nm they are called nanoplastics (Rocha-Santos, 2018). It was found that the polyester-polyurethane plastic particles can be enzymatically degraded, for example, by cutinase Tcur1278 from *Thermomonospora curvata* (Islam et al. 2019). Multiple enzymes can dock onto a nanoplastic particle and degrade it by hydrolysis. The detection and the degradation of nanoplastics by cutinase could be transferred to the SCP-RICM assay. A fusion protein of cutinase and class II hydrophobin has already been produced and successfully tested before (Ribitsch et al. 2015). The chip surface could be functionalized with fusion proteins and the SCPs with cutinase *via* EDC/NHS chemistry. The interaction of multiple cutinases with the nanoplastic particle should cause a deformation of the SCP and a measurable contact area. Furthermore, the degradation time could be analyzed by observing the size change of the contact area. The degradation of the nanoplastic should decrease the contact area. The usage of the SCP-RICM assay would add to the existing options to detect and degrade micro- and nanoplastics. There is a potential of expanding its application and it would be intriguing to test.

4.2.7 Exploiting the SCP-RICM Assay with Alternative Interactions

In the presented study, copper ion detection was presented as one possible proof-of-principle system using the analyte-dependent protein-protein interaction. Therefore, it created a novel, indirect detection system in the context of highly controlled chip surface functionalization with hydrophobin fusion proteins and the SCP-RICM assay as the detection method. So far, the SCP-RICM assay has been used in ligand-receptor model systems such as biotin-avidin (Wang et al. 2017), mannose-concanavalin A (Schmidt et al. 2015; Wang et al. 2017; Strzelczyk et al. 2020), and Glyphosate-EPSPS (Rettke et al. 2020). Combining RICM with colloidal probe AFM technique, the mannose-concanavalin A (Pussak et al. 2014) and hyaluronic acid-CD44 cell receptor system (Martin et al. 2016) were tested. Also, adhesion characteristics of proteins on different polymeric surfaces (Martin et al. 2015) were studied. Additionally, an indirect but rather unspecific approach of detecting antibodies exploiting its multiple binding-sites to interact with protein A, binding especially to many different IgG antibodies and the antigen FITC (Strzelczyk et al. 2017). Beyond those examples, further interactions to increase the application spectrum of the SCP-RICM assay could be interesting to test. Some possibilities have also been explored in our recent patent (Hannusch et al. 2020).

Instead of functionalizing both core detection components with proteins, there could also be possible applications with one protein- and one aptamer-functionalized component. An aptamer is a short (< 100 bases) DNA or RNA single strand, which has come to increasing attention over the last years also for application in a biosensor (so-called aptasensors) (Yoo et al. 2020). It could also be considered to

functionalize the SCPs with avidin *via* EDC/NHS chemistry and then bind biotin-labeled aptamers to avidin in a second step. This method employs the easy biotinylation of DNA and the highly specific interaction of avidin and biotin (Kim Hong and Jang 2020). One example of employing an interaction found in nature is the zinc finger protein for the indirect detection of zinc. Zinc fingers are proteins from a large group of proteins with various interaction partners (DNA, RNA, some proteins, etc.) and functions (Cassandri et al. 2017; Kluska et al. 2018). A protein can possess multiple zinc domains, while each domain usually coordinates one zinc ion (Zn^{2+}) through histidine and cysteine ligands by forming a stable, finger-like shaped zinc-finger structure. With a high affinity and specificity, this structure can bind to DNA (and in some cases also RNA) sequences (Laity et al. 2001). Transferring this interaction into the SCP-RICM detection system, an isolated zinc finger domain could be immobilized as a hydrophobin fusion protein to one component, e.g., the chip surface. The functionalized chip surface could be incubated with the Zn^{2+} solution. Bringing it into contact with the DNA-functionalized SCPs would trigger an interaction resulting in a contact area. This method would enable the indirect detection of Zn^{2+} ions.

An alternative option to aptamers but also synthetic receptors is the usage of small (3 – 5 nm) molecularly imprinted polymers (MIPs) (Naseri et al. 2020). Their high affinity and specificity, especially for small targets (antibiotics, heavy metals, pesticides), originates from complimentary cavities that function as recognition sites. The vast possibilities for function- and target-specific tuning of the MIPs combined with low development and production costs make them interesting for biosensor application. MIPs have also been found for copper and applied in biosensors (Qi et al. 2017; Wei et al. 2019). One interesting field of a possible application is the detection of the widely present antibiotic tetracycline with MIPs immobilized on a graphite-polyurethane composite electrode (Clarindo et al. 2020). For example, this interaction could be transferred into the SCP-RICM assay as a ligand-receptor detection system, as mentioned at the beginning of this chapter. A novel method for the functionalization of the SCPs or the glass chip would have to be developed since the immobilization of MIPs is not yet straightforward. A competitive binding situation between free tetracycline in solution and immobilized tetracycline on the chip surface with the MIP-SCPs would decrease the contact area.

It is also conceivable to substitute both analyte-specific interacting proteins by, for example, aptamers. For example, one biosensor design targeting the single-stranded DNA Circoviridae viruses with a genome consisting of circular, single-stranded DNA (Breitbart et al. 2017) could be analogous to the ligand-receptor system described above. The ligand would be a DNA sequence (ligand aptamer) specific for the target virus, and the receptor is the complementary DNA strand (receptor aptamer). Both aptamers can interact and cause a large contact area. The virus sample would have to be pretreated to extract the DNA and the chosen fraction of sequence (target aptamer). When the virus is present in the

sample, the target aptamer competes with the ligand aptamer, and the contact area decreases. The binding affinity between receptor and ligand aptamer can be tuned by altering the ligand's sequence, leading to unpaired bases and preferred binding of the receptor aptamer to the target aptamer rather than the ligand aptamer. While there was recently developed a new detection method using real-time fluorescence PCR (Yuan et al. 2020), the standard method to identify for example a novel porcine circovirus is using PCR with subsequent electrophoresis analysis (Palinski et al. 2017). This requires high different laboratory equipment and highly-trained personnel. The SCP-RICM assay would present an additional detection method which is slightly faster and with an assay which is easier to handle. Furthermore, detecting the analyte plasmodium lactate dehydrogenase (pLDH), an antigen and biomarker for malaria, could be another possible biosensor design again taking advantage of the interaction between DNA single strands and their complementary strand. The aptamer pL1 was found to interact specific with pLDH under secondary structure formation (Jeon et al. 2013). The aptamer pL1 could be functionalized on the SCP and its binding partner – the complementary aptamer – functionalized on the chip surface. The two aptamers will favorably interact, causing a high SCP deformation and a large contact area. By pre-incubating the surface with the pLDH sample, some of the pL1 aptamers will be occupied by specific binding of pLDH with the aptamer's secondary structure, which is forming upon target-binding. Consequently, some of the complementary aptamers cannot bind anymore; the contact area is decreased compared to the analyte-free case. These approaches could be extended in an analogous manner. For example, other biomarkers like the interleukin-17 receptor A (IL-17RA) are known to be involved in many autoimmune diseases (Vanden Eijnden et al. 2005), to mention one further example. There are malaria rapid diagnostic tests (RDTs) available for point-of-care applications (Cunningham et al. 2019). Those are practical to handle and fast but only qualitative. They do not eliminate the need of malaria microscopy – the standard method – because of their sensitivity. However, novel reports present quantitative detection methods for highly sensitive and new generation RDTs based of immunological detection (Martíáñez-Vendrell et al. 2020). The SCP-RICM assay would be a similarly time-consuming detection method but without the need of difficult to store and costly antibodies. The usage of DNA aptamers would be an advantage. When the components are prepared and storable, the SCP-RICM assay presents an advantageous and easy-to-handle detection method.

5 SUMMARY

The SCP-RICM assay employs the measurable surface energy (or adhesive work W_{adh}) of a micrometer-sized polymeric sphere (soft colloidal probe, SCP) interacting with a glass chip using reflection interference contrast microscopy (RICM). Depending on those two interacting surfaces' nature and functionalization, the SCP will deform, creating a contact area with the hard glass chip. This contact area is clearly distinguishable from the sphere's interference ring pattern and can be measured. The adhesive surface energy W_{adh} can be calculated from the size of the contact area.

Over the years, the SCP-RICM technique – often in conjunction with colloidal atomic force microscopy – has been extensively studied, for example, ligand-receptor interactions, cell adhesion, or the interaction of proteins on polymeric materials. The SCP-RICM assay has been employed as a detector for antibodies, polymers, and carbohydrates before. This ligand-receptor approach is based on the competitive binding of the receptor with the ligand (analyte) immobilized on the surface and the analyte in solution, which presents a limitation towards target selection. However, there are analytes that cannot or should not be immobilized. The immobilization can be overcome by choosing a two-component analyte-dependent interaction, here presented for the copper (Cu) detection.

The detection of Cu was chosen as a proof-of-concept system. However, detecting metal ions is an essential endeavor because, in excessive amounts, they present a severe threat to health and the environment. The copper-dependent interaction of the yeast chaperones yCox17 (also Cox17) and ySco1 (also Sco1) were chosen as the two-component analyte-dependent interaction. The chaperones participate *in vivo* in the formation of the electron transport chain of *S. cerevisiae* and interact in the mitochondrial inner membrane to transfer one Cu(I) ion from Cox17 to Sco1.

It was necessary to immobilize one protein to the SCPs and one to the chip surface, to transfer the copper chaperones' interaction into the SCP-RICM assay core detection components. Consequently, new vectors encoding for derivatives of Cox17 and Sco1 were produced using molecular cloning strategies and expressed in *E. coli*. Additionally, the transmembrane domain (95 amino acids) of Sco1 was truncated (Sco1 Δ 95) to achieve better solubility. A His-tag was added to the protein constructs to enable immunological detection and protein purification with Ni²⁺ affinity chromatography. A TEV cleavage site was added to later optionally cleave the His-tag using the TEV protease. The unique self-assembling characteristics of the class I hydrophobin Ccg-2 from *N. crassa* were used to immobilize one interaction partner to the chip surface. Class I hydrophobins are known for the formation of resistant and uniform layers at hydrophilic/hydrophobic interfaces.

There were three protein constructs designed for each copper chaperone: One for immobilizing to the SCPs (constructs a), one chaperone-hydrophobin fusion protein (constructs b), and one hydrophobin-chaperone fusion protein (constructs c). Molecular cloning of all constructs using the pET system was successful as were the recombinant expression in the *E. coli* strains T7 SHuffle Express *lysY* or Lemo21 (DE3), the solubility analysis, and the native or – if necessary – the denatured protein purification of all the protein constructs and the Ccg-2 protein construct (Figure 39-1). Expression and purification procedures of each protein construct were optimized regarding the following criteria: different expression temperatures, times, and *E. coli* strains; the effect of adding L-Rhamnose to the Lemo21 (DE3) expression; adaptation of the purification conditions; and the dialysis buffers. It was found that all Cox17 constructs and Sco1Δ95_a can be expressed in a soluble form. The availability of pure protein and the chance of burying the His-tag in the assembled Ccg-2 layer make construct c favorable. Consequently, Ccg-2, Sco1Δ95_a, and Cox17_c were chosen for elaborate testing with the SCP-RICM assay.

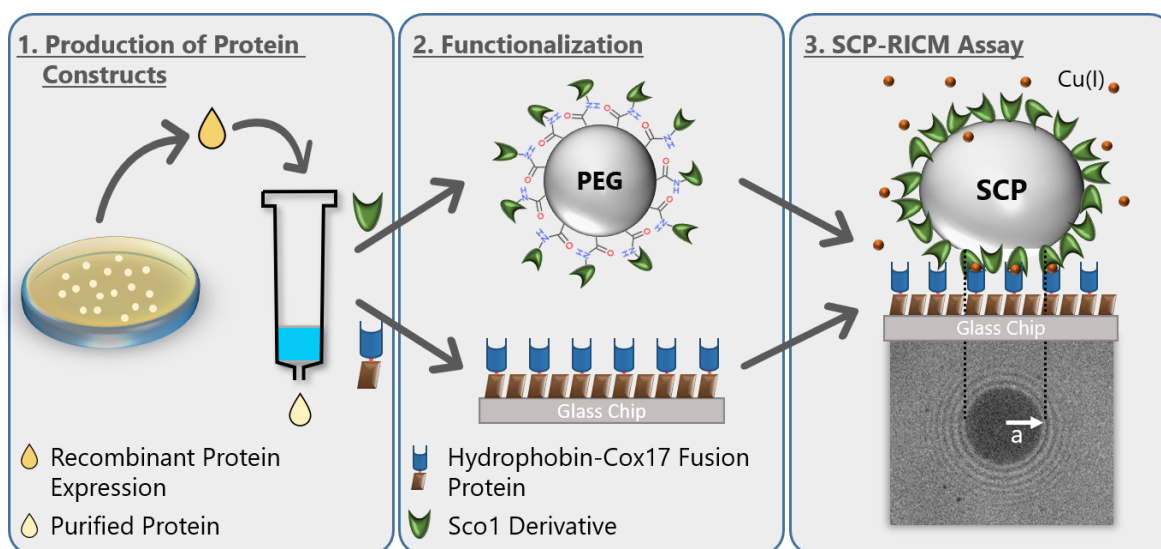


Figure 39. Schematic description of the work.

The protein constructs of the interaction partners were produced through molecular cloning, recombinant expression in *E. coli*, and subsequent protein purification *via* Ni²⁺ affinity chromatography (1). Suitable protein constructs were identified. The PEG spheres (SCPs) were functionalized with Sco1Δ95_a (green), and the glass chip was functionalized with hydrophobin and Cox17_c (fusion protein of hydrophobin (brown) and Cox17 (blue)) (2). The detector components are joined to measure the Cu(I) content of a solution with the SCP-RICM assay (3). Sco1 and Cox17 interact Cu(I)-dependent, and the contact area with radius *a* increases with increasing copper concentration.

Further, one of the interaction proteins – here shown for Sco1Δ95_a – has to be immobilized onto the PEG SCPs, which was done *via* EDC/NHS chemistry (Figure 39-2). The SCPs were received ready-to-use and functionalized with COOH-residues. The protein functionalization was shown to work successfully by FITC-staining, and the coating appeared evenly throughout the SCP's surface. This coupling method results in a randomized orientation of the proteins on the SCP surface, allowing only a fraction of the immobilized proteins to participate in the copper-dependent interaction with Cox17_c, immobilized on the chip surface.

The glass chip was thoroughly cleaned with Piranha etch to ensure a highly hydrophilic surface without any disturbances. The surface was functionalized with hydrophobin Ccg-2 because it self-assembles to form a stable, homogeneous monolayer at hydrophilic/hydrophobic interfaces. A ratio of 5:1 of hydrophobin to Cox17-hydrophobin fusion protein (here Cox17_c) and a 3-6 μM protein content were found to be suitable parameters for surface functionalization (Figure 39-2). The mixing of pure hydrophobin with the fusion protein is supposed to create a certain distance between the Cox17 proteins to prevent sterical hindering during copper-binding and transfer. This way, Cox17 should be monodispersed on the glass chip.

Initial SCP-RICM assay measurements with Sco1Δ95_a-SCPs and the Cox17_c-chips indicate that copper detection using the proposed mechanism is possible (Figure 39-3). Measurements can be differentiated between 0 and 0.1 mM Cu(I) concentration in solution. Further screening of concentrations below 0.1 mM is still necessary. The presented proof-of-principle system for the indirect detection of copper shows copper-dependent behavior. These positive results give rise to many more options to use the SCP-RICM assay as an indirect detection system. The application range of the SCP-RICM assay could be enlarged for different analytes such as other heavy metals, bacteriophages, biomarkers, *et cetera*, and is relevant for fields from medicine to environmental monitoring.

6 BIBLIOGRAPHY

- Abajian C, Rosenzweig AC. 2006. Crystal structure of yeast Sco1. *J Biol Inorg Chem*. 11(4):459–466. doi:10.1007/s00775-006-0096-7. [accessed 2018 Jan 25].
- Abajian C, Yatsunyk LA, Ramirez BE, Rosenzweig AC. 2004. Yeast Cox17 solution structure and copper(I) binding. *J Biol Chem*. 279(51):53584–53592. doi:10.1074/jbc.M408099200. [accessed 2018 Jan 25].
- Abdulazeez I, Basheer C, Al-Saadi AA. 2018. A selective detection approach for copper(II) ions using a hydrazone-based colorimetric sensor: spectroscopic and DFT study. *RSC Adv*. 8(70):39983–39991. doi:10.1039/C8RA08807A. [accessed 2019 Oct 4].
- Ács N, Gambino M, Brøndsted L. 2020. Bacteriophage Enumeration and Detection Methods. *Front Microbiol*. 11:1-15. doi:10.3389/fmicb.2020.594868. [accessed 2021 Apr 3].
- Adducci BA, Gruszeński HA, Khatibi PA, Schmale DG. 2016. Differential detection of a surrogate biological threat agent (*Bacillus globigii*) with a portable surface plasmon resonance biosensor. *Biosens Bioelectron*. 78:160–166. doi:10.1016/j.bios.2015.11.032. [accessed 2016 Apr 4].
- Adeniran A, Sherer M, Tyo KEJ. 2015. Yeast-based biosensors: Design and applications. *FEMS Yeast Res*. 15(1):1-15. doi:10.1111/1567-1364.12203. [accessed 2020 Dec 31].
- Ahlroos T, Hakala TJ, Helle A, Linder MB, Holmberg K, Mahlberg R, Laaksonen P, Varjus S. 2011. Biomimetic approach to water lubrication with biomolecular additives. *Proc Inst Mech Eng Part J J Eng Tribol*. 225(10):1013–1022. doi:10.1177/1350650111406635. [accessed 2021 Jan 1].
- Akyilmaz E, Yorganci E, Asav E. 2010. Do copper ions activate tyrosinase enzyme? A biosensor model for the solution. *Bioelectrochemistry*. 78(2):155–160. doi:10.1016/j.bioelechem.2009.09.007. [accessed 2019 Sep 8].
- Andruzzi L, Nakano M, Nilges MJ, Blackburn NJ. 2005. Spectroscopic Studies of Metal Binding and Metal Selectivity in *Bacillus subtilis* BSco, a Homologue of the Yeast Mitochondrial Protein Sco1p. *J Am Chem Soc*. 127(47):16548–16558. doi:10.1021/ja0529539. [accessed 2021 Jan 29].
- Arnesano F, Balatri E, Banci L, Bertini I, Winge DR. 2005. Folding studies of Cox17 reveal an important interplay of cysteine oxidation and copper binding. *Structure*. 13(5):713–722. doi:10.1016/j.str.2005.02.015. [accessed 2017 Aug 8]
- Askolin S, Linder M, Scholtmeijer K, Tenkanen M, Penttilä M, de Vocht ML, Wösten HAB. 2006. Interaction and comparison of a class I hydrophobin from *Schizophyllum commune* and class II Hydrophobins *Trichoderma reesei*. *Biomacromolecules*. 7(4):1295–1301. doi:10.1021/bm050676s. [accessed 2021 Jan 1].
- Askolin S, Nakari-Setälä T, Tenkanen M. 2001. Overproduction, purification, and characterization of the *Trichoderma reesei* hydrophobin HFBI. *Appl Microbiol Biotechnol*. 57:124–130. doi:10.1007/s002530100728. [accessed 2020 Dec 30].

- Bagherian G, Arab Chamjangali M, Shariati Evari H, Ashrafi M. 2019. Determination of copper(II) by flame atomic absorption spectrometry after its preconcentration by a highly selective and environmentally friendly dispersive liquid-liquid microextraction technique. *J Anal Sci Technol*. 10(3):1-15. doi:10.1186/s40543-019-0164-6. [accessed 2021 Jan 22].
- Balatri E, Banci L, Bertini I, Cantini F, Ciofi-Baffoni S. 2003. Solution Structure of Sco1: A Thioredoxin-like Protein Involved in Cytochrome c Oxidase Assembly. *Structure*. 11:1431–1443. doi:10.1016/j.str.2003.10.004. [accessed 2019 Aug 16].
- Banci L, Bertini I, Calderone V, Ciofi-Baffoni S, Mangani S, Martinelli M, Palumaa P, Wang S. 2006. A hint for the function of human Sco1 from different structures. *Proc Natl Acad Sci*. 103(23):8595–8600. doi:10.1073/pnas.0601375103. [accessed 2021 Jan 29].
- Banci L, Bertini I, Cantini F, Ciofi-Baffoni S, Gonnelli L, Mangani S. 2004. Solution structure of Cox11, a novel type of beta-immunoglobulin-like fold involved in CuB site formation of cytochrome c oxidase. *J Biol Chem*. 279(33):34833–9. doi:10.1074/jbc.M403655200. [accessed 2019 Feb 18].
- Banci L, Bertini I, Cantini F, Kozyreva T, Massagni C, Palumaa P, Rubino JT, Zovo K. 2012. Human superoxide dismutase 1 (hSOD1) maturation through interaction with human copper chaperone for SOD1 (hCCS). *Proc Natl Acad Sci USA*. 109(34):13555–13560. doi:10.1073/pnas.1207493109. [accessed 2021 Jan 28].
- Banci L., Bertini I, Ciofi-Baffoni S, Hadjiloi T, Martinelli M, Palumaa P. 2008. Mitochondrial copper(I) transfer from Cox17 to Sco1 is coupled to electron transfer. *Proc Natl Acad Sci*. 105(19):6803–6808. doi:10.1073/pnas.0800019105. [accessed 2018 Nov 14].
- Banci L, Bertini I, Ciofi-Baffoni S, Janicka A, Martinelli M, Kozlowski H, Palumaa P. 2008. A structural-dynamical characterization of human Cox17. *J Biol Chem*. 283(12):7912–20. doi:10.1074/jbc.M708016200. [accessed 2017 Jul 27].
- Banci L, Bertini I, Ciofi-Baffoni S, Leontari I, Martinelli M, Palumaa P, Sillard R, Wang S. 2007. Human Sco1 functional studies and pathological implications of the P174L mutant. *Proc Natl Acad Sci*. 104(1):15–20. doi:10.1073/pnas.0606189103. [accessed 2017 Jul 27].
- Barros MH, Johnson A, Tzagoloff A. 2004. COX23, a Homologue of COX17, Is Required for Cytochrome Oxidase Assembly. *J Biol Chem*. 279(30):31943–31947. doi:10.1074/JBC.M405014200. [accessed 2019 Aug 18].
- Baynes BM, Wang DIC, Trout BL. 2005. Role of arginine in the stabilization of proteins against aggregation. *Biochemistry*. 44(12):4919–4925. doi:10.1021/bi047528r. [accessed 2021 Jan 8].
- Bayry J, Aïmanianda V, Guijarro JI, Sunde M, Latgé J-P. 2012. Hydrophobins—Unique Fungal Proteins. *PLoS Pathog*. 8(5):e1002700. doi:10.1371/journal.ppat.1002700. [accessed 2019 Jul 17].
- Beers J, Glerum DM, Tzagoloff A. 1997. Purification, characterization, and localization of yeast Cox17p, a mitochondrial copper shuttle. *J Biol Chem*. 272(52):33191–33196. doi:10.1074/jbc.272.52.33191. [accessed 2017 Jul 27].

- Bell-Pedersen D, Dunlap JC, Loros JJ. 1992. The *Neurospora* circadian clock-controlled gene, *ccg-2*, is allelic to *eas* and encodes, a fungal hydrophobin required for formation of the conidial rodlet layer. *Genes Dev.* 6(12A):2382–2394. doi:10.1101/gad.6.12a.2382. [accessed 2017 Jul 30].
- Berger BW, Sallada ND. 2019. Hydrophobins: multifunctional biosurfactants for interface engineering. *J Biol Eng.* 13(10):1-8. doi:10.1186/s13036-018-0136-1. [accessed 2019 Feb 7].
- Biter AB, De La Peña AH, Thapar R, Lin JZ, Phillips KJ. 2016. DSF Guided Refolding As A Novel Method Of Protein Production. *Sci Rep.* 6:1-9. doi:10.1038/srep18906. [accessed 2021 Jan 9].
- Bode M, Woellhaf MW, Bohnert M, van der Laan M, Sommer F, Jung M, Zimmermann R, Schroda M, Herrmann JM. 2015. Redox-regulated dynamic interplay between Cox19 and the copper-binding protein Cox11 in the intermembrane space of mitochondria facilitates biogenesis of cytochrome c oxidase. *Mol Biol Cell.* 26(13):2385–401. doi:10.1091/mbc.E14-11-1526. [accessed 2019 Aug 18].
- Bradford MM. 1976. A rapid and sensitive method for the quantitation of microgram quantities of protein utilizing the principle of protein-dye binding. *Anal Biochem.* 72(1–2):248–254. doi:10.1016/0003-2697(76)90527-3. [accessed 2020 Dez 27].
- Buchwald P, Krummeck G, Rödel G. 1991. Immunological identification of yeast SCO1 protein as a component of the inner mitochondrial membrane. *Mol Gen Genet.* 229(3):413–420. doi:10.1007/BF00267464. [accessed 2019 Aug 18].
- Burnette WN. 1981. Western Blotting: Electrophoretic transfer of proteins from sodium dodecyl sulfate-polyacrylamide gels to unmodified nitrocellulose and radiographic detection with antibody and radioiodinated protein A. *Anal Biochem.* 112(2):195–203. doi:10.1016/0003-2697(81)90281-5. [accessed 2021 Jan 16].
- Butt HJ, Kappl M. 2010. Contact Mechanics and Adhesion. In: *Surface and Interfacial Forces*. Weinheim, Germany: Wiley-VCH Verlag GmbH & Co. KGaA. p. 219–250. [accessed 2016 Jul 7].
- Butt HJ, Pham JT, Kappl M. 2017. Forces between a stiff and a soft surface. *Curr Opin Colloid Interface Sci.* 27:82–90. doi:10.1016/j.cocis.2016.09.007. [accessed 2016 Jul 7].
- Carr HS, George GN, Winge DR. 2002. Yeast Cox11, a protein essential for cytochrome c oxidase assembly, is a Cu(I)-binding protein. *J Biol Chem.* 277(34):31237–31242. doi:10.1074/jbc.M204854200. [accessed 2021 Jan 6].
- Carr HS, Maxfield AB, Horng Y-C, Winge DR. 2005. Functional Analysis of the Domains in Cox11. *J Biol Chem.* 280(24):22664–22669. doi:10.1074/jbc.M414077200. [accessed 2018 Jan 9].
- Casanueva-Marengo MJ, Díaz-de-Alba M, Herrera-Armario A, Galindo-Riaño MD, Granado-Castro MD. 2020. Design and optimization of a single-use optical sensor based on a polymer inclusion membrane for zinc determination in drinks, food supplement and foot health care products. *Mater Sci Eng C.* 110:1-9. doi:10.1016/j.msec.2020.110680. [accessed 2021 Jan 9].
- Cassandri M, Smirnov A, Novelli F, Pitolli C, Agostini M, Malewicz M, Melino G, Raschellà G. 2017. Zinc-

finger proteins in health and disease. *Cell Death Discov.* 3:17071. doi:10.1038/cddiscovery.2017.71. [accessed 2019 Jan 10].

Cereghino JL, Cregg JM. 2000. Heterologous protein expression in the methylotrophic yeast *Pichia pastoris*. *FEMS Microbiol Rev.* 24(1):45–66. doi:10.1111/j.1574-6976.2000.tb00532.x. [accessed 2020 Dec 30].

Chan HN, Tan MJA, Wu H. 2017. Point-of-care testing: Applications of 3D printing. *Lab Chip.* 17(16):2713–2739. doi:10.1039/c7lc00397h. [accessed 2021 Jan 21].

Chang HJ, Lee M, Na S. 2019. Investigation of the role hydrophobin monomer loops using hybrid models via molecular dynamics simulation. *Colloids Surfaces B Biointerfaces.* 173:128–138. doi:10.1016/j.colsurfb.2018.09.062. [accessed 2019 Jul 23].

Charlton A, Zachariou M. 2007. Immobilized metal ion affinity chromatography of native proteins. *Methods Mol Biol.* 421:25–35. doi:10.1007/978-1-59745-582-4_2. [accessed 2020 Dec 30].

Cheng Y, Wang B, Wang Yanyan, Zhang H, Liu C, Yang L, Chen Z, Wang Yinan, Yang H, Wang Z. 2020. Soluble hydrophobin mutants produced in *Escherichia coli* can self-assemble at various interfaces. *J Colloid Interface Sci.* 573:384–395. doi:10.1016/j.jcis.2020.04.012. [accessed 2021 Jan 1].

Cherkouk C, Rebohle L, Lenk J, Keller A, Ou X, Laube M, Neuber C, Haase-Kohn C, Skorupa W, Pietzsch J. 2016. Controlled immobilization of His-tagged proteins for protein-ligand interaction experiments using Ni²⁺-NTA layer on glass surfaces. *Clin Hemorheol Microcirc.* 61(3):523–539. doi:10.3233/CH-151950. [accessed 2021 Feb 1].

Chinenov YV. 2000. Cytochrome c oxidase assembly factors with a thioredoxin fold are conserved among prokaryotes and eukaryotes. *J Mol Med.* 78(5):239–242. doi:10.1007/s001090000110. [accessed 2019 Sep 17].

Cicatiello P, Dardano P, Pirozzi M, Gravagnuolo AM, De Stefano L, Giardina P. 2017. Self-assembly of two hydrophobins from marine fungi affected by interaction with surfaces. *Biotechnol Bioeng.* 114(10):2173–2186. doi:10.1002/bit.26344. [accessed 2021 Jan 4].

Clarindo JES, Viana RB, Cervini P, Silva ABF, Cavalheiro ETG. 2020. Determination of Tetracycline Using a Graphite-Polyurethane Composite Electrode Modified with a Molecularly Imprinted Polymer. *Anal Lett.* 53(12):1932–1955. doi:10.1080/00032719.2020.1725540. [accessed 2021 Mar 1].

Cobine PA, Pierrel F, Winge DR. 2006. Copper trafficking to the mitochondrion and assembly of copper metalloenzymes. *Biochim Biophys Acta - Mol Cell Res.* 1763(7):759–772. doi:10.1016/j.bbamcr.2006.03.002. [accessed 2018 May 24].

Conibear AC, Watson EE, Payne RJ, Becker CFW. 2018. Native chemical ligation in protein synthesis and semi-synthesis. *Chem Soc Rev.* 47(24):9046–9068. doi:10.1039/c8cs00573g. [accessed 2021 Jan 3].

Corvis Y, Walcarius A, Rink R, Mrabet NT, Rogalska E. 2005. Preparing Catalytic Surfaces for Sensing Applications by Immobilizing Enzymes via Hydrophobin Layers. *Anal Chem.* 77(6):1622–1630.

doi:10.1021/ac048897w. [accessed 2020 Dec 30].

Coutard B, Danchin EGJ, Oubelaid R, Canard B, Bignon C. 2012. Single pH buffer refolding screen for protein from inclusion bodies. *Protein Expr Purif.* 82(2):352–359. doi:10.1016/J.PEP.2012.01.014. [accessed 2019 Aug 19].

Cregg JM, Tolstorukov I, Kusari A, Sunga J, Madden K, Chappell T. 2009. Expression in the Yeast *Pichia pastoris*. In: *Methods in Enzymology*. Vol 463. Cambridge, USA: Academic Press Inc. p. 169–189. [accessed 2021 Jan 14].

Culotta VC, Klomp LW, Strain J, Casareno RL, Krems B, Gitlin JD. 1997. The copper chaperone for superoxide dismutase. *J Biol Chem.* 272(38):23469–72. doi:10.1074/jbc.272.38.23469. [accessed 2019 Aug 17].

Cunningham J, Jones S, Gatton ML, Barnwell JW, Cheng Q, Chiodini PL, Glenn J, Incardona S, Kosack C, Luchavez J, et al. 2019. A review of the WHO malaria rapid diagnostic test product testing programme (2008-2018): Performance, procurement and policy. *Malar J.* 18(1):387. doi:10.1186/s12936-019-3028-z. [accessed 2021 Apr 5].

Dawson PE, Muir TW, Clark-Lewis I, Kent SBH. 1994. Synthesis of proteins by native chemical ligation. *Science* (80-). 266(5186):776–779. doi:10.1126/science.7973629. [accessed 2021 Jan 3].

Dempsey GP, Beever RE. 1979. Electron microscopy of the rodlet layer of *Neurospora crassa* conidia. *J Bacteriol.* 140(3):1050–1062. doi:10.1128/jb.140.3.1050-1062.1979. [accessed 2021 Jan 2].

Döring J, Rettke D, Rödel G, Pompe T, Ostermann K. 2019. Surface Functionalization by Hydrophobin-EPSPS Fusion Protein Allows for the Fast and Simple Detection of Glyphosate. *Biosensors.* 9(3):1-18. doi:10.3390/bios9030104. [accessed 2019 Oct 2].

Drummond TG, Hill MG, Barton JK. 2003. Electrochemical DNA sensors. *Nat Biotechnol.* 21(10):1192–1199. doi:10.1038/nbt873. [accessed 2021 Mar 4].

Vanden Eijnden S, Goriely S, De Wit D, Willems F, Goldman M. 2005. IL-23 up-regulates IL-10 and induces IL-17 synthesis by polyclonally activated naive T cells in human. *Eur J Immunol.* 35(2):469–475. doi:10.1002/eji.200425677. [accessed 2021 Jan 31].

Ejeian F, Etedali P, Mansouri-Tehrani H-A, Soozanipour A, Low Z-X, Asadnia M, Taheri-Kafrani A, Razmjou A. 2018. Biosensors for wastewater monitoring: A review. *Biosens Bioelectron.* 118:66–79. doi:10.1016/J.BIOS.2018.07.019. [accessed 2019 Aug 19].

Ekim Kocabey A, Kost L, Gehlhar M, Rödel G, Gey U. 2019. Mitochondrial Sco proteins are involved in oxidative stress defense. *Redox Biol.* 21:101079. doi:10.1016/J.REDOX.2018.101079. [accessed 2019 Jul 25].

Elbert DL. 2011. Liquid–liquid two-phase systems for the production of porous hydrogels and hydrogel microspheres for biomedical applications: A tutorial review. *Acta Biomater.* 7(1):31–56. doi:10.1016/j.actbio.2010.07.028. [accessed 2021 Jan 16].

- Erickson HP. 2009. Size and shape of protein molecules at the nanometer level determined by sedimentation, gel filtration, and electron microscopy. *Biol Proced Online*. 11:32–51. doi:10.1007/s12575-009-9008-x. [accessed 2019 Sep 4].
- Eryilmaz E, Shah NH, Muir TW, Cowburn D. 2014. Structural and dynamical features of inteins and implications on protein splicing. *J Biol Chem*. 289(21):14506–11. doi:10.1074/jbc.R113.540302. [accessed 2018 Aug 14].
- Fang G, Tang B, Liu Z, Gou J, Zhang Y, Xu H, Tang X. 2014. Novel hydrophobin-coated docetaxel nanoparticles for intravenous delivery: In vitro characteristics and in vivo performance. *Eur J Pharm Sci*. 60:1–9. doi:10.1016/j.ejps.2014.04.016. [accessed 2019 Jul 24].
- Fang GM, Li YM, Shen F, Huang YC, Li J Bin, Lin Y, Cui HK, Liu L. 2011. Protein chemical synthesis by ligation of peptide hydrazides. *Angew Chemie - Int Ed*. 50(33):7645–7649. doi:10.1002/anie.201100996. [accessed 2021 Jan 3].
- Fetherolf MM, Boyd SD, Taylor AB, Kim HJ, Wohlschlegel JA, Blackburn NJ, Hart PJ, Winge DR, Winkler DD. 2017. Copper-zinc superoxide dismutase is activated through a sulfenic acid intermediate at a copper-ion entry site. *J Biol Chem*. 292(29):12025–12040. doi:10.1074/jbc.M117.775981. [accessed 2021 Jan 3].
- Fetherolf M, Boyd SD, Winkler DD, Winge DR, Kieffer S, Perrot M, Boucherie H, Toledano MB, Labarre J, Sideris D, et al. 2017. Oxygen-dependent activation of Cu,Zn-superoxide dismutase-1. *Metallomics*. 7:22480–22489. doi:10.1039/C6MT00298F. [accessed 2017 Jul 27].
- Fischer NO, Tarasow TM, Tok JBH. 2007. Aptasensors for biosecurity applications. *Curr Opin Chem Biol*. 11(3):316–328. doi:10.1016/j.cbpa.2007.05.017. [accessed 2021 Jan 21].
- Flake MM, Nguyen PK, Scott RA, Vandiver LR, Kuntz Willits R, Elbert DL. 2011. Poly(ethylene glycol) microparticles produced by precipitation polymerization in aqueous solution. *Biomacromolecules*. 12(3):844–850. doi:10.1021/bm1011695. [accessed 2021 Jan 16].
- La Fontaine S, Mercer JFB. 2007. Trafficking of the copper-ATPases, ATP7A and ATP7B: Role in copper homeostasis. *Arch Biochem Biophys*. 463(2):149–167. doi:10.1016/j.abb.2007.04.021. [accessed 2019 Aug 17].
- Furukawa Y, Lim C, Tosha T, Yoshida K, Hagai T, Akiyama S, Watanabe S, Nakagome K, Shiro Y. 2018. Identification of a novel zinc-binding protein, C1orf123, as an interactor with a heavy metal-associated domain. *PLoS One*. 13(9):e0204355. doi:10.1371/journal.pone.0204355. [accessed 2019 Aug 17].
- Glerum DM, Shtanko A, Tzagoloff A. 1996. Characterization of COX17, a yeast gene involved in copper metabolism and assembly of cytochrome oxidase. *J Biol Chem*. 271(24):14504–9. doi:10.1074/jbc.271.24.14504. [accessed 2019 Sep 17].
- Gomez S, Urrea I, Valiente R, Rodriguez F. 2010. Spectroscopic study of Cu(2+) and Cu(+) ions in high-transmission glass. Electronic structure and Cu(2+) /Cu(+) concentrations. *J Phys Condens Matter*. 22(29):1–7. doi:10.1088/0953-8984/22/29/295505. [accessed 2021 Jan 21].

- González-Guerrero AB, Maldonado J, Herranz S, Lechuga LM. 2016. Trends in photonic lab-on-chip interferometric biosensors for point-of-care diagnostics. *Anal Methods*. 8(48):8380–8394. doi:10.1039/c6ay02972h. [accessed 2021 Jan 21].
- Grünbacher A, Throm T, Seidel C, Gutt B, Röhrig J, Strunk T, Vincze P, Walheim S, Schimmel T, Wenzel W, et al. 2014. Six hydrophobins are involved in hydrophobin rodlet formation in *Aspergillus nidulans* and contribute to hydrophobicity of the spore surface. *PLoS One*. 9(4):e94546. doi:10.1371/journal.pone.0094546. [accessed 2019 Jul 17].
- Gruner LJ, Ostermann K, Rödel G. 2012. Layer thickness of hydrophobin films leads to oscillation in wettability. *Langmuir*. 28(17):6942–9. doi:10.1021/la204252y. [accessed 2018 Apr 13].
- Grunér MS, Szilvay GR, Berglin M, Lienemann M, Laaksonen P, Linder MB. 2012. Self-assembly of class II hydrophobins on polar surfaces. *Langmuir*. 28(9):4293–4300. doi:10.1021/la300501u. [accessed 2021 Jan 4].
- Hahne K, Rödel G, Ostermann K. 2021 Jan 18. A fluorescence-based yeast sensor for monitoring acetic acid. *Eng Life Sci.:elsc.202000006*. doi:10.1002/elsc.202000006. [accessed 2021 Jan 21].
- Haider SR, Reid HJ, Sharp BL. 2012. Tricine-SDS-PAGE In: *Protein Electrophoresis*. 869. Totowa, USA: Humana Press. p. 81-91.
- Hakala TJ, Laaksonen P, Saikko V, Ahlroos T, Helle A, Mahlberg R, Hähl H, Jacobs K, Kuosmanen P, Linder MB, et al. 2012. Adhesion and tribological properties of hydrophobin proteins in aqueous lubrication on stainless steel surfaces. *RSC Adv*. 2(26):9867–9872. doi:10.1039/c2ra21018e. [accessed 2021 Jan 1].
- Hakanpää J, Linder M, Popov A, Schmidt A, Rouvinen J. 2006. Hydrophobin HFBI in detail: ultrahigh-resolution structure at 0.75 Å. *Acta Crystallogr Sect D Biol Crystallogr*. 62(4):356–367. doi:10.1107/S09074444906000862. [accessed 2020 Oct 21].
- Hakanpää J, Paananen A, Askolin S, Nakari-Setälä T, Parkkinen T, Penttilä M, Linder MB, Rouvinen J. 2004. Atomic resolution structure of the HFBI hydrophobin, a self-assembling amphiphile. *J Biol Chem*. 279(1):534–9. doi:10.1074/jbc.M309650200. [accessed 2021 Jan 4].
- Hakanpää J, Szilvay GR, Kaljunen H, Maksimainen M, Linder M, Rouvinen J. 2006. Two crystal structures of *Trichoderma reesei* hydrophobin HFBI - The structure of a protein amphiphile with and without detergent interaction. *Protein Sci*. 15(9):2129–2140. doi:10.1110/ps.062326706. [accessed 2019 Jul 23].
- Häkkinen ST, Reuter L, Nuorti N, Joensuu JJ, Rischer H, Ritala A. 2018. Tobacco BY-2 media component optimization for a cost-efficient recombinant protein production. *Front Plant Sci*. 9(45):1-9. doi:10.3389/fpls.2018.00045. [accessed 2020 Dec 30].
- Halliwell B, Gutteridge JMC. 1985. The importance of free radicals and catalytic metal ions in human diseases. *Mol Aspects Med*. 8(2):89–193. doi:10.1016/0098-2997(85)90001-9. [accessed 2019 Aug 17].
- Hannusch L, Rödel G, Dahmann C, Ostermann K, Pompe T, Rettke D, inventors. 2020 Sep 16. Verfahren und Kit zum Nachweis von Toxinen und Pathogenen. DE102020124279.4. [accessed 2020 Sep 24].

- Harrison MD, Jones CE, Solioz M, Dameron CT. 2000. Intracellular copper routing: The role of copper chaperones. *Trends Biochem Sci.* 25(1):29–32. doi:10.1016/S0968-0004(99)01492-9. [accessed 2017 Okt 20].
- Hasan NM, Lutsenko S. 2012. Regulation of Copper Transporters in Human Cells. In: *Metal Transporters*. Cambridge, USA: Academic Press. p. 137-161.
- Hatori Y, Inouye S, Akagi R. 2017. Thiol-based copper handling by the copper chaperone Atox1. *IUBMB Life.* 69(4):246–254. doi:10.1002/iub.1620. [accessed 2019 Sep 3].
- Hatori Y, Lutsenko S. 2016. The Role of Copper Chaperone Atox1 in Coupling Redox Homeostasis to Intracellular Copper Distribution. *Antioxidants.* 5(3):25. doi:10.3390/antiox5030025. [accessed 2017 Jul 20].
- He E, Cai L, Zheng F, Zhou Q, Guo D, Zhou Y, Zhang X, Li Z. 2019. Rapid Quantitative Fluorescence Detection of Copper Ions with Disposable Microcapsule Arrays Utilizing Functional Nucleic Acid Strategy. *Sci Rep.* 9(1):36. doi:10.1038/s41598-018-36842-x. [accessed 2019 Oct 4].
- Heaton D, Nittis T, Srinivasan C, Winge DR. 2000. Mutational analysis of the mitochondrial copper metallochaperone Cox17. *J Biol Chem.* 275(48):37582–37587. doi:10.1074/jbc.M006639200. [accessed 2021 Jan 11].
- Heaton DN, George GN, Garrison G, Winge DR. 2001. The mitochondrial copper metallochaperone Cox17 exists as an oligomeric, polycopper complex. *Biochemistry.* 40(3):743–51. doi:10.1021/bi002315x. [accessed 2019 Sep 17].
- Hennig S, Rödel G, Ostermann K. 2016. Hydrophobin-based surface engineering for sensitive and robust quantification of yeast pheromones. *Sensors.* 16(5). doi:10.3390/s16050602. [accessed 2017 Jul 10].
- Hewitt N. 2007. Silica as a reinforcing filler. In: *Compounding Precipitated Silica in Elastomers*. Cambridge, USA: Elsevier. p. 1–23.
- Hochuli E, Döbeli H, Schacher A. 1987. New metal chelate adsorbent selective for proteins and peptides containing neighbouring histidine residues. *J Chromatogr A.* 411(C):177–184. doi:10.1016/S0021-9673(00)93969-4. [accessed 2020 Dec 30].
- Horng Y-C, Cobine PA, Maxfield AB, Carr HS, Winge DR. 2004. Specific copper transfer from the Cox17 metallochaperone to both Sco1 and Cox11 in the assembly of yeast cytochrome C oxidase. *J Biol Chem.* 279(34):35334–35340. doi:10.1074/jbc.M404747200. [accessed 2018 May 24].
- Horng Y-C, Leary SC, Cobine PA, Young FB, George GN, Shoubridge EA, Winge DR. 2005. Human Sco1 and Sco2 function as copper-binding proteins. *J Biol Chem.* 280(40):34113–34122. doi:10.1074/jbc.M506801200. [accessed 2019 Sep 17].
- Hou S, Li X, Li X, Feng X-Z, Wang R, Wang C, Yu L, Qiao M-Q. 2009. Surface modification using a novel type I hydrophobin HGFI. *Anal Bioanal Chem.* 394(3):783–789. doi:10.1007/s00216-009-2776-y.

[accessed 2019 Jul 24].

Hubert M, Vandervieren E. 2008. An adjusted boxplot for skewed distributions. *Comput Stat Data Anal.* 52(12):5186–5201. doi:10.1016/j.csda.2007.11.008. [accessed 2021 Feb 15].

Imran M, Das KR, Naik MM. 2019. Co-selection of multi-antibiotic resistance in bacterial pathogens in metal and microplastic contaminated environments: An emerging health threat. *Chemosphere.* 215:846–857. doi:10.1016/J.CHEMOSPHERE.2018.10.114. [accessed 2018 Dec 6].

Islam S, Apitius L, Jakob F, Schwaneberg U. 2019. Targeting microplastic particles in the void of diluted suspensions. *Environ Int.* 123:428–435. doi:10.1016/j.envint.2018.12.029.

Jaiswal N, Tiwari I. 2017. Recent build outs in electroanalytical biosensors based on carbon-nanomaterial modified screen printed electrode platforms. *Anal Methods.* 9(26):3895–3907. doi:10.1039/c7ay01276d. [accessed 2021 Jan 21].

Janson J-C. 2011. *Protein Purification: Principles, High-Resolution Methods, and Applications.* 3rd ed. New York, USA: John Wiley & Sons, Inc. p. 532.

Janssen MI, Van Leeuwen MBM, Van Kooten TG, De Vries J, Dijkhuizen L, Wösten HAB. 2004. Promotion of fibroblast activity by coating with hydrophobins in the β -sheet end state. *Biomaterials.* 25(14):2731–2739. doi:10.1016/j.biomaterials.2003.09.060. [accessed 2019 Sep 3].

Jarmoskaite I, AlSadhan I, Vaidyanathan PP, Herschlag D. 2020. How to measure and evaluate binding affinities. *Elife.* 9:1–34. doi:10.7554/eLife.57264. [accessed 2019 Sep 3].

Jeon W, Lee S, DH M, Ban C. 2013. A colorimetric aptasensor for the diagnosis of malaria based on cationic polymers and gold nanoparticles. *Anal Biochem.* 439(1):11–16. doi:10.1016/j.ab.2013.03.032. [accessed 2021 Apr 05].

Joensuu JJ, Conley AJ, Lienemann M, Brandle JE, Linder MB, Menassa R. 2010. Hydrophobin fusions for high-level transient protein expression and purification in *Nicotiana benthamiana*. *Plant Physiol.* 152(2):622–633. doi:10.1104/pp.109.149021. [accessed 2020 Dec 30].

Johnson KL, Kendall K, Roberts AD. 1971. Surface energy and the contact of elastic solids. *Proc R Soc London A Math Phys Sci.* 324(1558):301–313. doi:10.1098/rspa.1971.0141. [accessed 2021 Jan 18].

Johnston M, Kim JH. 2005. Glucose as a hormone: Receptor-mediated glucose sensing in the yeast *Saccharomyces cerevisiae*. In: *Biochemical Society Transactions.* Vol. 33. London, UK: Portland Press. p. 247–252.

Jonkheijm P, Weinrich D, Schröder H, Niemeyer CM, Waldmann H. 2008. Chemical strategies for generating protein biochips. *Angew Chemie - Int Ed.* 47(50):9618–9647. doi:10.1002/anie.200801711. [accessed 2020 Jan 18].

Justino CIL, Freitas AC, Duarte AC, Santos TAP. 2015. Sensors and biosensors for monitoring marine contaminants. *Trends Environ Anal Chem.* 6:21–30. doi:10.1016/j.teac.2015.02.001. [accessed 2020 Jan 18].

- Kallio JM, Linder MB, Rouvinen J. 2007. Crystal Structures of Hydrophobin HFBII in the Presence of Detergent Implicate the Formation of Fibrils and Monolayer Films. *J Biol Chem.* 282(39):28733–28739. doi:10.1074/jbc.M704238200. [accessed 2020 Oct 21].
- Kastritis PL, Bonvin AMJJ. 2013. On the binding affinity of macromolecular interactions: daring to ask why proteins interact. *J R Soc Interface.* 10(79):1–27. doi:10.1098/rsif.2012.0835. [accessed 2015 May 18].
- Kern W. 1970. Cleaning Solution Based on Hydrogen Peroxide for Use in Silicon Semiconductor Technology. *RCA Rev.* 31:187–205. [accessed 2021 Jan 1].
- Kershaw MJ, Talbot NJ. 1998. Hydrophobins and Repellents: Proteins with Fundamental Roles in Fungal Morphogenesis. *Fungal Genet Biol.* 23(1):18–33. doi:10.1006/FGBI.1997.1022. [accessed 2019 Jul 16].
- Kershaw MJ, Wakley G, Talbot NJ. 1998. Complementation of the Mpg1 mutant phenotype in *Magnaporthe grisea* reveals functional relationships between fungal hydrophobins. *EMBO J.* 17(14):3838–3849. doi:10.1093/emboj/17.14.3838. [accessed 2019 Jul 17].
- Khalimonchuk O, Ostermann K, Rödel G. 2005. Evidence for the association of yeast mitochondrial ribosomes with Cox11p, a protein required for the CuB site formation of cytochrome c oxidase. *Curr Genet.* 47(4):223–233. doi:10.1007/s00294-005-0569-1. [accessed 2019 Aug 18].
- Kim Hong PT, Jang C-H. 2020. Sensitive and label-free liquid crystal-based optical sensor for the detection of malathion. *Anal Biochem.* 593:113589. doi:10.1016/j.ab.2020.113589. [accessed 2021 Jan 17].
- Kirkland BH, Keyhani NO. 2011. Expression and purification of a functionally active class I fungal hydrophobin from the entomopathogenic fungus *Beauveria bassiana* in *E. coli*. *J Ind Microbiol Biotechnol.* 38(2):327–335. doi:10.1007/s10295-010-0777-7. [accessed 2020 Dec 30].
- Kluska K, Adamczyk J, Krężel A. 2018. Metal binding properties, stability and reactivity of zinc fingers. *Coord Chem Rev.* 367:18–64. doi:10.1016/J.CCR.2018.04.009. [accessed 2019 Jan 10].
- Kohli R. 2018. Applications of water ice blasting for removal of surface contaminants. In: *Developments in Surface Contamination and Cleaning: Applications of Cleaning Techniques*. Vol 11. Amsterdam, Netherlands: Elsevier. p. 729–764.
- Kordts M, Kampe M, Kerth A, Hinderberger D. 2018. Structure Formation in Class I and Class II Hydrophobins at the Air-Water Interface under Multiple Compression/Expansion Cycles. *ChemistryOpen.* 7(12):1005–1013. doi:10.1002/open.201800176. [accessed 2019 Jan 7].
- Kottmeier K, Günther TJ, Weber J, Kurtz S, Ostermann K, Rödel G, Bley T. 2012. Constitutive expression of hydrophobin HFB1 from *Trichoderma reesei* in *Pichia pastoris* and its pre-purification by foam separation during cultivation. *Eng Life Sci.* 12(2):162–170. doi:10.1002/elsc.201100155. [accessed 2021 Feb 9].
- Kung CT, Gao H, Lee CY, Wang YN, Dong W, Ko CH, Wang G, Fu LM. 2020. Microfluidic synthesis control

technology and its application in drug delivery, bioimaging, biosensing, environmental analysis and cell analysis. *Chem Eng J.* 399:125748. doi:10.1016/j.cej.2020.125748. [accessed 2021 Jan 16].

Kwan AH, Macindoe I, Vukašin P V., Morris VK, Kass I, Gupte R, Mark AE, Templeton MD, Mackay JP, Sunde M. 2008. The Cys3–Cys4 Loop of the Hydrophobin EAS Is Not Required for Rodlet Formation and Surface Activity. *J Mol Biol.* 382(3):708–720. doi:10.1016/j.jmb.2008.07.034. [accessed 2019 Jul 23].

Kwan AHY, Winefield RD, Sunde M, Matthews JM, Haverkamp RG, Templeton MD, Mackay JP. 2006. Structural basis for rodlet assembly in fungal hydrophobins. *Proc Natl Acad Sci.* 103(10):3621–3626. doi:10.1073/pnas.0505704103. [accessed 2018 Nov 2].

Laaksonen P, Kainlahti M, Laaksonen T, Shchepetov A, Jiang H, Ahopelto J, Linder MB. 2010. Interfacial Engineering by Proteins: Exfoliation and Functionalization of Graphene by Hydrophobins. *Angew Chemie Int Ed.* 49(29):4946–4949. doi:10.1002/anie.201001806. [accessed 2019 Jul 25].

Laemmli UK. 1970. Cleavage of structural proteins during the assembly of the head of bacteriophage T4. *Nature.* 227(5259):680–685. doi:10.1038/227680a0. [accessed 2021 Mar 5].

Lahtinen T, Linder MB, Nakari-Setälä T, Oker-Blom C. 2008. Hydrophobin (HFBI): A potential fusion partner for one-step purification of recombinant proteins from insect cells. *Protein Expr Purif.* 59(1):18–24. doi:10.1016/j.pep.2007.12.014. [accessed 2018 Aug 20].

Laity JH, Lee BM, Wright PE. 2001. Zinc finger proteins: New insights into structural and functional diversity. *Curr Opin Struct Biol.* 11(1):39–46. doi:10.1016/S0959-440X(00)00167-6. [accessed 2019 Jan 10].

Lavanant H, Virelizier H, Hoppilliard Y. 1998. Reduction of copper(ii) complexes by electron capture in an electrospray ionization source. *J Am Soc Mass Spectrom.* 9(11):1217–1221. doi:10.1016/S1044-0305(98)00100-7. [accessed 2019 Sep 04].

Leary SC, Sasarman F, Nishimura T, Shoubridge EA. 2009. Human SCO2 is required for the synthesis of CO II and as a thiol-disulphide oxidoreductase for SCO1. *Hum Mol Genet.* 18(12):2230–2240. doi:10.1093/hmg/ddp158. [accessed 2018 Sep 05].

Lee ME, Dou X, Zhu Y, Phillips KJ. 2019. Refolding Proteins from Inclusion Bodies using Differential Scanning Fluorimetry Guided (DGR) Protein Refolding and MeltTraceur Web. *Curr Protoc Mol Biol.* 125(1):e78. doi:10.1002/cpmb.78. [accessed 2019 Aug 19].

Lee MH, Pankratz HS, Wang S, Scott RA, Finnegan MG, Johnson MK, Ippolito JA, Christianson DW, Hausinger RP. 1993. Purification and characterization of *Klebsiella aerogenes* UreE protein: a nickel-binding protein that functions in urease metallocenter assembly. *Protein Sci.* 2(6):1042–52. doi:10.1002/pro.5560020617. [accessed 2019 Aug 17].

Letarov AV., Kulikov EE. 2017. Adsorption of bacteriophages on bacterial cells. *Biochem.* 82(13):1632–1658. doi:10.1134/S0006297917130053. [accessed 2021 Jan 31].

Lévêque C, Ferracci G, Maulet Y, Mazuet C, Popoff MR, Blanchard M-P, Seagar M, El Far O. 2015. An

optical biosensor assay for rapid dual detection of Botulinum neurotoxins A and E. *Sci Rep.* 5:17953. doi:10.1038/srep17953. [accessed 2015 Dec 11].

Limozin L, Sengupta K. 2009. Quantitative Reflection Interference Contrast Microscopy (RICM) in Soft Matter and Cell Adhesion. *ChemPhysChem.* 10(16):2752–2768. doi:10.1002/cphc.200900601. [accessed 2019 Aug 19].

Linder M, Selber K, Nakari-Setälä T, Qiao M, Kula MR, Penttilä M. 2001. The hydrophobins HFBI and HFBII from *Trichoderma reesei* showing efficient interactions with nonionic surfactants in aqueous two-phase systems. *Biomacromolecules.* 2(2):511–517. doi:10.1021/bm0001493. [accessed 2020 Dec 30].

Linder MB, Qiao M, Laumen F, Selber K, Hyytiä T, Nakari-Setälä T, Penttilä ME. 2004. Efficient purification of recombinant proteins using hydrophobins as tags in surfactant-based two-phase systems. *Biochemistry.* 43(37):11873–11882. doi:10.1021/bi0488202. [accessed 2020 Dec 30].

Linder MB, Szilvay GR, Nakari-Setälä T, Penttilä ME. 2005. Hydrophobins: the protein-amphiphiles of filamentous fungi. *FEMS Microbiol Rev.* 29(5):877–896. doi:10.1016/j.femsre.2005.01.004. [accessed 2020 Oct 12].

Littlejohn KA, Hooley P, Cox PW. 2012. Bioinformatics predicts diverse *Aspergillus* hydrophobins with novel properties. *Food Hydrocoll.* 27(2):503–516. doi:10.1016/j.FOODHYD.2011.08.018. [accessed 2019 Jul 17].

Liu Y, Nevanen TK, Paananen A, Kempe K, Wilson P, Johansson L-S, Joensuu JJ, Linder MB, Haddleton DM, Milani R. 2019. Self-Assembling Protein–Polymer Bioconjugates for Surfaces with Antifouling Features and Low Nonspecific Binding. *ACS Appl Mater Interfaces.* 11(3):3599–3608. doi:10.1021/acsami.8b19968. [accessed 2019 Jan 7].

Lode A, Kuschel M, Paret C, Rödel G. 2000. Mitochondrial copper metabolism in yeast: interaction between Sco1p and Cox2p. *FEBS Lett.* 485(1):19–24. doi:10.1016/S0014-5793(00)02176-1. [accessed 2019 Aug 18].

Lowry OH, Rosebrough NJ, Farr AL, Randall RJ. 1951. Protein measurement with the Folin phenol reagent. *J Biol Chem.* 193(1):265–275. doi:10.1016/s0021-9258(19)52451-6. [accessed 2021 Mar 5].

Luo Y, Jiang C, Yu L, Yang A. 2020. Chemical Biology of Autophagy-Related Proteins With Posttranslational Modifications: From Chemical Synthesis to Biological Applications. *Front Chem.* 8:233. doi:10.3389/fchem.2020.00233. [accessed 2021 Jan 3].

Macindoe I, Kwan AH, Ren Q, Morris VK, Yang W, Mackay JP, Sunde M. 2012. Self-assembly of functional, amphipathic amyloid monolayers by the fungal hydrophobin EAS. *Proc Natl Acad Sci.* 109(14):E804–11. doi:10.1073/pnas.1114052109. [accessed 2019 Jul 23].

Martiáñez-Vendrell X, Jiménez A, Vásquez A, Campillo A, Incardona S, González R, Gamboa D, Torres K, Oyibo W, Faye B, et al. 2020. Quantification of malaria antigens PfHRP2 and pLDH by quantitative suspension array technology in whole blood, dried blood spot and plasma. *Malar J.* 19(1):12. doi:10.1186/s12936-019-3083-5. [accessed 2021 Jan 31].

- Martin S, Wang H, Hartmann L, Pompe T, Schmidt S. 2015. Quantification of protein–materials interaction by soft colloidal probe spectroscopy. *Phys Chem Chem Phys*. 17(5):3014–3018. doi:10.1039/C4CP05484A. [accessed 2018 Sep 17].
- Martin S, Wang H, Rathke T, Anderegg U, Möller S, Schnabelrauch M, Pompe T, Schmidt S. 2016. Polymer hydrogel particles as biocompatible AFM probes to study CD44/hyaluronic acid interactions on cells. *Polymer*. 102:342–349. doi:10.1016/j.polymer.2016.02.019. [accessed 2017 Jul 10].
- Maxfield AB, Heaton DN, Winge DR. 2004. Cox17 Is Functional When Tethered to the Mitochondrial Inner Membrane. *J Biol Chem*. 279(7):5072–5080. doi:10.1074/jbc.M311772200. [accessed 2021 Jan 10].
- McGill R, Tukey JW, Larsen WA. 1978. Variations of Box Plots. *Am Stat*. 32(1):12. doi:10.2307/2683468. [accessed 2021 Jan 20].
- Mehrotra P. 2016. Biosensors and their applications - A review. *J Oral Biol Craniofacial Res*. 6(2):153–159. doi:10.1016/j.jobcr.2015.12.002. [accessed 2021 Jan 21].
- Melcher M, Facey SJ, Henkes TM, Subkowski T, Hauer B. 2016. Accelerated Nucleation of Hydroxyapatite Using an Engineered Hydrophobin Fusion Protein. *Biomacromolecules*. 17(5):1716–1726. doi:10.1021/acs.biomac.6b00135. [accessed 2019 Jul 25].
- Mitrano DM, Wohlleben W. 2020. Microplastic regulation should be more precise to incentivize both innovation and environmental safety. *Nat Commun*. 11(1):1–12. doi:10.1038/s41467-020-19069-1. [accessed 2021 Jan 29].
- Moy VT, Jiao Y, Hillmann T, Lehmann H, Sano T. 1999. Adhesion energy of receptor-mediated interaction measured by elastic deformation. *Biophys J*. 76(3):1632–1638. doi:10.1016/S0006-3495(99)77322-4.
- Mueller LK, Baumruck AC, Zhdanova H, Tietze AA. 2020. Challenges and Perspectives in Chemical Synthesis of Highly Hydrophobic Peptides. *Front Bioeng Biotechnol*. 8:162. doi:10.3389/fbioe.2020.00162. [accessed 2021 Jan 3].
- Muir TW, Sondhi D, Cole PA. 1998. Expressed protein ligation: A general method for protein engineering. *Proc Natl Acad Sci*. 95(12):6705–6710. doi:10.1073/pnas.95.12.6705. [accessed 2021 Jan 3].
- Murray BS. 2007. Stabilization of bubbles and foams. *Curr Opin Colloid Interface Sci*. 12(4–5):232–241. doi:10.1016/j.cocis.2007.07.009. [accessed 2020 Sep 28].
- Naseri M, Mohammadniaei M, Sun Y, Ashley J. 2020. The use of aptamers and molecularly imprinted polymers in biosensors for environmental monitoring: A tale of two receptors. *Chemosensors*. 8(2):1–20. doi:10.3390/CHEMOSENSORS8020032. [accessed 2021 Mar 9].
- Nečas D, Klapetek P. 2012. Gwyddion: An open-source software for SPM data analysis. *Cent Eur J Phys*. 10(1):181–188. doi:10.2478/s11534-011-0096-2. [accessed 2020 Sep 30].
- Neumann E, Schaefer-Ridder M, Wang Y, Hofschneider PH. 1982. Gene transfer into mouse lyoma cells by electroporation in high electric fields. *EMBO J*. 1(7):841–845. doi:10.1002/j.1460-2075.1982.tb01257.x. [accessed 2021 Mar 5].

- Niemiec MS, Dingeldein APG, Wittung-Stafshede P. 2015. Enthalpy-entropy compensation at play in human copper ion transfer. *Sci Rep.* 5(1):10518. doi:10.1038/srep10518. [accessed 2018 Jan 25].
- Nittis T, George GN, Winge DR. 2001. Yeast Sco1, a protein essential for cytochrome c oxidase function is a Cu(I)-binding protein. *J Biol Chem.* 276(45):42520–6. doi:10.1074/jbc.M107077200. [accessed 2017 Aug 2].
- Niu B, Wang D, Yang Y, Xu H, Qiao M. 2012. Heterologous expression and characterization of the hydrophobin HFBI in *Pichia pastoris* and evaluation of its contribution to the food industry. *Amino Acids.* 43(2):763–771. doi:10.1007/s00726-011-1126-5. [accessed 2019 Jul 24].
- Nobrega MP, Bandeira SCB, Beers J, Tzagoloff A. 2002. Characterization of COX19, a widely distributed gene required for expression of mitochondrial cytochrome oxidase. *J Biol Chem.* 277(43):40206–40211. doi:10.1074/jbc.M207348200. [accessed 2019 Aug 18].
- Ó'Fágáin C. 2004. Lyophilization of Proteins. In: *Protein Purification Protocols*. Vol 244. 2nd Ed. New Jersey, USA: Humana Press. p. 309–322.
- Ornstein L. 1964. Disc Electrophoresis-I Background and Theory. *Ann N Y Acad Sci.* 121(2):321–349. doi:10.1111/j.1749-6632.1964.tb14207.x. [accessed 2020 Nov 6].
- Palinski R, Piñeyro P, Shang P, Yuan F, Guo R, Fang Y, Byers E, Hause BM. 2017. A Novel Porcine Circovirus Distantly Related to Known Circoviruses Is Associated with Porcine Dermatitis and Nephropathy Syndrome and Reproductive Failure. *J Virol.* 91(1):1-9. doi:10.1128/JVI.01879-16. [accessed 2021 Apr 5].
- Palmer I, Wingfield PT. 2004. Preparation and Extraction of Insoluble (Inclusion-Body) Proteins from *Escherichia coli*. *Curr Protoc Protein Sci.* 38(1):6.3.1-6.3.18. doi:10.1002/0471140864.ps0603s38. [accessed 2021 Jan 8].
- Palumaa P. 2013. Copper chaperones. The concept of conformational control in the metabolism of copper. *FEBS Lett.* 587(13):1902–1910. doi:10.1016/j.febslet.2013.05.019. [accessed 2017 Aug 15].
- Palumaa P, Kangur L, Voronova A, Sillard R. 2004. Metal-binding mechanism of Cox17, a copper chaperone for cytochrome c oxidase. *Biochem J.* 382(1):307–314. doi:10.1042/BJ20040360. [accessed 2017 Aug 15].
- Petris MJ, Mercer JF, Culvenor JG, Lockhart P, Gleeson PA, Camakaris J. 1996. Ligand-regulated transport of the Menkes copper P-type ATPase efflux pump from the Golgi apparatus to the plasma membrane: a novel mechanism of regulated trafficking. *EMBO J.* 15(22):6084–6095. doi:10.1002/j.1460-2075.1996.tb00997.x. [accessed 2019 Aug 17].
- Petzoldt S, Kahra D, Kovermann M, Dingeldein AP, Niemiec MS, Ådén J, Wittung-Stafshede P. 2015. Human cytoplasmic copper chaperones Atox1 and CCS exchange copper ions in vitro. *BioMetals.* 28(3):577–585. doi:10.1007/s10534-015-9832-1. [accessed 2017 Jul 20].
- Pham CLL, Rodríguez de Francisco B, Valsecchi I, Dazzoni R, Pillé A, Lo V, Ball SR, Cappai R, Wien F, Kwan

AH, et al. 2018. Probing Structural Changes during Self-assembly of Surface-Active Hydrophobin Proteins that Form Functional Amyloids in Fungi. *J Mol Biol.* 430(20):3784–3801. doi:10.1016/j.jmb.2018.07.025. [accessed 2019 Jul 23].

Phillips K, de la Peña AH. 2011. The Combined Use of the ThermoFluor Assay and ThermoQ Analytical Software for the Determination of Protein Stability and Buffer Optimization as an Aid in Protein Crystallization. *Curr Protoc Mol Biol.* 94(1):10.28.1-10.28.15. doi:10.1002/0471142727.mb1028s94. [accessed 2021 Jan 8].

Piscitelli A, Cicatiello P, Gravagnuolo AM, Sorrentino I, Pezzella C, Giardina P. 2017. Applications of Functional Amyloids from Fungi: Surface Modification by Class I Hydrophobins. *Biomolecules.* 7(3):1-11. doi:10.3390/biom7030045. [accessed 2019 Jul 24].

Polcarpo RL, Kang H, Liao X, Rabideau AE, Simon MD, Pentelute BL. 2014. Flow-Based Enzymatic Ligation by Sortase A. *Angew Chemie Int Ed.* 53(35):9203–9208. doi:10.1002/anie.201403582. [accessed 2019 Sep 23].

Prata JC, da Costa JP, Lopes I, Duarte AC, Rocha-Santos T. 2020. Environmental exposure to microplastics: An overview on possible human health effects. *Sci Total Environ.* 702:134455. doi:10.1016/j.scitotenv.2019.134455.

Pufahl RA, Singer CP, Peariso KL, Lin S-J, Schmidt PJ, Fahrni CJ, Culotta VC, Penner-Hahn JE, O'Halloran TV. 1997. Metal Ion Chaperone Function of the Soluble Cu(I) Receptor Atx1. *Science.* 278(5339):853–856. doi:10.1126/SCIENCE.278.5339.853. [accessed 2019 Aug 17].

Pussak D, Behra M, Schmidt S, Hartmann L. 2012. Synthesis and functionalization of poly(ethylene glycol) microparticles as soft colloidal probes for adhesion energy measurements. *Soft Matter.* 8(5):1664–1672. doi:10.1039/C2SM06911C. [accessed 2017 Jul 27].

Pussak D, Ponader D, Mosca S, Pompe T, Hartmann L, Schmidt S. 2014. Specific Adhesion of Carbohydrate Hydrogel Particles in Competition with Multivalent Inhibitors Evaluated by AFM. *Langmuir.* 30(21):6142–6150. doi:10.1021/la5010006. [accessed 2018 Sep 17].

Pussak D, Ponader D, Mosca S, Ruiz SV, Hartmann L, Schmidt S. 2013. Mechanical carbohydrate sensors based on soft hydrogel particles. *Angew Chemie - Int Ed.* 52(23):6084–6087. doi:10.1002/anie.201300469. [accessed 2021 Jan 16].

Qi J, Li B, Wang X, Zhang Z, Wang Z, Han J, Chen L. 2017. Three-dimensional paper-based microfluidic chip device for multiplexed fluorescence detection of Cu²⁺ and Hg²⁺ ions based on ion imprinting technology. *Sensors Actuators, B Chem.* 251:224–233. doi:10.1016/j.snb.2017.05.052. [accessed 2020 Sep 14].

Qiao Y, Yu G, Kratch KC, Wang XA, Wang WW, Leeuwon SZ, Xu S, Morse JS, Liu WR. 2020. Expressed Protein Ligation without Intein. *J Am Chem Soc.* 142(15):7047–7054. doi:10.1021/jacs.0c00252. [accessed 2021 Jan 3].

Qin M, Wang LK, Feng XZ, Yang YL, Wang R, Wang C, Yu L, Shao B, Qiao MQ. 2007. Bioactive surface

modification of mica and poly(dimethylsiloxane) with hydrophobins for protein immobilization. *Langmuir*. 23(8):4465–4471. doi:10.1021/la062744h. [accessed 2020 Dec 30].

Qu Y, Wu Y, Wang C, Zhao K, Wu H. 2019. A selective fluorescence probe for copper(II) ion in aqueous solution based on a 1,8-naphthalimide Schiff base derivative. *Zeitschrift für Naturforsch B*. 74(9):665–670. doi:10.1515/znb-2019-0095. [accessed 2021 Jan 22].

Radhika V, Proikas-Cezanne T, Jayaraman M, Onesime D, Ha JH, Dhanasekaran DN. 2007. Chemical sensing of DNT by engineered olfactory yeast strain. *Nat Chem Biol*. 3(6):325–330. doi:10.1038/nchembio882. [accessed 2021 Feb 9].

Radin I, Gey U, Kost L, Steinebrunner I, Rödel G. 2018. The mitochondrial copper chaperone COX11 plays an auxiliary role in the defence against oxidative stress. *bioRxiv*. doi:10.1101/438101. [accessed 2019 Jul 25].

Rädler J, Sackmann E. 1993. Imaging optical thicknesses and separation distances of phospholipid vesicles at solid surfaces. *J Phys II*. 3(5):727–748. doi:10.1051/jp2:1993163. [accessed 2021 Jan 16].

Raeeszadeh-Sarmazdeh M, Parthasarathy R, Boder ET. 2017. Fine-tuning sortase-mediated immobilization of protein layers on surfaces using sequential deprotection and coupling. *Biotechnol Prog*. 33(3):824–831. doi:10.1002/btpr.2449. [accessed 2019 Sep 23].

Rat der Europäischen Union. 2017. Vorschlag für eine Richtlinie des Europäischen Parlaments und des Rates über die Qualität von Wasser für den menschlichen Gebrauch (Neufassung). *J Chem Inf Model*. 110(9):1689–1699. [accessed 2021 Jan 15].

Ren Q, Kwan AH, Sunde M. 2013. Two forms and two faces, multiple states and multiple uses: Properties and applications of the self-assembling fungal hydrophobins. *Biopolymers*. 100(6):601–612. doi:10.1002/bip.22259. [accessed 2019 Jul 23].

Rettke D, Döring J, Martin S, Venus T, Estrela-Lopis I, Schmidt S, Ostermann K, Pompe T. 2020. Picomolar glyphosate sensitivity of an optical particle-based sensor utilizing biomimetic interaction principles. *Biosens Bioelectron*. 165. doi:10.1016/j.bios.2020.112262. [accessed 2020 Aug 15].

Reuter LJ, Ritala A, Linder M, Joensuu JJ. 2016. Novel Hydrophobin Fusion Tags for Plant-Produced Fusion Proteins. *PLoS One*. 11(10):e0164032. doi:10.1371/journal.pone.0164032. [accessed 2019 Jul 25].

Reuter LJ, Bailey MJ, Joensuu JJ, Ritala A. 2014. Scale-up of hydrophobin-assisted recombinant protein production in tobacco BY-2 suspension cells. *Plant Biotechnol J*. 12(4):402–410. doi:10.1111/pbi.12147. [accessed 2020 Dec 29].

Ribitsch D, Acero EH, Przylucka A, Zitzenbacher S, Marold A, Gamerith C, Tscheließnig R, Jungbauer A, Rennhofer H, Lichtenegger H, et al. 2015. Enhanced cutinase-catalyzed hydrolysis of polyethylene terephthalate by covalent fusion to hydrophobins. *Appl Environ Microbiol*. 81(11):3586–3592. doi:10.1128/AEM.04111-14. [accessed 2021 Jan 29].

Rieder A, Ladnorg T, Wöll C, Obst U, Fischer R, Schwartz T. 2011. The impact of recombinant fusion-

hydrophobin coated surfaces on *E. coli* and natural mixed culture biofilm formation. *Biofouling*. 27(10):1073–1085. doi:10.1080/08927014.2011.631168. [accessed 2021 Jan 2].

Robert P, Sengupta K, Puech PH, Bongrand P, Limozin L. 2008. Tuning the formation and rupture of single ligand-receptor bonds by hyaluronan-induced repulsion. *Biophys J*. 95(8):3999–4012. doi:10.1529/biophysj.108.135947. [accessed 2021 Jan 24].

Robinson NJ, Winge DR. 2010. Copper Metallochaperones. *Annu Rev Biochem*. 79(1):537–562. doi:10.1146/annurev-biochem-030409-143539. [accessed 2018 Mar 26].

Rocha-Santos TAP. 2018. Editorial overview: Micro- and nanoplastics. *Curr Opin Environ Sci Heal*. 1:52–54. doi:10.1016/j.coesh.2018.01.003.

Rose AS, Bradley AR, Valasatava Y, Duarte JM, Prlić A, Rose PW. 2018. NGL viewer: web-based molecular graphics for large complexes. *Bioinformatics*. 34(21):3755–3758. doi:10.1093/bioinformatics/bty419. [accessed 2019 Jun 3].

Van Rosmalen M, Krom M, Merckx M. 2017. Tuning the Flexibility of Glycine-Serine Linkers to Allow Rational Design of Multidomain Proteins. *Biochemistry*. 56(50):6565–6574. doi:10.1021/acs.biochem.7b00902. [accessed 2018 Jan 3].

Santhiya D, Burghard Z, Greiner C, Jeurgens LPH, Subkowski T, Bill J. 2010. Bioinspired deposition of TiO₂ thin films induced by hydrophobins. *Langmuir*. 26(9):6494–6502. doi:10.1021/la9039557. [accessed 2021 Jan 2].

Sarparanta M, Bimbo LM, Rytökönen J, Mäkilä E, Laaksonen TJ, Laaksonen P, Nyman M, Salonen J, Linder MB, Hirvonen J, et al. 2012. Intravenous delivery of hydrophobin-functionalized porous silicon nanoparticles: Stability, plasma protein adsorption and biodistribution. *Mol Pharm*. 9(3):654–663. doi:10.1021/mp200611d. [accessed 2021 Jan 2].

Schmidt M, Toplak A, Quaedflieg PJ, Nuijens T. 2017. Enzyme-mediated ligation technologies for peptides and proteins. *Curr Opin Chem Biol*. 38:1–7. doi:10.1016/j.cbpa.2017.01.017. [accessed 2021 Feb 20].

Schmidt S, Wang H, Pussak D, Mosca S, Hartmann L. 2015. Probing multivalency in ligand-receptor-mediated adhesion of soft, biomimetic interfaces. *Beilstein J Org Chem*. 11:720–9. doi:10.3762/bjoc.11.82. [accessed 2018 May 23].

Scholtmeijer K, Janssen MI, Gerssen B, de Vocht ML, van Leeuwen BM, van Kooten TG, Wösten HAB, Wessels JGH. 2002. Surface modifications created by using engineered hydrophobins. *Appl Environ Microbiol*. 68(3):1367–73. doi:10.1128/aem.68.3.1367-1373.2002. [accessed 2019 Jul 17].

Schuurs TA, Schaeffer EAM, Wessels JGH. 1997. Homology-Dependent Silencing of the SC3 Gene in *Schizophyllum commune*. *Genetics Society of America*. [accessed 2020 Dec 30].

Sherman R. 2018. Carbon dioxide snow cleaning applications. In: *Developments in Surface Contamination and Cleaning: Applications of Cleaning Techniques*. Vol 11. Amsterdam, Netherlands:

Elsevier. p. 97–115.

Shrivastava A, Gupta V. 2011. Methods for the determination of limit of detection and limit of quantitation of the analytical methods. *Chronicles Young Sci.* 2(1):21. doi:10.4103/2229-5186.79345. [accessed 2021 Mar 2].

Sies H. 1993. Strategies of antioxidant defense. *Eur J Biochem.* 215(2):213–219. doi:10.1111/j.1432-1033.1993.tb18025.x. [accessed 2019 Aug 17].

Silva JB, Storms Z, Sauvageau D. 2016. Host receptors for bacteriophage adsorption. *FEMS Microbiol Lett.* 363(4). doi:10.1093/femsle/fnw002. [accessed 2021 Jan 31].

Song D, Gao Z, Zhao L, Wang X, Xu H, Bai Y, Zhang X, Linder MB, Feng H, Qiao M. 2016. High-yield fermentation and a novel heat-precipitation purification method for hydrophobin HGFI from *Grifola frondosa* in *Pichia pastoris*. *Protein Expr Purif.* 128:22–28. doi:10.1016/j.pep.2016.07.014. [accessed 2020 Dec 30].

Sorrentino I, Giardina P, Piscitelli A. 2019. Development of a biosensing platform based on a laccase-hydrophobin chimera. *Appl Microbiol Biotechnol.* 103(7):3061–3071. doi:10.1007/s00253-019-09678-2. [accessed 2019 Aug 19].

Sousa JS, D’Imprima E, Vonck J. 2018. Mitochondrial Respiratory Chain Complexes. In: *Sub-cellular biochemistry*. Vol 87. Berlin, Germany: Springer. p. 167–227.

Spriestersbach A, Kubicek J, Schäfer F, Block H, Maertens B. 2015. Purification of His-Tagged Proteins. In: *Methods in Enzymology*. Vol. 559. Cambridge, USA: Academic Press. p. 1–15.

Stevens AJ, Sekar G, Shah NH, Mostafavi AZ, Cowburn D, Muir TW. 2017. A promiscuous split intein with expanded protein engineering applications. *Proc Natl Acad Sci.* 114(32):8538–8543. doi:10.1073/pnas.1701083114. [accessed 2021 Jan 3].

Strzelczyk AK, Paul TJ, Schmidt S. 2020. Quantifying Thermoswitchable Carbohydrate-Mediated Interactions *via* Soft Colloidal Probe Adhesion Studies. *Macromol Biosci.* 20(10):1–9. doi:10.1002/mabi.202000186. [accessed 2021 Jan 14].

Strzelczyk AK, Wang H, Lindhorst A, Waschke J, Pompe T, Kropf C, Luneau B, Schmidt S. 2017. Hydrogel Microparticles as Sensors for Specific Adhesion: Case Studies on Antibody Detection and Soil Release Polymers. *Gels.* 3(3):31. doi:10.3390/gels3030031. [accessed 2021 Jan 14].

Su L, Jia W, Hou C, Lei Y. 2011. Microbial biosensors: A review. *Biosens Bioelectron.* 26(5):1788–1799. doi:10.1016/j.bios.2010.09.005. [accessed 2020 Sep 20].

Sunde M, Kwan AHY, Templeton MD, Beever RE, Mackay JP. 2008. Structural analysis of hydrophobins. *Micron.* 39(7):773–784. doi:10.1016/j.MICRON.2007.08.003. [accessed 2019 Jul 16].

Tag K, Riedel K, Bauer HJ, Hanke G, Baronian KHR, Kunze G. 2007. Amperometric detection of Cu²⁺ by yeast biosensors using flow injection analysis (FIA). *Sensors Actuators, B Chem.* 122(2):403–409. doi:10.1016/j.snb.2006.06.007.

- Takeuchi I, Osada K, Azam AH, Asakawa H, Miyanaga K, Tanji Y. 2016. The presence of two receptor-binding proteins contributes to the wide host range of staphylococcal twort-like phages. *Appl Environ Microbiol.* 82(19):5763–5774. doi:10.1128/AEM.01385-16. [accessed 2021 Jan 31]. <http://dx.doi.org/10.1128>. [accessed 2020 Sep 22].
- Thielemann R. 2019. Derivate des Cox11p-Proteins aus *S. cerevisiae*: Expression und Reinigung [thesis]. [Dresden, Germany]: Technical University Dresden.
- Timón-Gómez A, Nývltová E, Abriata LA, Vila AJ, Hosler J, Barrientos A. 2018. Mitochondrial cytochrome c oxidase biogenesis: Recent developments. *Semin Cell Dev Biol.* 76:163–178. doi:10.1016/j.SEMCDB.2017.08.055. [accessed 2018 May 24].
- Tsukihara T, Aoyama H, Yamashita E, Tomizaki T, Yamaguchi H, Shinzawa-Itoh K, Nakashima R, Yaono R, Yoshikawa S. 1996. The whole structure of the 13-subunit oxidized cytochrome c oxidase at 2.8 Å. *Science.* 272(5265):1136–44. doi:10.1126/science.272.5265.1136. [accessed 2019 Aug 18].
- Uddayasankar U, Krull UJ. 2013. Analytical performance of molecular beacons on surface immobilized gold nanoparticles of varying size and density. *Anal Chim Acta.* 803:113–22. doi:10.1016/j.aca.2013.07.059. [accessed 2015 Dec 8].
- USEPA. 2009. National Primary Drinking Water Guidelines. Epa 816-F-09-004. [accessed 2021 Jan 22].
- Vagenende V, Yap MGS, Trout BL. 2009. Mechanisms of Protein Stabilization and Prevention of Protein Aggregation by Glycerol. *Biochemistry.* 48(46):11084–11096. doi:10.1021/bi900649t. [accessed 2018 Oct 16].
- Valo H, Kovalainen M, Laaksonen P, Häkkinen M, Auriola S, Peltonen L, Linder M, Järvinen K, Hirvonen J, Laaksonen T. 2011. Immobilization of protein-coated drug nanoparticles in nanofibrillar cellulose matrices—Enhanced stability and release. *J Control Release.* 156(3):390–397. doi:10.1016/J.JCONREL.2011.07.016. [accessed 2019 Jul 24].
- Valo HK, Laaksonen PH, Peltonen LJ, Linder MB, Hirvonen JT, Laaksonen TJ. 2010. Multifunctional Hydrophobin: Toward Functional Coatings for Drug Nanoparticles. *ACS Nano.* 4(3):1750–1758. doi:10.1021/nn9017558. [accessed 2019 Jul 24].
- Della Ventura B, Rea I, Calìò A, Giardina P, Gravagnuolo AM, Funari R, Altucci C, Velotta R, De Stefano L. 2016. Vmh2 hydrophobin layer entraps glucose: A quantitative characterization by label-free optical and gravimetric methods. *Appl Surf Sci.* 364:201–207. doi:10.1016/j.apsusc.2015.12.080. [accessed 2020 Dec 28].
- de Vocht ML, Scholtmeijer K, van der Vegte EW, de Vries OM, Sonveaux N, Wösten HA, Ruyschaert JM, Hadziloannou G, Wessels JG, Robillard GT. 1998. Structural characterization of the hydrophobin SC3, as a monomer and after self-assembly at hydrophobic/hydrophilic interfaces. *Biophys J.* 74(4):2059. [accessed 2019 Jul 23].
- Voronova A, Meyer-Klaucke W, Meyer T, Rompel A, Krebs B, Kazantseva J, Sillard R, Palumaa P. 2007. Oxidative switches in functioning of mammalian copper chaperone Cox17. *Biochem J.* 408:139–148.

doi:10.1042/BJ20070804. [accessed 2019 Sep 5].

Wang H, Jacobi F, Waschke J, Hartmann L, Löwen H, Schmidt S. 2017. Elastic Modulus Dependence on the Specific Adhesion of Hydrogels. *Adv Funct Mater.* 27(41):1702040. doi:10.1002/adfm.201702040. [accessed 2020 Dec 23].

Wang J. 2008. Electrochemical glucose biosensors. *Chem Rev.* 108(2):814–825. doi:10.1021/cr068123a. [accessed 2021 Jan 21].

Wang J, Zong Q. 2015. A new turn-on fluorescent probe for the detection of copper ion in neat aqueous solution. *Sensors Actuators, B Chem.* 216:572–577. doi:10.1016/j.snb.2015.04.095. [accessed 2021 Jan 6].

Wang R, Yang Y-L, Qin M, Wang L-K, Yu L, Shao B, Qiao M-Q, Wang C, Feng X-Z. 2007. Biocompatible Hydrophilic Modifications of Poly(dimethylsiloxane) Using Self-Assembled Hydrophobins. *Chem Mater.* doi:10.1021/CM070445N. [accessed 2019 Jul 25].

Wang X, Cohen L, Wang J, Walt DR. 2018. Competitive Immunoassays for the Detection of Small Molecules Using Single Molecule Arrays. *J Am Chem Soc.* 140(51):18132–18139. doi:10.1021/jacs.8b11185. [accessed 2021 Jan 22].

Wang X, Shi F, Wösten HAB, Hektor H, Poolman B, Robillard GT. 2005. The SC3 Hydrophobin Self-Assembles into a Membrane with Distinct Mass Transfer Properties. *Biophys J.* 88(5):3434–3443. doi:10.1529/BIOPHYSJ.104.057794. [accessed 2019 Jul 17].

Wang Y, van Oosterwijk N, Ali AM, Adawy A, Anindya AL, Dömling ASS, Groves MR. 2017. A Systematic Protein Refolding Screen Method using the DGR Approach Reveals that Time and Secondary TSA are Essential Variables. *Sci Rep.* 7(1):9355. doi:10.1038/s41598-017-09687-z. [accessed 2018 Oct 25].

Wang Z, Feng S, Huang Y, Li S, Xu H, Zhang X, Bai Y, Qiao M. 2010. Expression and characterization of a *Grifola frondosa* hydrophobin in *Pichia pastoris*. *Protein Expr Purif.* 72(1):19–25. doi:10.1016/j.pep.2010.03.017. [accessed 2020 Dec 31].

Wang Z, Feng S, Huang Y, Qiao M, Zhang B, Xu H. 2010. Prokaryotic expression, purification, and polyclonal antibody production of a hydrophobin from *Grifola frondosa*. *Acta Biochim Biophys Sin (Shanghai).* 42(6):388–395. doi:10.1093/abbs/gmq033. [accessed 2020 Dec 30].

Wang Z, Huang Y, Li S, Xu H, Linder MB, Qiao M. 2010. Hydrophilic modification of polystyrene with hydrophobin for time-resolved immunofluorometric assay. *Biosens Bioelectron.* 26(3):1074–1079. doi:10.1016/j.bios.2010.08.059. [accessed 2019 Sep 06].

Wang Z, Lienemann M, Qiao M, Linder MB. 2010. Mechanisms of protein adhesion on surface films of hydrophobin. *Langmuir.* 26(11):8491–8496. doi:10.1021/la101240e. [accessed 2020 Dec 30].

Wang Z, Wang Y, Huang Y, Li S, Feng S, Xu H, Qiao M. 2010. Characterization and application of hydrophobin-dispersed multi-walled carbon nanotubes. *Carbon N Y.* 48(10):2890–2898. doi:10.1016/j.carbon.2010.04.022. [accessed 2021 Jan 1].

- Wang ZA. 2019. The Recent Progresses in Chemical Synthesis of Proteins with Site-Specific Lysine Post-translational Modifications. *Curr Org Synth.* 16(3):369–384. doi:10.2174/1570179416666190328233918. [accessed 2021 Jan 3].
- Waschke J, Pompe T, Rettke D, Schmidt S, Hlawitschka M. 2019. Radial profile detection of multiple spherical particles in contact with interacting surfaces. *PLoS One.* 14(4):e0214815. doi:10.1371/journal.pone.0214815. [accessed 2019 Jul 9].
- Wei P, Zhu Z, Song R, Li Z, Chen C. 2019. An ion-imprinted sensor based on chitosan-graphene oxide composite polymer modified glassy carbon electrode for environmental sensing application. *Electrochim Acta.* 317:93–101. doi:10.1016/j.electacta.2019.05.136. [accessed 2021-02-15].
- Wessels JGH, De Vries O, Asgeirsdottir SA, Schuren F. 1991. Hydrophobin Genes Involved in Formation of Aerial Hyphae and Fruit Bodies in *Schizophyllum*. *Plant Cell.* 3(8):793–799. doi:10.1105/tpc.3.8.793. [accessed 2019 Jul 16].
- Wessels JGH. 1997. Hydrophobins: proteins that change the nature of the fungal surface. *Adv Microb Physiol.* 38:1–45. [accessed 2019 Jul 16].
- Wessels JGH. 1994. Developmental Regulation of Fungal Cell Wall Formation. *Annu Rev Phytopathol.* 32(1):413–437. doi:10.1146/annurev.py.32.090194.002213. [accessed 2019 Jul 22].
- Wessels JGH. 1999. Fungi in their own right. *Fungal Genet Biol.* 27(2–3):134–145. doi:10.1006/fgbi.1999.1125. [accessed 2021 Jan 2].
- Wessman P, Håkansson S, Leifer K, Rubino S. 2013. Formulations for freeze-drying of bacteria and their influence on cell survival. *J Vis Exp.* 78:4058. doi:10.3791/4058. [accessed 2020 Dec 31].
- Wickham H, Stryjewski L. 2011. 40 Years of Boxplots [Internet]. HadCoNz. Available from: <https://vita.had.co.nz/papers/boxplots.html>. [accessed 2021 Mar 04].
- Williams JC, Sue C, Banting GS, Yang H, Glerum DM, Hendrickson WA, Schon EA. 2005. Crystal structure of human SCO1: implications for redox signaling by a mitochondrial cytochrome c oxidase "assembly" protein. *J Biol Chem.* 280(15):15202–15211. doi:10.1074/jbc.M410705200. [accessed 2018 Jun 19].
- Winandy L, Hilpert F, Schlebusch O, Fischer R. 2018. Comparative analysis of surface coating properties of five hydrophobins from *Aspergillus nidulans* and *Trichoderma reesei*. *Sci Rep.* 8(1):12033. doi:10.1038/s41598-018-29749-0. [accessed 2019 Aug 19].
- Wingfield PT. 2016. Overview of the Purification of Recombinant Proteins. *Curr Protoc Protein Sci.* 80:1–50. doi: 10.1002/0471140864.ps0601s80.Overview. [accessed 2020 Nov 20].
- Wingfield PT, Palmer I, Liang S. 2014. Folding and Purification of Insoluble (Inclusion Body) Proteins from *Escherichia coli*. *Curr Protoc Protein Sci.* 78(1):6.5.1–6.5.30. doi:10.1002/0471140864.ps0605s78. [accessed 2021 Jan 8].
- Wohlleben W, Subkowski T, Bollschweiler C, Von Vacano B, Liu Y, Schrepp W, Baus U. 2010. Recombinantly produced hydrophobins from fungal analogues as highly surface-active performance

proteins. *Eur Biophys J.* 39(3):457–468. doi: 10.1007/s00249-009-0430-4. [accessed 2020 Dec 29].

Wösten HA, Asgeirsdóttir SA, Krook JH, Drenth JH, Wessels JG. 1994. The fungal hydrophobin Sc3p self-assembles at the surface of aerial hyphae as a protein membrane constituting the hydrophobic rodlet layer. *Eur J Cell Biol.* 63(1):122–129. [accessed 2019 Jul 16].

Wösten HAB, Schuren FHJ, Wessels JGH. 1994. Interfacial self-assembly of a hydrophobin into an amphipathic protein membrane mediates fungal attachment to hydrophobic surfaces. *EMBO J.* 13(24):5848–5854. doi:10.1002/j.1460-2075.1994.tb06929.x. [accessed 2019 Jul 16].

Wösten HAB, Van Wetter MA, Lugones LG, Van der Mei HC, Busscher HJ, Wessels JGH. 1999. How a fungus escapes the water to grow into the air. *Curr Biol.* 9(2):85–88. doi:10.1016/S0960-9822(99)80019-0. [accessed 2020 Dec 30].

Xu M-Q, Evans TC. 2001. Intein-Mediated Ligation and Cyclization of Expressed Proteins. *Methods.* 24(3):257–277. doi:10.1006/meth.2001.1187. [accessed 2021 Jan 20].

Xu S, Andrews D, Hill BC. 2015. The affinity of yeast and bacterial SCO proteins for CU(I) and CU(II): A capture and release strategy for copper transfer. *Biochem Biophys Reports.* 4:10–19. doi:10.1016/j.bbrep.2015.08.010. [accessed 2018 Mar 26].

Yamaguchi H, Miyazaki M. 2014. Refolding techniques for recovering biologically active recombinant proteins from inclusion bodies. *Biomolecules.* 4(1):235–51. doi:10.3390/biom4010235. [accessed 2018 Oct 25].

Yamasaki R, Takatsuji Y, Lienemann M, Asakawa H, Fukuma T, Linder M, Haruyama T. 2014. Electrochemical properties of honeycomb-like structured HFBI self-organized membranes on HOPG electrodes. *Colloids Surfaces B Biointerfaces.* 123:803–808. doi:10.1016/j.colsurfb.2014.10.018. [accessed 2020 Oct 02].

Yang L, Huang N, Huang L, Liu M, Li H, Zhang Y, Yao S. 2017. An electrochemical sensor for highly sensitive detection of copper ions based on a new molecular probe Pi-A decorated on graphene. *Anal Methods.* 9(4):618–624. doi:10.1039/c6ay03006h. [accessed 2021 Jan 22].

Yin R, Ling L, Shang C. 2018. Wavelength-dependent chlorine photolysis and subsequent radical production using UV-LEDs as light sources. *Water Res.* 142:452–458. doi:10.1016/j.watres.2018.06.018. [accessed 2020 Sep 20].

Yoo H, Jo H, Oh SS. 2020. Detection and beyond: challenges and advances in aptamer-based biosensors. *Mater Adv.* 1(8):2663–2687. doi:10.1039/d0ma00639d. [accessed 2021 Jan 21].

Yu L, Zhang B, Szilvay GR, Sun R, Jänis J, Wang Z, Feng S, Xu H, Linder MB, Qiao M. 2008. Protein HGFI from the edible mushroom *Grifola frondosa* is a novel 8 kDa class I hydrophobin that forms rodlets in compressed monolayers. *Microbiology.* 154(6):1677–1685. doi:10.1099/mic.0.2007/015263-0. [accessed 2021 Jan 2].

Yuan L, Liu Y, Chen Y, Gu X, Dong H, Zhang S, Han T, Zhou Z, Song X, Wang C. 2020. Optimized real-time

fluorescence PCR assay for the detection of porcine Circovirus type 3 (PCV3). *BMC Vet Res.* 16(1):249. doi:10.1186/s12917-020-02435-y. [accessed 2021 Apr 5].

Zampieri F, Wösten HAB, Scholtmeijer K. 2010. Creating Surface Properties Using a Palette of Hydrophobins. *Eur Biophys J.* 3(9):4607–4625. doi:10.3390/ma3094607. [accessed 2018 Apr 13].

Zhang M, Wang Zhexiang, Wang Zefang, Feng S, Xu H, Zhao Q, Wang S, Fang J, Qiao M, Kong D. 2011. Immobilization of anti-CD31 antibody on electrospun poly(ϵ -caprolactone) scaffolds through hydrophobins for specific adhesion of endothelial cells. *Colloids Surfaces B Biointerfaces.* 85(1):32–39. doi:10.1016/j.colsurfb.2010.10.042. [accessed 2020 Okt 02].

Zhao L, Liu J, Song D, Wang X, Tai F, Xu H, Qiao M. 2015. A visualized fusion protein based on self-assembly hydrophobin HGFI. *Chem Res Chinese Univ.* 31(5):781–786. doi:10.1007/s40242-015-5135-x. [accessed 2019 Jul 17].

Zhao Z-X, Qiao M-Q, Yin F, Shao B, Wu B-Y, Wang Y-Y, Wang X-S, Qin X, Li S, Yu L, et al. 2007. Amperometric glucose biosensor based on self-assembly hydrophobin with high efficiency of enzyme utilization. *Biosens Bioelectron.* 22(12):3021–3027. doi:10.1016/j.bios.2007.01.007. [accessed 2021 Jan 4].

Zhao Z-X, Wang H-C, Qin X, Wang X-S, Qiao M-Q, Anzai J, Chen Q. 2009. Self-assembled film of hydrophobins on gold surfaces and its application to electrochemical biosensing. *Colloids Surfaces B Biointerfaces.* 71(1):102–106. doi:10.1016/J.COLSURFB.2009.01.011. [accessed 2019 Jul 25].

Zhu Z, Yang CJ. 2017. Hydrogel droplet microfluidics for high-throughput single molecule/cell analysis. *Acc Chem Res.* 50(1):22–31. doi:10.1021/acs.accounts.6b00370. [accessed 2018 Feb 20].

7 APPENDIX

7.1 SEQUENCES OF PROTEIN CONSTRUCTS

7.1.1 Sequences of the Protein Construct Cox17_a

In the following, the nucleotide and amino acid sequences of the protein construct Cox17_a are shown. The His-tag, the sequences for the TEV cleavage site, and the target protein Cox17 sequences are colored in green, blue, and black, respectively. The restriction recognition sites used for molecular cloning are underlined.

```
1 CAT CAT CAT CAT CAT CAC AGC AGC GGC CTG GTG CCG CGC
1 H H H H H H S S G L V P R

40 GGC AGC CAT ATG GCT AGC GAG AAC CTT TAC TTT CAG GGA
14 G S H M A S E N L Y F Q G

79 ATG ACT GAA ACT GAC AAG AAA CAA GAA CAA GAA AAC CAC
27 M T E T D K K Q E Q E N H

118 GCG GAG TGC GAG GAC AAA CCT AAG CCA TGT TGC GTT TGT
40 A E C E D K P K P C C V C

157 AAG CCA GAA AAG GAG GAG CGG GAT ACA TGC ATC TTA TTC
53 K P E K E E R D T C I L F

196 AAT GGA CAA GAC TCT GAA AAA TGC AAG GAA TTC ATT GAA
66 N G Q D S E K C K E F I E

235 AAG TAC AAA GAG TGC ATG AAG GGT TAT GGC TTC GAA GTT
79 K Y K E C M K G Y G F E V

274 CCA AGT GCA AAT TAG CTC GAG
92 P S A N * L E
```

7.1.2 Sequences of the Hydrophobin-Cox17 Fusion Protein Cox17_b

In the following, the nucleotide and amino acid sequences of the protein construct Cox17_b are shown. The His-tag, the DNA sequence encoding for the TEV cleavage site and the corresponding amino acid sequence, and the glycine-serine linker are colored in green, blue, and red, respectively. The Cox17 target protein sequences followed by the hydrophobin Ccg-2 sequences are colored in black. The restriction recognition sites used for molecular cloning are underlined.

```
1 CAT CAT CAT CAT CAT CAC AGC AGC GGC CTG GTG CCG CGC
1 H H H H H H S S G L V P R

40 GGC AGC CAT ATG GCT AGC GAG AAC CTT TAC TTT CAG GGA
14 G S H M A S E N L Y F Q G
```

```

79 ATG ACT GAA ACT GAC AAG AAA CAA GAA CAA GAA AAC CAC
27 M T E T D K K Q E Q E N H

118 GCG GAG TGC GAG GAC AAA CCT AAG CCA TGT TGC GTT TGT
40 A E C E D K P K P C C V C

157 AAG CCA GAA AAG GAG GAG CGG GAT ACA TGC ATC TTA TTC
53 K P E K E E R D T C I L F

196 AAT GGA CAA GAC TCT GAA AAA TGC AAG GAA TTC ATT GAA
66 N G Q D S E K C K E F I E

235 AAG TAC AAA GAG TGC ATG AAG GGT TAT GGC TTC GAA GTT
79 K Y K E C M K G Y G F E V

274 CCA AGT GCA AAT GAA TTC GGC GGC GGC GGC AGC GGC GGC
92 P S A N E F G G G G S G G

313 GGC GGC AGC GGC GGC GGC AGC ATC GGC CCC AAC ACC TGC
105 G G S G G G S I G P N T C

352 TCC ATC GAC GAC TAC AAG CCT TAC TGC TGC CAG TCT ATG
118 S I D D Y K P Y C C Q S M

391 TCC GGC CCC GCC GGC TCC CCT GGT CTC CTC AAC CTC ATC
131 S G P A G S P G L L N L I

430 CCC GTC GAC CTC AGC GCC TCG CTC GGC TGC GTT GTC GGT
144 P V D L S A S L G C V V G

469 GTC ATC GGC TCC CAA TGT GGT GCC AGC GTC AAG TGC TGC
157 V I G S Q C G A S V K C C

508 AAG GAC GAT GTT ACC AAC ACC GGC AAC TCC TTC CTC ATC
170 K D D V T N T G N S F L I

547 ATC AAC GCT GCC AAC TGC GTT GCC TGA CTC GAG
183 I N A A N C V A * L E

```

7.1.3 Sequences of the Hydrophobin-Cox17 Fusion Protein Construct Cox17_c

In the following, the nucleotide and amino acid sequences of the protein construct Cox17_c are shown. The His-tag, the DNA sequence encoding for the TEV cleavage site and the corresponding amino acid sequence, and the glycine-serine linker are colored in green, blue, and red, respectively. The hydrophobin Ccg-2 sequences followed by the Cox17 target protein sequences are colored in black. The restriction recognition sites used for molecular cloning are underlined.

```

1 CAT CAT CAT CAT CAT CAC AGC AGC GGC CTG GTG CCG CGC
1 H H H H H H S S G L V P R

40 GGC AGC CAT ATG GCT AGC GAG AAC CTT TAC TTT CAG GGA
14 G S H M A S E N L Y F Q G

```



```

79 ATC GGC CCC AAC ACC TGC TCC ATC GAC GAC TAC AAG CCT
27 I G P N T C S I D D Y K P

118 TAC TGC TGC CAG TCT ATG TCC GGC CCC GCC GGC TCC CCT
40 Y C C Q S M S G P A G S P

157 GGT CTC CTC AAC CTC ATC CCC GTC GAC CTC AGC GCC TCG
53 G L L N L I P V D L S A S

196 CTC GGC TGC GTT GTC GGT GTC ATC GGC TCC CAA TGT GGT
66 L G C V V G V I G S Q C G

235 GCC AGC GTC AAG TGC TGC AAG GAC GAT GTT ACC AAC ACC
79 A S V K C C K D D V T N T

274 GGC AAC TCC TTC CTC ATC ATC AAC GCT GCC AAC TGC GTT
92 G N S F L I I N A A N C V

313 GCC GAA TTC GGC GGC GGC GGC AGC GGC GGC GGC GGC AGC
105 A E F G G G G S G G G G S

352 GGC GGC GGC AGC ATG ACT GAA ACT GAC AAG AAA CAA GAA
118 G G G S M T E T D K K Q E

391 CAA GAA AAC CAC GCG GAG TGC GAG GAC AAA CCT AAG CCA
131 Q E N H A E C E D K P K P

430 TGT TGC GTT TGT AAG CCA GAA AAG GAG GAG CGG GAT ACA
144 C C V C K P E K E E R D T

469 TGC ATC TTA TTC AAT GGA CAA GAC TCT GAA AAA TGC AAG
157 C I L F N G Q D S E K C K

508 GAA TTC ATT GAA AAG TAC AAA GAG TGC ATG AAG GGT TAT
170 E F I E K Y K E C M K G Y

547 GGC TTC GAA GTT CCA AGT GCA AAT TAG CTC GAG
183 G F E V P S A N * L E

```

7.1.4 Sequences of the Protein Construct Sco1_a and Sco1Δ95_a

In the following are shown the nucleotide and amino acid sequences of the protein constructs Sco1_a and Sco1Δ95_a. The His-tag, the sequences for the TEV cleavage site, and the target protein Sco1 (Sco1Δ95) sequences are colored in green, blue, and black, respectively. The 95 amino acid long trans-membrane domain highlighted in bold was truncated for the Sco1Δ95_a construct. The restriction recognition sites used for molecular cloning are underlined.

```

1 CAT CAT CAT CAT CAT CAC AGC AGC GGC CTG GTG CCG CGC
1 H H H H H H S S G L V P R

40 GGC AGC CAT ATG GCT AGC GAG AAC CTT TAC TTT CAG GGA
14 G S H M A S E N L Y F Q G

79 ATG CTG AAG TTG TCA AGA AGT GCC AAT CTA AGA TTG GTC
27 M L K L S R S A N L R L V

```

118 CAA TTG CCA GCC GCA AGA TTA AGT GGC AAT GGC GCT AAA
 40 Q L P A A R L S G N G A K
 157 TTG CTC ACT CAA AGG GGA TTC TTT ACT GTA ACG CGC TTA
 53 L L T Q R G F F T V T R L
 196 TGG CAG TCA AAT GGC AAG AAA CCA TTA AGC AGA GTA CCT
 66 W Q S N G K K P L S R V P
 235 GTG GGC GGT ACT CCC ATT AAG GAT AAC GGC AAA GTG CGA
 79 V G G T P I K D N G K V R
 274 GAA GGC TCG ATC GAG TTT TCC ACG GGA AAG GCC ATT GCT
 92 E G S I E F S T G K A I A
 313 CTA TTC CTA GCA GTC GGT GGG GCA CTT TCT TAT TTC TTC
 105 L F L A V G G A L S Y F F
 352 AAC AGG GAG AAA CGC AGA TTG GAA ACA CAG AAG GAG GCT
 118 N R E K R R L E T Q K E A
 391 GAA GCA AAC AGA GGA TAC GGT AAA CCT TCA CTT GGG GGA
 131 E A N R G Y G K P S L G G
 430 CCC TTC CAT CTG GAG GAT ATG TAT GGC AAT GAG TTT ACG
 144 P F H L E D M Y G N E F T
 469 GAG AAA AAC CTT CTC GGT AAG TTT TCT ATA ATA TAC TTT
 157 E K N L L G K F S I I Y F
 508 GGG TTT AGT AAC TGT CCT GAC ATC TGT CCT GAT GAA CTG
 170 G F S N C P D I C P D E L
 547 GAT AAG CTA GGT CTA TGG CTT AAT ACA CTC TCT TCA AAG
 183 D K L G L W L N T L S S K
 586 TAT GGT ATT ACT CTG CAG CCA TTA TTT ATA ACT TGT GAT
 196 Y G I T L Q P L F I T C D
 625 CCA GCA AGA GAC TCC CCT GCT GTA TTG AAA GAG TAT TTG
 209 P A R D S P A V L K E Y L
 664 AGC GAC TTT CAT CCC TCC ATC CTG GGT TTG ACG GGG ACG
 222 S D F H P S I L G L T G T
 703 TTC GAT GAG GTG AAG AAC GCA TGC AAG AAG TAC AGA GTA
 235 F D E V K N A C K K Y R V
 742 TAC TTT TCT ACG CCT CCA AAC GTC AAA CCG GGC CAA GAT
 248 Y F S T P P N V K P G Q D
 781 TAT TTG GTA GAC CAT TCC ATC TTC TTT TAT CTC ATG GAC
 261 Y L V D H S I F F Y L M D
 820 CCT GAA GGA CAG TTT GTT GAT GCT TTG GGT AGA AAT TAT
 274 P E G Q F V D A L G R N Y
 859 GAT GAA AAA ACG GGC GTG GAC AAG ATC GTG GAA CAC GTT
 287 D E K T G V D K I V E H V

898	AAG	AGT	TAT	GTG	CCT	GCA	GAG	CAG	CGC	GCC	AAG	CAG	AAG
300	K	S	Y	V	P	A	E	Q	R	A	K	Q	K
937	GAG	GCA	TGG	TAC	TCC	TTC	TTA	TTC	AAA	<u>TAA</u>	<u>CTC</u>	<u>GAG</u>	
313	E	A	W	Y	S	F	L	F	K	*	L	E	

7.1.5 Sequences of the Hydrophobin-Sco1 Fusion Protein Constructs

Sco1_b and Sco1Δ95_b

The nucleotide and amino acid sequences of the protein constructs Sco1_b and Sco1Δ95_b are shown in the following. The His-tag, the DNA sequence encoding for the TEV cleavage site and the corresponding amino acid sequence, and the glycine-serine linker are colored in green, blue, and red, respectively. The Sco1 (Sco1Δ95) target protein sequences followed by the hydrophobin Ccg-2 sequences are colored in black. The 95 amino acid long transmembrane domain highlighted in bold was truncated for the Sco1Δ95_b construct. The restriction recognition sites used for molecular cloning are underlined.

1	CAT	CAT	CAT	CAT	CAT	CAC	AGC	AGC	GGC	CTG	GTG	CCG	CGC
1	H	H	H	H	H	H	S	S	G	L	V	P	R
40	GGC	AGC	CAT	ATG	<u>GCT</u>	<u>AGC</u>	<u>GAG</u>	<u>AAC</u>	<u>CTT</u>	<u>TAC</u>	<u>TTT</u>	<u>CAG</u>	<u>GGA</u>
14	G	S	H	M	A	S	E	N	L	Y	F	Q	G
79	ATG	CTG	AAG	TTG	TCA	AGA	AGT	GCC	AAT	CTA	AGA	TTG	GTC
27	M	L	K	L	S	R	S	A	N	L	R	L	V
118	CAA	TTG	CCA	GCC	GCA	AGA	TTA	AGT	GGC	AAT	GGC	GCT	AAA
40	Q	L	P	A	A	R	L	S	G	N	G	A	K
157	TTG	CTC	ACT	CAA	AGG	GGA	TTC	TTT	ACT	GTA	ACG	CGC	TTA
53	L	L	T	Q	R	G	F	F	T	V	T	R	L
196	TGG	CAG	TCA	AAT	GGC	AAG	AAA	CCA	TTA	AGC	AGA	GTA	CCT
66	W	Q	S	N	G	K	K	P	L	S	R	V	P
235	GTG	GGC	GGT	ACT	CCC	ATT	AAG	GAT	AAC	GGC	AAA	GTG	CGA
79	V	G	G	T	P	I	K	D	N	G	K	V	R
274	GAA	GGC	TCG	ATC	GAG	TTT	TCC	ACG	GGA	AAG	GCC	ATT	GCT
92	E	G	S	I	E	F	S	T	G	K	A	I	A
313	CTA	TTC	CTA	GCA	GTC	GGT	GGG	GCA	CTT	TCT	TAT	TTC	TTC
105	L	F	L	A	V	G	G	A	L	S	Y	F	F
352	AAC	AGG	GAG	AAA	CGC	AGA	TTG	GAA	ACA	CAG	AAG	GAG	GCT
118	N	R	E	K	R	R	L	E	T	Q	K	E	A
391	GAA	GCA	AAC	AGA	GGA	TAC	GGT	AAA	CCT	TCA	CTT	GGG	GGA
131	E	A	N	R	G	Y	G	K	P	S	L	G	G
430	CCC	TTC	CAT	CTG	GAG	GAT	ATG	TAT	GGC	AAT	GAG	TTT	ACG
144	P	F	H	L	E	D	M	Y	G	N	E	F	T
469	GAG	AAA	AAC	CTT	CTC	GGT	AAG	TTT	TCT	ATA	ATA	TAC	TTT
157	E	K	N	L	L	G	K	F	S	I	I	Y	F

508	GGG	TTT	AGT	AAC	TGT	CCT	GAC	ATC	TGT	CCT	GAT	GAA	CTG
170	G	F	S	N	C	P	D	I	C	P	D	E	L
547	GAT	AAG	CTA	GGT	CTA	TGG	CTT	AAT	ACA	CTC	TCT	TCA	AAG
183	D	K	L	G	L	W	L	N	T	L	S	S	K
586	TAT	GGT	ATT	ACT	CTG	CAG	CCA	TTA	TTT	ATA	ACT	TGT	GAT
196	Y	G	I	T	L	Q	P	L	F	I	T	C	D
625	CCA	GCA	AGA	GAC	TCC	CCT	GCT	GTA	TTG	AAA	GAG	TAT	TTG
209	P	A	R	D	S	P	A	V	L	K	E	Y	L
664	AGC	GAC	TTT	CAT	CCC	TCC	ATC	CTG	GGT	TTG	ACG	GGG	ACG
222	S	D	F	H	P	S	I	L	G	L	T	G	T
703	TTC	GAT	GAG	GTG	AAG	AAC	GCA	TGC	AAG	AAG	TAC	AGA	GTA
235	F	D	E	V	K	N	A	C	K	K	Y	R	V
742	TAC	TTT	TCT	ACG	CCT	CCA	AAC	GTC	AAA	CCG	GGC	CAA	GAT
248	Y	F	S	T	P	P	N	V	K	P	G	Q	D
781	TAT	TTG	GTA	GAC	CAT	TCC	ATC	TTC	TTT	TAT	CTC	ATG	GAC
261	Y	L	V	D	H	S	I	F	F	Y	L	M	D
820	CCT	GAA	GGA	CAG	TTT	GTT	GAT	GCT	TTG	GGT	AGA	AAT	TAT
274	P	E	G	Q	F	V	D	A	L	G	R	N	Y
859	GAT	GAA	AAA	ACG	GGC	GTG	GAC	AAG	ATC	GTG	GAA	CAC	GTT
287	D	E	K	T	G	V	D	K	I	V	E	H	V
898	AAG	AGT	TAT	GTG	CCT	GCA	GAG	CAG	CGC	GCC	AAG	CAG	AAG
300	K	S	Y	V	P	A	E	Q	R	A	K	Q	K
937	GAG	GCA	TGG	TAC	TCC	TTC	TTA	TTC	AAA	<u>GAA</u>	<u>TTC</u>	GGC	GGC
313	E	A	W	Y	S	F	L	F	K	E	F	G	G
976	GGC	GGC	AGC	GGC	GGC	GGC	GGC	AGC	GGC	GGC	GGC	AGC	ATC
326	G	G	S	G	G	G	G	S	G	G	G	S	I
1015	GGC	CCC	AAC	ACC	TGC	TCC	ATC	GAC	GAC	TAC	AAG	CCT	TAC
339	G	P	N	T	C	S	I	D	D	Y	K	P	Y
1054	TGC	TGC	CAG	TCT	ATG	TCC	GGC	CCC	GCC	GGC	TCC	CCT	GGT
352	C	C	Q	S	M	S	G	P	A	G	S	P	G
1093	CTC	CTC	AAC	CTC	ATC	CCC	GTC	GAC	CTC	AGC	GCC	TCG	CTC
365	L	L	N	L	I	P	V	D	L	S	A	S	L
1132	GGC	TGC	GTT	GTC	GGT	GTC	ATC	GGC	TCC	CAA	TGT	GGT	GCC
378	G	C	V	V	G	V	I	G	S	Q	C	G	A
1171	AGC	GTC	AAG	TGC	TGC	AAG	GAC	GAT	GTT	ACC	AAC	ACC	GGC
391	S	V	K	C	C	K	D	D	V	T	N	T	G
1210	AAC	TCC	TTC	CTC	ATC	ATC	AAC	GCT	GCC	AAC	TGC	GTT	GCC
404	N	S	F	L	I	I	N	A	A	N	C	V	A
1249	TGA	<u>CTC</u>	<u>GAG</u>										
417	*	L	E										

7.1.6 Sequences of the Hydrophobin-Sco1 Fusion Protein Constructs

Sco1_c and Sco1Δ95_c

The nucleotide and amino acid sequences of the protein constructs Sco1_c and Sco1Δ95_c are shown in the following. The His-tag, the DNA sequence encoding for the TEV cleavage site and the corresponding amino acid sequence, and the glycine-serine linker are colored in green, blue, and red, respectively. The hydrophobin Ccg-2 sequences followed by the Sco1 (Sco1Δ95) target protein sequences are colored in black. The 95 amino acid long transmembrane domain highlighted in bold was truncated for the Sco1Δ95. The restriction recognition sites used for molecular cloning are underlined.

```

1 CAT CAT CAT CAT CAT CAC AGC AGC GGC CTG GTG CCG CGC
1  H  H  H  H  H  H  S  S  G  L  V  P  R

40 GGC AGC CAT ATG GCT AGC GAG AAC CTT TAC TTT CAG GGA
14  G  S  H  M  A  S  E  N  L  Y  F  Q  G

79 ATC GGC CCC AAC ACC TGC TCC ATC GAC GAC TAC AAG CCT
27  I  G  P  N  T  C  S  I  D  D  Y  K  P

118 TAC TGC TGC CAG TCT ATG TCC GGC CCC GCC GGC TCC CCT
40  Y  C  C  Q  S  M  S  G  P  A  G  S  P

157 GGT CTC CTC AAC CTC ATC CCC GTC GAC CTC AGC GCC TCG
53  G  L  L  N  L  I  P  V  D  L  S  A  S

196 CTC GGC TGC GTT GTC GGT GTC ATC GGC TCC CAA TGT GGT
66  L  G  C  V  V  G  V  I  G  S  Q  C  G

235 GCC AGC GTC AAG TGC TGC AAG GAC GAT GTT ACC AAC ACC
79  A  S  V  K  C  C  K  D  D  V  T  N  T

274 GGC AAC TCC TTC CTC ATC ATC AAC GCT GCC AAC TGC GTT
92  G  N  S  F  L  I  I  N  A  A  N  C  V

313 GCC GAA TTC GGC GGC GGC GGC AGC GGC GGC GGC GGC AGC
105  A  E  F  G  G  G  G  S  G  G  G  G  G  S

352 GGC GGC GGC AGC ATG CTG AAG TTG TCA AGA AGT GCC AAT
118  G  G  G  S  M  L  K  L  S  R  S  A  N

391 CTA AGA TTG GTC CAA TTG CCA GCC GCA AGA TTA AGT GGC
131  L  R  L  V  Q  L  P  A  A  R  L  S  G

430 AAT GGC GCT AAA TTG CTC ACT CAA AGG GGA TTC TTT ACT
144  N  G  A  K  L  L  T  Q  R  G  F  F  T

469 GTA ACG CGC TTA TGG CAG TCA AAT GGC AAG AAA CCA TTA
157  V  T  R  L  W  Q  S  N  G  K  K  P  L

508 AGC AGA GTA CCT GTG GGC GGT ACT CCC ATT AAG GAT AAC
170  S  R  V  P  V  G  G  T  P  I  K  D  N

547 GGC AAA GTG CGA GAA GGC TCG ATC GAG TTT TCC ACG GGA
183  G  K  V  R  E  G  S  I  E  F  S  T  G

```

586	AAG	GCC	ATT	GCT	CTA	TTC	CTA	GCA	GTC	GGT	GGG	GCA	CTT
196	K	A	I	A	L	F	L	A	V	G	G	A	L
625	TCT	TAT	TTC	TTC	AAC	AGG	GAG	AAA	CGC	AGA	TTG	GAA	ACA
209	S	Y	F	F	N	R	E	K	R	R	L	E	T
664	CAG	AAG	GAG	GCT	GAA	GCA	AAC	AGA	GGA	TAC	GGT	AAA	CCT
222	Q	K	E	A	E	A	N	R	G	Y	G	K	P
703	TCA	CTT	GGG	GGA	CCC	TTC	CAT	CTG	GAG	GAT	ATG	TAT	GGC
235	S	L	G	G	P	F	H	L	E	D	M	Y	G
742	AAT	GAG	TTT	ACG	GAG	AAA	AAC	CTT	CTC	GGT	AAG	TTT	TCT
248	N	E	F	T	E	K	N	L	L	G	K	F	S
781	ATA	ATA	TAC	TTT	GGG	TTT	AGT	AAC	TGT	CCT	GAC	ATC	TGT
261	I	I	Y	F	G	F	S	N	C	P	D	I	C
820	CCT	GAT	GAA	CTG	GAT	AAG	CTA	GGT	CTA	TGG	CTT	AAT	ACA
274	P	D	E	L	D	K	L	G	L	W	L	N	T
859	CTC	TCT	TCA	AAG	TAT	GGT	ATT	ACT	CTG	CAG	CCA	TTA	TTT
287	L	S	S	K	Y	G	I	T	L	Q	P	L	F
898	ATA	ACT	TGT	GAT	CCA	GCA	AGA	GAC	TCC	CCT	GCT	GTA	TTG
300	I	T	C	D	P	A	R	D	S	P	A	V	L
937	AAA	GAG	TAT	TTG	AGC	GAC	TTT	CAT	CCC	TCC	ATC	CTG	GGT
313	K	E	Y	L	S	D	F	H	P	S	I	L	G
976	TTG	ACG	GGG	ACG	TTC	GAT	GAG	GTG	AAG	AAC	GCA	TGC	AAG
326	L	T	G	T	F	D	E	V	K	N	A	C	K
1015	AAG	TAC	AGA	GTA	TAC	TTT	TCT	ACG	CCT	CCA	AAC	GTC	AAA
339	K	Y	R	V	Y	F	S	T	P	P	N	V	K
1054	CCG	GGC	CAA	GAT	TAT	TTG	GTA	GAC	CAT	TCC	ATC	TTC	TTT
352	P	G	Q	D	Y	L	V	D	H	S	I	F	F
1093	TAT	CTC	ATG	GAC	CCT	GAA	GGA	CAG	TTT	GTT	GAT	GCT	TTG
365	Y	L	M	D	P	E	G	Q	F	V	D	A	L
1132	GGT	AGA	AAT	TAT	GAT	GAA	AAA	ACG	GGC	GTG	GAC	AAG	ATC
378	G	R	N	Y	D	E	K	T	G	V	D	K	I
1171	GTG	GAA	CAC	GTT	AAG	AGT	TAT	GTG	CCT	GCA	GAG	CAG	CGC
391	V	E	H	V	K	S	Y	V	P	A	E	Q	R
1210	GCC	AAG	CAG	AAG	GAG	GCA	TGG	TAC	TCC	TTC	TTA	TTC	AAA
404	A	K	Q	K	E	A	W	Y	S	F	L	F	K
1249	<u>TAA</u>	<u>CTC</u>	<u>GAG</u>										
417	*	L	E										

7.1.7 Sequences of the Hydrophobin Ccg-2

The nucleotide and amino acid sequences of the hydrophobin protein Ccg-2 are shown in the following. The His-tag, the sequences for the TEV cleavage site, and the hydrophobin Ccg-2 sequences are colored in green, blue, and black, respectively. The restriction recognition sites used for molecular cloning are underlined.

1	CAT	CAT	CAT	CAT	CAT	CAC	AGC	AGC	GGC	CTG	GTG	CCG	CGC
1	H	H	H	H	H	H	S	S	G	L	V	P	R
40	GGC	AGC	CAT	ATG	<u>GCT</u>	<u>AGC</u>	GAG	AAC	CTT	TAC	TTT	CAG	GGA
14	G	S	H	M	A	S	E	N	L	Y	F	Q	G
79	ATC	GGC	CCC	AAC	ACC	TGC	TCC	ATC	GAC	GAC	TAC	AAG	CCT
27	I	G	P	N	T	C	S	I	D	D	Y	K	P
118	TAC	TGC	TGC	CAG	TCT	ATG	TCC	GGC	CCC	GCC	GGC	TCC	CCT
40	Y	C	C	Q	S	M	S	G	P	A	G	S	P
157	GGT	CTC	CTC	AAC	CTC	ATC	CCC	GTC	GAC	CTC	AGC	GCC	TCG
53	G	L	L	N	L	I	P	V	D	L	S	A	S
196	CTC	GGC	TGC	GTT	GTC	GGT	GTC	ATC	GGC	TCC	CAA	TGT	GGT
66	L	G	C	V	V	G	V	I	G	S	Q	C	G
235	GCC	AGC	GTC	AAG	TGC	TGC	AAG	GAC	GAT	GTT	ACC	AAC	ACC
79	A	S	V	K	C	C	K	D	D	V	T	N	T
274	GGC	AAC	TCC	TTC	CTC	ATC	ATC	AAC	GCT	GCC	AAC	TGC	GTT
92	G	N	S	F	L	I	I	N	A	A	N	C	V
313	GCC	TAA	<u>CTC</u>	<u>GAG</u>									
105	A	*	L	E									

7.2 PET-28B(+): PLASMID MAP

The Novagen pET-28a-c(+) vectors (Figure 40) from Merck KGaA (Germany) carry an N-terminal His•Tag®/thrombin/T7•Tag® configuration plus an optional C-terminal His•Tag sequence (Novagen pET-28a(+) datasheet from Merck KGaA (Germany)). In this study, the Novagen pET-28b(+) was used as cloning vector. Unique sites are shown on the circle map. Note that the sequence is numbered by the pBR322 convention, so the T7 expression region is reversed on the circular map. The cloning/expression region of the coding strand transcribed by T7 RNA polymerase is shown below.

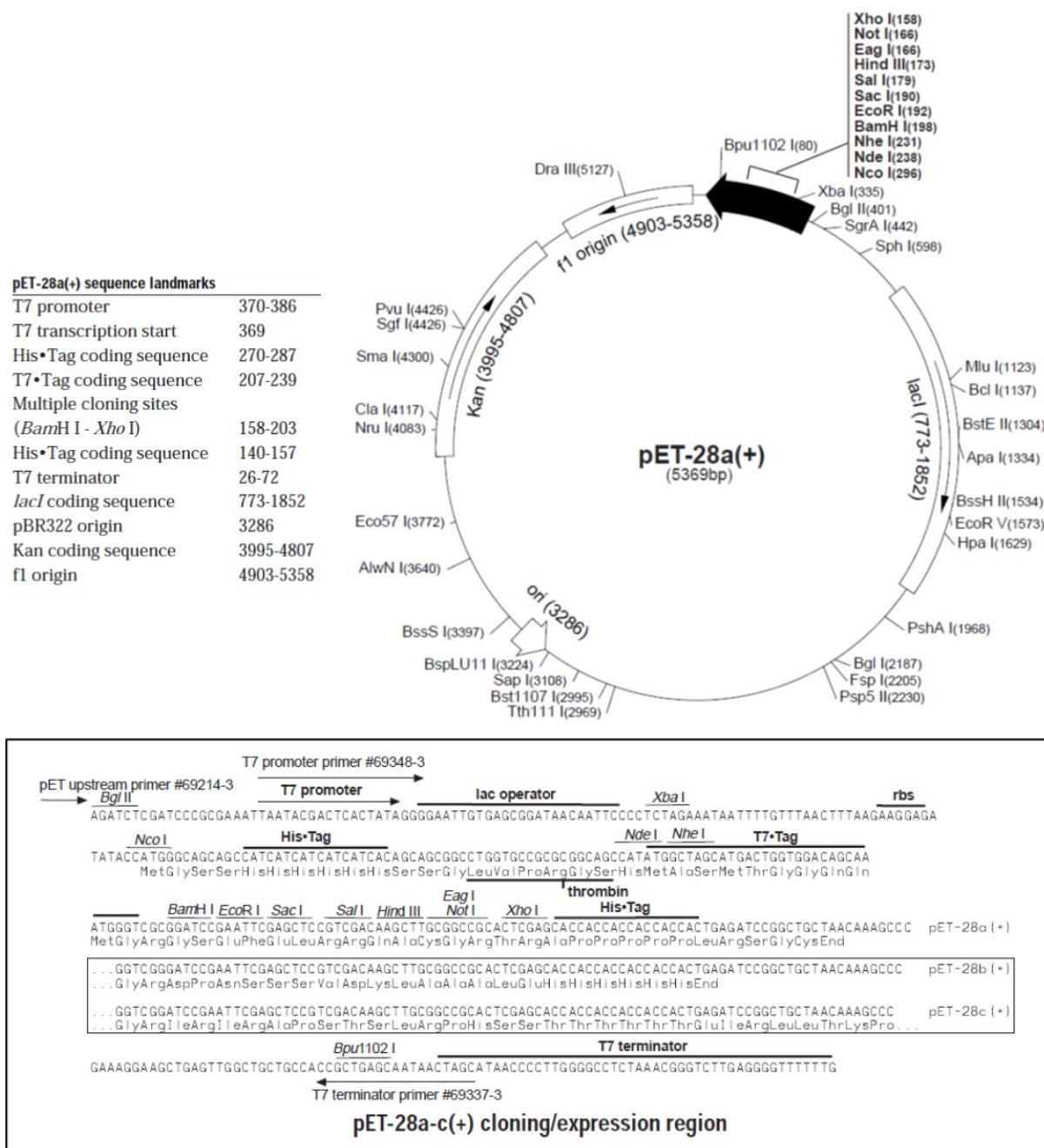


Figure 40. Novagen pET-28a-c(+) vector map and display of the cloning region. (Adapted from Merck KGaA (Germany))

The maps for Novagen pET-28b(+) and pET-28c(+) are the same as pET-28a(+) (shown) with the following exceptions: pET-28b(+) is a 5368bp plasmid; subtract 1bp from each site beyond *Bam*H I at 198. pET-28c(+) is a 5367bp plasmid; subtract 2bp from each site beyond *Bam*H I at 198 (Novagen pET-28a(+) datasheet from Merck KGaA (Germany)).

7.3 NICKEL REMOVAL DURING DIALYSIS

The protein constructs were purified *via* nickel (Ni^{2+}) affinity chromatography, using the high affinity of Ni^{2+} ions and the His-tag fused to the proteins. Ni^{2+} ions may wash down from the affinity column and stay in the purified protein solution. Those ions should be removed during dialysis but could, theoretically, also stay bound to the His-tag or the copper-binding motive of the here purified copper chaperone derivatives. Therefore, it is interesting to evaluate the Ni^{2+} content in the dialyzed protein samples.

Ni^{2+} ions in solution can be detected by adding ammonia (NH_3) to perform an alkaline reaction and form the metal ammine complexes $[\text{Ni}(\text{NH}_3)_6]^{2+}$, which will change the solution's color from green to blue in the first step. In the second step, in ethanol diluted dimethylglyoxime (DMG) is added and precipitates as red Ni^{2+} bis(dimethylglyoximate). The solution's color changes to red. The discoloring is Ni^{2+} -dependent and can be measured with a spectrophotometer at 550 nm. A standard curve is recorded to calibrate the Ni^{2+} concentration measurement.

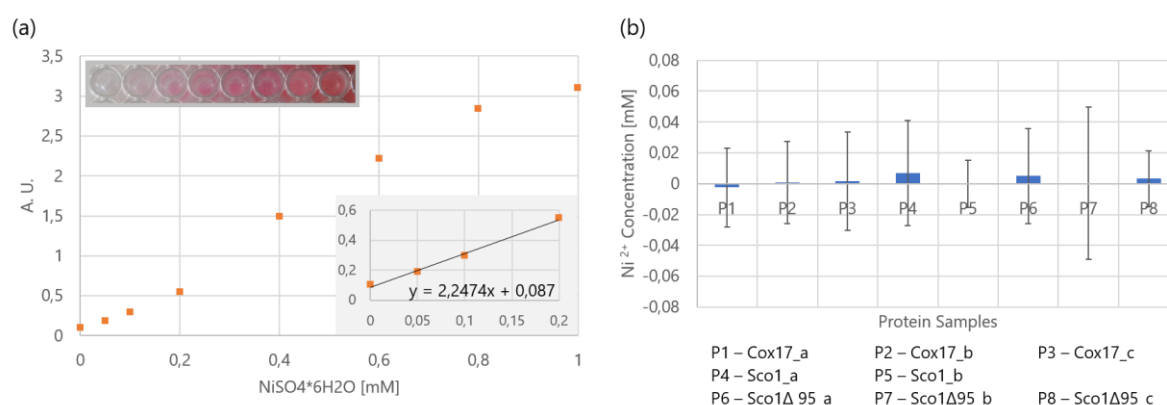


Figure 41. Quantification of Ni^{2+} residues in dialyzed protein samples *via* the NH_3 and DMG complexation.

The standard curve for Ni^{2+} in solution represented in (a) shows a monotonous behavior for photometric measurements at 550 nm. Saturation is reached between 1 and 5 mM. The inset graph shows a zoom-in for low concentrations between 0 and 0.2 mM and its linear regression. The Ni^{2+} concentration-dependent discoloration under the addition of ammonia (NH_3) and DMG is displayed in the inset image. The three-fold measured Ni^{2+} concentration of different protein samples after protein purification and dialysis is shown in (b).

The Ni^{2+} content of purified and dialyzed protein samples was measured using this method (Figure 41). A standard curve was recorded and a linear regression fitted to the linear and relevant range (Figure 41 a). The protein samples show no to very little Ni^{2+} concentration around the detection limit (Figure

41 b). The actual measured concentration should be handled with care because of high relative errors, but they imply no significant relevance of remaining Ni²⁺ ions in the dialyzed protein samples.

7.4 DGR ASSAY

Differential Scanning Fluorimetry Guided Refolding (DGR) was briefly introduced in Ch. 4.2.1. Initial tests were conducted with freshly purified Ccg-2 before dialysis. The RUBIC Buffer Screen from Molecular Dimensions (a company of Calibre Scientific, Inc, USA) was used to test 96 different buffers in a 96 well-plate during protein refolding. This way, buffer conditions should be found that facilitate a proper refolding of the proteins after denatured purification. The setup of the 96 buffers from the RUBIC Buffer Screen is shown in Figure 42.

	1	2	3	4	5	6	7	8	9	10	11	12
A	Water	100mM Citrate pH 4.0	100mM Na acetate pH 4.5	100mM Citrate pH 5.0	100mM MES pH 6.0	100mM K phosphate monobasic pH 6.0	100mM Citrate pH 6.0	100mM Bis-Tris pH 6.5	100mM MES pH 6.5	100mM Na2 phosphate monobasic pH 7.0	100mM K phosphate monobasic pH 7.0	100mM HEPES pH 7.0
B	100mM MOPS pH 7.0	100mM Am acetate pH 7.3	100mM Tris-HCl pH 7.5	100mM Na2 phosphate monobasic pH 7.5	100mM Imidazole pH 7.5	100mM HEPES pH 8.0	100mM Tris-HCl pH 8.0	100mM Tricine pH 8.0	100mM BICINE pH 8.0	100mM BICINE pH 8.5	100mM Tris-HCl pH 8.5	100mM CHES pH 9.0
C	Water 250mM NaCl	100mM Citrate 250mM NaCl pH 4.0	100mM Na acetate 250mM NaCl pH 4.5	100mM Citrate 250mM NaCl pH 5.0	100mM MES 250mM NaCl pH 6.0	100mM K phosphate 250mM NaCl pH 6.0	100mM Citrate 250mM NaCl pH 6.0	100mM Bis-Tris 250mM NaCl pH 6.5	100mM MES 250mM NaCl pH 6.5	100mM Na2 phosphate 250mM NaCl pH 7.0	100mM K phosphate 250mM NaCl pH 7.0	100mM HEPES 250mM NaCl pH 7.0
D	100mM MOPS 250mM NaCl pH 7.0	100mM Am acetate 250mM NaCl pH 7.3	100mM Tris-HCl 250mM NaCl pH 7.5	100mM Na2 phosphate 250mM NaCl pH 7.5	100mM Imidazole 250mM NaCl pH 7.5	100mM HEPES 250mM NaCl pH 8.0	100mM Tris-HCl 250mM NaCl pH 8.0	100mM Tricine 250mM NaCl pH 8.0	100mM BICINE 250mM NaCl pH 8.0	100mM BICINE 250mM NaCl pH 8.5	100mM Tris-HCl 250mM NaCl pH 8.5	100mM CHES 250mM NaCl pH 9.0
E	100mM SPG pH 4.0	100mM SPG pH 4.5	100mM SPG pH 5.0	100mM SPG pH 5.5	100mM SPG pH 6.0	100mM SPG pH 6.5	100mM SPG pH 7.0	100mM SPG pH 7.5	100mM SPG pH 8.0	100mM SPG pH 8.5	100mM SPG pH 9.0	100mM SPG pH 10.0
F	20mM HEPES pH 7.5	50mM HEPES pH 7.5	125mM HEPES pH 7.5	250mM HEPES pH 7.5	20mM Na2 phosphate monobasic pH 7.5	50mM Na2 phosphate monobasic pH 7.5	125mM Na2 phosphate monobasic pH 7.5	250mM Na2 phosphate monobasic pH 7.5	20mM Tris-HCl pH 8.0	50mM Tris-HCl pH 8.0	125mM Tris-HCl pH 8.0	250mM Tris-HCl pH 8.0
G	50mM HEPES 50mM NaCl pH 7.5	50mM HEPES 125mM NaCl pH 7.5	50mM HEPES 250mM NaCl pH 7.5	50mM HEPES 500mM NaCl pH 7.5	50mM HEPES 750mM NaCl pH 7.5	50mM HEPES 1000mM NaCl pH 7.5	50mM Tris-HCl 50mM NaCl pH 8.0	50mM Tris-HCl 125mM NaCl pH 8.0	50mM Tris-HCl 250mM NaCl pH 8.0	50mM Tris-HCl 500mM NaCl pH 8.0	50mM Tris-HCl 750mM NaCl pH 8.0	50mM Tris-HCl 1000mM NaCl pH 8.0
H	50mM MES / Bis-Tris pH 6.0	50mM MES / Imidazole pH 6.5	50mM Bis-Tris / PIPES pH 6.5	50mM MOPS / Bis-Tris propane pH 7.0	50mM Na phosphate / Citrate pH 7.5	50mM MOPS / Na HEPES pH 7.5	0.1M BICINE / Tris pH 8.5	50mM Imidazole 100mM NaCl pH 7.5	125mM Imidazole 100mM NaCl pH 7.5	250mM Imidazole 100mM NaCl pH 7.5	350mM Imidazole 100mM NaCl pH 7.5	500mM Imidazole 100mM NaCl pH 7.5

Figure 42. RUBIC Buffer Screen Setup.

The concentrations shown are final concentrations based on the 25 µL assay. The SPG buffer is a special buffer consisting of Succinic acid, Sodium phosphate monobasic monohydrate, and Glycine: pH 4.0-10.0. Orange – Buffer and pH screening with low ionic strength. White – water sample. Yellow – buffer and pH screens with high ionic strength. Pink – extended range pH buffer. Purple – ionic strength effect (buffer). Green – ionic strength effect (salt). Blue – buffer systems Imidazole. From: RUBIC Buffer Screen, MD1-96, Molecular Dimensions

The protocol was designed by adjusting the published DGR protocol to the needs of Ccg-2 refolding (Lee et al. 2019). The biggest obstacle is the necessary amount of protein. 120 µL of 1 mg/mL protein is needed, namely in an imidazole-free 8 M Urea buffer. The yielded Ccg-2 protein concentrations after denatured protein purification are by a factor 3 – 5 lower according to Lowry protein concentration

measurements. The concentrating procedure and buffer exchange using spin columns are time-consuming and might include protein loss due to the filter's clotting. The initial protein solution production needs optimization.

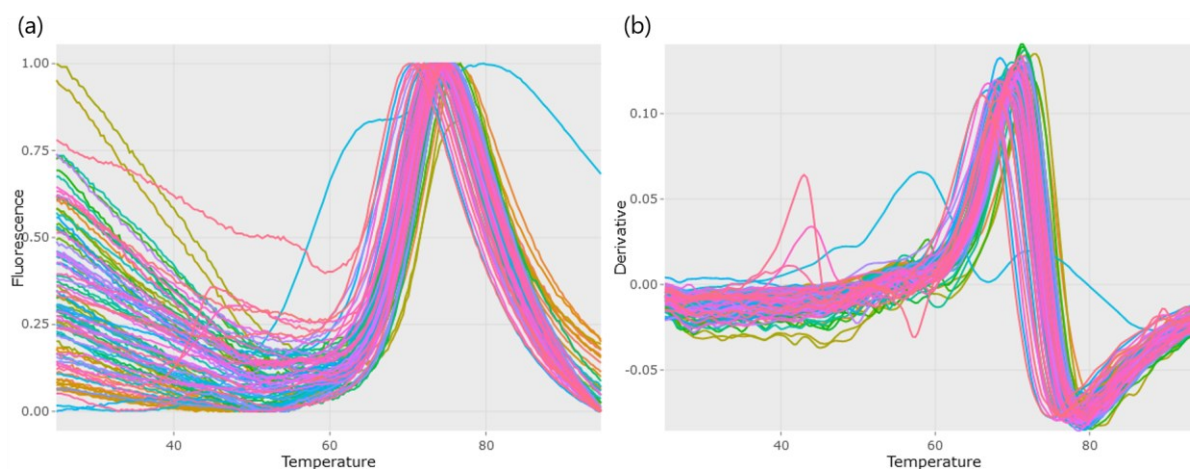


Figure 43. DGR measurements of hydrophobin Ccg-2 for all 96 buffers with the fluorescent dye SYPRO orange.

The temperature-dependent fluorescence measurements were normalized here (a). High initial fluorescence indicates unfolded or aggregated protein. The fluorescence graph's derivative (b) follows a sigmoidal shape with a melting temperature ($x(y = 0)$) between 40 and 80 °C if the protein undergoes a melting transition. Surprisingly, most buffers show evident melting of the hydrophobin Ccg-2. It indicates that the protein was first correctly refolded by some buffers and then melted under temperature increase.

The prepared 96-well plate was transferred to a quantitative PCR (qPCR) thermal cycler from Bio-Rad Laboratories GmbH (Germany) with gradient features. The program was set for a temperature ramp between 20 and 95 °C, and the FAM ($\lambda_{exc} = 495$ nm) and HEX ($\lambda_{em} = 556$ nm) detector were used. The results were saved in a CSV-format. The MeltTraceur Web App (<https://melttraceur.com>) is a free online tool used in the DGR protocol (Lee et al. 2019). The data were loaded (Figure 43) and analyzed step by step as described. The objectives are to exclude some buffer conditions for clearly showing unfolded protein and find clusters of beneficial buffer conditions.

The graph selection basing on curve analysis shows three clusterings of wells (Figure 44). The RUBIC Buffer Screen was set up as a systematic screen. Consequently, neighboring wells might have similar conditions that also support properly folded protein. Surprisingly, simple buffer matrices – even water – and throughout an extensive pH range of pH 4.0 – 7.0 (A2 – A10) appear to exhibit folded protein that undergoes melting transition at high temperatures. A small cluster is found for buffers around pH 4.0 – 5.0 (A2 - 4, C3) with relatively high T_m , which resembles the redox-refolding buffer (pH 5.3) the

best. Surprisingly, an accumulation of high T_m values can be found roughly for wells E9 – G12 with almost exclusively pH 8.0 values (E11 has pH 9.0). E9 and E11 are based on the SPG buffer. The other wells' buffers are based on a Tris-HCl base.

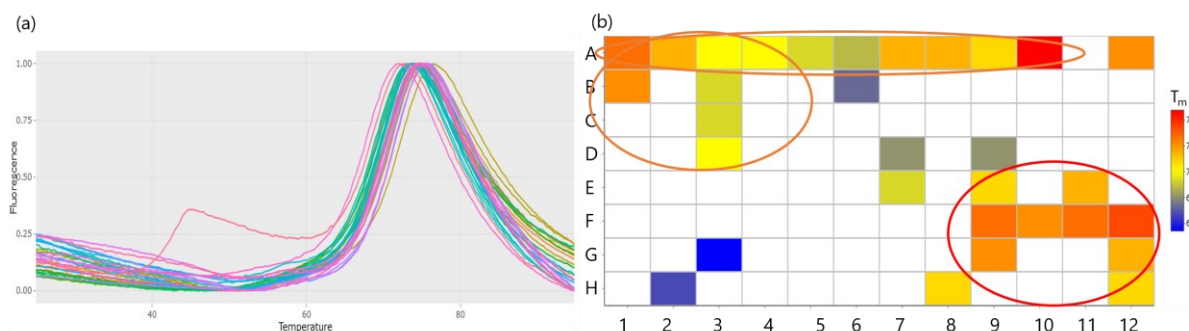


Figure 44. Selection of graphs and 96 well-plate representation of the melting temperatures T_m .

By manually filtering the graphs based on the presented data analysis of, for example, a histogram of the distribution of melting temperatures T_m , a selection of buffers remains (a), and clustering of wells becomes visible (b). Three clusters could be roughly identified (circles) High melting temperatures are favorable. Single promising-looking measurements (e.g., H2 (pink, irregular graph) or G3) are most likely false positives due to measuring air bubbles or other irritations.

Furthermore, the redox-refolding buffer should be tested in the DGR assay to verify its functionality compared to the other screened buffers. Triplet measurements would verify the results, make it easier to exclude samples due to measuring air bubbles. Furthermore, the RUBIC Buffer Additive Screen from Molecular Dimensions (a company of Calibre Scientific, Inc, USA) could be tested in secondary screening. It includes small molecules that might affect the stability and the folding, aggregation, or solubility state of proteins. A secondary screening can be conducted testing the effect of additional molecules.

7.5 SCP DIAMETER

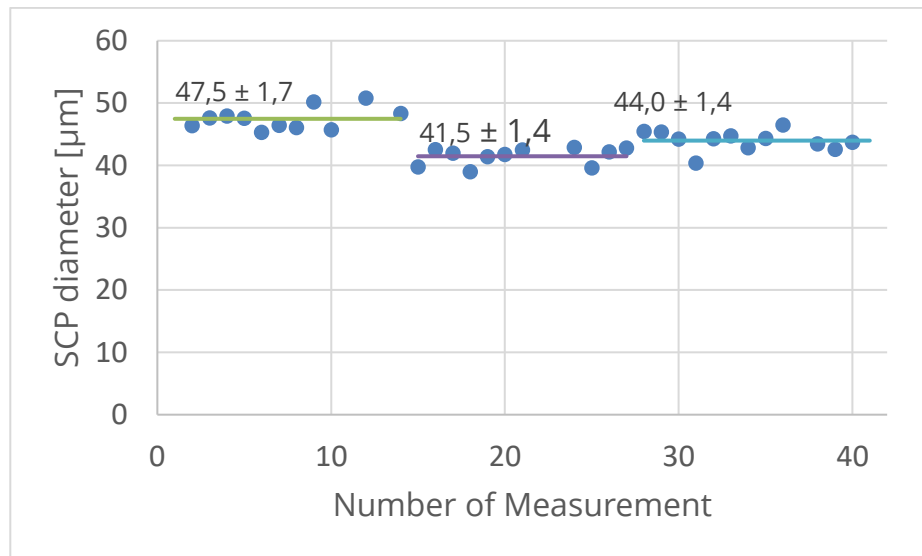


Figure 45. Measurements of SCP diameters.

The diameter of SCPs was measured on three different days and from SCPs from different syntheses. Each day's mean value was marked by a green, purple, and blue line. The mean value and the standard deviation are in micrometer. Relative errors of 3.5%, 3.4%, and 3.2%, respectively, result.

ACKNOWLEDGEMENTS

The process of creating this work has been a great challenge for me and, at the same time, an immensely fascinating venture. It would not have been possible if it was not for the tremendous support of several people.

First, I would like to thank my supervisors Professor Gerhard Rödel and Dr. Kai Ostermann. I am grateful to have been given this opportunity to be part of Prof. Rödel's research group and to learn every day. Only through this support was I able to perform my PhD study. I would like to express my deep gratitude to Dr. Kai Ostermann for his scientific guidance and moral support at every stage of the research project. Continuously, he through and through encouraged me to overcome obstacles.

Furthermore, I want to thank all my present and former colleagues for their help, patience, and fruitful discussions in our office. I could always be sure of their support especially in any biological questions and laboratory matters; and colleagues have even turned to be friends. I am particularly thankful for working closely together with my colleague Julia Döring and our regular scientific exchange.

I highly appreciated being a part of the projects PARTOS and GlyHo. They made my research possible. Furthermore, I would like to greatly acknowledge Professor Tilo Pompe for scientific consultancy and vast help with the microscope challenges. Additionally, I highly enjoyed and appreciated the close collaboration with his research group at Leipzig University. I am also very thankful for the TU Dresden Graduate Academy's extensive training opportunities, which supported me highly in my writing process and preparation for further career steps.

I owe my deepest gratitude to my family and close friends. I truly thank my parents: I could always be sure of their great support, their help, and their love. Also, I want to highly thank my husband and my two great children, who have always had my back. I could not have done it without them.

Thank you!

DECLARATION OF AUTHORSHIP

I, Lisa Hannusch, hereby certify that I have prepared this thesis without the unauthorized assistance of third parties and without the use of any aids other than those indicated; Any ideas taken directly or indirectly from external sources are identified as such. The same or similar work has not been submitted to any other examining authority, neither in Germany nor abroad.

Hiermit versichere ich, Lisa Hannusch, dass ich die vorliegende Arbeit ohne unzulässige Hilfe Dritter und ohne Benutzung anderer als der angegebenen Hilfsmittel angefertigt habe; die aus fremden Quellen direkt oder indirekt übernommenen Gedanken sind als solche kenntlich gemacht. Die Arbeit wurde bisher weder im Inland noch im Ausland in gleicher oder ähnlicher Form einer anderen Prüfungsbehörde vorgelegt.

Datum, Unterschrift

Diese Dissertation wurde unter der wissenschaftlichen Betreuung von Professor Dr. Gerhard Rödel im Fachbereich Biologie am Institut für Genetik der TU Dresden angefertigt.